



HAL
open science

Characterization and modeling of microstructural evolutions during the thermal treatment of cold-rolled Dual-Phase steels

Mélanie Ollat

► **To cite this version:**

Mélanie Ollat. Characterization and modeling of microstructural evolutions during the thermal treatment of cold-rolled Dual-Phase steels. Materials. Université de Lyon, 2017. English. NNT : 2017LY-SEI097 . tel-01920855

HAL Id: tel-01920855

<https://theses.hal.science/tel-01920855>

Submitted on 13 Nov 2018

HAL is a multi-disciplinary open access archive for the deposit and dissemination of scientific research documents, whether they are published or not. The documents may come from teaching and research institutions in France or abroad, or from public or private research centers.

L'archive ouverte pluridisciplinaire **HAL**, est destinée au dépôt et à la diffusion de documents scientifiques de niveau recherche, publiés ou non, émanant des établissements d'enseignement et de recherche français ou étrangers, des laboratoires publics ou privés.



N°d'ordre
2017LYSEI097

NNT :

THESE de DOCTORAT **DE L'UNIVERSITE DE LYON**
opérée au sein de
L'Institut National des Sciences Appliquées de Lyon

Ecole Doctorale N° EDA 034
Matériaux de Lyon

Spécialité de doctorat : Matériaux

Soutenue publiquement le 20/10/2017, par :
Mélanie Ollat

Characterization and modeling of
microstructural evolutions during the
thermal treatment of cold-rolled
Dual-Phase steels

Devant le jury composé de :

Sybrand Van Der ZWAAG	Professeur	TU Delft	Rapporteur
Elisabeth GAUTIER	Directeur de recherches	Jean Lamour	Rapporteur
Yves BRECHET	Professeur	SIMAP	Examineur
Mohamed GOUNE	Professeur	ICMCB Bordeaux	Examineur
Véronique MASSARDIER	Maitre de conférences	INSA Lyon	Directeur de thèse
Michel PEREZ	Professeur	INSA Lyon	Directeur de thèse
Damien FABREGUE	Professeur	INSA Lyon	Directeur de thèse
Eric BUSCARLET	Docteur	FIVES KEODS	Examineur
Philippe ROCABOIS	Docteur	FIVES KEODS	Invité

Département FEDORA – INSA Lyon - Ecoles Doctorales – Quinquennal 2016-2020

SIGLE	ECOLE DOCTORALE	NOM ET COORDONNEES DU RESPONSABLE
CHIMIE	CHIMIE DE LYON http://www.edchimie-lyon.fr Sec : Renée EL MELHEM Bat Blaise Pascal 3 ^e etage secretariat@edchimie-lyon.fr Insa : R. GOURDON	M. Stéphane DANIELE Institut de Recherches sur la Catalyse et l'Environnement de Lyon IRCELYON-UMR 5256 Équipe CDFA 2 avenue Albert Einstein 69626 Villeurbanne cedex directeur@edchimie-lyon.fr
E.E.A.	ELECTRONIQUE, ELECTROTECHNIQUE, AUTOMATIQUE http://edeea.ec-lyon.fr Sec : M.C. HAVGOUDOUKIAN Ecole-Doctorale.eea@ec-lyon.fr	M. Gérard SCORLETTI Ecole Centrale de Lyon 36 avenue Guy de Collongue 69134 ECULLY Tél : 04.72.18 60.97 Fax : 04 78 43 37 17 Gerard.scorletti@ec-lyon.fr
E2M2	EVOLUTION, ECOSYSTEME, MICROBIOLOGIE, MODELISATION http://e2m2.universite-lyon.fr Sec : Sylvie ROBERJOT Bât Atrium - UCB Lyon 1 04.72.44.83.62 Insa : H. CHARLES secretariat.e2m2@univ-lyon1.fr	M. Fabrice CORDEY CNRS UMR 5276 Lab. de géologie de Lyon Université Claude Bernard Lyon 1 Bât Géode 2 rue Raphaël Dubois 69622 VILLEURBANNE Cédex Tél : 06.07.53.89.13 cordey@univ-lyon1.fr
EDISS	INTERDISCIPLINAIRE SCIENCES-SANTE http://www.ediss-lyon.fr Sec : Sylvie ROBERJOT Bât Atrium - UCB Lyon 1 04.72.44.83.62 Insa : M. LAGARDE secretariat.ediss@univ-lyon1.fr	Mme Emmanuelle CANET-SOULAS INSERM U1060, CarMeN lab, Univ. Lyon 1 Bâtiment IMBL 11 avenue Jean Capelle INSA de Lyon 696621 Villeurbanne Tél : 04.72.68.49.09 Fax :04 72 68 49 16 Emmanuelle.canet@univ-lyon1.fr
INFOMATHS	INFORMATIQUE ET MATHEMATIQUES http://infomaths.univ-lyon1.fr Sec : Renée EL MELHEM Bat Blaise Pascal, 3 ^e étage Tél : 04.72. 43. 80. 46 Fax : 04.72.43.16.87 infomaths@univ-lyon1.fr	M. Luca ZAMBONI Bâtiment Braconnier 43 Boulevard du 11 novembre 1918 69622 VILLEURBANNE Cedex Tél :04 26 23 45 52 zamboni@maths.univ-lyon1.fr
Matériaux	MATERIAUX DE LYON http://ed34.universite-lyon.fr Sec : Marion COMBE Tél:04-72-43-71-70 –Fax : 87.12 Bat. Direction ed.materiaux@insa-lyon.fr	M. Jean-Yves BUFFIERE INSA de Lyon MATEIS Bâtiment Saint Exupéry 7 avenue Jean Capelle 69621 VILLEURBANNE Cedex Tél : 04.72.43 71.70 Fax 04 72 43 85 28 Ed.materiaux@insa-lyon.fr
MEGA	MECANIQUE,ENERGETIQUE,GENIE CIVIL,ACOUSTIQUE http://mega.universite-lyon.fr Sec : Marion COMBE Tél:04-72-43-71-70 –Fax : 87.12 Bat. Direction mega@insa-lyon.fr	M. Philippe BOISSE INSA de Lyon Laboratoire LAMCOS Bâtiment Jacquard 25 bis avenue Jean Capelle 69621 VILLEURBANNE Cedex Tél : 04.72 .43.71.70 Fax : 04 72 43 72 37 Philippe.boisse@insa-lyon.fr
ScSo	ScSo* http://recherche.univ-lyon2.fr/scso/ Sec : Viviane POLSINELLI Brigitte DUBOIS Insa : J.Y. TOUSSAINT Tél : 04 78 69 72 76 viviane.polsinelli@univ-lyon2.fr	M. Christian MONTES Université Lyon 2 86 rue Pasteur 69365 LYON Cedex 07 Christian.montes@univ-lyon2.fr

*ScSo : Histoire, Géographie, Aménagement, Urbanisme, Archéologie, Science politique, Sociologie, Anthropologie

Contents

Liste des ecoles doctorales	i
Contents	iii
List of Figures	ix
List of Tables	xix
Introduction	xxi
1 Literature Review	1
1.1 Dual-Phase steels	2
1.2 Microstructural evolutions during the thermal treatments of DP steels	4
1.2.1 Intercritical annealing	4
1.2.1.1 Recovery/recrystallization	5
1.2.1.2 Cementite spheroidization	5
1.2.1.3 Phase transformation $\alpha + \text{Fe}_3\text{C} \rightarrow \gamma$	6
1.2.1.4 Interaction recrystallization/phase transformation	11
1.2.2 Quenching	14
1.2.2.1 Products of austenite decomposition	14
1.2.2.2 $\gamma \rightarrow \alpha'$ phase transformation	15
1.2.3 Tempering	19
1.2.3.1 Tempering stages	19
1.2.3.2 Influence of alloying elements	20
1.2.3.3 Tempering of dual-phase microstructure	21
1.3 Modeling tools for the prediction of microstructural evolutions	22
1.3.1 Empirical modeling	23
1.3.1.1 Johnson-Mehl-Avrami-Kolmogorov (JMAK) law	23
1.3.1.2 Koistinen-Marburger (KM) law	26
1.3.2 Thermodynamics of phase transformation	26
1.3.2.1 Binary Fe-C system	27
1.3.2.2 Ternary Fe-C-X system	28
1.3.2.3 Multicomponent system	31
1.3.3 Physically based modeling	32
1.3.3.1 Diffusion-controlled	32

1.3.3.2	Interface-controlled	33
1.3.3.3	Mixed-mode	34
1.3.3.4	Other modeling approaches	34
1.4	Conclusion	37
2	Material and experimental techniques	39
2.1	Material	39
2.2	Experimental strategy	43
2.3	Experimental techniques	44
2.3.1	Thermal treatments	44
2.3.1.1	<i>Gleeble</i> thermomechanical simulator	44
2.3.1.2	Salt baths and furnaces	44
2.3.2	Microstructural observations	46
2.3.3	In-situ techniques	49
2.3.3.1	Dilatometry	49
2.3.3.2	In-situ XRD	51
2.3.4	Ex-situ techniques	54
2.3.4.1	TEP	54
2.3.4.2	Hardness	56
2.3.5	Thermodynamic database	56
3	Characterization and empirical modeling of the microstructural evolutions during intercritical annealing	59
3.1	Preliminary works on the non-isothermal austenite formation kinetics . . .	60
3.1.1	Comparison of the non-isothermal austenite formation kinetics obtained with various techniques	60
3.1.2	Non-isothermal austenite formation kinetics on the cold-rolled steel and on the prior recrystallized steel	61
3.2	Decorrelation of mechanisms	64
3.2.1	Austenite formation without recrystallization	64
3.2.1.1	Non-isothermal conditions	64
3.2.1.2	Typical industrial annealing conditions: heating plus isothermal holding cycles	66
3.2.1.3	Microstructural observations	67
3.2.2	Recrystallization without austenite formation	69
3.2.2.1	Isothermal conditions	69
3.2.2.2	Typical industrial annealing conditions: heating plus isothermal holding cycles	71
3.2.2.3	Microstructural observations	72
3.3	Case of the cold-rolled steel: interaction between recrystallization and austenite formation	73
3.3.1	Interaction map	74
3.3.2	Austenite formation with recrystallization	76
3.3.2.1	Non-isothermal conditions	77

3.3.2.2	Typical industrial annealing conditions: heating plus isothermal holding cycles	78
3.3.2.3	A tool to predict microstructural evolutions during the intercritical treatments of CR-steels	80
3.4	Discussion	81
3.4.1	Influence of the initial state on the austenite formation kinetics . . .	81
3.4.2	Influence of the temperature and of the heating rate on the austenite formation kinetics	83
3.4.2.1	Case of the ReX-steel	83
3.4.2.2	Case of the CR-Steel	85
3.5	Conclusion	87
4	Mixed-mode model for austenite formation	89
4.1	Adaptation of the Mixed-mode model	89
4.1.1	Theory	89
4.1.2	Numerical algorithm	91
4.1.3	Initial state and model parameters	92
4.2	Mixed-mode model <i>versus</i> experimental kinetics	94
4.2.1	Dependence of the kinetics with the mobility parameter M	95
4.2.2	Comparison with experiments	96
4.2.2.1	Typical industrial cycles: heating plus isothermal holding	96
4.2.2.2	Non-isothermal cycles	99
4.3	Discussion	100
4.4	Conclusion	102
5	Ternary Fe-C-Mn diffusive model for austenite formation	105
5.1	DICTRA simulation conditions	106
5.1.1	Definition of a representative system	106
5.1.2	Preliminary study: investigation of DICTRA options	108
5.2	Influence of microstructural parameters	113
5.2.1	System size	113
5.2.2	Cementite's Mn content	114
5.2.2.1	Low-Mn enrichment in cementite ($C_{Mn}^{Fe_3C} < 15$ wt%)	114
5.2.2.2	High-Mn enrichment in cementite ($C_{Mn}^{Fe_3C} > 15$ wt%)	116
5.2.2.3	Qualitative comparison	116
5.3	Application to austenite formation kinetics on the ReX-steel and on the CR-steel	122
5.3.1	Influence of Mn content in cementite	122
5.3.2	Influence of the representative size	125
5.4	Discussion	125
5.4.1	DICTRA applications to model the austenite formation	125
5.4.2	Others concomitant phenomena	128
5.5	Conclusion	129
6	Characterization of the microstructural evolutions during the cooling	

and the tempering stages	131
6.1 Austenite decomposition during cooling stage	132
6.1.1 Characterization of the two initial states considered in this study . .	132
6.1.2 Cooling of a fully austenitic state (100% γ -state)	133
6.1.2.1 Kinetics of austenite decomposition of the 100% γ -state . .	133
6.1.2.2 Microstructural observations after cooling of the 100% γ -state	134
6.1.3 Cooling of a ferrite-austenite mixture (60% γ -state)	136
6.1.3.1 Kinetics of austenite decomposition of the 60% γ -state . . .	136
6.1.3.2 Microstructural observations after cooling a 60% γ -state . .	139
6.1.4 Comparison between the CCT diagrams of the 100% γ -state and the 60% γ -state	139
6.1.5 Analysis of the martensite formation kinetics of the steel in the 100% γ -state and in the 60% γ -state	141
6.1.5.1 Martensite start temperature (M_S)	141
6.1.5.2 Austenite-to-martensite transformation kinetics ($f_{\alpha'}$) . . .	143
6.1.5.3 Conclusion	144
6.2 Martensite tempering of the fully martensitic steel	145
6.2.1 Identification of the martensite tempering mechanisms between 200 and 500°C	145
6.2.1.1 TEP kinetics	145
6.2.1.2 EDS analysis on TEM replicas	147
6.2.2 Quantification of the amount of precipitated carbon during tempering	148
6.2.2.1 Quantification by TEP	148
6.2.2.2 Quantification by FIB/SEM tomography	150
6.2.2.3 Prediction of the fraction of precipitated carbon	153
6.2.3 Hardness evolution during tempering	154
6.2.3.1 Hardness kinetics	154
6.2.3.2 Comparison of estimated carbon content in solid solution and segregated	155
6.3 Prospective works on the tempering of a ferrite-martensite microstructure .	157
6.4 Discussion and conclusion	158
 Conclusion and Perspectives	 161
 A Local Equilibrium conditions for the $\gamma \rightarrow \alpha$ transformation	 169
A.1 Two-modes of ferrite formation: LEP <i>versus</i> LENP	169
A.2 Local Equilibrium with Partitioning (LEP)	171
A.3 Local Equilibrium with Negligible Partitioning (LENP)	171
 B Monitoring of austenite formation by experimental techniques	 175
B.1 Isothermal monitoring of austenite formation	175
B.2 Overview of strength/error sources of experimental techniques	175
 C XRD method to follow microstructure evolutions	 179
C.1 Annealing in the austenitic domain	179
C.1.1 Case of the ReX-steel	179

C.1.2 CR-steel case	180
C.2 Annealing in the intercritical domain	181
D Modeling of the austenite formation kinetics on the CR-steel	183
D.1 JMAK parametrization of non-isothermal conditions	183
D.2 Recrystallization inhibition in non-isothermal conditions	184
E DICTRA calculation of the $\text{Fe}_3\text{C}+\alpha \rightarrow \gamma$ transformation	189
References	195

List of Figures

1	Typical thermal cycle used for the processing of DP steels composed of an intercritical annealing treatment followed by a cooling stage and a tempering stage. Variables written in red colour refer to evaluated data during this PhD-work.	xxiii
1.1	(a) Overview of tensile strength and total elongation for various AHSS grades [MAT 12]; (b) Examples of AHSS used in the body-in-white structure of a commercialized Ford Fusion [AUT].	2
1.2	(a) SEM micrograph of a DP steel combining a ferrite matrix (α) and a hard phase (martensite (α')); (b) Typical thermal treatment of DP steels.	3
1.3	(a) Tensile and (b) work hardening curves of DP steels containing 15% martensite and different carbon levels [PIE 14].	4
1.4	SEM micrographs of a cold-rolled DP steel during a heating stage at 1°C/s up to various temperatures: (a) 510, (b) 670 and (c) 730°C [AZI 11].	6
1.5	SEM micrographs highlighting austenite nucleation sites during intercritical annealing treatments at 700°C for (a) 180 s and (b) 1 h [LAI 16].	8
1.6	(a) Various transformation steps and (b) associated TTT graph of the austenite formation according to Speich <i>et al.</i> [SPE 81].	9
1.7	(a) Cementite dissolution regime as a function of Mn content in cementite and temperature defined by Gouné <i>et al.</i> [GOU 12] (b) Calculated kinetics on DICTRA of austenite growth at 740°C for 7 and 25 wt%Mn in cementite [LAI 14].	10
1.8	Effect of the heating rate (1 or 100°C/s) on the isothermal austenite formation kinetics for hot-rolled and cold-rolled Fe-0.06C-1.86Mn-0.11Mo (wt%) steels at 750°C [HUA 04].	10
1.9	(a) SEM micrograph highlighting the recrystallization and phase transformation interaction by the presence of recrystallized ferrite (F), deformed ferrite (DF) and martensite grains (M, prior austenite grain) [AZI 11]. (b) Interaction map of intercritical phenomena proposed by Kulakov <i>et al.</i> [KUL 13a].	11
1.10	(a) Schematic representation of the heating rate influence [5-500°C/s] on the microstructure after annealing at 770°C and (b-d) corresponding optical micrographs [LI 13].	13

1.11	Microstructural evolutions during holding at (a) 740 and (b) 780°C in the case of a strong interaction (obtained with high heating rate: 100°C/s) [BAR 15a].	14
1.12	Various austenite decomposition paths as a function of the cooling rate for a 0.41C-1.04Cr-0.71Mn-0.22Si-0.26Ni wt% alloy (points correspond to experimental dilatometry data while lines are predicted by a modified Koistinen-Marburger law) [VAN 10].	15
1.13	Schematic representation of (a) the <i>bct</i> martensitic cell: iron atoms are displaced to accord with carbon atoms presence [KRA 99]; and of (b) the complex martensite microstructure [FUR 04].	18
1.14	Various stages of martensite tempering as a function of the tempering temperature for binary Fe-C steels [SPE 72].	20
1.15	(a) Influence of 0.5 wt%Mn addition on hardness of tempered steel at different tempering temperatures [GRA 77]. (b) Evolution of the Mn and Si concentrations during tempering at 650°C. SEM micrographs of (c) Fe-0.6C, (d) Fe-0.6C-1Mn and (e) Fe-0.6C-2Mn steels tempered for 1800 s at 650°C [MIY 07].	22
1.16	(a) Algorithm and (b) various phenomenological laws combined in Kulakov's model considering recrystallization, austenite formation, austenite decomposition into ferrite and bainite phases [KUL 14].	25
1.17	Schematic representation of phase diagram and associated Gibbs free energy diagram at temperature T at thermodynamic equilibrium [GOU 15]. The equilibrium carbon contents in phases (C_C^α, C_C^γ) are represented for the steel containing a carbon content C_C^0	27
1.18	(a) 3D-schematic representation of Gibbs free energy diagram highlighting the iso-chemical potential plane [GOU 15]. (b) Isothermal section of Fe-C-Mn system at 760°C. C (C_C^α, C_C^γ) and Mn ($C_{Mn}^\alpha, C_{Mn}^\gamma$) equilibrium concentrations are emphasised for the nominal composition (C_C^0, C_{Mn}^0).	28
1.19	Model and experimental kinetics of austenite formation during isothermal holding of a quaternary Fe-0.1C-3Mn-1.5Si (wt%) alloy [WEI 13]. The ORTHO equilibrium is achieved after 10^6 s. Intermediate equilibriums are reported (<i>i.e.</i> LENP and LEP).	29
1.20	Isothermal section of the Fe-C-Mn system at 760°C. C and Mn concentration profiles are reported for the $\alpha \rightarrow \gamma$ phase transformation according to the LENP condition. A characteristic Mn narrow "spike" is present at the γ/α interface.	31
1.21	Schematical representation of (a) the Gibbs free energy diagram and (b) the phase diagram in the case of the $\gamma \rightarrow \alpha$ transformation supposing PE condition.	32
1.22	Schematic representation of the mixed-mode model system. Carbon concentration profiles are plotted at different times: at t_0 , at an intermediate time t and at the infinite time t_∞ (for which the γ/α equilibrium is reached). The interface velocity is evaluated as the deviation to the equilibrium by the relation $v = M \times \Delta G$ with $\Delta G = \chi(T) \times (C_C^{\gamma,int} - C_C^{\gamma,eq})$ [MEC 15].	35

1.23	(a) Comparison of experimental and phase field kinetics during heating stages at 10 and 100°C/s. Experimental and model microstructures at 800°C are compared in (b) and (c) respectively (A: austenite; M: martensite; F: recrystallized ferrite; NF: deformed ferrite) [ZHU 15].	37
2.1	SEM micrographs of the (a-b) cold-rolled steel (CR-steel) and (c-d) recrystallized steel (ReX-steel). Cold-rolled steel is characterized by bands of deformed ferrite and pearlite while bands of spheroidized cementite islands and recrystallized ferrite grains are present in the prior recrystallized state.	41
2.2	TEM micrographs on carbon replicas and examples of EDS spectra used to determine the chemical composition in (a-d) the cold-rolled steel and (e-h) the recrystallized steel.	42
2.3	Histograms of (a) Mn and (b) Cr contents quantified by EDS analysis in the cementite particles of the CR-steel and the ReX-steel	43
2.4	(a) Geometry of the samples used for the treatment in the <i>Gleeble</i> machine. (b) Example of thermal cycle performed in the <i>Gleeble</i> machine composed of a quick heating at 100°C/s, followed by a short holding at 800°C during 0.1 s and by a water quench.	46
2.5	(a) Optical micrograph after Bandoch etching: martensite appears white while (ferrite+pearlite) are brown. An example of martensite quantification using <i>ImageJ</i> software is given in (b).	47
2.6	(a) Dilatometry curve obtained during the heating of the steel from 20 to 1000°C and then during rapid cooling down to room temperature. The two slope changes correspond to the ferrite-to-austenite transformation (700-850°C) and to the austenite-to-martensite transformation (200-300°C). (b) Austenite formation kinetics determined from dilatometry experiments.	50
2.7	(a) Dilatometry curves obtained during the cooling of the steel from 850 to 20°C at two different cooling rates: 20 and 40°C/s. The two slope changes, during cooling at 20°C/s are analysed individually in (b), before plotting the complete austenite decomposition (d). The martensite fraction for the steel cooled at 20°C/s was evaluated thanks to the complete martensite transformation kinetics determined at 40°C/s (c).	51
2.8	(a) P07-PETRA beamline with (c) modified <i>Bahr</i> dilatometer for thermal treatment. (c) Schematic representation of the beamline.	52
2.9	(a) Diffraction patterns obtained on the initial cold-rolled steel and after heating at 5°C/s to 710, 750 and 900°C. (b) Example of the <i>Maud</i> analysis identifying austenite and ferrite phases.	53
2.10	Schematic representation of (a) TEP technique and (b) the effect of different defects (solute atoms, segregated atoms, dislocations and precipitates) on the TEP of iron [LAM 14].	54

3.1	Austenite formation kinetics on (a) the ReX-steel and (b) the CR-steel during continuous heating at 5°C/s using different experimental techniques: optical phase quantification, XRD, Bahr dilatometry of the XRD experiment, conventional Bahr dilatometry and Led dilatometry set up on the <i>Gleeble 3500</i> simulator.	62
3.2	Austenite formation kinetics obtained by dilatometry on the: (a) ReX-steel and (b) CR-steel during continuous heating from room temperature to 1000°C with various heating rates (R_H) from 0.5 to 30°C/s. The ORTHO, PARA and LE curves correspond respectively to the orthoequilibrium, paraequilibrium and local equilibrium conditions calculated from Thermo-Calc.	63
3.3	Comparison of the austenite formation kinetics obtained by dilatometry on the ReX-steel and on the CR-steel during continuous heating with three heating rates: (a) $R_H = 0.5$, (b) $R_H = 10$ and (c) $R_H = 30$ °C/s.	63
3.4	Determination of the parameters of the JMAK law: (a) Q and (b) n by the Kissinger method using the non-isothermal kinetics of figure 3.2.a with a heating rate $R_H = 5, 7.5, 10$ or 30°C/s.	65
3.5	Comparison between the experimental austenite formation kinetics of the ReX-steel during continuous heating and the JMAK parametrization. The following parameters were used for the JMAK fit: $Q = 900$ kJ/mol, $n = 0.62$, $b_0 = 6 \times 10^{43}$ s ⁻¹	66
3.6	Comparison between the experimental austenite formation kinetics and the JMAK model for the ReX-steel during isothermal holding at 735, 760, 780°C after a heating ramp with (a) $R_H = 5$ and (b) $R_H = 100$ °C/s. The fractions determined with the JMAK model were calculated considering the local equilibrium condition calculated with Thermo-Calc. The JMAK parameters were determined in continuous heating conditions on the ReX-steel.	67
3.7	SEM micrographs of the ReX-steel heated to 780°C with two heating rates: (a-b) $R_H = 5$ and (c-d) $R_H = 100$ °C/s. Yellow rows point out non-dissolved cementite particles inside newly formed austenite grains.	68
3.8	(a) Hardness and (b) deduced recrystallized fraction evolutions during isothermal holding at 650, 675 and 700°C.	69
3.9	(a) Time-temperature equivalence used to determine the activation energy ($Q = 326$ kJ/mol) for recrystallization. (b) Linearization of the JMAK law to determine the Avrami exponent ($n = 1$).	70
3.10	JMAK fit of the experimental recrystallization kinetics during isothermal holding at 650, 675, 700°C. JMAK parameters are fixed to: $Q = 326$ kJ/mol, $n = 1$ and $b_0 = 3.0 \times 10^{15}$ /s.	71
3.11	Experimental and predicted hardness evolution during a complex cycle (heating at 1°C/s, then holding at 700°C) validating the JMAK model for recrystallization.	72
3.12	SEM micrographs of CR-steel treated at 700°C and water quench after different holding times: (a) 10, (b) 80 and (c) 1200 s. RF= Recrystallized ferrite; DF= Deformed ferrite.	73

3.13	SEM observations of the microstructural states of the CR-steel after heating at 5°C/s to 780°C. The microstructure is composed of a mixture of martensite (M, austenite prior cooling), recrystallized ferrite (RF) and deformed ferrite (DF).	74
3.14	(a) Method to evaluate R_{start} and R_{end} temperatures (resp. start and end temperatures of recrystallization) from continuous heating conditions; (b) Interaction map between recrystallization (blue area) and austenite formation (red) in non-isothermal condition.	75
3.15	Evolution of the recrystallized fraction at A_{c1} temperature as a function of the heating rate.	76
3.16	Comparison between the experimental austenite formation kinetics of the CR-steel and the theoretical kinetics based on a mixture law during continuous heating at 30°C/s: (a) without recrystallization inhibition; (b) with recrystallization inhibition for austenite fractions higher than 10%. The different components of the mixture law were reported in dash points.	78
3.17	(a) Comparison between the experimental austenite formation kinetics of the CR-steel and the theoretical kinetics based on a mixture law during isothermal holding at 720, 735, 760, 780°C after a heating stage with $R_H = 5^\circ\text{C/s}$. The stars correspond to the end of recrystallization and solid lines consider recrystallization inhibition for austenite fraction higher than 10%. (b) Effect of the heating rate on the experimental and modeled austenite formation kinetics during isothermal holding at 760°C	79
3.18	Impact of the recrystallization inhibition consideration on the normalized recrystallization and austenite formation kinetics during a holding at 760°C and after a heating rate equal to (a) $R_H = 5$ and (b) 30°C/s	80
3.19	Screen print of the developed worksheet to describe microstructural evolutions during intercritical annealing as a function of different thermal parameters: heating rate (R_H), holding temperature (T_s) and holding time (t_s).	82
3.20	SEM observations of microstructural states of a cold-rolled steel after heating at (a) 5 and (b) 30°C/s to 720°C. A full spheroidization of cementite is observed after 5°C/s while spheroidization is partial with 30°C/s heating rate.	83
3.21	Effect of the heating rate (R_H) on the austenite formation kinetics during isothermal holding at (a) 760 and (b) 780°C of the ReX-steel. The kinetics were predicted using the JMAK model defined in section 3.2.1.	84
3.22	Effect of the heating rate R_H on the austenite formation kinetics during isothermal holding at (a) 760 and (b) 780°C of a cold-rolled steel. The kinetics were predicted using the JMAK model defined in section 3.2.1.	86
3.23	Comparison of Thermo-Calc and experimental austenite fraction on CR-steel after 1 h and 4 h of isothermal holding as a function of the temperature.	87

4.1	Schematic representation of the mixed-mode model system. Carbon concentration profiles are plotted at different times: the initial time t_0 , an intermediate time t and the infinite time when the γ/α equilibrium is reached t_∞ . The interface velocity is evaluated as the deviation to the equilibrium by the relation $v = M\Delta G$ with $\Delta G = \chi(T) (C_C^{\gamma,int} - C_C^{\gamma,eq})$	91
4.2	Schematic representation of the integration scheme for the austenite formation using the mixed-mode model (around the interface class noted i^*). The green and blue meshing respectively represent the special integration at time t and $t + dt$	93
4.3	Carbon contents in α and γ phases for the nominal composition Fe-0.17C-1.763Mn wt% as a function of temperature assuming LENP condition (Thermo-Calc).	94
4.4	(a) Gibbs energy of the austenite phase as a function of temperature and carbon content (Thermo-Calc). (b) Representation of $\partial G_C^\gamma / \partial C_C^\gamma$ as a function of temperature to express $\chi(T)$ parameter of the equation: $\Delta G = \chi(T) (C_C^{\gamma,int} - C_C^{\gamma,eq})$	95
4.5	(a) Kinetics and (b) respective mode parameter S of austenite formation during isothermal holding at 760°C, for different conditions: diffusion-controlled ($M = 7.4 \times 10^{-7}$ mol.m.J ⁻¹ .s ⁻¹), mixed-mode ($M = 10^{-8}$ mol.m.J ⁻¹ .s ⁻¹) and interface-controlled ($M = 10^{-12}$ mol.m.J ⁻¹ .s ⁻¹).	96
4.6	Carbon concentration profiles in γ/α phases during austenite formation at 760°C for different times. Three conditions are plotted: (a) diffusion-controlled ($M = 7.4 \times 10^{-7}$ mol.m.J ⁻¹ .s ⁻¹), (b) mixed-mode ($M = 10^{-8}$ mol.m.J ⁻¹ .s ⁻¹) and (c) interface-controlled ($M = 10^{-12}$ mol.m.J ⁻¹ .s ⁻¹).	97
4.7	Evolution of the average mode parameter $\langle S \rangle$ as a function of the mobility value at 760°C.	98
4.8	Experimental and mixed-mode model kinetics for austenite formation during isothermal holding after a heating stage of (a) 5 and (b) 100°C/s. Mobility parameters were fixed to $Q_m=900$ kJ/mol and $M_0 = 5 \times 10^{35}$ mol.m.J ⁻¹ .s ⁻¹	99
4.9	Experimental and mixed-mode model kinetics for austenite formation during continuous heating with a heating rate of 5, 7.5, 10 and 30°C/s. Mobility parameters were fixed to $Q_m=900$ kJ/mol and $M_0 = 5 \times 10^{35}$ mol.m.J ⁻¹ .s ⁻¹	100
4.10	Evolution of the carbon evolution profile during a heating at 30°C/s interrupted at different temperatures between 685 and 835°C. Mobility parameters were fixed to $Q_m=900$ kJ/mol and $M_0 = 5 \times 10^{35}$ mol.m.J ⁻¹ .s ⁻¹	101
5.1	Schematic representation of four different modeling configurations: (i) austenite growth within ferrite bands; (ii) cementite lamella dissolution, (iii) isolated carbide dissolution and (iv) austenite growth inside ferrite grains.	107
5.2	Initial state of the DICTRA simulation system used for modeling austenite formation in a cementite-ferrite microstructure.	109
5.3	Study of the influence of the different DICTRA capabilities on the austenite formation kinetics during an isothermal holding at 760°C of a steel containing 14 wt%Mn in cementite (system size fixed at 6 μ m).	110

5.4	Study of the influence of the austenite nucleation on the austenite formation kinetics during an isothermal holding at 760°C varying (a) the system size and (b) the manganese enrichment in cementite.	111
5.5	(a) Comparison of the austenite formation kinetics for the linear geometry and for the spherical geometry. (b) Schematic representation of the spherical geometry.	113
5.6	Influence of the system size on the austenite formation kinetics at 760°C considering 14 wt%Mn in cementite. Four system lengths are compared: 5, 10, 100 and 1000 μm	114
5.7	Influence of the cementite manganese content on austenite formation kinetics at 760°C (system size fixed at 6 μm). Seven manganese enrichments in cementite are compared: 10, 13, 15, 17, 20, 25 and 30 wt%.	115
5.8	C and Mn (a-b) concentration profile and (c-d) activity profile during austenite formation of a steel containing 10 wt%Mn in cementite for different holding times at 760°C: 0, 0.1, 1, 10, 10 ² , 10 ³ , 10 ⁴ , 10 ⁵ , 10 ⁶ , 10 ⁷ and 3 \times 10 ⁷ s.	117
5.9	C and Mn (a-b) concentration profile and (c-d) activity profile during austenite formation of a steel containing 30 wt%Mn in cementite for different holding times at 760°C: 0, 0.1, 1, 10, 10 ² , 10 ³ , 10 ⁴ , 10 ⁵ , 10 ⁶ , 10 ⁷ and 10 ⁸ s.	118
5.10	Evolutions of the “operative” tie-lines as a function of holding times supposing (a) 10 and (b) 30 wt% of Mn enrichment in cementite.	119
5.11	Isothermal section of the Fe-C-Mn ternary system at 760°C. Dotted lines correspond to C isoactivity lines passing through Mn composition at the $\gamma/\text{Fe}_3\text{C}$ interface equal to 10 and 30 wt%Mn. Circles point out interfacial composition of austenite and cementite phases.	121
5.12	Isothermal section of the Fe-C-Mn ternary system at 760°C. Dotted lines correspond to C isoactivity lines passing through different Mn composition at the $\gamma/\text{Fe}_3\text{C}$ interface: 10, 13, 15, 17, 20, 25 and 30 wt%Mn.	121
5.13	Comparison of DICTRA predictions with experimental kinetics of austenite formation on the ReX-steel and on the CR-steel during isothermal holding at (a) 780, (b) 760 and (c) 735°C. Two different conditions were used to differentiate the CR-steel and the ReX-steel considering the difference of Mn enrichment in cementite: (i) $C_{Mn}^{\text{Fe}_3\text{C}} = 10$ wt%Mn in the case of the CR-steel and (ii) $C_{Mn}^{\text{Fe}_3\text{C}} = 13$ wt%Mn for the ReX-steel.	123
5.14	Isothermal section of the Fe-C-Mn ternary system at (a) 735 and (b) 780°C. Dotted lines correspond to C isoactivity lines passing through different Mn composition at the $\gamma/\text{Fe}_3\text{C}$ interface: 10 and 13 wt%Mn.	124
5.15	Comparison of DICTRA predictions with experimental kinetics of austenite formation on the ReX-steel and on the CR-steel during isothermal holding at (a) 780, (b) 760 and (c) 735°C. Two different conditions were compared: (1) a system of size 5 μm with 10 wt%Mn in the cementite to represent the deformed microstructure of the CR-steel and (2) a system of size 10 μm with 13 wt%Mn in cementite corresponding to larger microstructure of the ReX-steel.	126

6.1	Optical micrographs of the two considered states after water quench from (a) the 100% γ -state (850°C - 120 s) and (b) the 60% γ -state (760°C - 300 s). Bandoh etching.	133
6.2	(a) Cooling rate evolutions, (b) Dilatation curves, (c) Austenite decomposition fractions and (d) CCT diagram of the 100% γ -state during continuous cooling from 850°C to room temperature at 1, 5, 10, 20, 30 and 40°C/s. . .	135
6.3	OM micrographs of the 100% γ -state cooled at $R_C = 1, 5, 10, 20, 30$ and 40°C/s (resp. (a-f)). Nital etching. Quantified phase fractions, evaluated by dilatometry analysis, are reported in the caption of each micrograph. . .	137
6.4	(a) Austenite decomposition fractions and (b) evaluated CCT diagram during the continuous cooling from 760°C to room temperature at 1, 5, 10, 20, 30 and 40°C/s.	138
6.5	OM micrographs of the 60% γ -state cooled at $R_C = 1, 5, 10, 20, 30$ and 40°C/s (resp. (a-f)). Nital etching.	140
6.6	Comparison of the CCT diagrams obtained during continuous cooling of the 100% γ -state (dashed lines) and of the 60% γ -state (full lines).	141
6.7	Comparison of the values of the martensite start temperature (M_S) calculated with the empirical formulae from the literature review with the experimental value for the 100% γ -state and the 60% γ -state.	142
6.8	Comparison of the austenite-to-martensite transformation kinetics based on empirical formulae from the literature with the experimental kinetics for the 100% γ -state and the 60% γ -state.	144
6.9	(a) TEP kinetics during isothermal tempering treatments at 200, 250, 300, 350, 450 and 550°C. (b) Master curve at 200°C obtained by a time-temperature equivalence.	146
6.10	(a) TEM micrograph and (b) EDS analysis of carbide particles after 10 days at 450°C.	148
6.11	Determination of (a) the precipitated carbon content (C_C^{pre}) and (b) the fraction of precipitated carbon (f_C^{pre}) in martensite determined from TEP experiments.	149
6.12	(a) BSE image and (b) corresponding analyzed image revealing carbides. (c) 3D-reconstruction by FIB/SEM tomography of a volume showing precipitates present in the steel treated for 30 s at 450°C.	150
6.13	TEM micrograph of carbo-nitrides rich in Ti and Nb observed after a martensite tempering of 30 s at 450°C (carbon replica).	151
6.14	Scenario of C distribution during a tempering treatment at 450°C for 30 s: only 35% of the total carbon content contributes to cementite precipitation.	152
6.15	(a) Linearization of the isothermal JMAK law for the determination of the Avrami coefficient. (b) JMAK modeling of the precipitated carbon during tempering for intermediate carbide and cementite precipitation as given in table 6.3.	154
6.16	(a) Evolution of the hardness during isothermal tempering treatments at 200, 250, 300, 350 and 450°C. (b) Time-temperature equivalence at 200°C of hardness values using the same activation energies as those determined from TEP measurements.	155

6.17	Hardness evolution of the tempered martensite as a function of the tempering temperature for different tempering times: 30, 120 and 3600 s.	155
6.18	Hardness evolution of the tempered martensite as a function of its non-precipitated carbon content assessed by TEP or FIB. Comparison with data of the literature for “fresh” martensite with different carbon contents.	156
6.19	(a) Evolution of the hardness during isothermal tempering treatments of the ferrite-martensite mixture. (b) Time-temperature equivalence at 250°C using two activation energies for intermediate carbide (110 kJ/mol) and cementite (200 kJ/mol) precipitation.	157
6.20	Cycle parameters-Microstructure-Mechanical properties relationship to optimize steels.	167
A.1	(a) Schematical representation of an isothermal section of the Fe-C-X system. Examples of interface composition (IC) and velocity (IV) contours are represented for some given tie-lines. (b) Composition locus (named as IC-contours) for a given tie-line as a function of diffusivity ratio. (c) Interface velocity for high diffusivity ratio, it highlights the “zero-partition line” differentiating the LEP and LENP domains [COA 72].	170
A.2	Schematic representation of LEP condition for the $\gamma \rightarrow \alpha$ transformation. Isothermal C and Mn concentration profiles are reported.	172
A.3	Schematic representation of LENP condition for the $\gamma \rightarrow \alpha$ transformation. Isothermal C and Mn concentration profiles are reported.	173
B.1	Austenite formation kinetics monitored by (a) TEP; (b) hardness and (c) optical phase quantification during isothermal holding at 735, 760 and 780°C. Normalized austenite fraction are represented in (d).	176
C.1	XRD analysis during a thermal cycle including a heating stage at 5°C/s to 900°C, a holding of 600 s and finally a cooling at 5°C/s. Case of the ReX-steel.	180
C.2	XRD analysis of a thermal cycle realized on the CR-steel and composed of a heating at 5°C/s to 900°C, an holding of 600 s and finally a cooling at 5°C/s.	181
C.3	XRD analysis of a thermal cycle realized on the CR-steel and composed of a heating at 5°C/s to 760°C, an holding of 1800 s and finally a cooling at 5°C/s rate.	182
D.1	Methodology to determine JMAK parameters: (a) Q for heating rates equal to $R_H=5, 7.5, 10$ and 30°C/s ; and (b) n using the experimental kinetics at 30°C/s , <i>i.e.</i> austenite forms on fully deformed ferrite ($Q=901$ kJ/mol). (c) Influence of the Avrami parameter on the austenite formation kinetics with $n=0.32$ or 0.62 ($Q=901$ kJ/mol; $b_0=3 \times 10^{43}$ /s).	184
D.2	Comparison of austenite formation kinetics for different heating rates (a-b) 0.5, (c-d) 5 and (e-f) 7.5°C/s predicted with (a) the 3-JMAK mixture model and (b) taking into account recrystallization inhibition above 10% of austenite fraction.	186

D.3 Comparison of austenite formation kinetics for different heating rates (a-b) 10, (c-d) 30 and (e-f) 100°C/s predicted with (a) the 3-JMAK mixture model and (b) taking into account recrystallization inhibition above 10% of austenite fraction. 187

List of Tables

1.1	Austenite start and austenite finish temperatures (Ae_1 and Ae_3) as a function of steel chemistry (composition in wt%).	7
1.2	Martensite start (M_S) temperature as a function of steel chemistry (composition in wt%).	16
1.3	Martensite start (M_S) temperature as a function of steel chemistry (composition in wt%).	17
1.4	Temperature range and activation energy data for the martensite tempering.	20
1.5	Expression of M_S and α_m parameters for the Koistinen-Marburger equation (compositions in wt%).	26
2.1	Chemical composition of the investigated steel.	40
2.2	Various applied experimental techniques for each investigated thermal stage.	45
2.3	Experimental parameters of the P07-PETRA experiments.	52
3.1	JMAK parameters for recrystallization and for austenite formation kinetics in recrystallized ferrite or in deformed ferrite.	77
3.2	Comparison of Thermo-Calc and experimental austenite fraction on CR-steel after 1 h and 4 h of isothermal holding.	86
4.1	Interface mobility parameter M values at 735, 760 and 780°C considering $Q_m=900$ kJ/mol and $M_0 = 5 \times 10^{35}$ mol.m.J ⁻¹ .s ⁻¹	98
5.1	C and Mn concentrations and characteristic length of ferrite, cementite and austenite used in DICTRA simulations of austenite formation.	108
5.2	Diffusion coefficients of C and Mn in ferrite and austenite phases for 735, 760 and 780°C (Thermo-Calc with MOBFE2 database).	124
6.1	Start and finish temperatures for ferrite and pearlite ($(F + P)_S$, $(F + P)_F$), bainite (B_S , B_F) and martensite (M_S , M_F) formation during continuous cooling of the 100% γ -state with various cooling rates. Evaluated fraction of austenite decomposition products are also reported.	136
6.2	Start and finish temperatures for ferrite and pearlite ($(F + P)_S$, $(F + P)_F$), bainite (B_S , B_F) and martensite (M_S , M_F) formation during continuous cooling of the 60% γ -state with various cooling rates. In addition, fraction of austenite decomposition products are also reported.	138

6.3	JMAK parameters for the two tempering mechanisms: (i) precipitation of intermediate carbides (JMAK_1) and (ii) precipitation of cementite (JMAK_2).	153
B.1	Comparison of various in-situ experimental techniques to monitor the kinetics of austenite formation.	177
B.2	Comparison of various indirect experimental techniques to monitor the kinetics of austenite formation.	178

Introduction

Industrial context

Awareness of environmental issues and new international legislations have driven car-makers to develop and set up new solutions to reduce their environmental footprints. Namely, the European commission has fixed the challenging objective to reduce carbon emissions for new passenger cars from 154 g/km (in 2012) to 90 g/km by 2020 [COU 14]. Various means of actions were undertaken by car-makers passing from the optimization of transmission train, the automotive weight reduction, the decrease in the rolling resistance and also the improvement of vehicle aerodynamics. After the optimization of engine and filter parts, the weight reduction of the body-in-white structure is the second factor enabling to reduce carbon emissions: a lightening of 100 kg ensures a decrease in CO₂ emission of 8 g per kilometre. Moreover, a decrease of 20% of the total vehicle weight leads to a diminution up to 13% of carbon emission [AUT].

In this sense, car-makers have sought for “material” solutions with enhanced mechanical properties. High-performance materials may lead to the reduction of the total vehicle weight and maintain good mechanical properties. The latter point is of major importance because body-in-white components have for main goal to ensure passenger security. They should be able not only to store impact energy but also to play an anti-intrusion role in the passenger compartment. Maximal passenger protection is continuously searched to satisfy new tests and standards to evaluate vehicle security. This led to the development of the family of the Advanced High Strength Steels (AHSS) from the mid-seventies to nowadays.

Among all the developed AHSS, Dual-Phase steels (DP) appear to be promising and sustainable material for the body-in-white structure. Not only ensuring a high strength-ductility compromise, DP steels also respect and adapt to various industrial constraints like the shaping, the welding or the coating. Moreover, their low price and quite easy production strengthen car-makers’ interest. The shared challenge for steel-makers is therefore to get a better knowledge of the microstructural evolutions occurring during the processing of these steels.

Dual-phase steels: microstructure and processing

DP steels are characterized by a two-phase microstructure composed of a hard martensite phase (α') embedded in a soft ferrite matrix (α). The typical ferrite-martensite microstructure of DP steels is obtained by a thermal treatment represented in figure 1 [BUS 15]. The major microstructural changes are specified for the different stages of the cycle. The thermal cycle used to produce DP steels from a cold-rolled ferrite-pearlite microstructure is

composed of three main stages:

1. *Intercritical annealing stage:* First, the steel is heated in the intercritical annealing range ($Ae_1 < T < Ae_3$, $\sim 720-800^\circ\text{C}$) to produce a two phase microstructure combining ferrite and austenite (γ) grains. Austenite formation is usually accompanied by the recrystallization of the cold-rolled microstructure. In most annealing conditions, recrystallization and austenite formation will overlap and interact. The intercritical annealing temperature is usually reached by two kinds of heating rate value depending on the heating technologies: the average heating rate is equal to 5°C/s in the case of radiant tube furnace (RFT) and to 30°C/s for direct flame furnace (DFF).
2. *Cooling stage:* After the intercritical annealing, the steel is cooled with the objective to obtain the austenite-to-martensite transformation and to produce the final ferrite-martensite microstructure. However, austenite may decompose into other products (bainite and/or ferrite-pearlite) depending on the steel chemistry, the cooling rate (R_C) and on the intercritical microstructure before cooling.
3. *Tempering stage:* In a final step, the DP thermal treatment may be continued to protect the steel from the corrosion. Several industrial coating techniques are possible: (1) the steel may be coated by a Zn protection film done by immersion of the steel sheet in a zinc liquid bath ($\sim 400-460^\circ\text{C}$) for a few seconds ($\sim 5-10$ s), such treatment is called Galvanization (GI) [SON 11]; (2) an alliation of the prior formed Zn film may then be performed (holding $\sim 500^\circ\text{C}$ - 10-20 s) to generate Fe-Zn alloy protection, such step is called as GalvAnnealing step (GA) [MAR 00]. An Over-Ageing treatment (OA) may also be performed either directly after the cooling stage or after the Zn coating (GI or GA) to soften the brittle martensite phase. The OA treatment may also be realized before the Zn coating. All these additional treatments (GI, GA and OA) may be performed either directly at the end of the quenching stage or after having formed the martensite phase as represented in figure 1. As a consequence, the metastable martensite may evolve to reach a more stable configuration. This is assumed to lead to a progressive softening of the steel associated with a decrease in its mechanical strength and with an increase in its ductility and toughness. Such evolutions are important to consider because they will considerably modify the mechanical properties of the as-quenched ferrite-martensite mixture.

Since the last forty years, many research works were focused on the characterization of the microstructural and mechanical property evolutions during the thermal treatments of multi-phased steels. Modeling efforts were also undertaken in order to describe such evolutions. However, despite the number of studies, difficulties and misunderstanding points still persist because the DP thermal cycle is complex (such as the recrystallization and austenite formation overlapping during the intercritical annealing stage). Indeed, (i) various processing parameters (such as the heating rate, intercritical annealing temperature and time or cooling rate) govern the microstructural evolutions, (ii) each evolution depends on the previous ones and (iii) several mechanisms may occur more or less simultaneously.

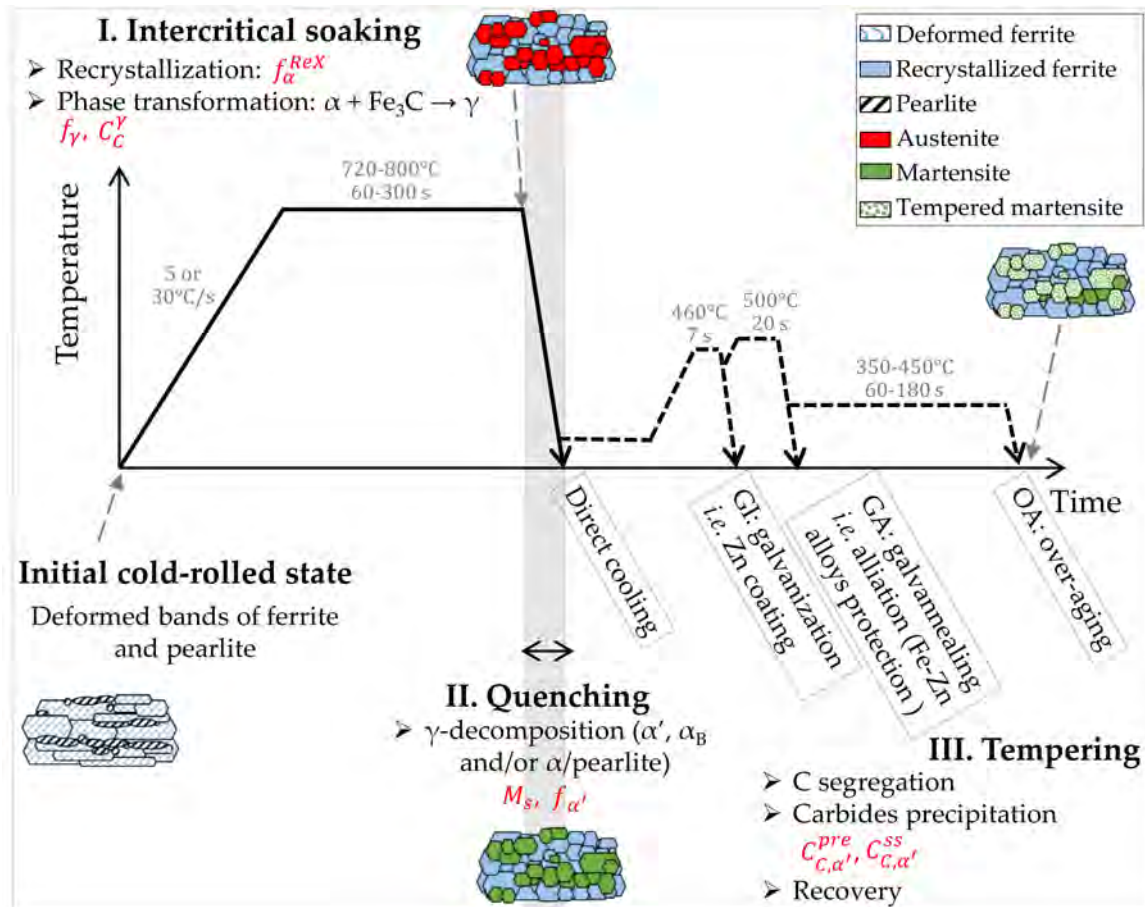


Figure 1: Typical thermal cycle used for the processing of DP steels composed of an intercritical annealing treatment followed by a cooling stage and a tempering stage. Variables written in red colour refer to evaluated data during this PhD-work.

PhD-objectives

Launched in October 2014, this PhD-work aims at characterizing experimentally and at modeling the microstructural evolutions occurring during the three major stages involved in the thermal treatment of DP1000 steels. The goal of this study is to get a better understanding of microstructural evolutions during complex thermal treatments and to develop predictive tools to follow and forecast changes. Parameters written in red colour in figure 1 indicate various informations expected to be modeled at the end of the different stages of the DP thermal treatment:

1. Intercritical stage:

- the recrystallized (f_{α}^{ReX}) and deformed (f_{α}^{CR}) ferrite fractions according to the degree of recrystallization progress and also the sites on which austenite nucleates and grows;
- the austenite fraction (f_{γ}) according to the phase transformation: $\alpha + \text{Fe}_3\text{C} \rightarrow$

γ taking place either on deformed or recrystallized ferrite grains;

- the carbon content in the austenite phase (C_C^γ) which will drive the austenite decomposition during the cooling of the steel;

2. *Cooling stage:*

- the martensite start temperature (M_S) defining the initiation of the austenite-to-martensite transformation;
- the martensite fraction ($f_{\alpha'}$) at the end of the cooling, function of the $\gamma \rightarrow \alpha'$ transformation kinetics;

3. *Tempering stage:*

- the precipitated ($C_{C,\alpha'}^{pre}$) and solute ($C_{C,\alpha'}^{ss}$) carbon contents in martensite after a given tempering condition. These values allow the precipitated fraction (f_{pre}) to be evaluated;

Given the extent and the ambition of this task, the present PhD-work was mainly focused on the microstructural evolutions occurring during the intercritical annealing stage with the objective to model the recrystallization and austenite formation interaction. This study enables to describe the intercritical state before the cooling which will be determinant for the austenite decomposition and the final ferrite-martensite ratio.

Prospective studies were then realized on the cooling and the tempering stages of the thermal treatment. As in the case of the intercritical annealing stage, models were proposed to describe the steel evolutions.

A particular care was brought on the capability and versatility of the modeling approaches in order to extend developed model to other steel chemistry and even family. Physical based models are preferred because they should be more stable to describe metallurgical phenomena and should prevent from an extended work of calibration.

On the one hand, modeling tools may lead to an optimization of thermal treatments. The final aim is to allow a better management of cycle conditions in order to (i) improve steel efficiency, (ii) improve yield and cost of production structure and also (iii) reduce energy consumption of production lines.

On the other hand, modeling tools may be used as on-site tools for production. In that case, they need to be fast and to give answers to eventual industrial problems, they are also necessary to reduce number of industrial trials and to follow on-line steel quality during thermal treatment.

This PhD-work is included in a global study with the objective to predict *in-fine* the mechanical properties after a complex thermal cycle (yield strength, ultimate tensile stress (UTS or Rm), uniform elongation, work hardening behaviour).

PhD-manuscript outline

This current PhD-manuscript is composed of 6 chapters organized in the following manner:

- **Chapter 1** proposes a state-of-the-art of the microstructural evolutions occurring during the three major stages of DP heat treatments and of the modeling tools available in the literature going from phenomenological approaches to thermodynamic and physical based ones. This literature review ends with difficulties and possible progress tracks in relation with the different chapters of this thesis.
- **Chapter 2** describes the investigated DP1000 steel, its two initial states (*i.e.* cold-rolled and prior recrystallized) as well as the experimental techniques used in this work. Especially, experimental conditions are specified.
- **Chapter 3** is focused on the experimental characterization of the microstructural evolutions occurring during the intercritical stage of DP thermal cycle. The two major evolutions, namely the recrystallization and the austenite formation, were first investigated separately: (i) the recrystallization was monitored below the austenite formation temperature and (ii) the austenite formation was investigated on prior recrystallized steels. Then, the more complex case of the cold-rolled steels, where both recrystallization and austenite formation may occur concomitantly, was analysed. A mixture law based on three JMAK laws was implemented to predict the recrystallization and phase transformation overlapping in cold-rolled DP1000 steels. This approach led to a discussion on the effect of cycle parameters (heating rate, holding temperature and time), the influence of the initial state and the effect of the established recrystallization inhibition on the austenite formation kinetics.
- **Chapter 4** proposes to model the kinetics of austenite formation using a mixed-mode approach. It allows the austenite formation kinetics to be predicted thanks to a model based on carbon diffusivity and interface mobility motions. The mixed-mode model was adjusted to a given experimental database and validated on a wider experimental range (*i.e.* modifying the heating rate). Model strength and weakness are finally discussed.
- **Chapter 5** proposes another modeling approach of the austenite formation with the expectation to develop a more physical based model. For this, DICTRA software was used to model the phase transformation based on the combined diffusion of carbon and manganese elements. Results of this purely diffusive calculation are compared to an experimental database to evaluate the weight of realized hypothesis and discuss the capacity of such tool to describe the austenite formation in the case of complex industrial steels (alloyed chemistry and non-homogeneous morphology).
- **Chapter 6** finally investigates microstructural evolutions occurring during the cooling and the tempering stages of DP thermal cycle.

This manuscript ends with an overall conclusion summarizing major results of this study. Then different perspectives are finally proposed.

Chapter 1

Literature Review

This chapter proposes a state-of-the-art relative to the microstructural evolutions occurring during the thermal treatment of DP steels and available modeling approaches to describe these evolutions.

It is divided into three parts. In a first part, dual-phase (DP) steels are shortly presented. In a second part, microstructural evolutions occurring during the thermal treatments of dual-phase steels are described. Evolution is specifically described during the three major stages involved in the thermal treatment of cold-rolled DP steels: (1) the intercritical annealing, (2) the quenching and (3) the tempering occurring partly during the steel galvanization. The third part is focused on modeling tools. It presents an overview of models (from empirical to thermodynamic or physically based models) developed to describe microstructure evolutions during thermal treatments.

This literature review concerns the production of DP steels from a cold-rolled ferrite-pearlite initial microstructure. This type of microstructure is the one typically obtained during the cooling of steel sheets after hot-rolling.

Contents

1.1	Dual-Phase steels	2
1.2	Microstructural evolutions during the thermal treatments of DP steels	4
1.2.1	Intercritical annealing	4
1.2.2	Quenching	14
1.2.3	Tempering	19
1.3	Modeling tools for the prediction of microstructural evolutions	22
1.3.1	Empirical modeling	23
1.3.2	Thermodynamics of phase transformation	26
1.3.3	Physically based modeling	32
1.4	Conclusion	37

1.1 Dual-Phase steels

Dual-phase (DP) steels are one of the most used Advanced High Strength Steels (AHSS) in the automotive industry. Developed in the mid-seventies and produced in the form of steel sheets, DP steels present enhanced mechanical properties compared to conventional ferritic steels [MAT 12] [BOU 13]. Figure 1.1.a locates DP steels in AHSS grades in a graph “total elongation *versus* tensile strength”. DP steels are characterized by a good compromise between strength and ductility obtained with a low-carbon and low-alloyed chemistry. Moreover, the good capability of DP steels to answer to several industrial constraints (formability, assembling, coating *etc.*) has driven the choice of car-makers to use such steels for producing a wide range of components in modern cars. Figure 1.1.b shows the example of a commercialized Ford Fusion, for which various AHSS are used in the body-in-white structure [AUT].

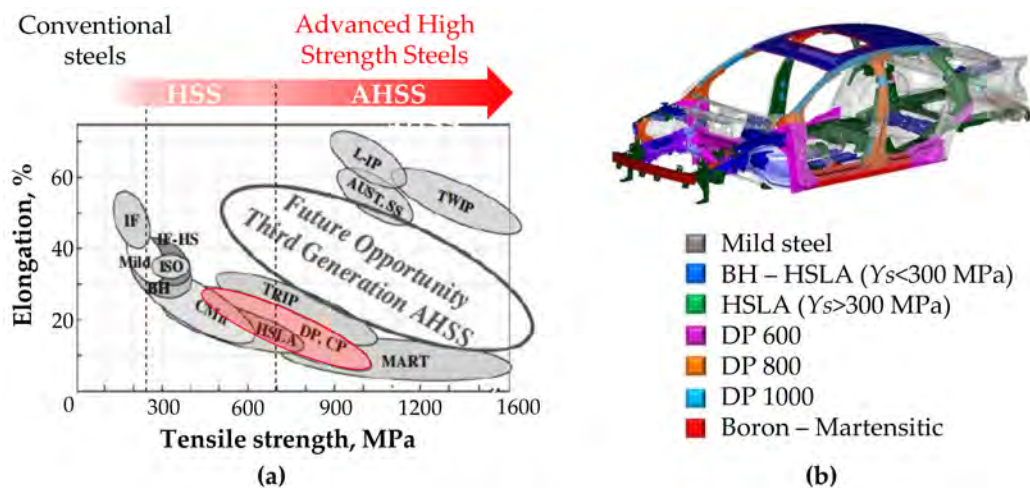


Figure 1.1: (a) Overview of tensile strength and total elongation for various AHSS grades [MAT 12]; (b) Examples of AHSS used in the body-in-white structure of a commercialized Ford Fusion [AUT].

As already mentioned, DP steels are characterized by a two-phase microstructure composed of ferrite (α) and martensite (α'). Such combination leads to a composite microstructure mixing a hard phase (α') embedded in a soft ferrite matrix. Figure 1.2.a. shows an example of a typical DP microstructure. Phase volume fraction as well as the morphology, size and distribution of martensite islands govern the mechanical behaviour of DP steels.

The typical ferrite-martensite microstructure of DP steels is obtained, from a cold-rolled state, by a typical thermal treatment represented in figure 1.2.b. In a first stage, the steel is heated in the intercritical annealing range ($Ac_1 < T < Ac_3$) ensuring austenite (γ) formation. Then a rapid quench leads to the austenite-to-martensite transformation and to the final ferrite-martensite microstructure. In a final step, the steel is galvanized to protect it from corrosion. This is done by immersion of the steel sheet in a zinc liquid bath ($\sim 400\text{-}460^\circ\text{C}$) for a few seconds ($\sim 5\text{-}10$ s). The processing parameters such as the

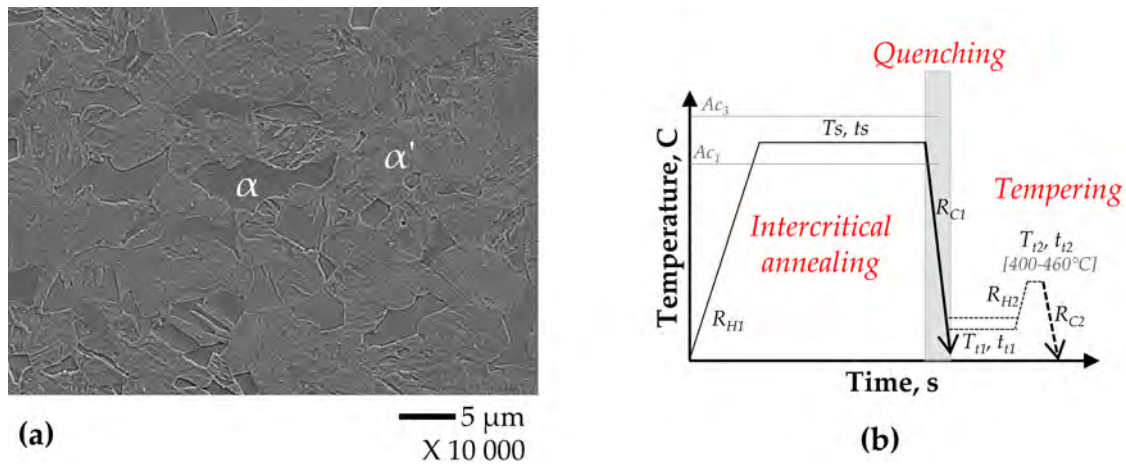


Figure 1.2: (a) SEM micrograph of a DP steel combining a ferrite matrix (α) and a hard phase (martensite (α')); (b) Typical thermal treatment of DP steels.

heating rate, intercritical annealing temperature or cooling rate govern the microstructural evolutions at each stage and need to be carefully chosen to optimize the processing and the final microstructure.

From a mechanical point of view, DP steels present attractive properties. High strength and total elongation may be obtained as illustrated in figure 1.3.a [PIE 14]. Elongations in between 10 and 15% are achievable combined with yield strength around 800-1100 MPa. The nomenclature DP-X defines the expected ultimate tensile strength X (in MPa) of the DP steel grade (*i.e.* 1000 MPa of σ_R is expected for a DP1000). Moreover, tensile curves of DP steels do not exhibit yield point elongation (YPE, also called Lüders strain) and show consolidation work-hardening during the deformation. As an example, figure 1.3.b presents the evolution of the incremental work hardening exponent defined as $n_{incr} = \left(\frac{d\sigma}{d\varepsilon} \cdot \frac{\varepsilon}{\sigma} \right)$ as a function of the deformation (ε) for steels containing 15% of martensite and three different carbon contents (0.15, 0.3 and 0.6wt%C). The Considere's criterion for the onset of necking is reported in the figure by the straight line corresponding to the equation $n = \varepsilon$. The intersection of the incremental work hardening (n_{incr}) curve with Considere's criterion defines the uniform deformation (ε_u) before necking and highlights work hardening of DP steels.

Owing to these good mechanical properties and the capability to respect numbers of industrial constraints, DP steels are recognised as a sustainable AHSS family for future automotive applications. There is consequently a need to have a good knowledge of steel evolution during the thermal treatment and a need of predictive tools to manage and optimize the industrial processing. In this respect, this PhD chapter aims at: (i) detailing the metallurgical evolutions during the different stages involved in the thermal treatment of DP steels and (ii) presenting major modeling tools.

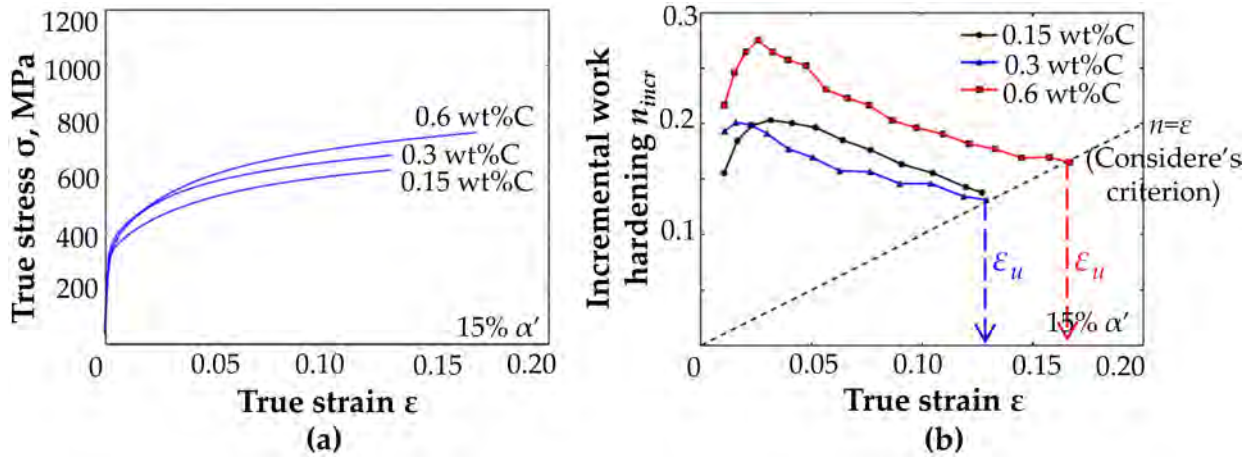


Figure 1.3: (a) Tensile and (b) work hardening curves of DP steels containing 15% martensite and different carbon levels [PIE 14].

1.2 Microstructural evolutions during the thermal treatments of DP steels

This section proposes a detailed overview of the main metallurgical phenomena likely to occur during the thermal treatments of DP steels. Steel evolution is presented during the three major stages involved in the thermal treatments of DP steels: (1) the intercritical annealing, (2) the cooling and (3) the tempering (galvanization).

1.2.1 Intercritical annealing

The first step of the thermal treatment is the intercritical annealing during which the steel is heated in the ferrite-austenite ($\alpha + \gamma$) domain. This stage leads to the formation of the austenite that will transform into martensite during the quench. The fraction of austenite and its carbon content govern austenite decomposition and, consequently, the microstructure and mechanical properties after quench. In addition to the austenite formation, the deformed microstructure evolves towards a more stable configuration during the heating stage. The stored energy after cold-rolling is reduced by recovery, recrystallization and cementite spheroidization: these three mechanisms may occur before or in parallel to the phase transformation. The overlapping of these phenomena is likely to modify the kinetics of microstructural evolutions. In the following, a particular care will be attached to the interaction of these different phenomena.

In the next section, recovery/recrystallization, cementite spheroidization and phase transformation will be described successively. Then, the interaction between recrystallization and austenite formation, deeply discussed since the last thirty years in the literature, will be considered.

1.2.1.1 Recovery/recrystallization

The microstructure after cold-rolling is thermodynamically unstable due to a large density of dislocations and interfaces. The heat brought during the intercritical annealing enables microstructural reorganization through two mechanisms: recovery and recrystallization [HUM 95] [CHR 81] [OYA 08]. These spontaneous mechanisms lead to a lowering of the energy of the system by annihilation or rearrangement of the defects. They modify the steel microstructure and soften the mechanical behaviour.

Recovery is associated with a decrease in the dislocation density thanks to annihilation phenomenon. When the temperature is higher than the third of fusion temperature, dislocations become mobile and can hence rearrange themselves and annihilate when two dislocations exhibiting an opposite Burger vector meet. The increased mobility is also accompanied by dislocation reorganization. Dislocations gather together thus reducing the energy of the system by recovery of dislocation stress fields [MCQ 77]. Dislocation rearrangement forms substructures inside grains but this does not modify interfaces between deformed grains. The microstructure is generally assumed to be hardly affected by recovery.

In parallel, the stored energy is drastically decreased by the recrystallization of the cold-rolled microstructure. The microstructure is considerably modified by this phenomenon. Deformed grains are replaced by equiaxed and dislocations-free grains. The recrystallization is a diffusive mechanism which occurs by nucleation [HUM 95] and growth processes. Recrystallized grains appear to preferentially nucleate at grain boundaries or substructures formed during the recovery. These sites have a high stored energy which increases the driving force for the recrystallization process. The recrystallization kinetics is driven by diffusion with an activation energy commonly associated with the self-diffusion of iron in ferrite [LU 11]. While the activation energy for self-diffusion of iron into ferrite is in the range of 220-270 kJ/mol [YAN 85a], larger activation values (~ 350 -380 kJ/mol) were reported due to a solute drag effect of alloying elements, like Mn or Mo, on migrating grain boundaries [HUA 04] [KUL 13a].

1.2.1.2 Cementite spheroidization

While pearlite spheroidization is known as a slow process (hundreds of hours around 700°C) [MAT 17], Yang *et al.* [YAN 85a] highlighted rapid cementite spheroidization during the annealing of a ferrite-pearlite cold-rolled steel (Fe-0.08C-1.45Mn-0.21Si, wt%). Substantial spheroidization was observed after 30 s of holding at 700°C. Other authors confirmed the rapidity of this phenomenon and showed the presence of fully or partially spheroidized cementite after intercritical annealing treatments of DP steels [KUL 13a] [AZI 11]. Figure 1.4 shows SEM micrographs of a cold-rolled steel (Fe-0.17C-0.74Mn, wt%) heated at 1°C/s up to different temperatures and subsequently water quenched [AZI 11]. At 510°C (figure 1.4.a), the microstructure is characterized by deformed ferrite grains with pearlite lamellae inside. At 670°C (figure 1.4.b), ferrite recrystallized and some cementite particles have yet spheroidized. Figure 1.4.c emphasizes a moving front of recrystallization across a pearlite colony: it leaves behind rows of spheroidized carbides. The recrystallization near pearlite area thus promotes cementite spheroidization. The quick pearlite spheroidization is also

due to cementite fragmentation during the cold-rolling which introduces several defects (*i.e.* vacancies, dislocations) in the pearlite islands [TIA 87] [LUP 72] [CHO 68]. It can be noted that the pearlite island distribution and the directionality of the cold-rolling are maintained after pearlite spheroidization. Lastly, Rocha *et al.* [ROC 05] pointed out the coarsening of carbides during the annealing stage.

It should be underlined that cementite spheroidization is an important phenomenon because it can delay austenite formation kinetics [HUA 04].

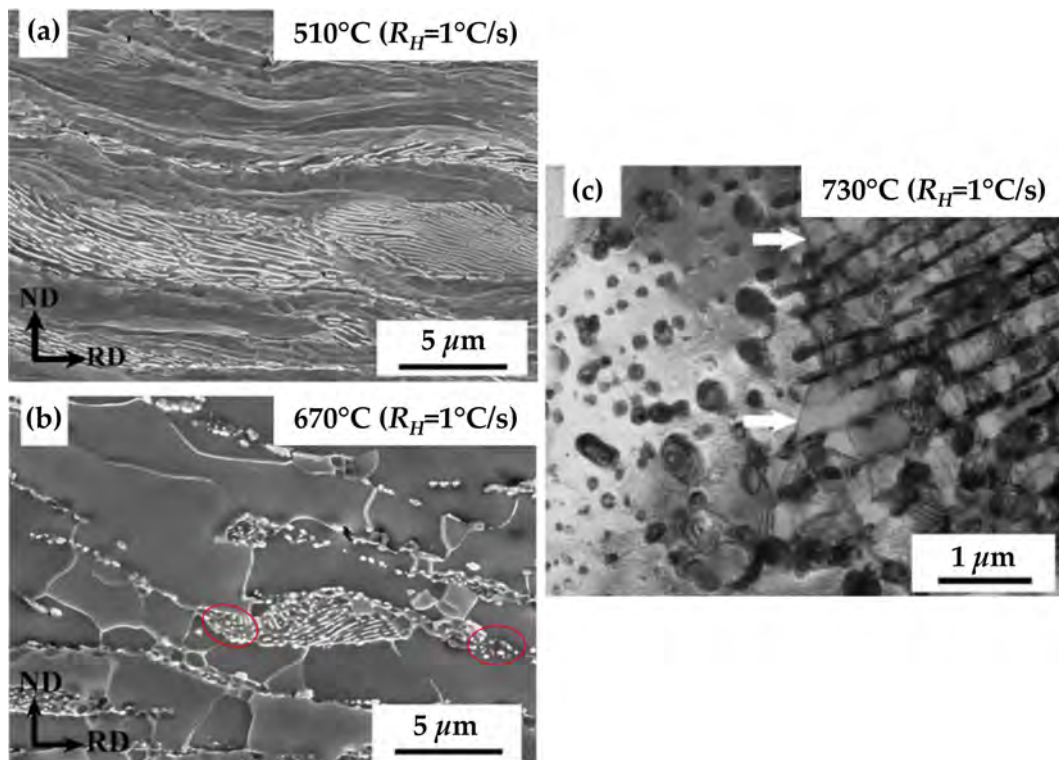


Figure 1.4: SEM micrographs of a cold-rolled DP steel during a heating stage at 1°C/s up to various temperatures: (a) 510, (b) 670 and (c) 730°C [AZI 11].

1.2.1.3 Phase transformation $\alpha + \text{Fe}_3\text{C} \rightarrow \gamma$

The austenite phase is formed by a solid-state transformation when the temperature exceeds A_{c1} . The initial ferrite-pearlite microstructure evolves towards a ferrite-austenite structure for thermal treatments in the intercritical domain ($A_{c1} < T < A_{c3}$) and to a fully austenitic structure above A_{c3} . Table 1.1 proposes some chemical dependent expressions of the austenite start temperature (A_{e1}) and of the austenite finish temperature (A_{e3}) proposed in the literature. While the A_{e1} temperature does not depend on the carbon content of the steel, the A_{e3} temperature is greatly influenced by this parameter.

Authors	Equations (All values are dimensionless, compositions are in weight percent, Ae_1 and Ae_3 are in °C if not specified)	Validity domains
Grange [GRA 47]	$Ae_1(^{\circ}F) = 1333 - 25Mn + 40Si + 42Cr - 26Ni$ $Ae_3(^{\circ}F) = 1570 - 323C - 25Mn + 80Si + 3Cr - 32Ni$	
Andrews [AND 65]	$Ae_1 = 723 - 16.9Ni + 29.1Si + 6.38W - 10.7Mn + 16.9Cr + 290As$ $Ae_3 = 910 - 203\sqrt{C} + 44.7Si - 15.2Ni + 31.5Mo + 104V + 13.1W$ $- 30Mn + 11Cr + 20Cu - 700P - 400Al - 120As - 400Ti$	$C < 0.6$
Elvis	$Ae_1 = 712 - 17.8Mn - 19.1Ni + 20.1Si + 11.9Cr + 9.8Mo$ $Ae_3 = 871 - 254.4\sqrt{C} - 14.2Ni + 51.7Si$	$C < 0.6$
Park	$Ae_3 = 935 - 350C - 25Mn - 51Si + 106Nb + 100Ti + 68Al - 11Cr$ $- 33Ni - 16Cu + 67Mo$	

Table 1.1: Austenite start and austenite finish temperatures (Ae_1 and Ae_3) as a function of steel chemistry (composition in wt%).

The complexity of this phase transformation is due to the fact that austenite can nucleate and grow on various sites of the initial microstructure composed of two different phases (*i.e.* cementite and ferrite).

a. Austenite nucleation

Austenite nucleates preferentially on non-equilibrium high-energy defects and high-carbon areas. Most favourable nucleation sites are therefore :

- (i) Fe_3C carbides which act as high-carbon supplying sources for austenite formation. Austenite nucleation is different as a function of Fe_3C carbide morphologies:
 - (a) *Pearlite (Fe_3C and ferrite lamellae)*: Nucleation in pearlite is quick thanks to short diffusion distance [SAV 07]. Moreover, nucleation is promoted on pearlite grain boundaries (which are highly-disorder due to high energy orientation) compared to cementite/ferrite interfaces.
 - (b) *Spheroidized Fe_3C islands*: As was shown by Yang *et al.* [YAN 85b], Lai *et al.* [LAI 16] and as illustrated in figure 1.5, intergranular Fe_3C carbides are preferential nucleation sites compared to intragranular carbides. Austenite first nucleates on intergranular carbides because their crystallography is highly disordered (*i.e.* high energy nucleation sites).
- (ii) Triple grain boundaries of ferrite which appear to be a second-step nucleation site [OFF 12] [SAV 07] [SAV 10].

b. Austenite growth

Austenite growth occurs in two-steps: (i) the pearlite dissolution and then (ii) the ferrite-to-austenite transformation [OLI 07]. Speich *et al.* [SPE 81] divided the kinetics of austenite formation into three steps as illustrated in figure 1.6.a:

- *Stage 1* : fast nucleation and growth driven by carbide (or pearlite) dissolution;

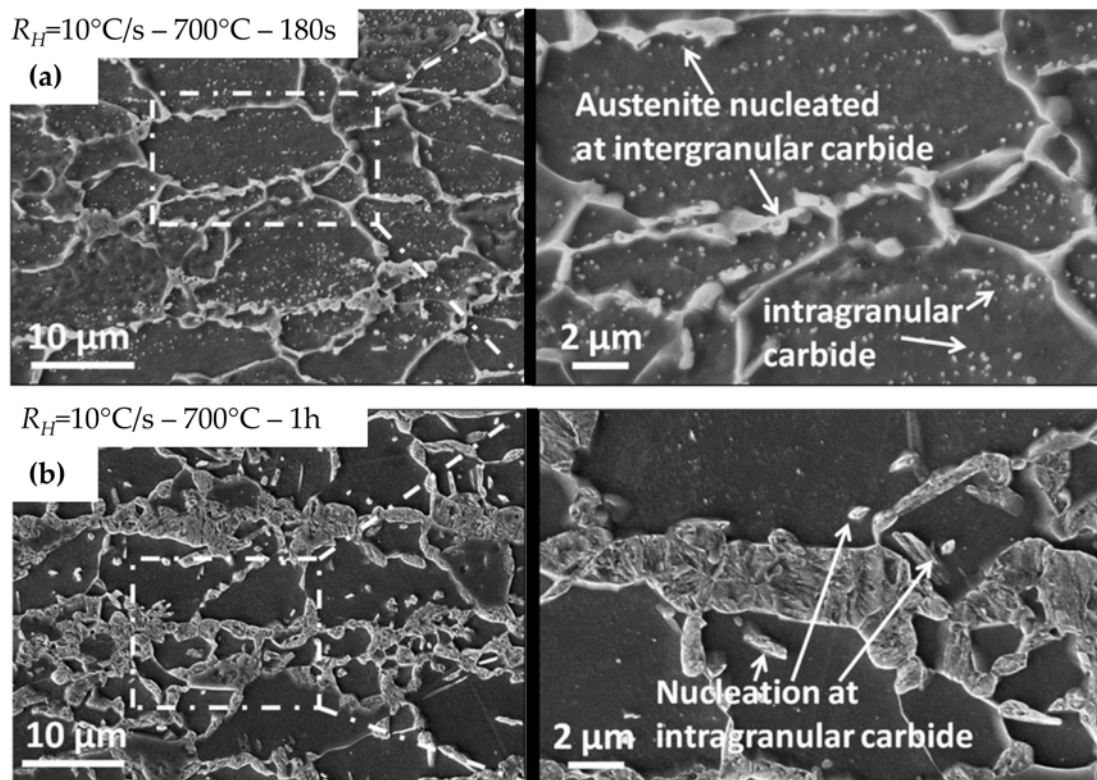


Figure 1.5: SEM micrographs highlighting austenite nucleation sites during intercritical annealing treatments at 700°C for (a) 180 s and (b) 1 h [LAI 16].

- *Stage 2* : austenite growth controlled by C diffusion in austenite (2.a) and slow Mn diffusion in ferrite (2.b);
- *Stage 3* : very slow equilibration of phases limited by Mn diffusion in austenite.

These various steps were reported in a TTT (Time Temperature Transformation) graph by the same authors as shown in figure 1.6.b. Early transformation times are controlled by pearlite dissolution or carbon diffusion. Between 10 and 10^7 s, the transformation is managed by manganese diffusion while the final equilibrium is only achieved above 10^7 s.

It should be noted that the first stage of carbide dissolution may be considerably delayed with the addition of alloying elements such as manganese, resulting thus in a global delay of austenite formation kinetics. Gouné *et al.* studied the dissolution of spheroidized cementite in a Fe-0.149C-1.58Mn (wt%) alloy and defined a useful criterion to evaluate the cementite dissolution regime [GOU 12]. Figure 1.7.a represents the two dissolution regime regions as a function of Mn enrichment of cementite and temperature. In addition, figure 1.7.b shows the austenite formation kinetics calculated with DICTRA software at 740°C and for two Mn enrichments in cementite [LAI 14]. As predicted by Gouné *et al.*, fast dissolution of cementite is obtained on the steel containing 7 wt%Mn in cementite while slower dissolution was predicted on the one with 25 wt% of Mn in cementite.

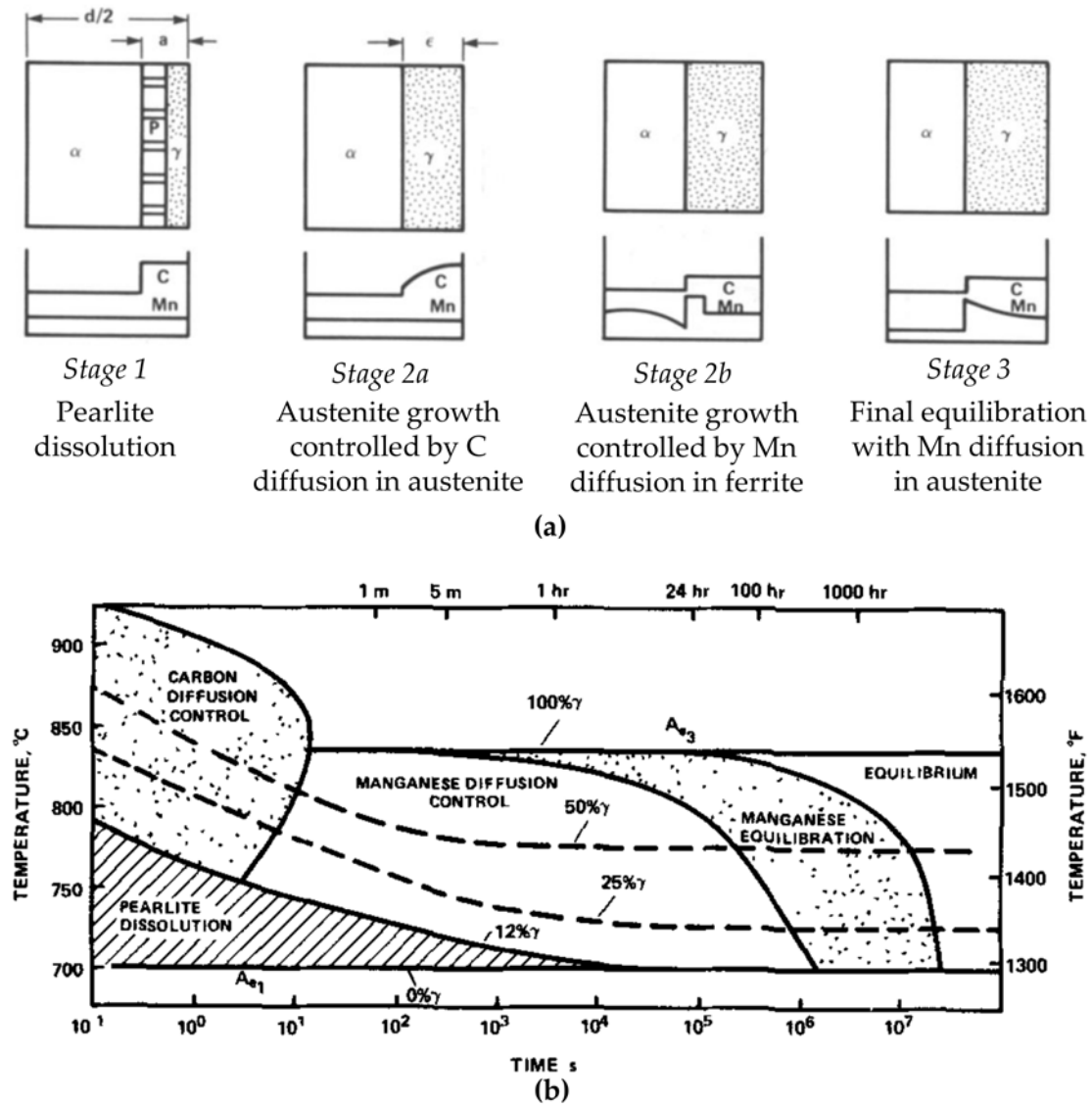


Figure 1.6: (a) Various transformation steps and (b) associated TTT graph of the austenite formation according to Speich *et al.* [SPE 81].

From a kinetics point of view, Huang *et al.* [HUA 04] pointed out a significant influence of the heating rate (R_H) on the isothermal kinetics of austenite formation as shown in figure 1.8. These authors observed that the austenite formation kinetics obtained at 750°C on a hot-rolled Fe-0.06C-1.85Mn-0.11Mo (wt%) steel was different after a slow heating (1°C/s) or after a rapid heating (100°C/s). For an identical isothermal holding temperature (750°C), higher austenite fractions were obtained after a heating rate of 100°C/s compared to 1°C/s on the hot-rolled state. Moreover, they noted that the measured austenite fractions were much lower when the heating rate was slow without providing any physically based argument. Another notable aspect observable in figure 1.8 is that the austenite formation

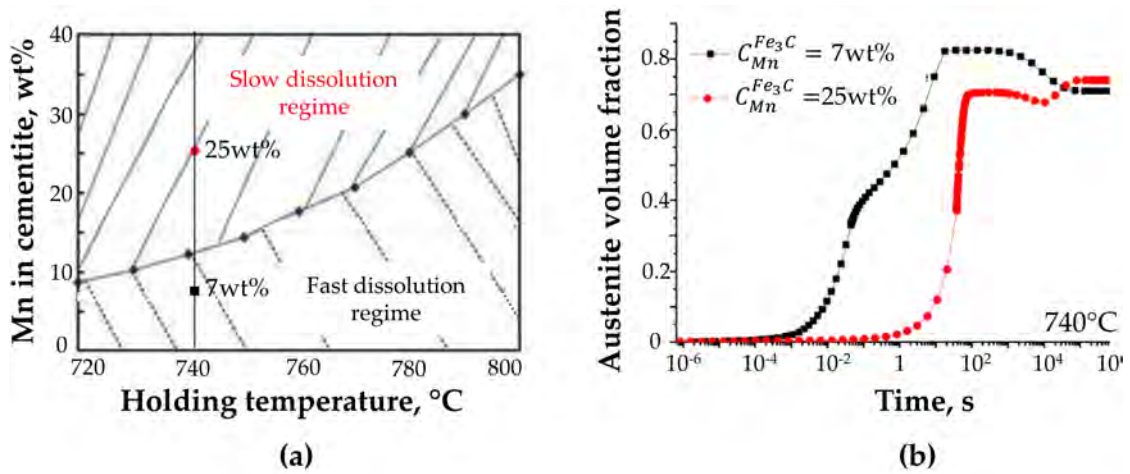


Figure 1.7: (a) Cementite dissolution regime as a function of Mn content in cementite and temperature defined by Gouné *et al.* [GOU 12] (b) Calculated kinetics on DICTRA of austenite growth at 740°C for 7 and 25 wt%Mn in cementite [LAI 14].

kinetics also depends on the steel state (*i.e.* hot-rolled or cold-rolled). As in the case of the hot-rolled steel, the heating rate influences the austenite formation kinetics in cold-rolled steels: lower austenite fractions were formed at low heating rate. Chbihi *et al.* [CHB 14] obtained also the same conclusions on a cold-rolled Fe-0.15C-1.48Mn (wt%) steel treated at 740 and 780°C. However, it has to be mentioned that their results concern short treatment times (less than 600 s), for which no equilibrium is reached. The difference between hot-rolled and cold-rolled steels may be due to the fact that recrystallization occurs on the cold-rolled state and may possibly interact with the phase transformation as discussed below.

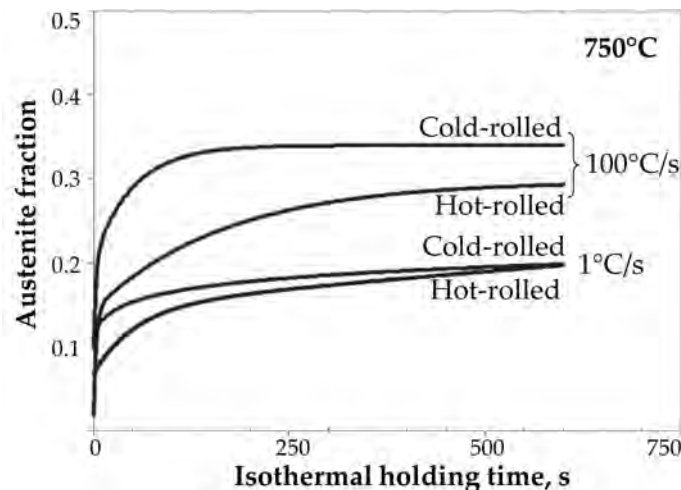


Figure 1.8: Effect of the heating rate (1 or 100°C/s) on the isothermal austenite formation kinetics for hot-rolled and cold-rolled Fe-0.06C-1.86Mn-0.11Mo (wt%) steels at 750°C [HUA 04].

1.2.1.4 Interaction recrystallization/phase transformation

The interaction between recrystallization and austenite formation has been widely reported in the literature [YAN 85a] [HUA 04] [AZI 11] [OGA 10] [MOH 11] [KUL 13a] [LI 13] [CHB 14] [BAR 15a]. It strongly modifies the microstructural evolutions in several aspects as detailed below.

a. Interaction map

Figure 1.9.a points out a non-complete ferrite recrystallization resulting from the overlapping between recrystallization and austenite formation during intercritical annealing. It is clearly visible by the simultaneous presence of recrystallized ferrite grains (F), deformed ferrite grains (DF) and martensite (M, *i.e.* austenite before quench) after an intercritical annealing. Such mixtures highlighting the overlapping were also reported by several authors [YAN 85a] [KUL 13a] [BAR 15a]. The importance of the overlapping was emphasised thanks to an interaction map proposed by Kulakov *et al.* [KUL 13a] as illustrated in figure 1.9.b. Based on individual modeling of both recrystallization kinetics and phase transformation kinetics, expected microstructural evolutions were located as a function of temperature and heating rate conditions. It clearly appears that the overlapping occurs above a critical heating rate of $3^{\circ}\text{C}/\text{s}$ - which is commonly the case in industrial processing lines. The large overlapping domain strengthens the importance to study cold-rolled steel evolution during intercritical annealing because the recrystallization and the austenite formation kinetics may interact each other and modify their kinetics.

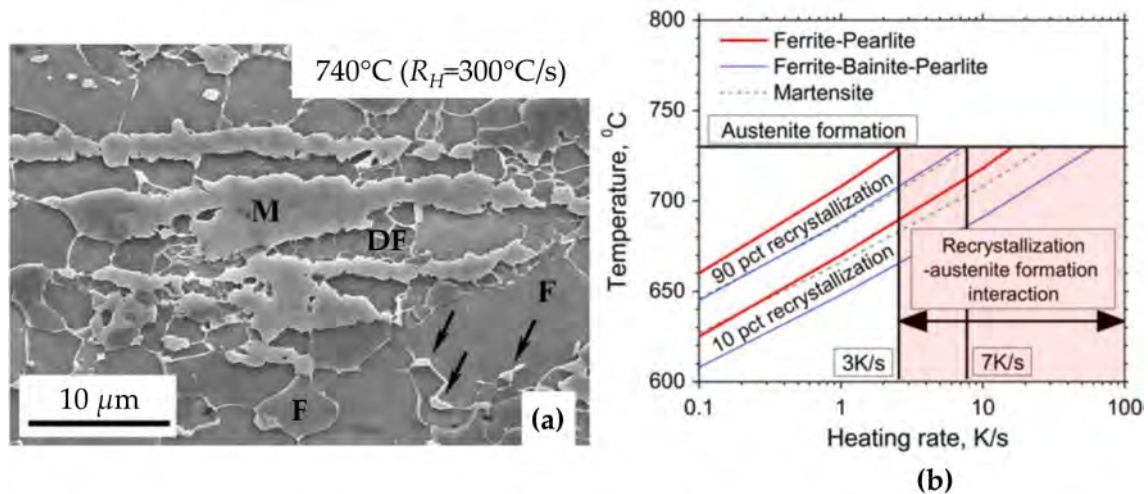


Figure 1.9: (a) SEM micrograph highlighting the recrystallization and phase transformation interaction by the presence of recrystallized ferrite (F), deformed ferrite (DF) and martensite grains (M, prior austenite grain) [AZI 11]. (b) Interaction map of intercritical phenomena proposed by Kulakov *et al.* [KUL 13a].

b. “Weak” or “Strong” interaction: definition and corresponding microstructures

The overlapping leads to two types of interactions called “weak” or “strong” by Chbihi *et al.* [CHB 14] [BAR 15a]. The “weak” interaction defines conditions where recrystallization is already or almost finished when austenite starts to form. This case is equivalent to austenite formation on normalized or prior recrystallized steels. The recrystallized ferrite grain size is the only parameter likely to modify the austenite formation. In a “strong” interaction, both recrystallization and austenite formation occur simultaneously. It significantly impacts steel evolution as it affects (i) the nucleation and growth of austenite and (ii) the recrystallization kinetics. As a consequence, the microstructure is influenced by the interaction. From a practical point of view, a “strong” interaction occurs when ferrite recrystallization is shifted towards higher temperature (above A_{c1}) - *i.e.* for high heating rates [AZI 11] [BAR 15a] [LI 13] and/or for a steel chemistry enriched in Nb, B [BLE 05], Mn or Mo [HUA 04] as these elements retard ferrite recrystallization.

In the case of a strong interaction, a globally coarse and non-homogeneous microstructure was reported in the literature by several authors [HUA 04] [MOH 11] [LI 13] [CHB 14]. Li *et al.* [LI 13] schematized the microstructural evolutions as a function of the heating rate (figure 1.10.a). At low heating rate (5°C/s), there is sufficient time for recrystallization to complete before austenite formation : the interaction is so-called “weak”. Austenite nucleates preferentially at carbide areas and ferrite grain boundaries so that austenite forms a relatively homogeneous network as observed in figure 1.10.b. At higher heating rates (50 or 500°C/s), recrystallization is delayed and the interaction is strong. This leads to the formation of a coarse, banded and heterogeneous microstructure due to various explanations: (i) Moving recrystallizing ferrite boundaries are not favourable for austenite nucleation [HUA 04]; (ii) Deformed ferrite grains are high energy nucleation sites. Therefore, carbides close to unrecrystallized grains are preferential nucleation sites; (iii) Deformed grains promote long-range carbon diffusion.

c. Influence of the interaction on the recrystallization kinetics and on the austenite formation kinetics

As already mentioned, both austenite nucleation and growth are affected by the interaction with recrystallization. Austenite globally develops in deformed regions which are high-energy sites. Moreover, deformed areas may enhance the diffusivities of elements such as C and Mn [KUL 13a]. Austenite formation kinetics is hence globally accelerated in cold-rolled steels. However, unusual high volume fractions were mentioned after long treatment times by several authors [HUA 04] [KUL 13a] [CHB 14] [BAR 15a]. For one-hour holding, fractions are relatively high compared to expected orthoequilibrium or paraequilibrium fractions. Barbier *et al.* introduced the concept of austenite diffusionless transformation to explain these large deviations.

The recrystallization kinetics is also modified by the overlapping with the $\alpha \rightarrow \gamma$ transformation. Yang [YAN 85a] and Ogawa [OGA 15] clearly showed that recrystallization is not affected by the $\alpha \rightarrow \gamma$ transformation as long as austenite fraction is below 10%. However, several authors pointed out a recrystallization inhibition above a critical austenite fraction ($\sim 10\text{-}30\%$) [OGA 10] [CHB 14] [BAR 15a]. Figure 1.11 presents the kinetics of microstructural evolution during holding at (a) 740 and (b) 780°C in the case of a

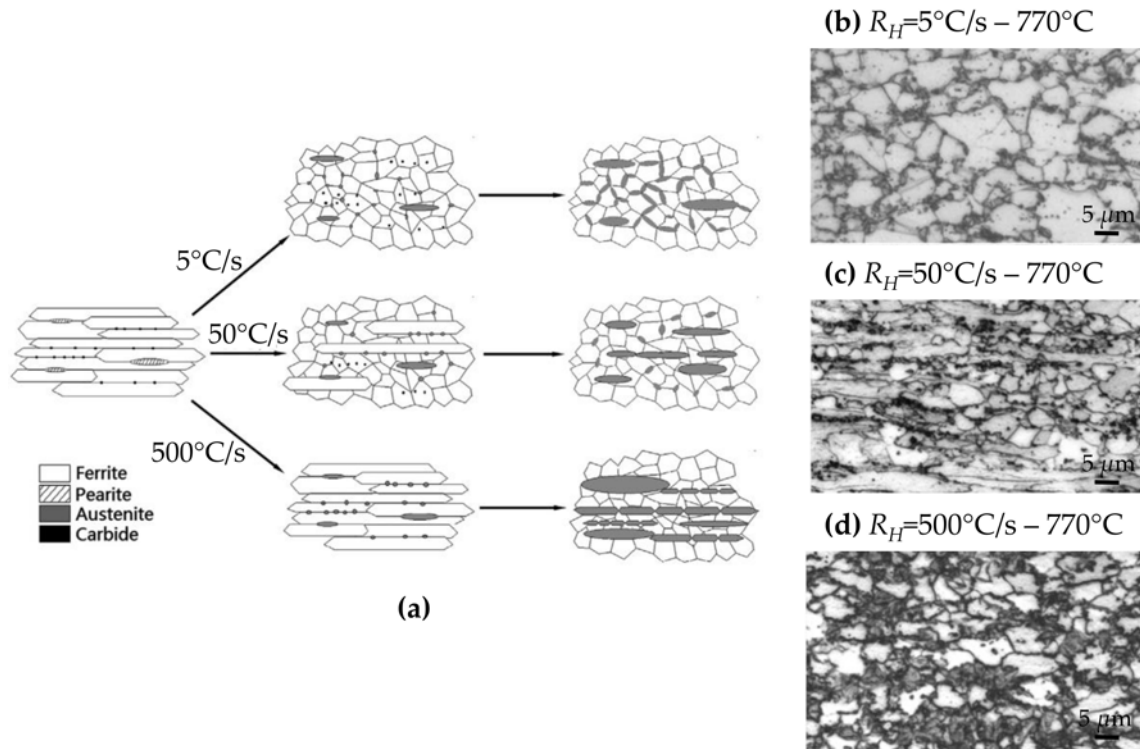


Figure 1.10: (a) Schematic representation of the heating rate influence [5-500°C/s] on the microstructure after annealing at 770°C and (b-d) corresponding optical micrographs [LI 13].

strong interaction obtained by 100°C heating rate [BAR 15a]. At 740°C, recrystallization is momentarily interrupted during austenite formation and slowly restarts after completion of austenite formation. At 780°C, some non-recrystallized ferrite grains seem to persist even after long treatment times. Two explanations were given for recrystallization inhibition [CHB 14] [BAR 15a]: (i) Austenite formation may (partially) relax the elastic energy stored in deformed ferrite grains (through crystal variants leading to a lowering of the local elastic stress fields), which are preferential nucleation sites for recrystallization nucleation; (ii) Stabilization of deformed structures acting as long-distance diffusion paths for the massive transformation.

The microstructural evolutions in a cold-rolled steel are particularly complex due to the possible recrystallization and massive transformation interaction. While various investigations were related in the literature, some points remain unclear such as (i) the unexpected high austenite fraction formed after 1 h holding; (ii) the influence of the interaction on the microstructure and kinetic evolutions. These difficulties compromise modeling efforts to predict the microstructural changes.

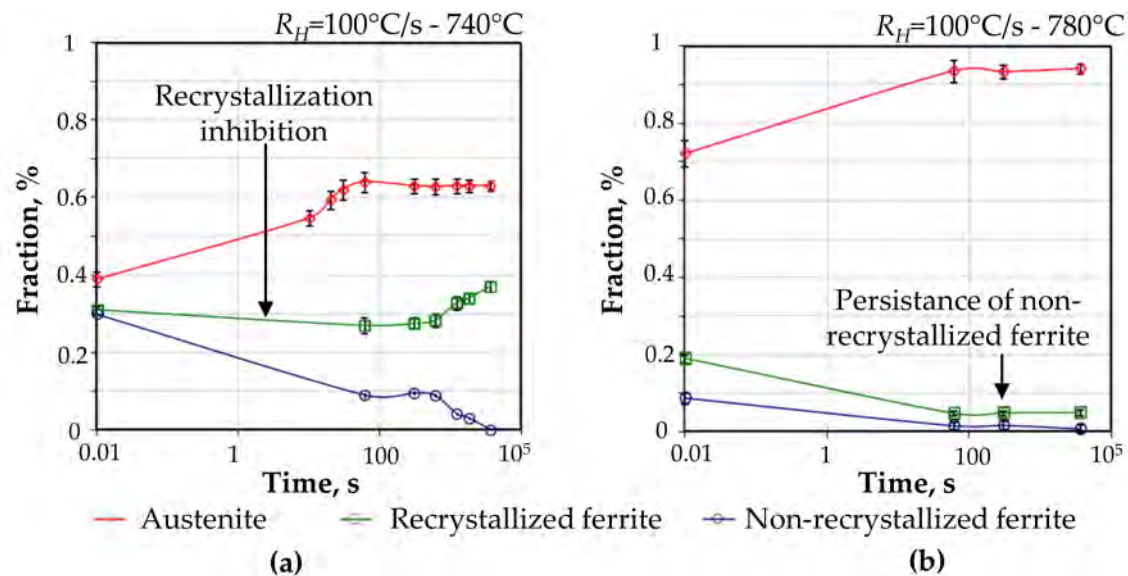


Figure 1.11: Microstructural evolutions during holding at (a) 740 and (b) 780°C in the case of a strong interaction (obtained with high heating rate: 100°C/s) [BAR 15a].

1.2.2 Quenching

Once austenite phase has formed, the steel is cooled down to room temperature or to an intermediate temperature in the case of direct coating. In this case, the steel is immersed in the zinc liquid bath directly during the quench. The martensitic transformation, occurring at low temperature, is possibly not complete before the cooling down to room temperature or even before the coating step that is why it is important to predict this transformation kinetics.

1.2.2.1 Products of austenite decomposition

Austenite may decompose in different products during the cooling stage from the intercritical annealing. Ferrite-pearlite, bainite and/or martensite may form as a function of the applied cooling rate (R_C) [THO 90]. Figure 1.12 presents different kinetics of austenite decomposition as a function of the cooling rate [VAN 10]. Three distinct regions may be observed as a function of temperature range: above 600°C, the ferrite/pearlite domain; between 300-600°C, the bainitic domain; and below 300°C, the martensitic domain. Hence, at low cooling rate (2.2 and 3.3°C/s), austenite decomposes first in ferrite-pearlite then in bainite and finally in martensite below 300°C. At intermediate rate (5.2-13.5°C/s), austenite transforms first into bainite and then into martensite while at high heating rate (51°C/s), austenite directly transforms into martensite. The austenite decomposition is very complex because it depends on number of parameters: (i) the cooling rate [VAN 10]; (ii) the steel carbon content; (iii) the intercritical annealing treatment conditioning both austenite grain size and carbon content; (iv) the other decomposition products [ZHU 13]. The following of this section is focused on the martensitic transformation expected in DP

steel to create the ferrite-martensite microstructure.

1.2.2.2 $\gamma \rightarrow \alpha'$ phase transformation

Martensite is formed by a fast quench of austenite. It is created by a crystallographic change due to a transformation of a face centred cubic phase (austenite, *fcc*) austenite into a body centred tetragonal phase (martensite, *bct*) represented in figure 1.13.a [OLS 76a] [OLS 76b] [OLS 76c] [KRA 99]. Atoms reorganize themselves with very short order displacement (order of interatomic spacing) so that the $\gamma \rightarrow \alpha'$ transformation is defined as a displacive or diffusionless transformation. Martensite has the same composition as its parent phase (austenite). It is therefore a metastable phase with a high carbon supersaturation. Large strains and dislocation cell networks, due to the specific volume change, characterize this phase. The martensitic microstructure is also complex and mixes various scales as illustrated in figure 1.13.b (*i.e.* packet, block, laths) [MOR 15].

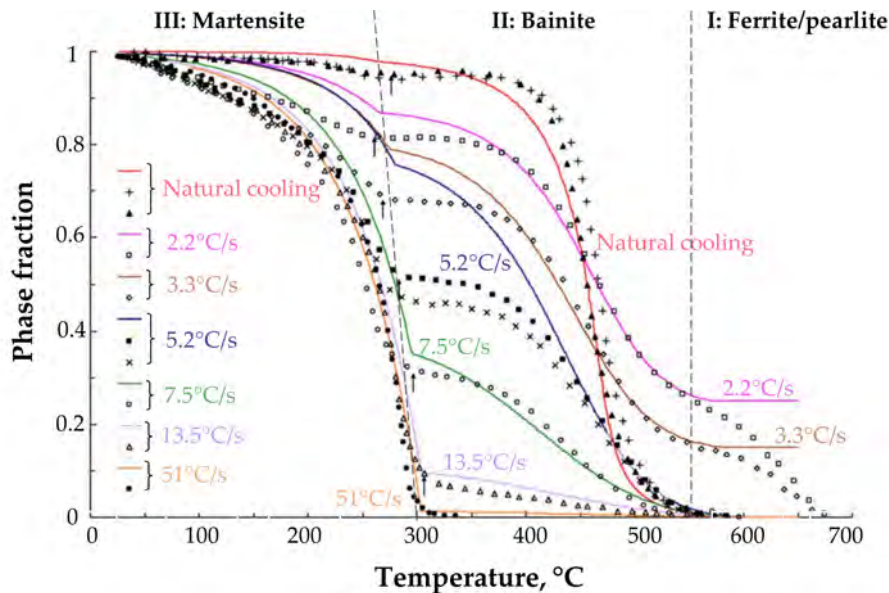


Figure 1.12: Various austenite decomposition paths as a function of the cooling rate for a 0.41C-1.04Cr-0.71Mn-0.22Si-0.26Ni wt% alloy (points correspond to experimental dilatometry data while lines are predicted by a modified Koistinen-Marburger law) [VAN 10].

Concerning the kinetics of the austenite-to-martensite transformation, no influence of the cooling rate has been pointed out so that the transformation is supposed to be athermal [VAN 14]. Another characteristic of the transformation is that nucleation is autocatalytic [BHA 01]; *i.e.* the dislocations generated by the transformation support subsequent nucleation of martensite. However, on the other side, the plastic deformation (associated with the change in length) in the vicinity of the transformed area induces a mechanical stabilization of the austenite. Higher driving force is consequently needed for martensite transformation.

The martensitic transformation is controlled by a number of parameters. Firstly, it is influenced by carbon enrichment and heterogeneity in austenite grains [KHA 90]. The

Authors	Equations (All values are dimensionless, compositions are in weight per-cent, M_S is in °C)	Validity domains
Payson & Savage [PAY 44]	$M_S(K) = 772 - 317C - 33Mn - 11Si - 28Cr - 17Ni - 11Mo - 11W$	
Payson & Savage [PAY 44]	$M_S = 499 - 308C - 32.4Mn - 10.8Si - 27Cr - 16.2Ni - 10.8Mo - 10.8W$	
Nehrenberg (1946)[BAR 14]	$M_S = 499 - 292C - 32.4Mn - 10.8Si - 22Cr - 16.2Ni - 10.8Mo$	
Grange & Steward (1946)[BAR 14]	$M_S = 538 - 350C - 37.7Mn - 18.9Ni - 27Mo$	
Eichman & Hull (1953)[BAR 14] [BAR 14]	$M_S = 41.7(14.6Cr) + 61.1(8.9Ni) + 33.3(1.33Mn) + 27.8(0.47Si) + 1666.7(0.068(C+N)) - 17.8$	
Steven & Haynes (1956)[BAR 14] [BAR 14]	$M_S = 561 - 474C - 33Mn - 17Cr - 17Ni - 21Mo$	
Andrews (1965)	$M_S = 462 - 273C - 26Mn - 13Cr - 16Ni - 30Mo$	
Andrews (1965)[BAR 14]	$M_S = 539 - 423C - 30.4Mn - 11Si - 12.1Cr - 17.1Ni - 7Mo$	
Andrews (1965)[BAR 14]	$M_S = 512 - 453C - 71.5Mn + 15Cr - 16.9Ni - 9.5Mo - 67.7C^*Cr$	
Eldis (1977)[BAR 14]	$M_S = 531 - 391.2C - 43.3Mn - 16.2Cr - 21.8Ni$	
Kung & Rayment (1982)[BAR 14]	$M_S = 539 - 423C - 30.4Mn - 7.5Si - 12.1Cr - 17.7Ni - 7.5Mo + 10Co$	
Sverdlin & Ness (1997)[BAR 14]	$M_S = 520 - 320C - 50Mn - 30Cr - 20(Ni + Mo) - 5(Cu + Si)$	
Wang (2000) [WAN 00]	$M_S = 545 - 470.7C - 37.7Mn - 21.5Cr - 3.96Si + 38.9Mo$	$0.2 < C < 0.5$, $0.2 < Si, Mn, Cr < 2$, $0.1 < Mo < 0.7$
Wang (2000) [WAN 00]	$M_S = 545 - 470.7C - 37.7Mn - 21.5Cr - 3.96Si + 38.9Mo$	$0.2 < C < 0.5$, $0.2 < Si, Mn, Cr < 2$, $0.1 < Mo < 0.7$

Table 1.2: Martensite start (M_S) temperature as a function of steel chemistry (composition in wt%).

Authors	Equations (All values are dimensionless, compositions are in weight per-cent, M_S is in °C)	Validity domains
Wang (2000) [WAN 00]	$M_S = 540 - 584.9C - 117.7Mn - 23.1Si - 42.5Cr + 49.9Mo - 62.5C.Si + 178.3C.Mn - 10C.Cr + 52.5C.Mo + 117.2Si.Mn + 50.9Si.Cr - 142.2Si.Mo - 29.2Mn.Cr - 9.7Mn.Mo + 69.9Cr.Mo$	
Capdevilla (2002)	$M_S (K) = 764.2 - 302.6C - 30.6Mn - 14.5Si - 8.9Cr - 16.6Ni + 2.4Mo - 11.3Cu + 8.58Ci + 7.4W$	
Carapella (2012) [BAR 14]	$M_S = 496(1 - 0.62C)(1 - 0.092Mn)(1 - 0.033Si)(1 - 0.045Ni)(1 - 0.07Cr)(1 - 0.029Mo)(1 - 0.018W)(1 - 0.012Co)$	
Bohemen (2012)	$M_S (K) = 565 - 600(1 - \exp(-0.96C)) - 31Mn - 13Si - 10Cr - 18Ni - 12Mo$	$0.1 < C < 1.9$, $3 < Mn$, $2 < Si$, $4 < Cr$, $5 < Ni$, $0.8 < Mo$
Barbier (2014) [BAR 14]	$M_S = 545 - 601.2(1 - \exp(-0.868C)) - 34.4Mn - 13.7Si - 9.2Cr - 17.3Ni - 15.4Mo + 10.8V + 4.7Co - 1.4Al - 16.3Cu - 361Nb - 2.44Ti - 3448B$	$0.002 < C < 1.86$, $10.24 < Mn$, $1.9 < Si$, $17.9 < Cr$, $29.5 < Ni$, $5.4 < Mo$, $1.19 < V$, $16 < Co$, $3 < Al$, $2.17 < Cu$, $0.11 < Nb$, $1.614 < Ti$, $0.004 < B$

Table 1.3: Martensite start (M_S) temperature as a function of steel chemistry (composition in wt%).

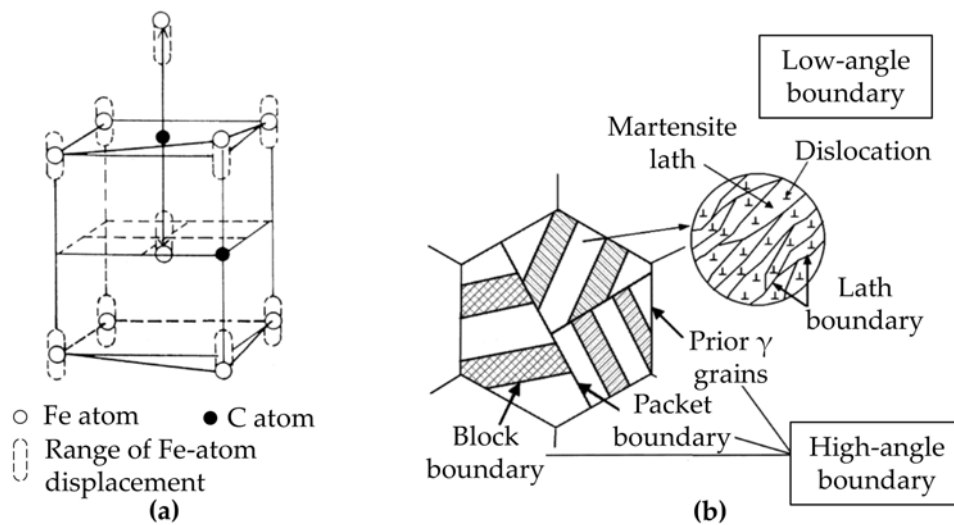


Figure 1.13: Schematic representation of (a) the *bct* martensitic cell: iron atoms are displaced to accord with carbon atoms presence [KRA 99]; and of (b) the complex martensite microstructure [FUR 04].

increase in austenite carbon content retards the martensitic transformation (which occurs at lower temperature) since it decreases the driving force for the transformation. Secondly, the size of the prior austenite grains (D_γ) modifies the kinetics, the start temperature for the martensitic transformation (M_S) and the morphology of martensite laths [MOR 05]. With a decrease in the austenite grain size, M_S temperature is shifted towards lower temperatures. Various explanations were proposed. However, the strengthening of austenite thanks to a Hall-Petch mechanism is privileged: fine austenite grains could increase the resistance of austenite to plastic deformation and thus retard martensite transformation.

Identically to austenite formation, expressions have been proposed to evaluate the martensitic start temperature (M_S) and the martensitic finish temperature (M_F) as a function of the chemistry. Table 1.2 lists some of them. It should be noted that all the equations were developed for steels quenched from the fully austenitic domain.

The studies of martensitic transformation on partially austenitic steels are relatively restricted while the martensitic transformation is different from a fully austenitic state for several reasons: (i) the austenite grain size is globally smaller; (ii) the carbon enrichment of the remaining austenite due to ferrite rejection is different; (iii) ferrite/austenite interfaces have been added in the microstructure [ZHU 13]. As a consequence, the martensite transformation takes place at lower temperature because of the combined effect of the decrease in austenite grain size and the increase in austenite carbon content. The additional ferrite/austenite interface boundaries may be favourable nucleation sites but have an apparent negligible effect compared to the strong influence of the carbon content.

1.2.3 Tempering

The last stage of DP thermal treatment is associated with steel coating. In industrially continuous annealing line, coating is performed by steel immersion in a liquid zinc bath that induces ferrite-martensite evolution (especially martensite evolution). For this reason, the coating is commonly referred to a tempering stage which involves an improvement of steel toughness and remarkable softening dependent on the tempering temperature.

1.2.3.1 Tempering stages

The metastable martensite phase evolves progressively towards an equilibrium state. A succession of phenomena may occur during this tempering stage as detailed in figure 1.14 in the case of binary Fe-C steels [SPE 72]:

- *Stage 0: Carbon segregation.* Carbon redistributes towards low-energy sites such as vacancies, dislocations or grains boundaries. Such segregation takes place at low temperatures (60-120°C) and may eventually occur during the martensitic quench if the M_S temperature is high (*i.e.* auto-tempering effect);
- *Stage 1: Intermediate carbide precipitation.* Carbon atoms are expected to precipitate for temperatures between 100 and 390°C. Various intermediate carbides (ε , η , Hägg) were mentioned in the literature depending on the steel chemistry:
 - Epsilon carbides (ε , Fe_{2-4}C , hexagonal) evenly distributed in martensite. ε precipitation does not take place for steel lower than 0.2 wt% because large amount of carbon has already segregated on dislocations [SPE 72];
 - Eta carbides (η , Fe_2C , orthorhombic) which are transition metal carbides of type M_2C . ε and η carbides considerably decrease the tetragonality of martensite [WAT 06];
 - Hägg carbides (χ , Fe_5C_2) forming at higher temperature between 220 and 300°C, after ε and η precipitations [WAT 06] [SCH 07]. It appears as the precursor for cementite precipitation [NAR 14];
- *Stage 3: Austenite decomposition.* Retained austenite may remain after the martensitic quench and decompose into cementite and ferrite between 200 and 300°C. Retained austenite fractions are however relatively negligible for steel with carbon content lower than 0.4 wt% [SPE 72];
- *Stage 4: Cementite precipitation (θ , Fe_3C , orthorhombic).* Appearing between 290 and 390°C, cementite adopts a plate-like morphology inside martensite laths or interfaces. Cementite succeeds to prior intermediate carbides (*i.e.* ε , η , Hägg) because it is more stable at this temperature range. At higher temperatures, cementite spheroidizes and coarsens [MAS 14];
- *Stage 5: Recovery/Recrystallization.* Recovery initiates for temperatures superior to 400°C and ferrite recrystallization may occur above 600°C.

The activation energies and temperature ranges of the different phenomena occurring during martensite tempering are summarized in table 1.4.

Phenomenon	Temperature range	Activation energy	Reference
C segregation	60-120°C	80 kJ/mol	[CHE 88]
		100.6 kJ/mol	[WAT 06]
Precipitation of ϵ and η -carbides	120-195°C	120-200 kJ/mol	[CHE 88]
	150-180°C	123.8 kJ/mol	[WAT 06]
Precipitation of Hägg carbides	220-300°C	105-120 kJ/mol	[MIT 88] [MOR 01]
		136 kJ/mol	[WAT 06]
Retained γ transformation	250-350°C	176.1 kJ/mol	[WAT 06]
		154.7 kJ/mol	[CHE 88]
Cementite precipitation	290-390°C	163-212 kJ/mol	[MIT 88] [MOR 01]
	300-350°C		

Table 1.4: Temperature range and activation energy data for the martensite tempering.

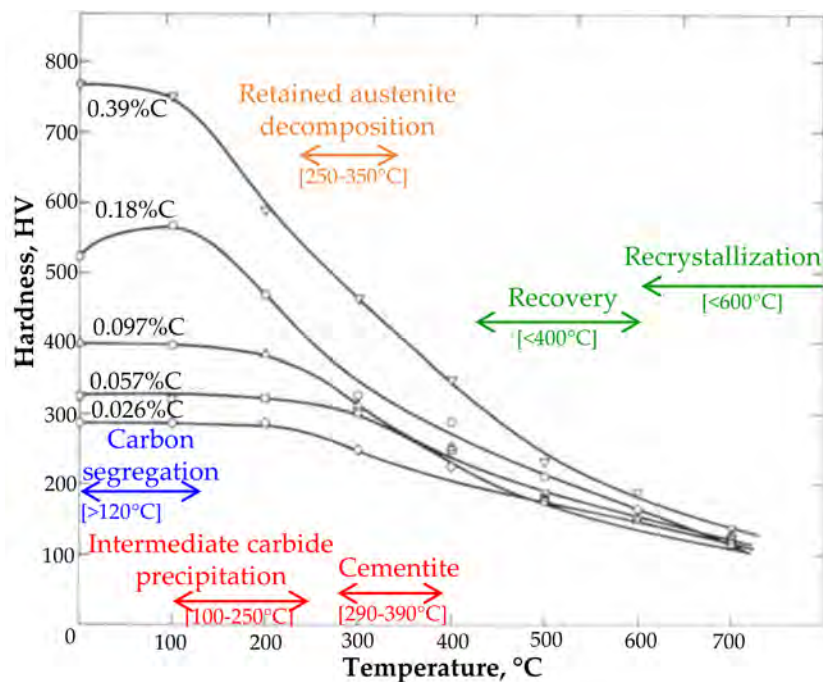


Figure 1.14: Various stages of martensite tempering as a function of the tempering temperature for binary Fe-C steels [SPE 72].

1.2.3.2 Influence of alloying elements

The addition of alloying elements in the steel tends to modify evolutions during the tempering [GRA 77] [MIY 07]. The influence of alloying elements appears above 200°C; below

200°C, same phenomena as those highlighted in the binary Fe-C system are expected. At higher temperature, the addition of alloying elements modifies the kinetics of tempering mechanisms. Carbides enriched in alloying elements form for alloyed steels above 500°C. Such carbides are thermodynamically more stable than cementite and form for sufficient amounts of Cr, V, Mo, W and Ti [HAN 10] [BAB 94]. Diffusion of substitutional atoms is required that is why they form at high tempering temperatures.

Figure 1.15.a shows the effect of the addition of 0.5 wt% Mn on the hardness of tempered martensite containing different carbon contents [GRA 77]. No influence of this addition is observable below 200°C tempering treatment. But substantially higher hardness values are obtained for the Fe-C-0.5Mn steel above 315°C. Such hardness increase is caused by the delay of carbide coarsening generated by Mn addition. Figure 1.15.(c-e) presents the effect of 1 wt%Mn addition on the carbide morphology after 1800 s at 650 °C [MIY 07]. Mn-enriched microstructure shows finer carbides than the binary Fe-C system. Silicon, molybdenum and chromium elements have also the same effect on retarding carbide coarsening.

Others atoms have no marked effect on carbide morphology but lead to a strong solid-solution hardening. This is the case for phosphorus and silicon atoms. In the same way, hardness of tempered steels is increased with the addition of such elements compared to Fe-C steels.

Vanadium has the strongest effect on hardness of tempered martensite because it forms VC or V₄C₃ carbides, replacing cementite and persisting until A_{c1} . Vanadium carbides strengthen thus tempered steels. On the contrary, nickel has a low effect on martensite tempering.

Alloying elements do not only influence the mechanical behavior and carbide morphology; they also change precipitation kinetics. Elements need to redistribute between the martensitic matrix and the newly formed cementite. The addition of Mn, Cr and Si remarkably retard the growth of cementite as illustrated in figure 1.15.b [MIY 07] [THO 97]. Long tempering times (10^4 - 10^5 s) are required at 650°C for reaching the thermodynamic composition, calculated with Thermo-Calc, in the case of Mn-added alloys. The partitioning of substitutional elements therefore controls the growth of the cementite in multicomponent systems.

1.2.3.3 Tempering of dual-phase microstructure

As for the quenching stage, the tempering of dual-phase microstructure is influenced by the respective ratio of ferrite and martensite phases. In theory, the tempering of martensite phase present in DP steels is similar to that of fully martensitic steels [BAL 11].

The tempering of a dual-phase microstructure also leads to a tempering of ferrite [CHE 16a]. During the tempering treatment, residual strains relax and dislocation density decreases (especially in the vicinity of martensite). Moreover, at high temperature ($\sim 400^\circ\text{C}$), carbides may be formed in ferrite thanks to carbon liberated from the martensite tempering [WAT 03]. Ferrite evolution is however relatively minor compared to martensite in a tempering treatment.

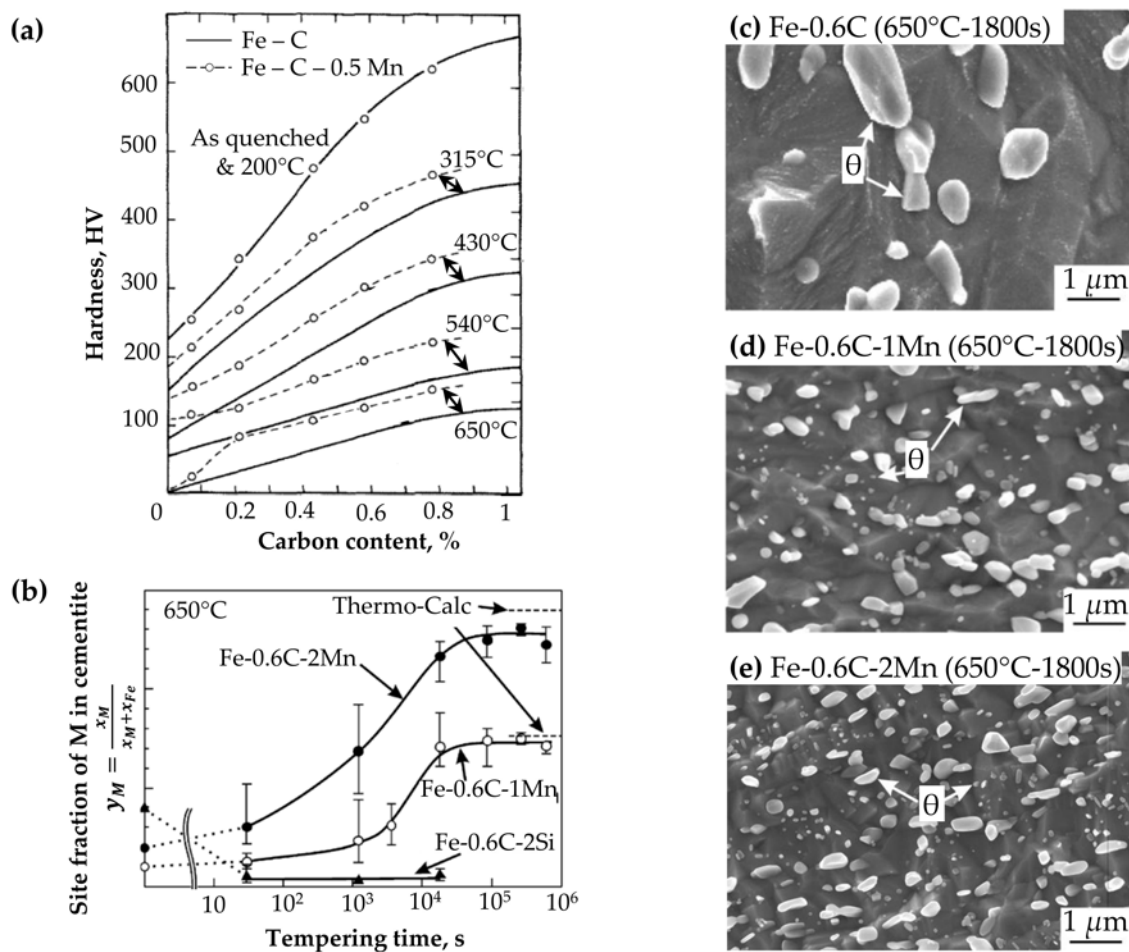


Figure 1.15: (a) Influence of 0.5 wt%Mn addition on hardness of tempered steel at different tempering temperatures [GRA 77]. (b) Evolution of the Mn and Si concentrations during tempering at 650°C. SEM micrographs of (c) Fe-0.6C, (d) Fe-0.6C-1Mn and (e) Fe-0.6C-2Mn steels tempered for 1800 s at 650°C [MIY 07].

1.3 Modeling tools for the prediction of microstructural evolutions

This part is focused on modeling tools available in the literature to describe metallurgical evolutions occurring during thermal treatments. It is divided into three sections. Firstly, empirical based models are presented. The second section is dedicated to thermodynamic aspect of phase transformation. The different equilibrium conditions, named as orthoequilibrium, local equilibrium (LE, LEP and LEPN) and paraequilibrium, cited in the literature will be detailed. In the last section, some numerical and physically based approaches are presented.

1.3.1 Empirical modeling

A number of phenomenological models have been defined to describe microstructural evolutions. The most frequently used are shortly presented in this section.

1.3.1.1 Johnson-Mehl-Avrami-Kolmogorov (JMAK) law

Isothermal condition

Diffusive transformations are usually described by the Johnson-Mehl-Avrami-Kolmogorov formalism (JMAK) [JOH 39] [AVR 39] [KOL 37]. In isothermal conditions, the JMAK law is expressed by the following relation:

$$Y = 1 - \exp(-bt)^n \quad (1.1)$$

where Y represents the transformed fraction (*i.e.* $0 < Y < 1$), n is the Avrami exponent assumed to be constant with the temperature for a given transformation. b is the rate constant (in s^{-1}) defined as follows:

$$b = b_0 \exp\left(-\frac{Q}{RT}\right) \quad (1.2)$$

where b_0 is a constant, Q is the activation energy of the transformation (J/mol), R is the gas constant and T the temperature (K). Such an equation allows to reproduce the sigmoidal shape of transformations driven by nucleation and growth. The final saturation regime is also well reproduced.

The activation energy (Q) of the law may be experimentally determined thanks to the application of a time-temperature equivalence to the kinetics of transformation determined at different temperatures [LAM 16]. This time-temperature equivalence is based on the hypotheses that the diffusion length should be the same for two time-temperature couples (t_A, T_A) and (t_B, T_B) .

$$\begin{cases} t_A = t_0 \exp\left(\frac{Q}{RT_A}\right) \\ t_B = t_0 \exp\left(\frac{Q}{RT_B}\right) \end{cases} \quad (1.3)$$

Hence, the equivalent time t_B^{eq} at temperature T_B for the thermal treatments performed at temperature T_A is expressed by the following relation:

$$t_B^{eq} = \exp\left(\frac{Q}{R}\left(\frac{1}{T_B} - \frac{1}{T_A}\right)\right) t_A \quad (1.4)$$

The Avrami exponent n may also be derived from the experimental kinetics by a linearisation of equation 1.1:

$$\ln\left(\ln\left(\frac{1}{1-Y}\right)\right) = n \ln t + n \ln b \quad (1.5)$$

The n parameter corresponds to the slope of the curves plotting $\ln\left(\ln\left(\frac{1}{1-Y}\right)\right)$ as a function of $\ln(t)$. The latter parameter b_0 is a fit parameter which can be adjustable after

Q and n determination.

The isothermal JMAK equation may also be expressed as a function of the half transformation time t_{50} as used by Kulakov *et al.* [KUL 13a]:

$$Y = 1 - \exp\left(-0.693\left(\frac{t}{t_{50}}\right)^n\right) \quad (1.6)$$

with t_{50} also a temperature dependent parameter such as:

$$t_{50} = (t_{50})_0 \exp\left(\frac{Q}{RT}\right) \quad (1.7)$$

All three parameters Q , n and $(t_{50})_0$ are adjustable parameters and lead to different values from those determined from the equation (1.1).

Non-isothermal condition

In non-isothermal conditions, the JMAK law is expressed in its original differential form:

$$\frac{dY}{dt} = nb^n t^{n-1} (1 - Y) \quad (1.8)$$

As in the case of the isothermal conditions, Q and n parameters may be determined from the experimental transformation kinetics obtained in non-isothermal conditions for different heating rates (R_H) thanks to Kissinger method [KIS 57]. The activation energy Q may be obtained by plotting $\ln\left(\frac{R_H}{T_{max}^2}\right)$ (unit: R_H in K/s, T_{max} in K) as a function of $\left(-\frac{1}{RT_{max}^2}\right)$ where T_{max} corresponds to the temperature for which the kinetics velocity is maximal and R_H is the heating rate. Points obtained for different heating rates should align on a straight line, the slope of which is equal to Q parameter. Considering the sigmoidal shape of kinetics, T_{max} is maximal at the inflexion point (*i.e.* 50% of transformation). In the same way, the Avrami coefficient n may be determined as the slope of the straight line describing the evaluation of $\ln(-\ln(1-Y))$ as a function of $\ln\left(\frac{T_{max}}{R_H} \exp\left(\frac{Q}{RT}\right)\right)$.

The JMAK law was successfully used to describe many transformations such as ferrite recrystallization [HUA 04] [LI 13] [KUL 13a] [KUL 14], ferrite-to-austenite transformation [KUL 14] [KUL 13a], austenite-to-ferrite transformation [ASH 17] and austenite-to-bainite [KUL 14] transformation. In 2014, Kulakov *et al.* [KUL 13b][KUL 14] combined different JMAK models to predict phase evolutions on complex cycles considering multiple transformation as shown in figure 1.16. The model predicts the recrystallization, the austenite formation, the austenite decomposition into ferrite and bainite phases. However, the combination of recrystallization and austenite formation is not described in this approach.

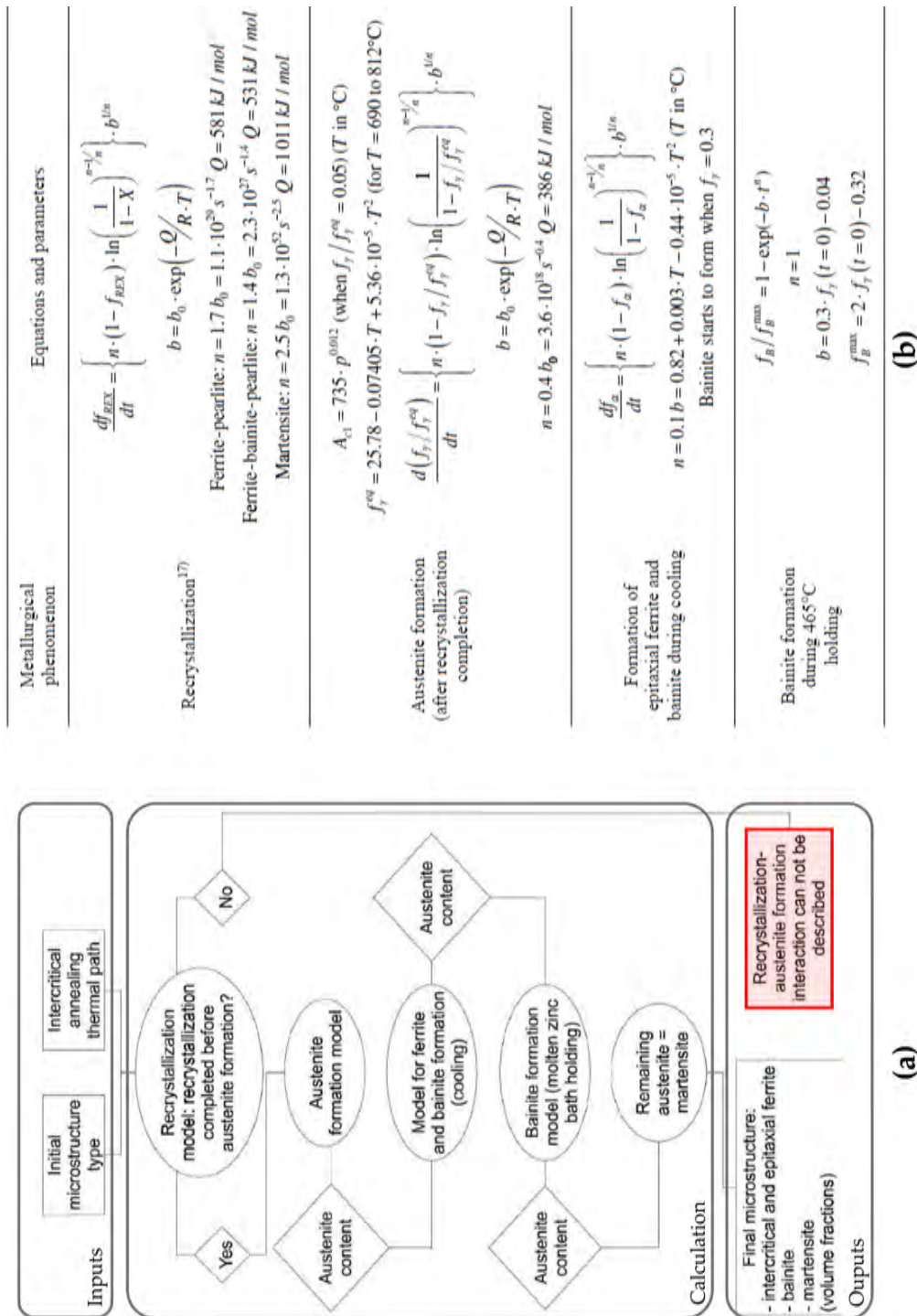


Figure 1.16: (a)Algorithm and (b) various phenomenological laws combined in Kulakov’s model considering recrystallization, austenite formation, austenite decomposition into ferrite and bainite phases [KUL 14].

1.3.1.2 Koistinen-Marburger (KM) law

The Koistinen-Marburger (KM) law is commonly used to describe the martensitic transformation kinetics [KOI 59] [BOH 09a] [BOH 09b] [BOH 12]. It is expressed by the relation:

$$f_{\alpha'} = 1 - \exp(-\alpha_m (M_s - T)) \quad (1.9)$$

with M_S the martensitic start temperature and α_m the parameter governing the slope of the curve. Some authors have expressed M_S and α_m as a function of the steel chemistry as given in table 1.5.

Authors	Equations (All values are dimensionless, compositions are in weight percent, M_S is in °C)	Validity domains
Andrew [BOH 09a]	$\alpha_m = 0.0224 - 0.0107C - 0.0007Mn - 0.00005Ni - 0.00012Cr - 0.0001Mo$ $M_S = 462 - 273C - 26Mn - 16Ni - 13Cr - 30Mo$	C < 1.9, Ni < 14.9, Cr < 8
Bohemen [BOH 12]	$\alpha_m = (27.2 - 19.8(1 - \exp(-1.56C)) - 0.14Mn - 0.21Si - 0.11Cr - 0.08Ni - 0.05Mo) 10^{-3}$ $M_S = 565 - 600(1 - \exp(-0.96C)) - 31Mn - 13Si - 10Cr - 18Ni - 12Mo$	C < 1.9, Mn < 3, Si < 2, Cr < 4, Ni < 5, Mo < 0.8

Table 1.5: Expression of M_S and α_m parameters for the Koistinen-Marburger equation (compositions in wt%).

The KM equation was initially developed for fully austenitized Fe-C systems with carbon contents in the range 0.3-1.1 wt%. Bohemen *et al.* [BOH 09b] adjusted the equation to adapt it to partially austenitized system:

$$f_{\alpha'} = (1 - f^{\alpha_0}) (1 - \exp(-\alpha_m (M_s - T))) \quad (1.10)$$

with f^{α_0} the ferrite fraction before the martensitic quench and $f_{\alpha'}$ defined as the martensite fraction. M_S and α_m parameters were determined considering the austenite carbon content thanks to a classical mass balance such as:

$$C_C^\gamma = \frac{C_C^0 - f^{\alpha_0} C_C^\alpha}{1 - f^{\alpha_0}} \quad (1.11)$$

C_C^0 is the steel carbon content. C_C^α and C_C^γ are respectively the ferrite (usually taken as 0.02 wt%) and austenite carbon content. An example of application of the KM model was given in figure 1.12.

1.3.2 Thermodynamics of phase transformation

This section provides an overview on thermodynamic aspects considering phase transformations [HIL 98] [AGR 06] [POR 09] [GOU 15]. For sake of clarity, thermodynamics of binary Fe-C system will be first recalled before considering ternary Fe-C-X and multicomponent systems.

1.3.2.1 Binary Fe-C system

At constant temperature and pressure, the thermodynamic equilibrium condition is characterized by the minimum of the Gibbs free energy (G) of the system. In the two-phase ($\alpha + \gamma$) region, it was demonstrated that the equilibrium concentrations of phases (C_X^α , C_X^γ) correspond to the common tangent of Gibbs energies [AGR 06]. By construction, the thermodynamic equilibrium is therefore defined by the equality of chemical potentials in phases for each component (*i.e.* Fe and C):

$$\begin{cases} \mu_{Fe}^\alpha = \mu_{Fe}^\gamma \\ \mu_C^\alpha = \mu_C^\gamma \end{cases} \quad (1.12)$$

Figure 1.17 presents a schematic Fe-C binary diagram with the respective Gibbs free energies for the α and γ phases at temperature T . The equilibrium fractions in phases (f^α, f^γ) are obtained by the lever-rule in the phase diagram. The operative tie-line or iso-activity line for both C and Fe is therefore unique in binary Fe-C system: there is a unique thermodynamic equilibrium.

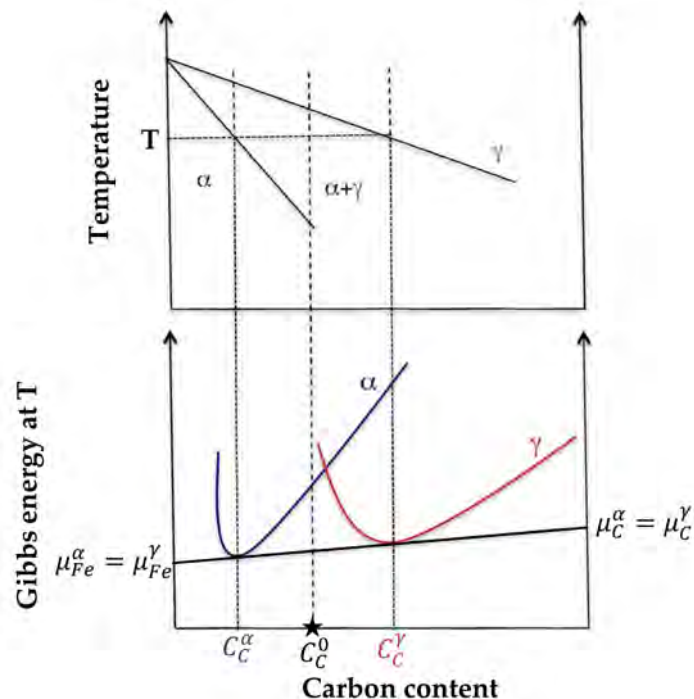


Figure 1.17: Schematic representation of phase diagram and associated Gibbs free energy diagram at temperature T at thermodynamic equilibrium [GOU 15]. The equilibrium carbon contents in phases (C_C^α, C_C^γ) are represented for the steel containing a carbon content C_C^0 .

1.3.2.2 Ternary Fe-C-X system

Orthoequilibrium, OE

In ternary systems, the Gibbs free energy is a function of the temperature and of the concentrations of not only Fe and C elements but also of X element. Figure 1.18.a proposes a 3D-representation of the Gibbs energies of the ferrite and austenite phases. As for binary systems, the thermodynamic equilibrium between ferrite and austenite is defined by the equality of chemical potential in both phases of all components:

$$\begin{cases} \mu_{Fe}^{\alpha} = \mu_{Fe}^{\gamma} \\ \mu_C^{\alpha} = \mu_C^{\gamma} \\ \mu_X^{\alpha} = \mu_X^{\gamma} \end{cases} \quad (1.13)$$

The common tangent rule is therefore transposed to a tangent plane of the α and γ Gibbs energies as plotted in 1.18.a. The basal plane is a projection of the plane corresponding to an equality of Fe, C and X chemical potentials. Identically, the plotted tie-line determines the equilibrium concentrations in α and γ phases for the given composition marked by a star.

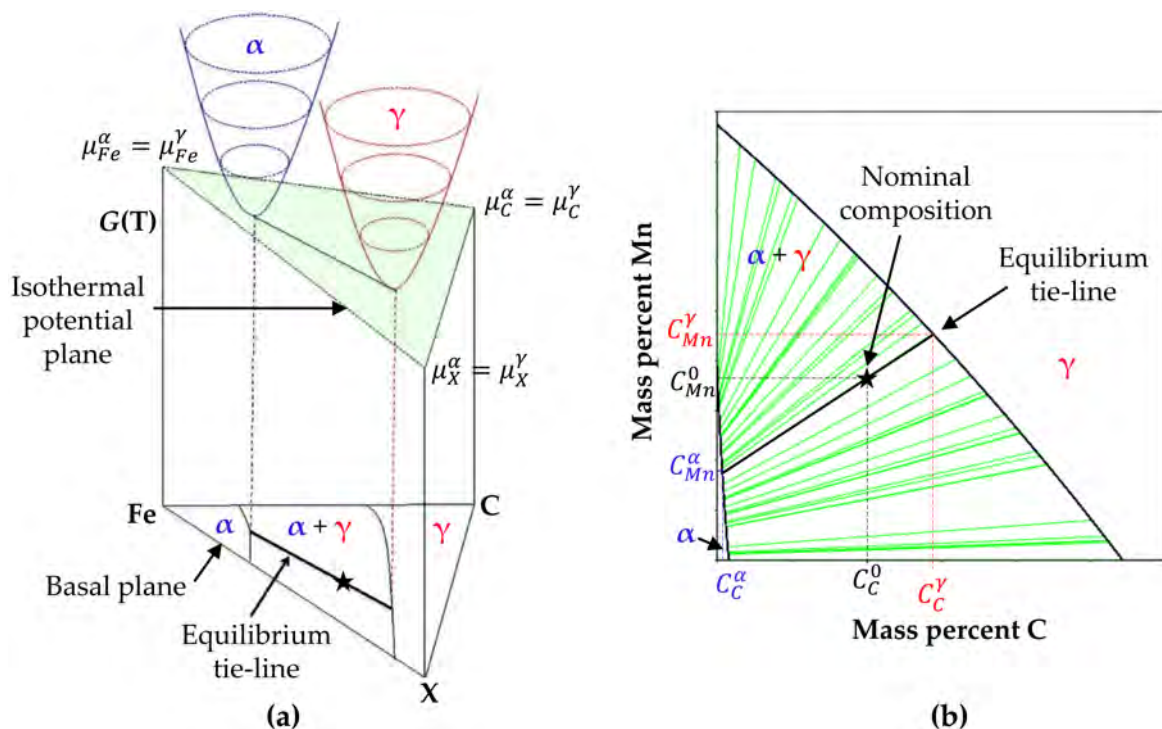


Figure 1.18: (a) 3D-schematic representation of Gibbs free energy diagram highlighting the iso-chemical potential plane [GOU 15]. (b) Isothermal section of Fe-C-Mn system at 760°C. C (C_C^{α} , C_C^{γ}) and Mn (C_{Mn}^{α} , C_{Mn}^{γ}) equilibrium concentrations are emphasised for the nominal composition (C_C^0 , C_{Mn}^0).

For sake of simplicity, the ternary diagram is usually represented in 2D-orthogonal system. Figure 1.18.b gives an example of an isothermal representation of the Fe-C-Mn

system at 760°C. The area with green lines defines the two-phase ($\alpha + \gamma$) region. Each green line is named as tie-line and defines equilibrium conditions of the two phase mixture. The ($\alpha + \gamma$) equilibrium of a given nominal composition (C_C^0, C_{Mn}^0) (identified by a star) is defined by the tie-line passing through this composition. Such tie-line defines the orthoequilibrium condition where all elements are at the equilibrium in phases. It refers to the equilibrium state achieved after long treatment times by Speich *et al.* [SPE 81]. The equilibrium composition in the ferrite ($C_C^\alpha, C_{Mn}^\alpha$) and austenite ($C_C^\gamma, C_{Mn}^\gamma$) phases are reported in figure 1.18.b.

Intermediate equilibriums

As the diffusivities of carbon and substitutional elements differ substantially in steels, orthoequilibrium is achieved after very long holding times ($\sim 10^5 - 10^6$ s) as shown in figure 1.19. The phase transformation kinetics may be decomposed in four stages: (i) first stage, below 10^{-2} s, driven by carbon diffusion with negligible Mn partitioning (*i.e.* LENP); (ii) second stage ($10^{-2} - 10^3$ s) controlled by Mn diffusion in ferrite; (iii) third stage ($10^3 - 10^5$ s) controlled by Mn diffusion in austenite (*i.e.* LEP); and finally (iv) the orthoequilibrium where all elements are at the thermodynamic equilibrium. LENP (Local Equilibrium with Negligible Partitioning) and LEP (Local Equilibrium with Partitioning), reported in figure 1.19, are examples of intermediate equilibriums that will be defined in the following.

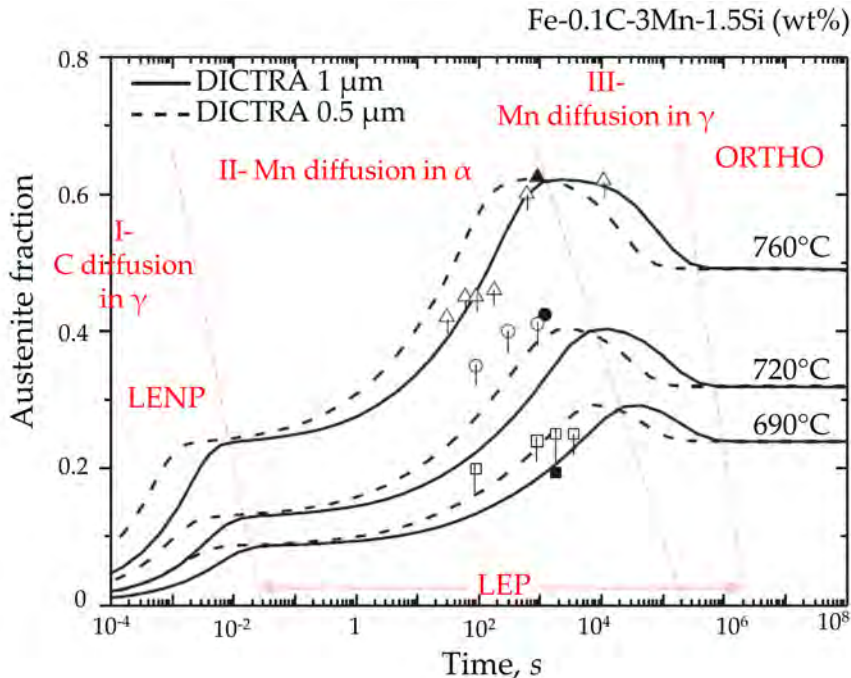


Figure 1.19: Model and experimental kinetics of austenite formation during isothermal holding of a quaternary Fe-0.1C-3Mn-1.5Si (wt%) alloy [WEI 13]. The ORTHO equilibrium is achieved after 10^6 s. Intermediate equilibriums are reported (*i.e.* LENP and LEP).

Local equilibrium, LE

A first approach of intermediate equilibrium is based on the respect of an equilibrium condition at the α/γ interface. The large difference of diffusivities $\left(\frac{D_C^\gamma}{D_X^\gamma}\right)$ between C and X elements induces a deviation from the orthoequilibrium tie-line to satisfy both (i) the respect of local equilibrium at the α/γ interface; and (ii) the same interface velocity of C and X elements despite the large difference of diffusivities. The tie-line defining the local equilibrium condition at the α/γ interface evolves therefore during the phase transformation. At a given time, the tie-line defining the local equilibrium condition at the α/γ interface is named as “operative” tieline.

Such LE approach was first developed for the $\gamma \rightarrow \alpha$ transformation as detailed in appendix A. An analog approach was then developed for the reverse $\alpha \rightarrow \gamma$ transformation. The LE condition may be applied to the $\alpha \rightarrow \gamma$ phase transformation in a Fe-C-Mn system supposing a low redistribution of manganese which is globally the case in typical industrial conditions (*i.e.* <1 hour of holding time). The corresponding LE tie-line is reported in figure 1.20 (also named as LENP tie-line based on an analogy to ferrite formation described in appendix A [WEI 13] [CHE 14]). Austenite forms with negligible redistribution of Mn. The LE condition at the interface generates therefore a Mn concentration “spike” at the α/γ interface. The equality of Mn concentration in the newly formed austenite phase with the bulk Mn composition defines the LENP tie-line which is different from the orthoequilibrium tie-line. LENP condition will then evolve towards orthoequilibrium condition with Mn diffusion in ferrite and austenite phases as emphasised by Wei *et al.* in figure 1.19 [WEI 13].

Paraequilibrium, PE

In another approach, the paraequilibrium (PE) model lies on the hypotheses that the phase transformation is only triggered by the diffusion of carbon and all other elements are not diffusing; even across the interface [AGR 06]. It is supposed that the transformation is partitionless and alloying elements are unaffected by the interface motion. Consequently, only the chemical potential of carbon specie is supposed to be equal in ferrite and austenite phases such as:

$$\begin{cases} \mu_C^\alpha = \mu_C^\gamma \\ \mu_X^\gamma - \mu_X^\alpha = \frac{x_{Fe}}{x_X} (\mu_{Fe}^\gamma - \mu_{Fe}^\alpha) \end{cases} \quad (1.14)$$

with x_{Fe} and x_X respectively the iron and X mole fractions.

Figure 1.21.a shows the Gibbs energy diagram considering PE assumption. The corresponding PE diagram is added in figure 1.21.b and differs substantially from full equilibrium diagram. Other equilibriums are achieved considering the non-diffusion of X element. The PE tie-lines are horizontal and the concentration of Mn at interface is equal to the one of the bulk composition.

This PE model has originally been developed for the reverse phase transformation $\gamma \rightarrow \alpha$ where ferrite forms from a homogeneous austenite phase. In this case, the non-diffusion of alloying elements can be an acceptable assumption.

The PE assumption is however not questionable in the case of austenite formation. Indeed, austenite forms from a non-homogeneous cementite and ferrite mixture with im-

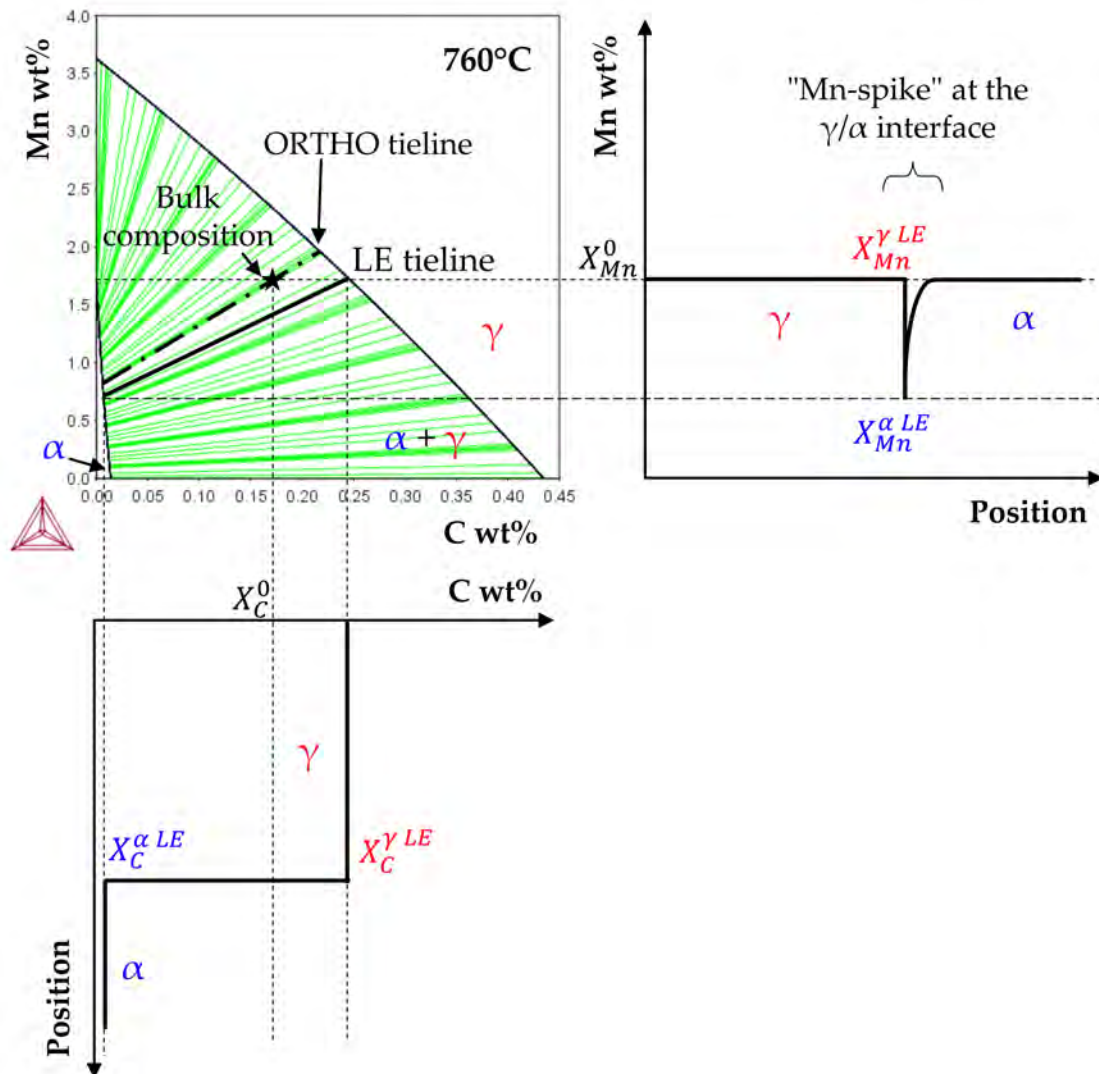


Figure 1.20: Isothermal section of the Fe-C-Mn system at 760°C. C and Mn concentration profiles are reported for the $\alpha \rightarrow \gamma$ phase transformation according to the LEMP condition. A characteristic Mn narrow “spike” is present at the γ/α interface.

portant concentrations gradient. Substitutional elements will hence diffuse across the interface and such PE condition is no longer viable for austenite formation.

1.3.2.3 Multicomponent system

In a multicomponent system, the situation becomes much more complex. The chemical potential equality plane for orthoequilibrium is transposed to determine the tangent hyperplane in a space of N -dimensions with N the number of species.

From a practical point of view, orthoequilibrium also defines the equilibrium of all species in all phases. The paraequilibrium assumption may also be used considering only

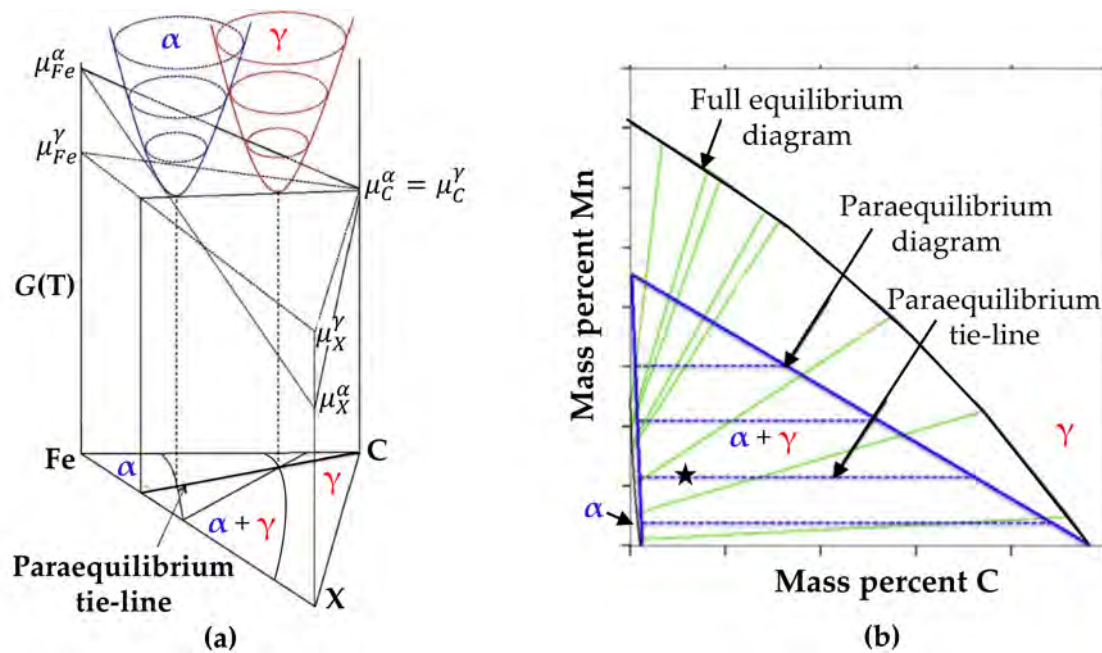


Figure 1.21: Schematical representation of (a) the Gibbs free energy diagram and (b) the phase diagram in the case of the $\gamma \rightarrow \alpha$ transformation supposing PE condition.

C diffusion and equilibrium. All other hypothesis (LE, LEP or LENP) have however no sense in the case of multicomponent system.

1.3.3 Physically based modeling

While empirical modelings are in many cases useful, they present some limitations. For example, the generalization of an empirical model outside the range of experimental parameters on which it has been developed is risky because its physical basis is not verified [FIN 03]. As a consequence, there is a strong motivation to develop physically based approaches.

This section is focused on numerical models used in this PhD-work although other approaches, like the phase-field models [MIL 11], brought interesting and promising results. Such choice was realized to focus the modeling efforts on phase transformation kinetics and to achieve a good compromise between calculation time and physical justifications.

1.3.3.1 Diffusion-controlled

The phase transformation may be modelled considering the diffusive character of the transformation [AKB 93] [ATK 94]. Hence, the kinetics of the massive transformation is based on the diffusion of elements across a moving interface. The interface between phases is defined as a sharp interface with discontinuities of properties (especially discontinuity of concentration values). In addition, a thermodynamic equilibrium is supposed to be

established on both side of the interface. In other words, no pressure is exercised at the moving interface. It means that the chemical potential of X in the ferrite and austenite phases, μ_X^α and μ_X^γ , are equal at the interface :

$$\mu_X^\alpha(C_X^{\alpha,eq}, T) = \mu_X^\gamma(C_X^{\gamma,eq}, T) \quad (1.15)$$

The respect of this condition drives the displacement of the interface until reaching thermodynamic equilibrium in all phases. Therefore, the migration of the interface triggers the kinetics of the massive transformation.

From a practical point of view, the algorithm for migrating interface rests on the numerical resolution of Fick's equation for the diffusion of elements:

$$\frac{\partial C_X^i}{\partial t} = D_X^i \frac{\partial^2 C_X^i}{\partial z^2} \quad (1.16)$$

with D_X^i and C_X^i respectively the diffusion coefficient and concentration of X element in the phase i . The Fick's equation is solved in a finite difference system and the interface motion is obtained supposing the respect of local thermodynamic equilibrium at the interface. The interface velocity v is therefore expressed by a mass balance:

$$v = \frac{dz}{dt} = \frac{J_X^\gamma - J_X^\alpha}{C_X^{\gamma,eq} - C_X^{\alpha,eq}} \quad (1.17)$$

where J_X^α and J_X^γ are fluxes of X at ferrite and austenite side of the interface. $C_X^{\gamma,eq}$ and $C_X^{\alpha,eq}$ correspond to the solubility limits of X element which are determined thanks to thermodynamics.

Diffusion-controlled models were successfully used in the case of binary, ternary [LAI 16] or even quaternary [WEI 13] systems. However, to our knowledge, this type of models was not extended to more complex systems while DICTRA software enables to do it.

This diffusion-controlled approach is also commonly associated with the classical theory of nucleation to describe the nucleation and growth of precipitates [PER 08].

1.3.3.2 Interface-controlled

On an opposite approach, Christian [CHR 81] introduced the concept of interface-controlled kinetics. It supposes that the diffusion occurs at infinite rate compared to the interface velocity. The transformation kinetics is hence managed by the interface velocity as expressed below:

$$v = M \times \Delta G \quad (1.18)$$

ΔG corresponds to the driving force for the transformation. The interface mobility M is usually supposed to obey to an Arrhenius law of the type:

$$M = M_0 \exp\left(-\frac{Q}{RT}\right) \quad (1.19)$$

with Q the activation energy and M_0 a mobility constant.

The interface-controlled mode is the extreme opposite to diffusion-controlled mode.

1.3.3.3 Mixed-mode

In general, neither the interface mobility nor the diffusion are infinite [PUR 11] [GOU 15]. The transformation appears to be mixed-mode character controlled both by diffusion and interface mobility.

First, mixed-mode models were developed for the austenite-ferrite transformation [KRI 97] [SIE 04] [BOS 07] [BOS 09]. Supposing a finite interface mobility, authors have implemented an algorithm allowing a deviation from equilibrium at the interface. The interface concentrations are no longer at equilibrium (as for fully diffusion-controlled model) but depend on diffusion fluxes (mass balance). This deviation from equilibrium defines the driving force ΔG for the austenite formation:

$$\Delta G = \chi(T) \times (C_C^{\gamma,int} - C_C^{\gamma,eq}) \quad (1.20)$$

with $C_C^{\gamma,int}$ and $C_C^{\gamma,eq}$ corresponding respectively to the interfacial and equilibrium carbon content in austenite. $\chi(T)$ is a temperature dependent parameter. The interface velocity v is then proportional to this driving force ΔG and to the mobility M according to equation (1.18).

Figure 1.22 presents an illustration of the profile evolution of carbon in the mixed-mode model for different transformation times [MEC 15]. Initially, at time t_0 , the system is composed of pearlite and ferrite. At Ac_1 temperature, pearlite is no longer at thermodynamic equilibrium and carbon needs to diffuse to reach equilibrium plotted for the infinite time t_∞ . At an intermediate time t , the carbon profile is characterized by an interfacial carbon concentration in austenite ($C_C^{\gamma,int}$) different from the equilibrium value ($C_C^{\gamma,eq}$). Moreover, the shape of austenite carbon profile is a footpath of diffusion and interface velocity combination.

To our knowledge, there is a significant lack of comparisons with an experimental database. The main studies are limited to numerical implementation and analysis without confrontation with experimental. Bos *et al.* numerically investigated the effect of the cooling rate during ferrite formation without link with experimental ferrite formation kinetics [BOS 09]. Latter, in 2015, Mecozzi *et al.* applied such an approach for ferrite-to-austenite transformation [MEC 15]. They realized a comparative study between the diffusion-controlled, interface-controlled and the mixed-mode model changing both the holding temperature and mobility values. However they did not validate this model with an experimental database.

1.3.3.4 Other modeling approaches

Recently number of numerical models have been proposed to describe microstructural evolutions in 2D or 3D scales. Two main approaches may be distinguished: the Cellular Automaton (CA) and the phase field (PF).

Cellular Automaton models (CA)

CA models are based on discretized system on which each cell (i) depends on the state of neighbouring cells. The growth length $l_i^{G_{Bcell}}$, of a given grain boundary cell i , is updated

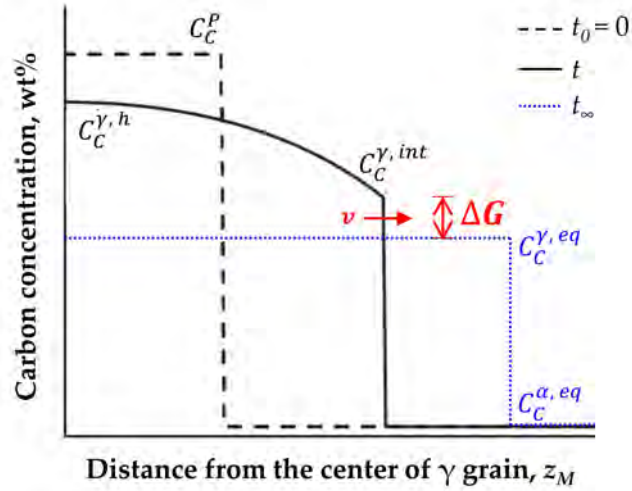


Figure 1.22: Schematic representation of the mixed-mode model system. Carbon concentration profiles are plotted at different times: at t_0 , at an intermediate time t and at the infinite time t_∞ (for which the γ/α equilibrium is reached). The interface velocity is evaluated as the deviation to the equilibrium by the relation $v = M \times \Delta G$ with $\Delta G = \chi(T) \times (C_C^{\gamma,int} - C_C^{\gamma,eq})$ [MEC 15].

by Euler time integration:

$$l_i^{GBcell}(t + \Delta t) = l_i^{GBcell}(t) + v_i^{GBcell}(t)\Delta t \quad (1.21)$$

with v_i^{GBcell} is the grain boundary velocity.

Bos *et al.* [BOS 10] developed an interesting 3D-CA model describing the microstructure evolution during the annealing of a cold-rolled ferrite-pearlite steel. The model originality rests on the fact that the transformation takes place at grain boundary cells according to sub-models to calculate the grain boundary velocity of (i) the ferrite recrystallization, (ii) pearlite-to-austenite and (iii) ferrite-to-austenite and (iv) austenite-to-ferrite transformations. The first three sub-models are based on an interface-controlled approach where the velocity of the grain boundaries are expressed by a mobility and driving force. All phenomena are expected to occur sequentially one by one, *i.e.* no recrystallization/phase transformation interaction was considered.

Latter, Zheng and Raabe [ZHE 13] published on 2D-CA model considering this interaction. In this model, the austenite formation is treated in a mixed-mode growth taking into account both the C diffusion and interface motion. The results of the simulation allows to capture number of experimental observations observed by Azizi-Alizamini *et al.* [AZI 11] such as austenite formation at pearlite area, ferrite grain boundaries, deformed ferrite area or intragranular ferrite. However, the model was not compared to an experimental database from a kinetic point of view.

Phase Field models (PF)

In parallel, other authors focused on PF approaches [MIL 11]. Each grain i is defined by its own phase field parameter ϕ_i assigning the belonging to the grain: ϕ_i is equal to 1 inside the grain i and 0 outside the grain. Within the width interface η , ϕ_i evolves continuously from 1 to 0. The phase-field parameter ϕ_i represents the local fraction of each grain implying that a constraint of $\sum_i \phi_i = 1$ exists. A set of attributes is hence attributed to each grain (phase nature, crystallography *etc.*). The temporal evolution of each field parameter is obtained by the superposition of pair-wise interaction with its neighbouring grains according to the equation:

$$\frac{d\phi_i}{dt} = \sum_{i \neq j} m_{ij} \left\{ \sigma_{ij} \left[(\phi_j \nabla^2 \phi_i - \phi_i \nabla^2 \phi_j) + \frac{\pi^2}{2\eta^2} (\phi_i - \phi_j) \right] + \frac{\pi}{\eta} \sqrt{\phi_i \phi_j} \Delta G_{ij} \right\} \quad (1.22)$$

The equation (1.22) is a function of the interface mobility m_{ij} , the interface energy σ_{ij} and the driving pressure ΔG_{ij} between grains i and j .

In 2011, Rudnizki *et al.* [RUD 11] [RUD 12] used a 2D-PF model (commercial software MICRESS) to describe austenite formation in a prior recrystallized ferrite-pearlite steel. A high value of interface mobility was applied to ensure carbon diffusion controlled of the austenite formation. Moreover, the global equilibrium consideration was replaced by Local Equilibrium with Negligible Partitioning (LENP) and paraequilibrium (PE) conditions in order to investigate the role of the substitutional elements on austenite formation kinetics. It appears that the LENP condition is more appropriated to describe the heat at 1°C/s of the Fe-0.1C-1.65Mn (wt%) steel.

Zhu and Militzer [ZHU 15] proposed a rather complete 2D-PF model accounting for: (i) nucleation of austenite (classical nucleation theory); (ii) growth from pearlite and/or ferrite based on mixed-mode model including solute drag effect to account for slow partitioning of substitutional elements; (iii) recrystallization of deformed ferrite grains [ZHU 12]. Figure 1.23.a shows a good agreement between experimental and phase-field kinetics of austenite formation during heating stages at 10 and 100°C/s. Moreover, phase-field model captures microstructural features of cold-rolled steel evolution during the intercritical annealing as illustrated in figure 1.23.b and c. It clearly appears that the recrystallization and phase transformation overlap. Austenite forms mainly in prior pearlite area, generating a banded morphology, but also at ferrite grain boundaries (intergranular nucleation) and inside ferrite grains (due to migration of recrystallized ferrite grains).

More recently, PF models were also used to describe banding in steels (based on Mn microsegregation) [MAA 16] and cyclic thermal cycles of austenite-ferrite transformation in Fe-C-Mn alloys [CHE 16b].

PF models enables to have 2D or 3D presentations of microstructural evolutions as previously shown in figure 1.23.b and c. However, some PF model parameters may be difficult to estimate (ex. the interface energy σ_{ij} or the width interface η).

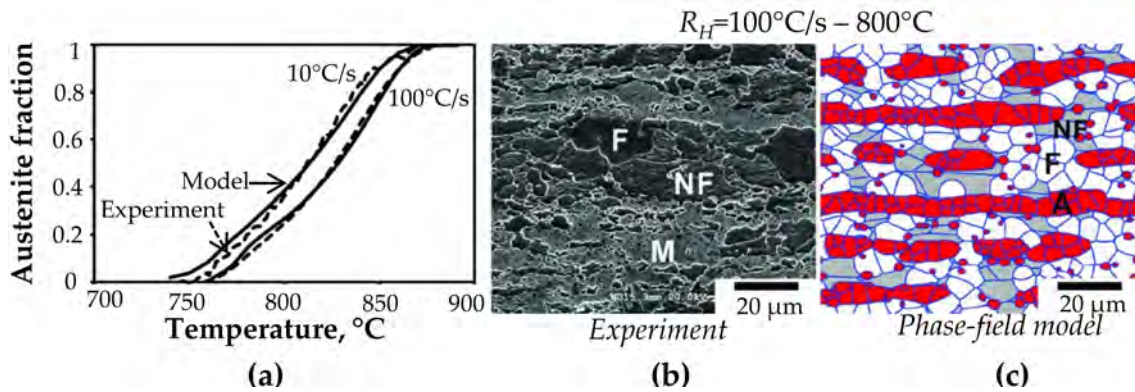


Figure 1.23: (a) Comparison of experimental and phase field kinetics during heating stages at 10 and 100°C/s. Experimental and model microstructures at 800°C are compared in (b) and (c) respectively (A: austenite; M: martensite; F: recrystallized ferrite; NF: deformed ferrite) [ZHU 15].

1.4 Conclusion

This state-of-the-art has described different microstructural evolutions during the DP thermal treatment and main available predicting tools passing from phenomenological to thermodynamic and physically based approaches.

Intercritical annealing

During the intercritical stage, recrystallization, carbide spheroidization and austenite formation are the major mechanisms. It was pointed out that the carbides, already present in deformed pearlite lamellae, quickly spheroidize around 700°C (due to the high stored energy and to a fragmented morphology after the cold-rolling). The critical point of this treatment rests on the fact that for typical industrial range of cycle parameter conditions (ex. heating rate above 3°C/s), the recrystallization and phase transformation occur simultaneously. It is admitted that the overlapping induces interaction between the recrystallization and the austenite formation phenomena. Namely, the interaction modifies the kinetics of the recrystallization and of the phase transformation. The austenite formation is accelerated when the recrystallization is not completed before the austenite formation start temperature. On the contrary, an inhibition of the recrystallization was suggested above a critical austenite fraction ($\sim 10\text{-}30\%$) [CHB 14][BAR 15a].

From a modeling point of view, the description of the recrystallization and austenite formation interaction was not widely investigated. Some mesoscale models (cellular automaton and phase field) were developed to model the overlapping ensuring a 2D or 3D description of the microstructural evolutions [ZHU 15]. However, such models are often computational cost with some model parameters that may be difficult to estimate. Lastly, to our knowledge, there is no published pragmatic tool available to describe the interaction and the overlapping is deliberately excluded in some studies [KUL 14].

After experimentally characterizing the recrystallization before austenite formation, the

austenite formation without recrystallization and finally the austenite formation in parallel to the recrystallization, a simple model will be proposed in **chapter 3** to deal with the recrystallization and austenite formation interaction. The proposed model accounts for the recrystallization inhibition, the dependence of cycle parameters and the influence of the initial state (*i.e.* cold-rolled or recrystallized).

The austenite formation on it self is also difficult to model with physically based approaches due to the diffusion of elements with very different diffusivities (thousand times different between C and Mn) and the presence of complex chemistry in the case of industrial compositions. The mixed-mode model appears like a first step in the implementation of physical based model while, at the present time, there is no comparison with experimental database of the use of mixed-mode model for the austenite formation. **Chapter 4** proposes an implementation of the mixed-mode model approach to describe the austenite formation with successful comparison with the developed experimental database defining an unique interface mobility parameter to model isothermal and non-isothermal conditions.

Then, a fully diffusive model (using DICTRA software), based on the diffusion of the two main elements driving the transformation (C and Mn), was finally tested to compare with the austenite formation kinetics of typical industrial steel (containing various alloying element and complex morphology) in **chapter 5**. A particular care was brought to discuss the strengths and limitations of each modeling effort.

Cooling and tempering stages

After annealing, austenite is then transformed into martensite thanks to a fast cooling from the intercritical stage. The austenite-to-martensite transformation occurs at low temperature so that the phase transformation may be not completed in the case of direct coating. It is hence necessary to have a correct prediction of the phase transformation kinetics on such cycles. Moreover, the coating is realized by a Zn liquid bath immersion at 460°C which may induce considerable tempering on the metastable martensite. **Chapter 6** will investigate the microstructural evolutions taking place during the cooling and tempering stage of ferrite-martensite microstructure.

Chapter 2

Material and experimental techniques

This chapter aims at describing the initial states of the investigated DP1000 steel. Processing conditions and characteristic microstructural features are detailed for the steel in its two initial states: recrystallized (“ReX-steel”) and cold-rolled (“CR-steel”). Various techniques and corresponding experimental conditions used in this PhD-work are then exposed.

Contents

2.1	Material	39
2.2	Experimental strategy	43
2.3	Experimental techniques	44
2.3.1	Thermal treatments	44
2.3.2	Microstructural observations	46
2.3.3	In-situ techniques	49
2.3.4	Ex-situ techniques	54
2.3.5	Thermodynamic database	56

2.1 Material

This PhD-work was conducted on an industrially manufactured DP1000 steel. The steel was hot-rolled (at 874°C) and then coiled at 630°C before being naturally cooled to room temperature. It was then cold-rolled with a 55% reduction ratio to produce steel sheets 1.5 mm thick.

The chemical composition of the studied steel is given in table 2.1. It corresponds to that of a low-carbon and low-alloyed steel. Low additions of alloying elements attest of an industrial chemistry and were added to improve the steel processing.

Element	C	Mn	Cr	Si	Cu	Ni	Al	Nb
Content, wt%	0.17	1.763	0.427	0.345	0.069	0.047	0.037	0.031
	Ti	Mo	P	V	S	N	B	
	0.027	0.013	0.015	0.004	0.002	0.0006	0.0006	

Table 2.1: Chemical composition of the investigated steel.

In order to decorrelate the recrystallization and phase transformation phenomena, some samples were recrystallized by a treatment of 1200 s at 700°C ($<A_{c1}$). Hence, two initial states were investigated in this PhD-work: (i) the industrial cold-rolled steel referred to “CR-steel” and (ii) the prior recrystallized steel, so-called “ReX-steel”. Microstructures of these two states are shown in figure 2.1.

For the CR-steel (Fig. 2.1.(a-b)), the microstructure is composed of strongly deformed bands of ferrite and pearlite. Ferrite grains are difficult to identify because of the cold-rolled work. Pearlite bands have an average thickness of 3 μm with an interlamellar spacing of about 200 nm. Pearlite lamellae were deformed and broken by cold-rolling.

For the ReX-steel (Fig. 2.1.(c-d)), the microstructure is characterized by the simultaneous presence of bands of spheroidized cementite particles and recrystallized ferrite grains. Some deformed ferrite areas remain after the treatment as observed in figure 2.1.d but the non-recrystallized ferrite fraction is very low. Ferrite grains remain elongated in the rolling direction: their width ranges from 4 to 15 μm .

In addition, the chemistry of cementite was measured by EDS analysis using carbon replicas prepared according to the protocol detailed in section 2.3.2. Figure 2.2 presents some TEM micrographs obtained on carbon replicas of the two states. Histogram of Mn and Cr contents, quantified by EDS analysis in the cementite particles, are given in figure 2.3.

The complex morphology of pearlite lamellae in CR-steel is shown in figure 2.2.a. Figure 2.2.(b-c) shows cementite lamellae on which EDS analysis were performed. An example of EDS spectra realized on a cementite particle of the CR-steel is given in figure 2.2.d. The average cementite composition in Mn and Cr was evaluated to be 10.4 ± 1.6 wt%Mn and 4.1 ± 0.7 wt%Cr. Hence, after cold-rolling, cementite is already enriched in Mn and Cr (compared to the bulk composition equal to 1.763 wt%Mn and 0.427 wt%Cr). However, cementite is not at thermodynamic equilibrium. Namely, the equilibrium cementite composition at 600°C is supposed to contain 18.78 wt%Mn and 9.8 wt%Cr (according to Thermo-Calc).

The chemical composition of the particles present in the ReX-steel was also analysed. Spheroidized cementite particles with diameters between 50 and 300 nm are observed in figure 2.2.(e-g). Identically, an example of EDS spectra realized on a cementite particle of the ReX-steel is given in figure 2.2.h. The manganese content in spheroidized cementite was evaluated to be 13 ± 1 wt%. In the same way, chromium content has increased to 6.5 ± 1.4 wt%. Both Mn and Cr compositions get closer to the equilibrium state.

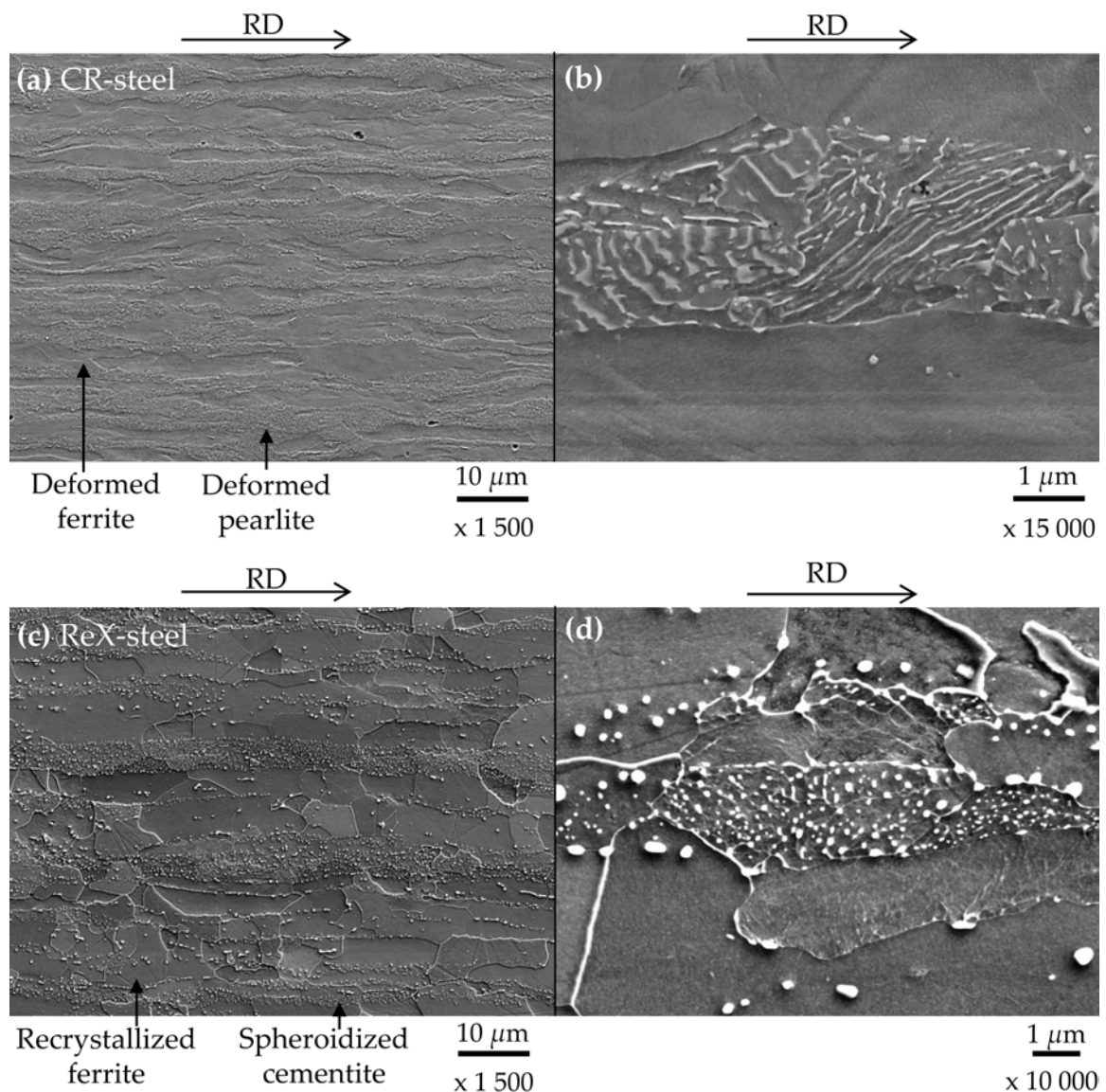


Figure 2.1: SEM micrographs of the (a-b) cold-rolled steel (CR-steel) and (c-d) recrystallized steel (ReX-steel). Cold-rolled steel is characterized by bands of deformed ferrite and pearlite while bands of spheroidized cementite islands and recrystallized ferrite grains are present in the prior recrystallized state.

As a conclusion, the prior recrystallization treatment leads to an increase in the Mn content of cementite of about 3% and in the Cr content of about 2 wt%. It has to be noted that no dependence between cementite size and Mn (or Cr) enrichment was outlined.

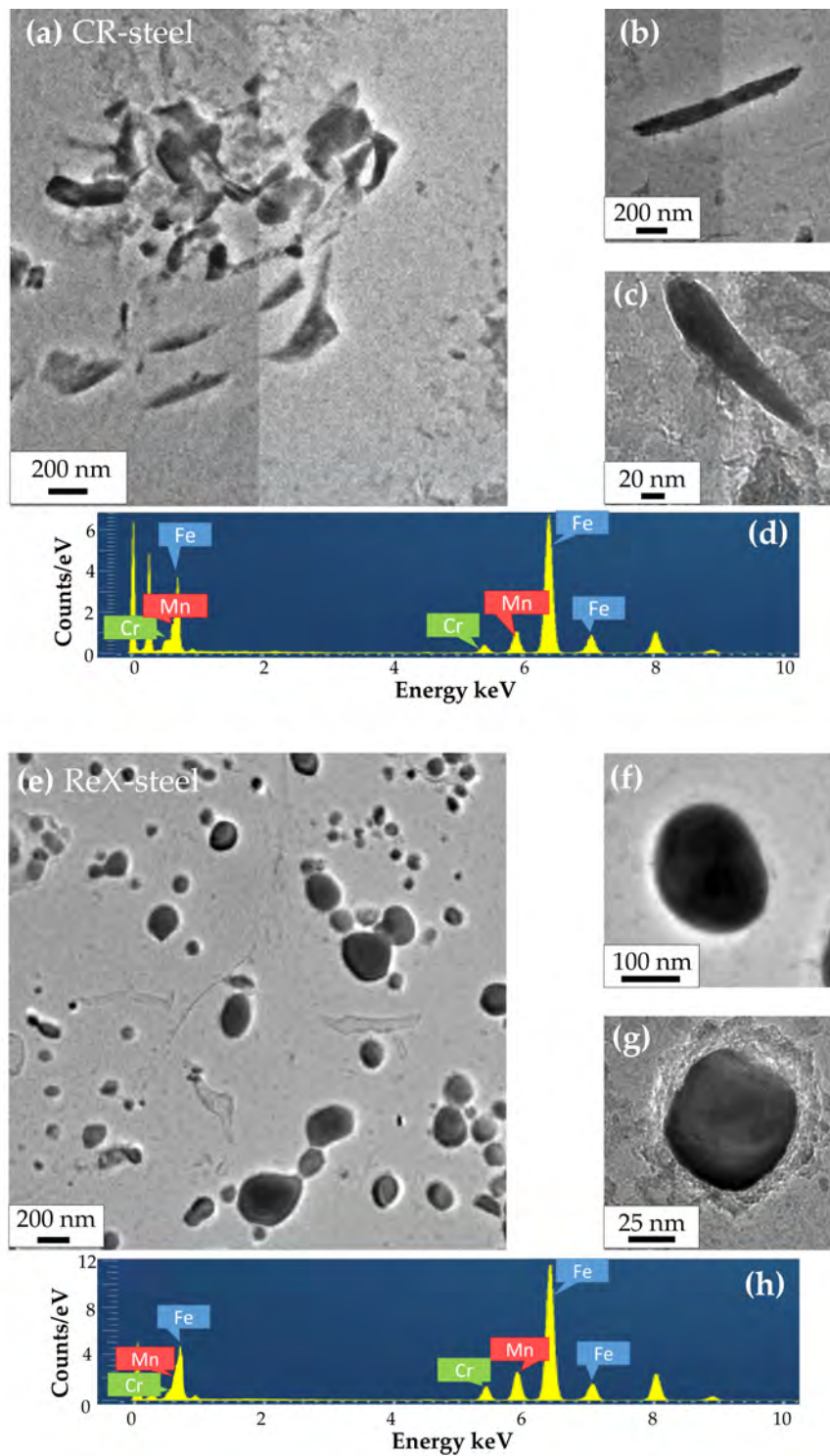


Figure 2.2: TEM micrographs on carbon replicas and examples of EDS spectra used to determine the chemical composition in (a-d) the cold-rolled steel and (e-h) the recrystallized steel.

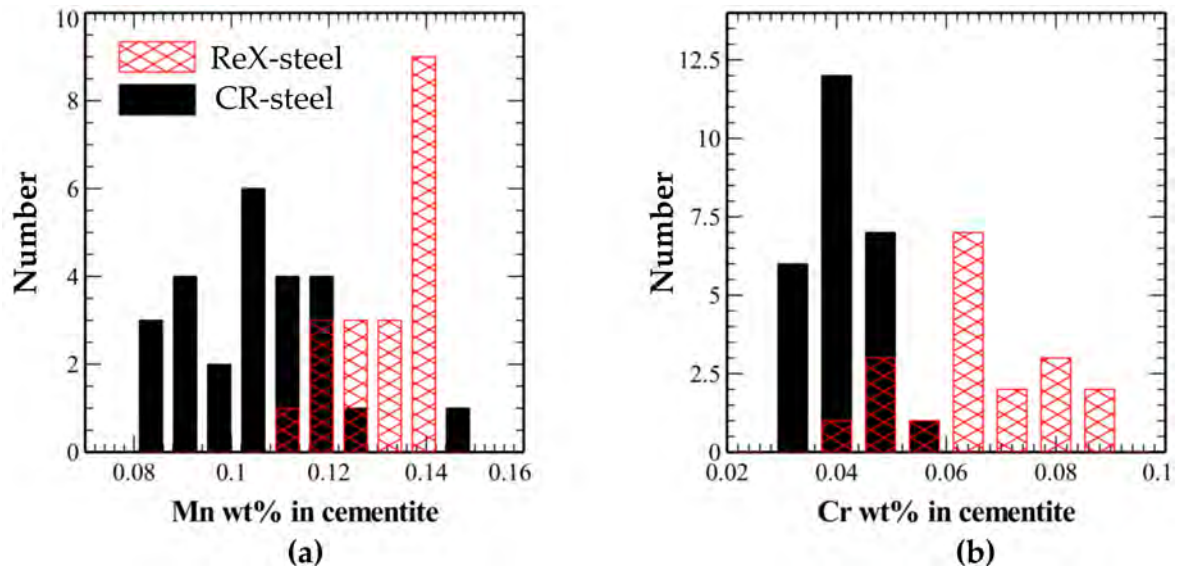


Figure 2.3: Histograms of (a) Mn and (b) Cr contents quantified by EDS analysis in the cementite particles of the CR-steel and the ReX-steel

2.2 Experimental strategy

A set of experimental techniques was combined in order to follow the different metallurgical phenomena likely to occur during the different stages of the thermal treatment of the steel. Table 2.2 proposes an overview of the applied techniques as a function of the investigated metallurgical mechanisms. Experimental techniques are described in section 2.3. The PhD-strategy may be summed up in several steps following the thermal treatment stages:

- *Initial states* were characterized by scanning or transmission electron microscopy as detailed in the previous section. Mechanical properties were also evaluated thanks to hardness.
- *Intercritical annealing* : Microstructural evolutions during intercritical annealing were first studied separately: recrystallization was followed on the CR-steel below austenite formation temperature ($< A_{c1}$) and austenite formation kinetics was first investigated in the case of the prior recrystallized steel where no recrystallization occurs. Then, the more complex case where recrystallization and austenite formation occur simultaneously was studied with the CR-steel. Different techniques were used for the study:
 - (i) Recrystallization kinetics of the cold-rolled steel was determined from hardness measurements performed on the CR-steel treated for different times at 650, 675 and 700°C. These measurements were coupled with SEM observations in order to check the degree of recrystallization;
 - (ii) Austenite formation kinetics was mainly studied by means of dilatometry and optical phase quantification on interrupted treatments. Kinetics were conformed by hardness measurements and by in-situ XRD tests;

- (iii) Carbide spheroidization was highlighted by SEM observations.
- *Quenching* : The austenite decomposition kinetics was followed by dilatometry for different cooling rates R_C (between 1 and 40°C/s). After cooling, microstructures were observed by optical microscopy.
- *Tempering* : The metallurgical phenomena occurring during tempering of fully martensitic or ferrite-martensite microstructures were followed by the evolution of the thermoelectric power (TEP) and of the hardness. The precipitated cementite fraction estimated thanks to TEP study was then compared to the volume fraction evaluated by a 3D-reconstruction of a volume of matter by FIB/SEM tomography.

2.3 Experimental techniques

This section aims at describing the experimental techniques used in this PhD-work and details the conditions used for the experiments.

2.3.1 Thermal treatments

Most of the thermal treatments conducted in this work were performed using a *Gleeble 3500* thermomechanical simulator. For specific studies, salt baths or furnaces were also used for the treatments.

2.3.1.1 *Gleeble* thermomechanical simulator

Treatments requiring a perfect management of heating/cooling rate, temperature and holding time were performed on the *Gleeble 3500* thermomechanical simulator. For example, this simulator was used for the study of the recrystallization and austenite formation kinetics occurring in less than 1 hour.

The *Gleeble 3500* thermomechanical simulator [GLE b] is based on heating by Joule effect and cooling through direct water (or air) projection on the samples. Samples of 100x10x1.5 mm³ were treated, as shown in figure 2.4.a, after being fixed on clamping jaws at 30 mm of each sides. Type K-thermocouples were welded in the centre of the specimen surface allowing a precise temperature control ($\pm 4^\circ\text{C}$). Figure 2.4.b. shows the example of a thermal cycle composed of a rapid heating at 100°C/s to 800°C, a short holding (0.1 s) at 800°C and a rapid water cooling. The short holding time (0.1 s) at 800°C, presents small deviations of 0.02 s and an overshoot of 4°C. In this PhD-work, it was checked that the overshoot does not exceed 3°C and is corrected in less than 1 s. Moreover, the water quench enables to cool down the sample from 800 to 20°C in less than 0.5 s.

2.3.1.2 Salt baths and furnaces

Some thermal treatments were realized using salt baths or furnaces. Such tools were used to realize either systematic interrupted treatments (as for martensite tempering study) or specimens with a wider thermal homogeneity zone compared to *Gleeble* (useful for tensile test specimens) or for long treatment times (daily, weekly or monthly treatments).

Experimental techniques	Initial states	Intercritical annealing			Quenching	Tempering
		Recrystallization	γ -formation	Fe ₃ C spheroidization		
<i>In-situ techniques</i>						
Dilatometry	-	-	✓	-	✓	-
DRX	-	-	✓	-	✓	-
<i>“Indirect” techniques</i>						
TEP	-	-	✓	-	-	✓
Hardness	✓	✓	✓	-	✓	✓
<i>Microstructural observations</i>						
Optical microscopy	✓	-	✓	-	✓	-
SEM	✓	✓	✓	✓	-	-
TEM	✓	-	-	-	-	✓
FIB tomography	-	-	-	-	-	✓

Table 2.2: Various applied experimental techniques for each investigated thermal stage.

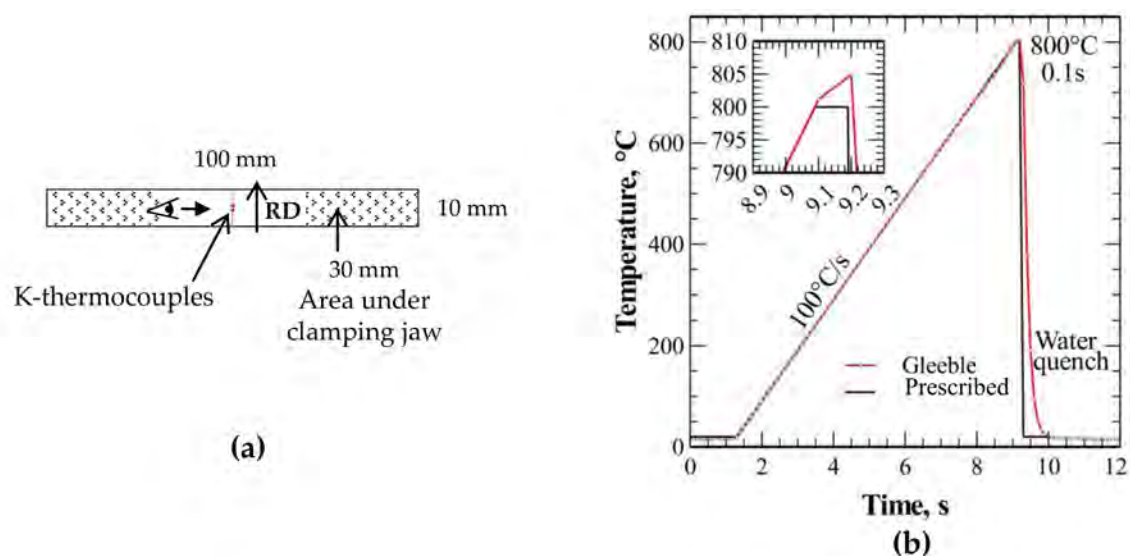


Figure 2.4: (a) Geometry of the samples used for the treatment in the *Gleeble* machine. (b) Example of thermal cycle performed in the *Gleeble* machine composed of a quick heating at 100°C/s, followed by a short holding at 800°C during 0.1 s and by a water quench.

Two kinds of salt baths were used: sodium nitrite bath, mainly used for tempering treatments in the low temperature range (150-500°C), and baryum chloride bath, for higher temperature range (600-900°C). Salt baths present several advantages: treatment of larger specimens and rapid heating rates (close to 200°C/s).

Treatments in furnace under vacuum ampoule were performed to study austenite formation for long holding times at 760°C. Treatments of 24, 168 and 720 hours were realized in a *Nabertherm* furnace using vacuum quartz ampoules (with a pressure of $\sim 10^{-2}$ bar) to avoid any decarburization. In such conditions, the non-management of the heating rate is of low importance considering the long holding times.

2.3.2 Microstructural observations

The steel microstructure was characterized at different scales. For reproducibility, microstructural observations were conducted at quarter thickness in the plane parallel to the rolling direction. Moreover, samples treated with the *Gleeble* machine were observed in the plane where a precise temperature control with type-K thermocouples was performed.

Standard polishing procedure

Samples were prepared using SiC polishing papers (P-800, P-1200 and P-2500) and polishing cloths with diamond solutions of 6, 3 and 1 μm . For SEM observations or FIB experiments, colloidal silica suspension (0.06 μm - 8 min) was also used for finer polishing finish.

Optical microscopy (OM)

For optical observations of the microstructure, samples were etched with different solutions:

- Nital etching (4 mL acid nitric + 100 mL ethanol - 15 s): this type of etching was used to reveal ferrite grains and the presence of carbides.
- Bandoh etching (2.3 mL picral + 2.3 mL Metabisulfite + 1 mL Nital - 30 s), kind of modified Lepera, allows ferrite and martensite phases to be differentiated. Ferrite is usually colored in brown/blue while martensite appears white/yellow. As shown in figure 2.5.a, martensite appears white while ferrite plus pearlite appear brown. Clear phase delimitation is obtained thanks to this film etching. However, the Bandoh etching is sensitive to the steel oxydation. It has to be done directly after the final polishing (or after kept the sample in an ethanol bath) and the rinsing is delicate (water immersion and final ethanol rinsing near the etched sample).

Phase fractions were then quantified using *ImageJ* software to treshold martensite phase. Figure 2.5.b shows an example of typical treshold. The quantified martensite is colored in red. Each phase fraction was determined from the analysis of at least 20 micrographs.

It should be noticed that the errors bars for austenite fractions were fixed to 10% as the austenite fractions were evaluated by phase quantification on optical micrographs where errors may come from various sources (chemical etching, analysis of micrographs, threshold).

ReX-steel: $R_H=5^\circ\text{C/s} - (760^\circ\text{C} - 5\text{ s})$

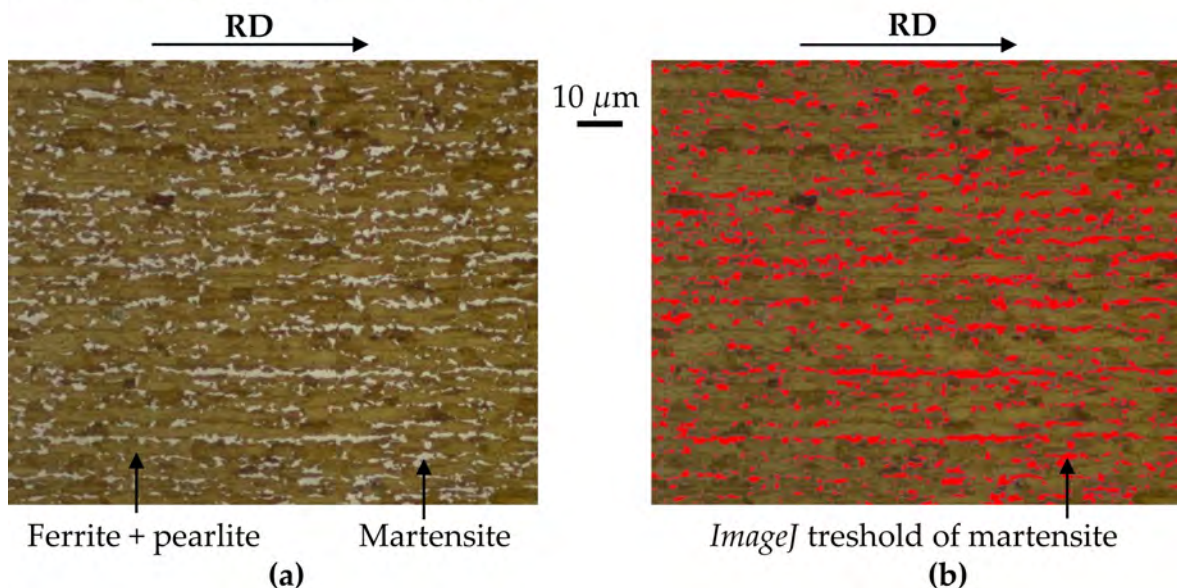


Figure 2.5: (a) Optical micrograph after Bandoh etching: martensite appears white while (ferrite+pearlite) are brown. An example of martensite quantification using *ImageJ* software is given in (b).

Scanning Electron Microscopy (SEM)

SEM observations were conducted on a *Zeiss Supra 55VP SEM* with an accelerating voltage of 10 kV, a diaphragm of 60 μm and a working distance close to 8.4 mm. The samples for SEM observations were etched with a flash Nital 2% after a standard grinding procedure to 0.06 μm .

Transmission Electron Microscopy (TEM)

Transmission electron microscopy was performed on a *JEOL 2010 FEG* microscope operating at 200 kV. Energy Dispersive Spectroscopy (EDS) was used to analyse the chemical composition of the iron carbides present in the steel and to highlight their possible enrichment in substitutional elements (Mn, Cr). For these studies, cementite particles were extracted from the surrounding iron matrix to avoid any quantification error associated with the matrix presence. Carbon replicas were thus performed thanks to the following procedure:

1. Nital 4% etching (20 s) was realized on the steel surface polished to 1 μm ;
2. A carbon film of approximately 20-30 nm thickness was deposited on the steel surface with a *Baltech* evaporator. The deposit was realized under the following conditions: voltage of 8 V, current of 50-60 A and vacuum in the range of 10^{-4} – 10^{-5} mbar;
3. The steel surface was then criss-crossed with a cutter to realize a grid pattern composed of $1 \times 1 \text{ mm}^2$ squares;
4. The coated steel was then immersed in a Nital 4% solution (several hours) until the carbon film is peeling off;
5. Carbon replicas were collected on copper grids and carefully cleaned up with three consecutive ethanol baths.

An average of 20 EDS measurements was realized to evaluate the chemical composition of carbides. Only Fe, Mn and Cr elements were quantified and the carbon content was corrected supposing a $(\text{Fe}_x\text{Mn}_y\text{Cr}_z)_3\text{C}$ stoichiometry and full equilibrium of C which is the fast diffuser element. x , y and z coefficients were identified thanks to the respective Fe/Mn and Fe/Cr atomic ratios and the equality $x + y + z = 1$.

Focused Ion Beam (FIB)

In order to quantify the carbide volume fraction which precipitated after a tempering treatment, 3D-analyses by FIB/SEM tomography were performed in a *Zeiss NVI-SION 40* microscope. The ionic abrasion was realized with a voltage of 30 kV and a ionic current of 300 pA. Two kinds of electrons were collected: BSE (back-scattered electrons), electrons of high energy resulting from volume interaction, and in-lens electrons, secondary electrons collected with the column detector. Two complementary volumes were obtained. The total FIB acquisition volume was $10 \times 10 \mu\text{m}^2$ with a voxel size of 5 nm^3 .

Only the BSE volume was analyzed using *ImageJ* software. Sub-volumes were analyzed by 3D-threshold on prior segmented regions.

2.3.3 In-situ techniques

Microstructural evolutions were followed during complex thermal cycles by means of dilatometry, in-situ XRD measurements or Differential Scanning Calorimetry (DSC).

2.3.3.1 Dilatometry

The austenite formation kinetics of the CR-steel and of the ReX-steel were experimentally obtained by means of dilatometry. This technique is based on the monitoring of the change in the length of the samples during the thermal cycle. The dilatometer used for the experiment was an optical dilatometer set up on a *Gleeble* machine [GLE a]. The optical system allows a non-contact measurement of the length change in the alignment of thermocouples and avoids any dilatometer stress on the sample. To avoid any oxidation forming on the specimen surface, dilatometry measurements were performed under $\sim 10^{-5}$ bar pressure. However, in the study of austenite decomposition, pressure was limited to $\sim 10^{-1}$ bar due to the air nozzle used to manage various cooling rates.

Phase transformations are usually accompanied by a crystallographic change inducing a volume variation. Each transformation with volume modification therefore leads to a change in the slope of the linear dilatation with temperature. Figure 2.6.a. illustrates the evolution of the dilatation during the heating of a steel from 20 to 1000°C followed by a direct quench to room temperature. Two slope changes appear corresponding respectively to the ferrite-to-austenite transformation between 700 and 850°C and then to the austenite-to-martensite transformation (200-300°C) occurring during the cooling to room temperature.

The tangent method was applied to characterize the kinetics of transformation. At a given temperature, the austenite fraction may be evaluated by the relation: $f = \frac{AB}{AC}$ with *A*, *B* and *C* points reported on the dilatometry curve in figure 2.6.a. The austenite formation may thus be monitored during continuous heating from room temperature to 1000°C as shown in figure 2.6.b.

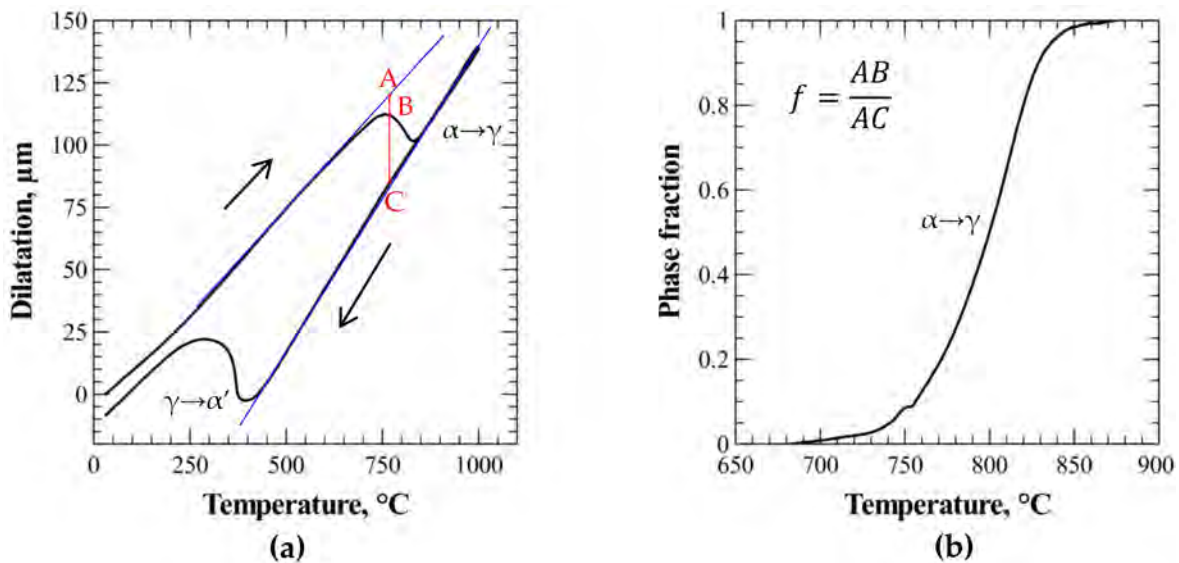


Figure 2.6: (a) Dilatometry curve obtained during the heating of the steel from 20 to 1000°C and then during rapid cooling down to room temperature. The two slope changes correspond to the ferrite-to-austenite transformation (700-850°C) and to the austenite-to-martensite transformation (200-300°C). (b) Austenite formation kinetics determined from dilatometry experiments.

As in the case of the austenite formation kinetics, dilatometry was used to determine the austenite decomposition kinetics during continuous cooling. As several phases may form during cooling, phase transformations were determined individually before evaluating the complete kinetics of austenite decomposition based on the full austenite-to-martensite transformation as illustrated in figure 2.7. Figure 2.7.a shows the dilatation evolution during a cooling at 20 and 40°C/s of a steel fully austenitized. At 40°C/s, a full martensite transformation occurs while this transformation is partial at 20°C/s as the austenite first transformed in bainite between 500 and 600°C.

The analysis of austenite decomposition at 20°C/s during the first and second slope change are given in figure 2.7.b respectively using the same tangent method as for austenite formation. The martensite fraction formed during the second slope change, detected during cooling at 20°C/s, was evaluated using the martensite transformation kinetics obtained at 40°C/s (figure 2.7.c). Knowing this fraction, the complete austenite decomposition curve can be plotted (figure 2.7.d).

Some dilatometry tests were also realized on a conventional (contact) *Bähr 805 A/D* dilatometer (see techniques comparison in figure 3.1).

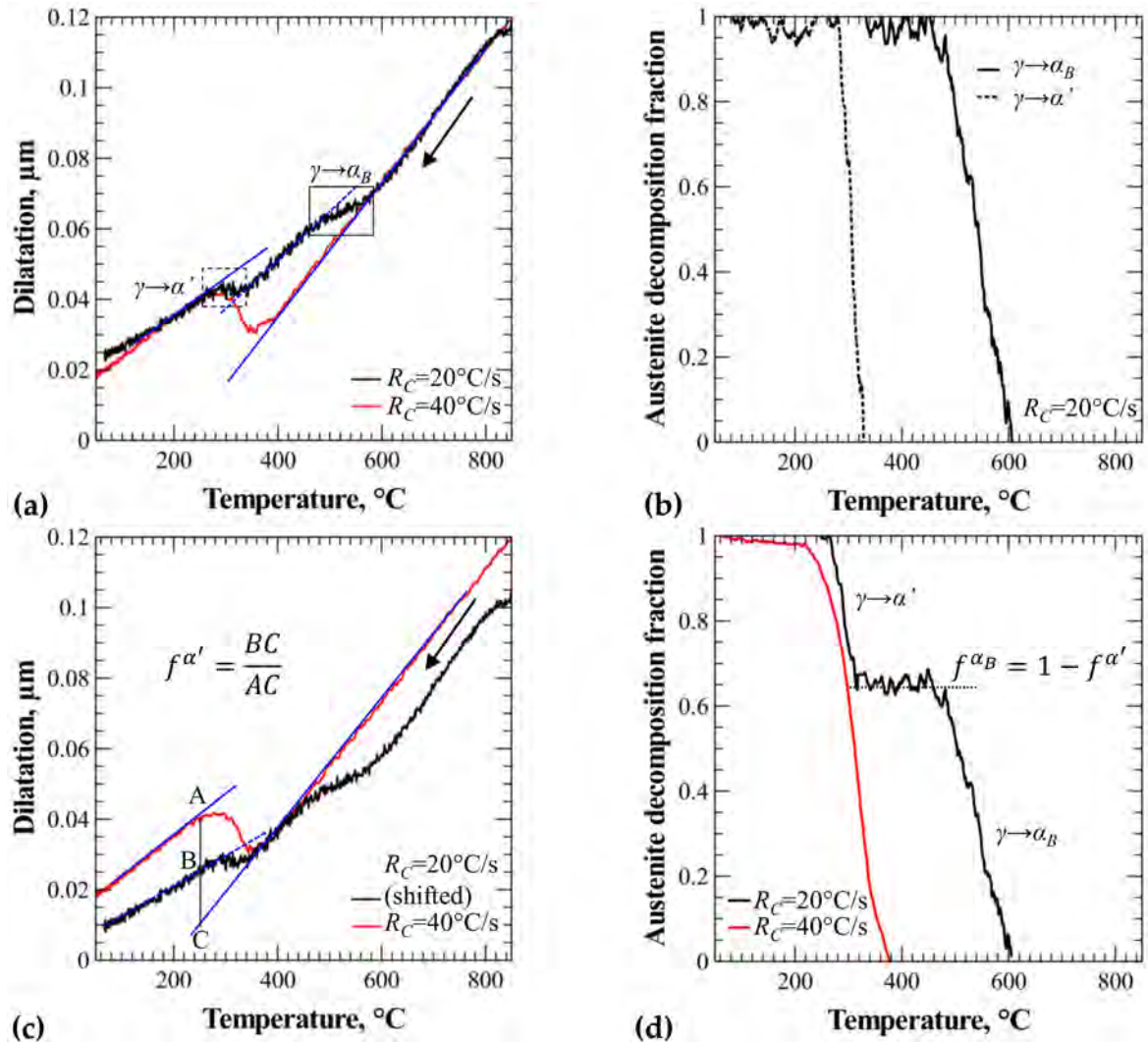


Figure 2.7: (a) Dilatometry curves obtained during the cooling of the steel from 850 to 20°C at two different cooling rates: 20 and 40°C/s. The two slope changes, during cooling at 20°C/s are analysed individually in (b), before plotting the complete austenite decomposition (d). The martensite fraction for the steel cooled at 20°C/s was evaluated thanks to the complete martensite transformation kinetics determined at 40°C/s (c).

2.3.3.2 In-situ XRD

Two in-situ High Energy Synchrotron X-Ray Diffraction (HEXRD) experiments were performed on the CR-steel and ReX-steel. The HEXRD experiments were carried out with an energy of 100 keV on P07-HEMS beamline at PETRA III, Deutsches Elektronen-Synchrotron (DESY, Hambourg) [III]. Thermal treatments were realized using a modified dilatometer *Bähr 805 A/D* inside P07 beamline as shown in figure 2.8. The whole HEXRD conditions are also summed up in table 2.3.

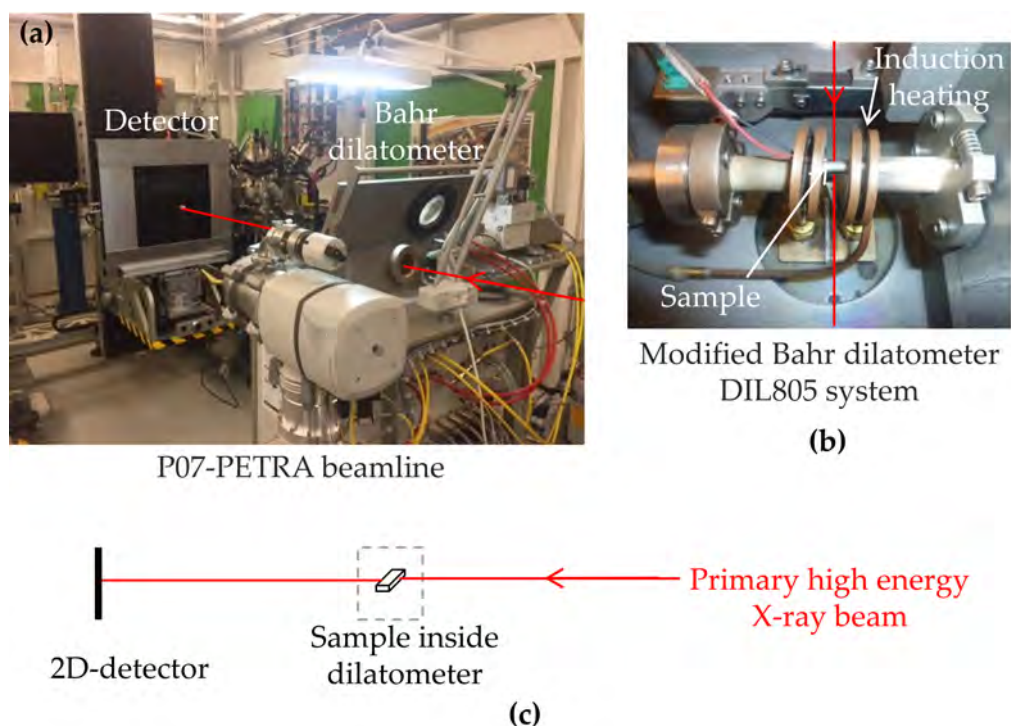


Figure 2.8: (a) P07-PETRA beamline with (c) modified *Bahr* dilatometer for thermal treatment. (c) Schematic representation of the beamline.

Beamline	P07-PETRA
Energy	100 keV
Wavelength	0.124 Å
Detector	PerkinElmer XRD
Sample to detector distance	1918 mm
Split aperture size	1x1 mm ²
Sample dimension	10x5x1.5 mm ³
Acquisition time	2 s
Read-out time	1 s

Table 2.3: Experimental parameters of the P07-PETRA experiments.

Samples of size 1.5x5x10 mm³ were prepared to fit with dilatometer device. The fine grain size of our samples ($\sim 1\text{-}5\ \mu\text{m}$) ensured a good statistic on the diffraction patterns, allowing a precise recording of the microstructural evolutions during thermal treatments.

Microstructural evolutions were monitored by continuous diffraction in transmission mode using image-plate detector. Complete sequence of Debye-Scherrer rings were recorded using PerkinElmer detector in parallel to the thermal treatments. Figure 2.9.a. shows 4 diffraction patterns obtained on the initial CR-steel and then during the heating at 5°C/s

to three temperatures: 710, 750 and 900°C. The pattern of the initial CR-steel is composed of diffraction rings due to ferrite plus pearlite. The inhomogeneity of the ring thickness is linked to the cold-rolling which has generated texture in the steel. The diffraction pattern at 900°C is only composed of austenite diffraction rings while the pattern at 750°C is a mixed between ferrite and austenite diffraction rings.

The analyses of 2D-patterns was realized by Rietveld method using *Maud* software. First, all Debye-Scherrer rings obtained during treatment were integrated to obtain intensity as a function of 2θ angle. Instrumental conditions of the experiments were inquired in *Maud* software (sample to detector distance, energy etc.). A standard LaB₆ powder was used as experimental reference. Then, intensity data were analysed in batch mode with the Rietveld algorithm which minimizes a residual function using a non-linear least square method and refines thus the crystal structures. Figure 2.9.b. shows an example of intensity- 2θ graph in the range of 3 to 6°. *Maud* software was used to identify and quantify phases. The result of *Maud* analysis is plotted in black line and fits with good accuracy diffraction points. The peaks correspond to angles where Bragg law is respected. The analysis of peak position and intensity brings informations on the nature, fraction and texture of the phases [BAR 15c] [BAR 15b].

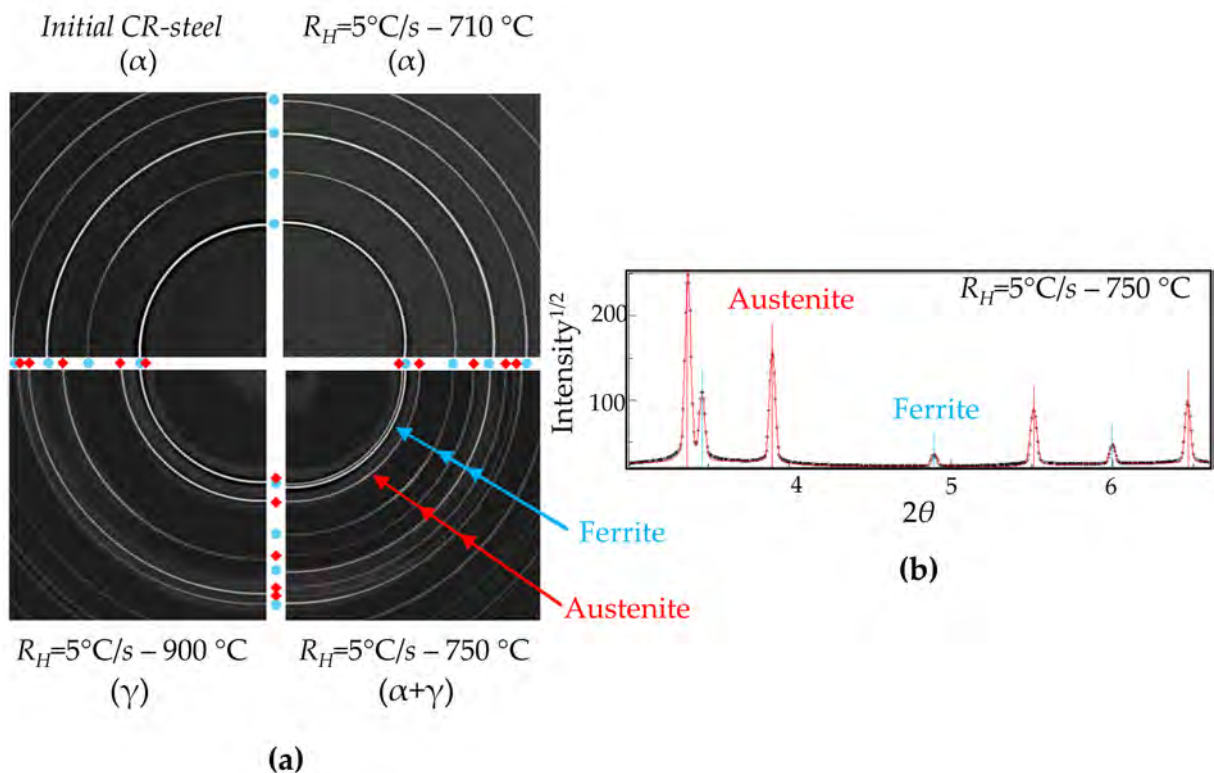


Figure 2.9: (a) Diffraction patterns obtained on the initial cold-rolled steel and after heating at 5°C/s to 710, 750 and 900°C. (b) Example of the *Maud* analysis identifying austenite and ferrite phases.

2.3.4 Ex-situ techniques

Other techniques may be named as ex-situ techniques because they were performed after interrupted thermal treatments and not on-going thermal treatment. The optical phase quantification, detailed earlier, may be considered as an ex-situ technique.

2.3.4.1 TEP

The thermoelectric power (TEP) is an indirect technique which is used to follow global microstructural evolutions as it is very sensitive to crystallographic defects (*i.e.* solute atoms, precipitates or dislocations) [KLE 05]. The principle of the TEP device rests on the application of a thermal gradient on the two junctions between the sample and two reference metal blocks (here, pure iron blocks). This induces a potential difference due to the Seebeck effect as illustrated in figure 2.10.a. The relative TEP of the sample with respect to the TEP of the reference metal (or Seebeck coefficient) $S_{S/R}$ is defined by the relation:

$$S_{S/R} = S_{sample} - S_{reference\ metal} = \frac{\Delta V}{\Delta T} \quad (2.1)$$

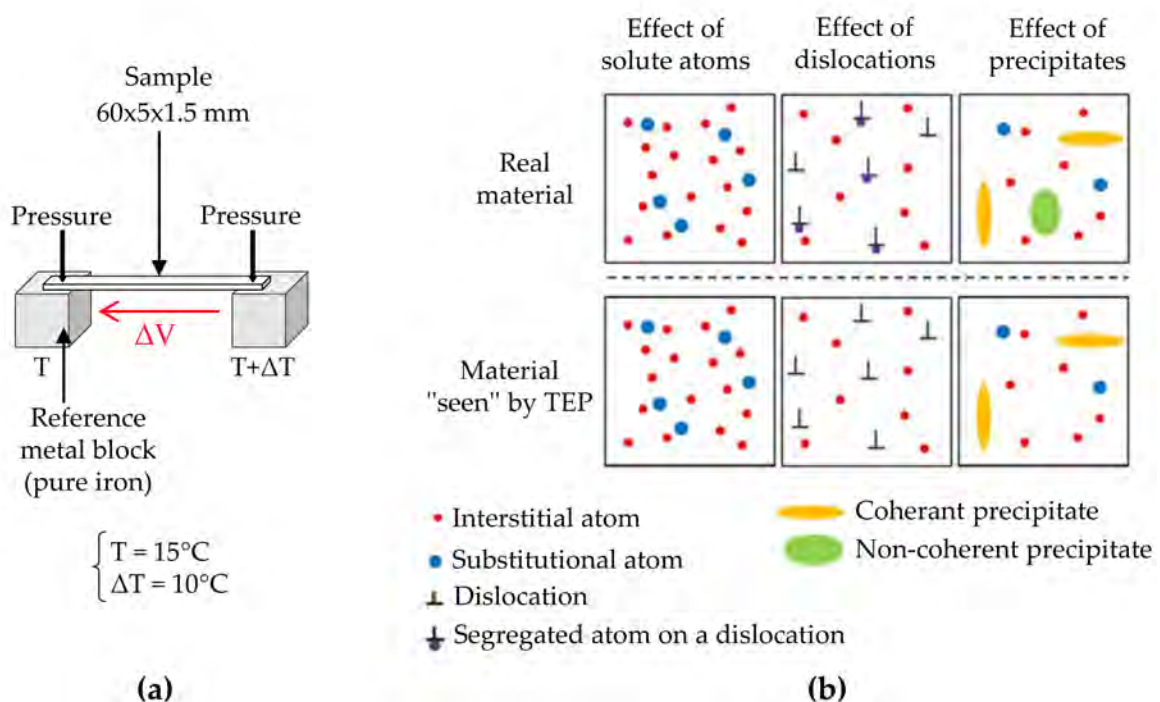


Figure 2.10: Schematic representation of (a) TEP technique and (b) the effect of different defects (solute atoms, segregated atoms, dislocations and precipitates) on the TEP of iron [LAM 14].

The TEP of a steel is influenced by the defects of its microstructure as schematically represented in figure 2.10.b and can be written as followed:

$$S_{steel\ sample} = S_{pure\ iron} + \Delta S_{ss} + \Delta S_{pre} + \Delta S_{dis} \quad (2.2)$$

with $S_{pure-iron}$ the TEP of pure iron. ΔS_{ss} , ΔS_{pre} and ΔS_{dis} respectively correspond to the TEP variation due to solute atoms, precipitates and dislocations. Further details of each contribution are presented below:

- *Solute atoms* generate a strong TEP variation (ΔS_{ss}) which can be either positive or negative depending on the nature of the considered atoms. It may be described by the Gorter-Nordheim law [NOR 35]:

$$\rho \times \Delta S_{ss} = \sum_i \rho_i \times s_i = \sum_i \alpha_i \times c_i \times s_i \quad (2.3)$$

where:

- ρ is the steel resistivity equal to $\rho_0 + \sum_i \rho_i$ (Mathiessen law) with ρ_0 the resistivity of the pure metal of reference (*i.e.* pure iron) and ρ_i the resistivity variation due to the presence of element “*i*” in solid solution;
- ΔS_{ss} is the TEP variation due to the presence of alloying elements in solid solution in the steel;
- s_i is the specific TEP of element “*i*” (unit: $\mu\text{V}/^\circ\text{C}$);

In the case of low-alloyed steel, the resistivity of element *i* (ρ_i) varies linearly with the concentration c_i of element *i*:

$$\rho_i = \alpha_i \times c_i \quad (2.4)$$

The proportionality coefficient α_i represents the specific resistivity of element *i* (unit: $\mu\Omega\cdot\text{cm}/\text{wt}\%$)

Combining equations (2.1), (2.3) and (2.4), it is possible to express ΔS_{ss} with the concentration of solute atoms c_i :

$$\Delta S_{ss} = \sum_i \frac{\alpha_i \times s_i}{\rho} \times c_i \quad (2.5)$$

However, in the case of alloys with low solute element concentrations or involving low variations in solute concentrations during thermal treatments, the alloy resistivity can be assumed constant (*i.e.* $\sum_i (\alpha_i \times c_i) \sim \text{constant}$). Thus, equation (2.5) can be written as:

$$\Delta S_{ss} = \sum_i P_i \times c_i \quad (2.6)$$

with $P_i = \frac{\alpha_i \times c_i}{\rho}$ the influence coefficient of the element *i* on the TEP of iron.

If only carbon atoms are in solid solution, equation (2.5) becomes:

$$\Delta S_{ss} = P_C \times \Delta C_C \quad (2.7)$$

with $P_C = \frac{\alpha_C \times s_C}{\rho}$ the influence coefficient of carbon on the TEP of iron. α_C and s_C are the specific resistivity and the specific thermoelectric power of C in iron. The product $\alpha_C \times s_C$ was defined as being equal to $517.4 \mu \text{ V}/^\circ\text{C} \cdot \mu\Omega \cdot \text{cm}/\text{wt}\%$ at 20°C [BRA 93]. Knowing the values of α_C , s_C and ρ , the TEP variations may be linked to the variation of the solute carbon atoms.

- *Precipitates* may have a non-negligible effect on the TEP (ΔS_{pre}) in the case of coherent or semi-coherent precipitates. Precipitation results in both (i) the disappearance of solute atoms and (ii) atoms clustering. Consequently, the TEP variation due to precipitation is the result of two contributions: (i) the departure of alloying elements from the solid solution; (ii) the effect of precipitates. The effect of the precipitates is expected to depend on the nature, size, morphology and volume fraction of precipitates but there is no law to predict this effect. On the contrary, non-coherent precipitates are known to have a negligible effect on the TEP if their volume fraction is less than 10%.
- *Dislocations* (ΔS_{dis}) decrease substantially the TEP value of iron. The decrease seems to be proportional to the hardening so that TEP variation is supposed to be linked to the dislocation density.

2.3.4.2 Hardness

Vickers hardness measurements were performed at quarter thickness and with a 0.5 kg load on a *Buehler* machine. Hardness values were obtained by an average of 15 measurements ensuring the standard deviation to be equal to 5 HV in the study of the recrystallization. It has to be noticed that the standard deviation is much larger (~ 20 HV) when the hardness is measured on a ferrite-martensite microstructure.

2.3.5 Thermodynamic database

In addition to experimental results, volume fractions at thermodynamic equilibrium of the different phases were calculated from Thermo-Calc [AND 02] using the TCFE8 Steels database [THE]. Three equilibrium conditions were differentiated :

1. *Orthoequilibrium* (OE) condition assuming that the thermodynamic equilibrium is reached for all elements. This type of equilibrium requires long treatments times [SPE 72] [LAI 16]. The OE condition was calculated on the simplified system Fe-0.17C-1.763Mn-0.427Cr-0.345Si-0.037Al (wt%).
2. *Paraequilibrium* (PE) condition: it supposes a constraint equilibrium without partitioning of substitutional alloying elements, *i.e.* only C is at equilibrium, as defined by Hultgren [HUL 47]. The PE fractions were also calculated on the simplified system used for OE condition.
3. *Local Equilibrium with Negligible Partitioning* (LENP) calculated on the ternary system Fe-0.17C-1.763Mn (wt%). The newly formed austenite has the same Mn composition as the parent ferrite phase [WEI 13] [CHE 14]. However a “spike” of Mn is created in order to satisfy the local equilibrium at the interface for both C

and Mn as shown in figure 1.20 of the literature review. As highlighted by Chbihi *et al.* [CHB 14], the LENP condition applied for the $\alpha \rightarrow \gamma$ transformation is different from the LENP (Local Equilibrium with Negligible Partitioning) classically used in the $\gamma \rightarrow \alpha$ case [ZUR 09] [GOU 15]. The LENP is however an analogy applied to the $\alpha \rightarrow \gamma$ phase transformation. From a practical point of view, LE fraction at a given temperature was calculated from the tie-line of the Fe-C-Mn ternary system for which the manganese content in austenite is equal to the one of the bulk material (*i.e.* here 1.763 wt%Mn).

Chapter 3

Characterization and empirical modeling of the microstructural evolutions during intercritical annealing

This chapter focuses on the microstructural evolutions which are expected to occur more or less simultaneously during the intercritical annealing treatment of cold-rolled dual-phase steels. These microstructural evolutions (recrystallization, cementite spheroidization and austenite formation) were described in detail in section 1.2.1 of the literature review (chapter 1). The challenge is to decorrelate concomitant phenomena for which their respective kinetics may be influenced by the overlapping and interact together. The difficulty is also to model various mechanisms and their possible interaction. This chapter aims therefore at (i) getting a better understanding of these microstructural evolutions and (ii) developing a simple empirical model allowing the austenite formation kinetics of cold-rolled DP1000 steels to be predicted during typical industrial continuous annealing cycles.

In a first step, recrystallization and phase transformation were studied separately: (i) austenite formation was monitored without recrystallization (*i.e.* on the prior recrystallized steel - so-called “ReX-steel”) and (ii) recrystallization was investigated below austenite formation temperature (*i.e.* at $T < A_{c1}$) on the cold-rolled steel (referred to “CR-steel”). Then, the more complex case of cold-rolled steels for which austenite formation and recrystallization may interact was considered. The role of different parameters (initial state of the steel, heating rate and annealing temperature) on the austenite formation kinetics will be discussed at the end of this chapter.

Results of this chapter have been published in the journal *Metallurgical and Materials Transactions A* in reference [OLL 17].

Contents

3.1 Preliminary works on the non-isothermal austenite formation kinetics	60
3.1.1 Comparison of the non-isothermal austenite formation kinetics obtained with various techniques	60
3.1.2 Non-isothermal austenite formation kinetics on the cold-rolled steel and on the prior recrystallized steel	61
3.2 Decorrelation of mechanisms	64
3.2.1 Austenite formation without recrystallization	64
3.2.2 Recrystallization without austenite formation	69
3.3 Case of the cold-rolled steel: interaction between recrystallization and austenite formation	73
3.3.1 Interaction map	74
3.3.2 Austenite formation with recrystallization	76
3.4 Discussion	81
3.4.1 Influence of the initial state on the austenite formation kinetics	81
3.4.2 Influence of the temperature and of the heating rate on the austenite formation kinetics	83
3.5 Conclusion	87

3.1 Preliminary works on the non-isothermal austenite formation kinetics

Before going further in the microstructural characterization, a preliminary study was realized to compare the austenite formation kinetics obtained with different experimental techniques. This stage was considered necessary to valid the experimental procedure.

Then, the austenite formation kinetics on the ReX-steel and the CR-steel were compared under non-isothermal conditions.

3.1.1 Comparison of the non-isothermal austenite formation kinetics obtained with various techniques

Five different techniques were used to capture the kinetics of austenite formation during a continuous heating at 5°C/s from room temperature to 900°C of the ReX-steel and of the CR-steel as shown in figure 3.1. The phase transformation was monitored by (1) in-situ XRD analysis, (2) Bahr dilatometry set up on the XRD beamline, (3) conventional Bahr dilatometry, (4) Led dilatometry set up on the *Gleeble 3500* simulator and finally by (5) optical phase quantifications made after direct water quench from different temperatures.

In the case of the ReX-steel (figure 3.1.a), the austenite formation kinetics determined with different techniques superpose on a same master curve with a deviation in the determination of austenite fraction inferior to $\pm 5\%$, validating thus the austenite formation

kinetics. Deviations between different techniques are related to uncertainty of measurements associated with each technique.

In the CR-steel, the superposition of the austenite formation kinetics determined with the different techniques is less satisfying (figure 3.1.b). Deviations in the determination of austenite fraction may reach $\pm 15\%$ deviation. However, it should be noticed that the gap between different dilatometry tools (Bahr, XRD Bahr and Led) and the optical quantification is in a uncertainty range of 15%. The deviation of the austenite fraction determined by the in-situ XRD experiment could be due to errors in texture modeling in the case of CR-steel. More details on XRD results are given in appendix C which highlights some misunderstanding points especially in the CR-steel case. As experiments have not been duplicated, results from XRD experiment have been put aside of this PhD-work. Further works are needed in the analysis of XRD experiments and the management of texture modeling in *Maud* software.

Despite “slight” dispersion between the different measurement techniques, it should be noted that all methods give the same evolution with a shift (more or less pronounced) in the temperature scale. A further discussion on the advantages and sources of possible errors associated with each technique is given in appendix B.2. In the following, it was chosen to use always the same technique to compare different non-isothermal austenite formation kinetics in order to avoid superposition of experimental errors. Non-isothermal kinetics were thus determined by Led dilatometry because it is an in-situ technique monitoring the phase transformation in parallel to the thermal treatment. Moreover, it avoids specimen stress that may be induced by a contact dilatometer and it enables fast heating rate compared to in-situ XRD which is restricted by the acquisition frequency.

Similarly to this study in non-isothermal conditions, austenite formation kinetics during isothermal holding were determined and compared by different methods (optical phase quantification, TEP, hardness) in appendix B.1. Optical phase quantification was the preferential method because it avoids any normalization issue detailed in this appendix.

Dilatometry was not used in isothermal conditions but it has to be pointed out that optical quantification and results from Led dilatometry give really comparable austenite fractions (figure 3.1). This validates the comparison between austenite fraction monitored by Led dilatometry in non-isothermal conditions and austenite fraction evaluated by optical microscopy in isothermal conditions.

3.1.2 Non-isothermal austenite formation kinetics on the cold-rolled steel and on the prior recrystallized steel

Due to the possible interaction between recrystallization and phase transformation in cold-rolled state, the kinetics of austenite formation was determined for the CR-steel and for the ReX-steel.

Figure 3.2 shows the non-isothermal austenite formation kinetics obtained by Led dilatometry on (a) the ReX-steel and on (b) the CR-steel during continuous heating from room temperature to 1000°C at different heating rates. The ORTHO, PARA and LE austenite volume fractions, calculated with Thermo-Calc, were also plotted. While

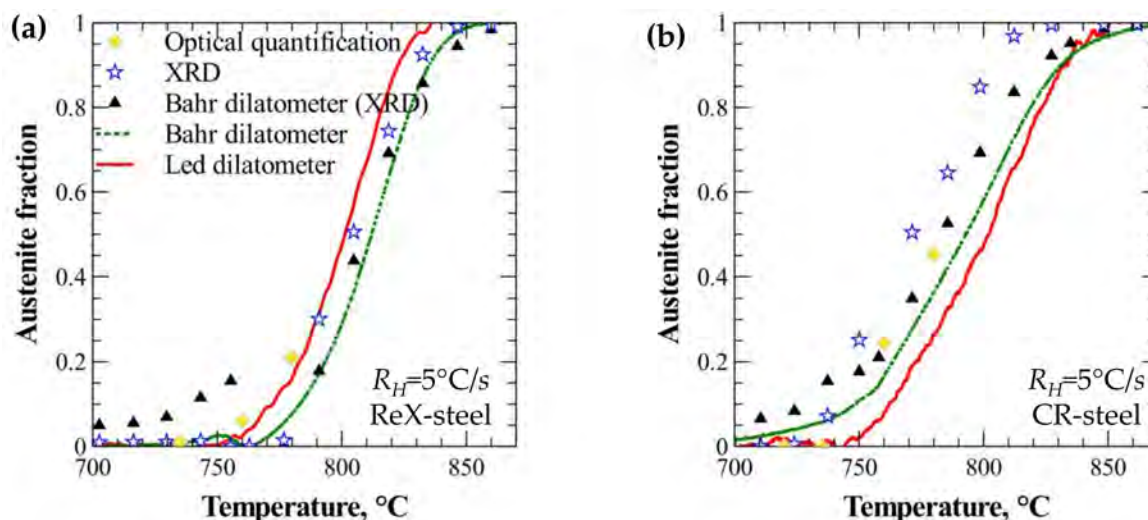


Figure 3.1: Austenite formation kinetics on (a) the ReX-steel and (b) the CR-steel during continuous heating at 5°C/s using different experimental techniques: optical phase quantification, XRD, Bahr dilatometry of the XRD experiment, conventional Bahr dilatometry and Led dilatometry set up on the *Gleeble 3500* simulator.

the ORTHO and PARA austenite fractions are quite similar at low temperatures (below 735°C), they tend to be notably different at higher temperatures.

The deviation between the thermodynamic database and the non-isothermal experimental austenite formation kinetics is linked to the fact that the thermodynamic equilibrium is not achieved during continuous heating conditions – even at the lower heating rate 0.5°C/s . The diffusion of substitutional elements is so slow that more time is required to achieve the equilibrium condition.

In the case of the ReX-steel, the austenite formation kinetics is regularly shifted to higher temperature when the heating rate is increased, suggesting that austenite formation is a thermally activated phenomenon governed by a measurable activation energy. By contrast, for the CR-steel, the austenite formation kinetics are all superimposed and no clear evolution of the kinetics with the heating rate can be highlighted, supporting the idea that austenite formation could be strongly influenced by an interaction with recrystallization. In fact, one can note that the kinetics obtained for $R_H=10$ or 30°C/s are slightly accelerated compared to the kinetics determined for $R_H=0.5$ and 5°C/s , thus comforting the preceding assumption.

In another representation, figure 3.3 compares the austenite formation kinetics of the CR-steel and that of the ReX-steel for three heating rates: (a) $R_H = 0.5$, (b) 10 and (c) 30°C/s . At very low heating rate ($R_H = 0.5^\circ\text{C/s}$), the austenite formation kinetics on CR-steel and ReX-steel are superimposed. For higher heating rate, the kinetics of the CR-steel tends to be accelerated compared to that of the ReX-steel and the acceleration appears to be all the more pronounced as the heating rate is increased. This tends to indicate that the presence of deformed ferrite grains in the CR-steel could play a major role on

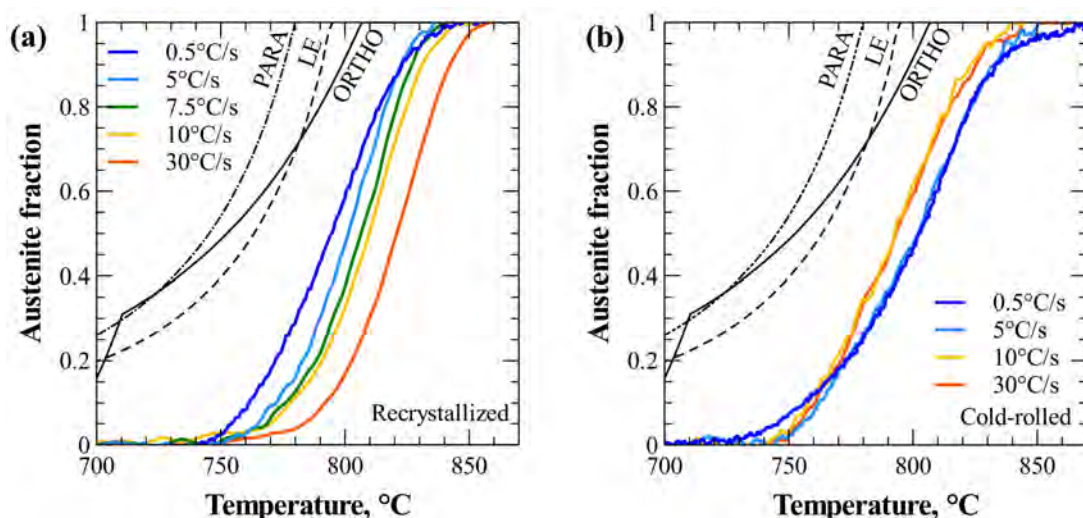


Figure 3.2: Austenite formation kinetics obtained by dilatometry on the: (a) ReX-steel and (b) CR-steel during continuous heating from room temperature to 1000°C with various heating rates (R_H) from 0.5 to 30°C/s. The ORTHO, PARA and LE curves correspond respectively to the ortho-equilibrium, para-equilibrium and local equilibrium conditions calculated from Thermo-Calc.

the austenite formation kinetics, as was already suggested by different authors [KUL 13a] [CHB 14]. Namely, non-recrystallized ferrite grains could promote austenite nucleation, as the energy stored in these grains during cold-rolling could increase the driving force for the austenite formation. Moreover, the higher fraction of deformed ferrite grains may also increase the number of austenite nucleation sites as suggested by Ogawa *et al* [OGA 17].

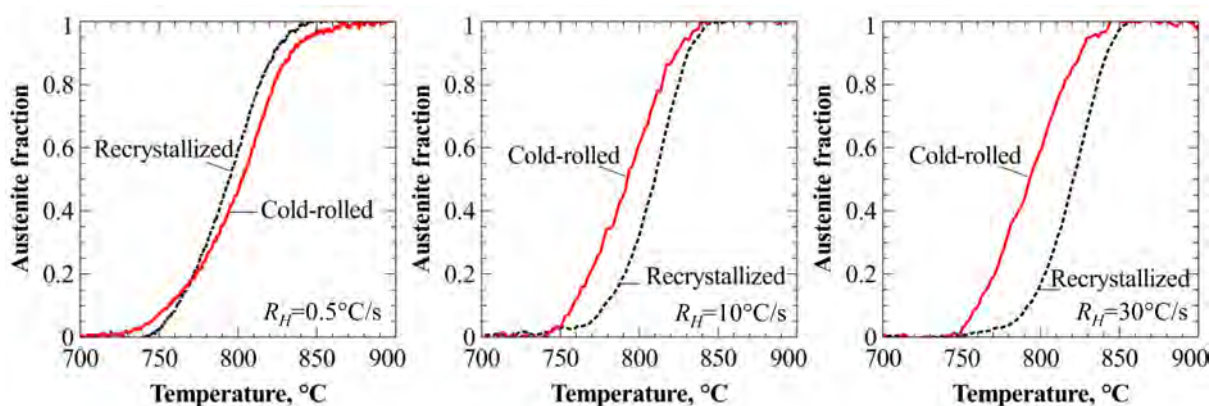


Figure 3.3: Comparison of the austenite formation kinetics obtained by dilatometry on the ReX-steel and on the CR-steel during continuous heating with three heating rates: (a) $R_H = 0.5$, (b) $R_H = 10$ and (c) $R_H = 30$ °C/s.

It is also important to note that two other phenomena different from recrystallization mechanism may also accelerate austenite formation in the CR-state compared to the ReX-state:

- (i) The lower Mn enrichment of cementite in CR-steel (10 wt%) compared to ReX-steel (13 wt%) may accelerate the kinetics of cementite dissolution as shown by different studies [GOU 12] [LAI 14] [LAI 16]. The effect of Mn enrichment in cementite will be analysed in detail in chapter 5 dealing with diffusive modeling of the austenite formation and taking into account initial compositions of ferrite and cementite. The possible effect of the Mn variation induced by the prior recrystallization treatment was supposed negligible in the present chapter as the Mn enrichment is weak (passing from 10 to 13 wt%Mn in cementite). Moreover, austenite formation kinetics during continuous heating at 0.5°C/s are not strongly different on the ReX-steel and the CR-steel (figure 3.3.a) while the Mn enrichment in cementite differs in the two states. The Mn enrichment may therefore be supposed negligible in the delay of austenite formation on the ReX-steel.
- (ii) The degree of cementite spheroidization before austenite nucleation could also play a role in the phase transformation kinetics [HUA 04].

These effects will be considered and discussed in section 3.4.

As already explained in the introduction, the main objective of the present works is to develop a simple model allowing the austenite formation kinetics of the CR-steel to be predicted. Due to the possible interaction between austenite formation and recrystallization in the intercritical domain, a progressive approach was chosen before treating this complex case. This is why, in a first step, the austenite formation kinetics of the ReX-steel was investigated when recrystallization is absent. Then, the recrystallization kinetics of the CR-steel was analysed and modeled when no austenite formation occurs (that is to say, below the A_{c1} temperature). The results of these studies are presented in section 3.2.

3.2 Decorrelation of mechanisms

3.2.1 Austenite formation without recrystallization

Kinetics of austenite formation was studied on the prior recrystallized state to withdraw the possible interaction with recrystallization in the cold-rolled state.

3.2.1.1 Non-isothermal conditions

The non-isothermal austenite formation kinetics, monitored in the previous section (figure 3.2.a), were first analysed using the differential form of the JMAK law:

$$\frac{dY}{dt} = nb^n t^{n-1} (1 - Y) \quad (3.1)$$

with Y the austenite fraction (*i.e.* $0 < Y < 1$) and n the Avrami exponent supposed to be constant with the temperature. b is the rate constant (in s^{-1}) defined by the following

relation:

$$b = b_0 \exp\left(-\frac{Q}{RT}\right) \quad (3.2)$$

where b_0 is a constant, Q is the activation energy of the austenite formation (J/mol), R is the gas constant and T the temperature (K).

The Kissinger analysis method was applied to determine the Q and n parameters of the law from the non-isothermal database of the ReX-steel (shown in figure 3.2.a).

The activation energy (Q) was determined from the representation of $\ln\left(\frac{R_H}{T_{max}^2}\right)$ as a function of $\frac{1}{RT_{max}}$ plotted in figure 3.4.a. The T_{max} parameter represents the inflexion point of transformation and was evaluated as the time of half-transformation (*i.e.* 50% f_γ). From experimental kinetics, T_{max} is equal to 801, 806, 810 and 820°C for respectively 5, 7.5, 10 and 30°C/s heating rates. Points corresponding to the four heating rates line up on a straight line. Its slope defines an apparent activation energy Q of the phase transformation equal to 900 kJ/mol.

The Avrami coefficient (n) was then evaluated from the curve giving $\ln(-\ln(1 - f_\gamma))$ as a function of $\left(\ln\left(\frac{T_{max}^2}{R_H}\right) \times \exp\left(-\frac{Q}{RT}\right)\right)$ for austenite fraction between 25 and 75%. Four kinetics superimpose on a same master curve as shown in figure 3.4.b. The slope of the curves defines the n parameter equal to 0.62.

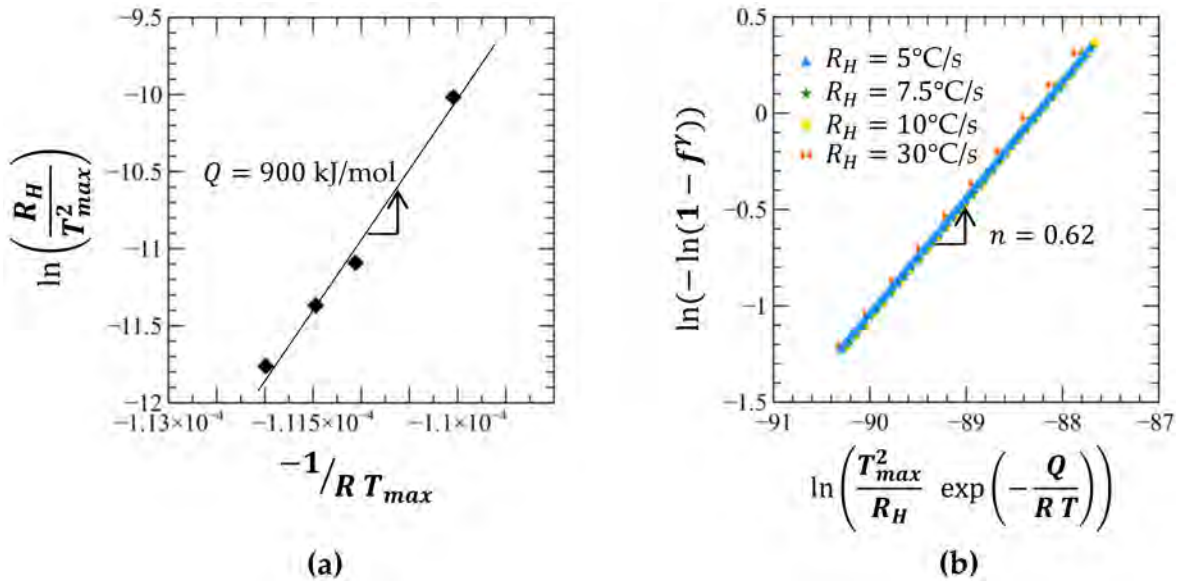


Figure 3.4: Determination of the parameters of the JMAK law: (a) Q and (b) n by the Kissinger method using the non-isothermal kinetics of figure 3.2.a with a heating rate $R_H = 5, 7.5, 10$ or 30°C/s .

The latter parameter of the JMAK law (b_0) was adjusted to obtain the best experimental fit. Figure 3.5 shows the JMAK parametrization of the austenite formation kinetics of

the ReX-steel with the following parameters: $Q = 900$ kJ/mol, $n = 0.62$, $b_0 = 6 \times 10^{43}$ s⁻¹. As can be seen, the agreement between the experimental and fitted curves is excellent for the heating rates ranging from 5 to 30°C/s.

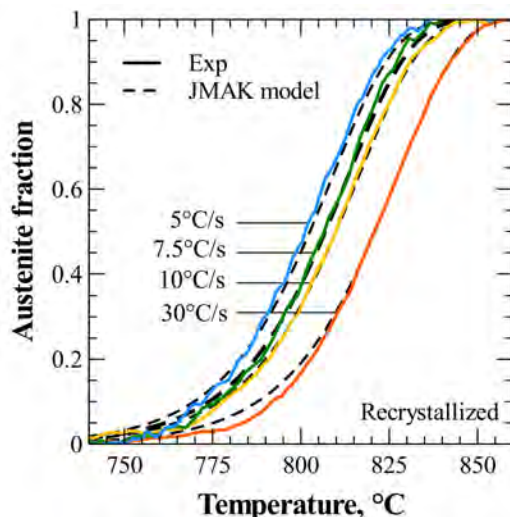


Figure 3.5: Comparison between the experimental austenite formation kinetics of the ReX-steel during continuous heating and the JMAK parametrization. The following parameters were used for the JMAK fit: $Q = 900$ kJ/mol, $n = 0.62$, $b_0 = 6 \times 10^{43}$ s⁻¹.

It has to be noted that the high value of the activation energy found in this work is in agreement with the values (from 843 to 1155 kJ/mol) which were found by Kulakov *et al.* [KUL 13a] on a DP600 steel with different initial microstructures (ferrite-pearlite, ferrite-bainite-pearlite, martensite). However, the high value of the determined activation energy for austenite formation has no physical justification. The activation energy of the JMAK law should better be named as “apparent” activation energy.

3.2.1.2 Typical industrial annealing conditions: heating plus isothermal holding cycles

The JMAK model presented in section 3.2.1.1 was applied in the case of thermal cycles including a heating stage (with $R_H = 5$ or 100°C/s) and an isothermal holding at a given annealing temperature (735, 760 and 780°C). For this study, the experimental austenite formation kinetics were determined by optical microscopy and they were compared with the predictions of the JMAK model which predict the transformed fraction (Y) as a function of time (figure 3.6). In order to obtain the real fractions during the kinetics, the transformed fractions (Y) given by the JMAK law were multiplied by the local equilibrium with negligible partitioning (LENP) fractions predicted by the Thermo-Calc software.

As can be seen in figure 3.6, after an initial increase, the austenite fraction measured at a given annealing temperature tends to stabilize to a maximum value depending on the temperature. This suggests that the steel has reached an equilibrium at each temperature. Two main points have to be noted : (i) the agreement between the JMAK description and

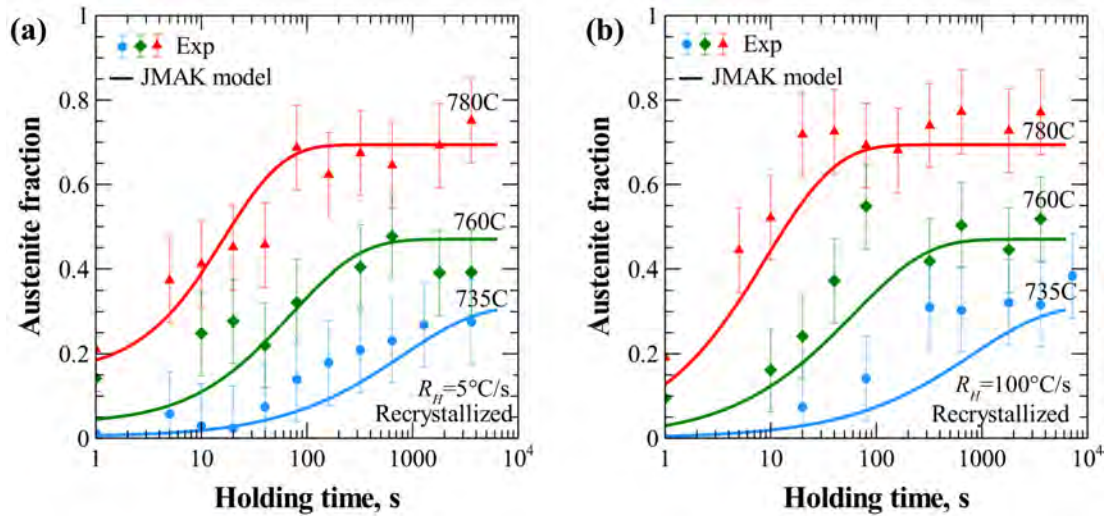


Figure 3.6: Comparison between the experimental austenite formation kinetics and the JMAK model for the ReX-steel during isothermal holding at 735, 760, 780°C after a heating ramp with (a) $R_H = 5$ and (b) $R_H = 100^\circ\text{C/s}$. The fractions determined with the JMAK model were calculated considering the local equilibrium condition calculated with Thermo-Calc. The JMAK parameters were determined in continuous heating conditions on the ReX-steel.

experiment is quite good when the LENP fraction is taken into account. This is consistent with the works of Chbihi *et al.* [CHB 14] who also highlighted the establishment of a local equilibrium at the ferrite/austenite interface thanks to Mn redistribution; (ii) the heating rate has no strong influence on the austenite formation kinetics and on the final austenite fractions for a given annealing temperature contrary to previous results reported in the literature [HUA 04] [CHB 14]. One can, however, notice that the increase in the heating rate tends to accelerate the isothermal austenite formation kinetics.

3.2.1.3 Microstructural observations

In addition to the determination of the austenite formation kinetics, the microstructure was studied by SEM observations shown in figure 3.7. Two intercritical states, water quenched from 780°C, were analyzed after heating at (a-b) $R_H = 5$ and (c-d) 100°C/s. SEM microstructures are characterized by the presence of: (i) recrystallized ferrite grains (in the background), (ii) bands of spheroidized cementite and (iii) martensite islands (*i.e.* austenite before quench, at the forefront).

The martensite volume fraction appears slightly higher in the steel heated at 5°C/s than in the steel heated at 100°C/s. There is indeed less time for transformation at higher heating rate which is in accordance with the optical quantification of figure 3.6.

It can be noted that in both conditions, austenite forms preferentially in prior spheroidized cementite areas and at ferrite grain boundaries. This leads to bands of martensite as observed in figure 3.7.a. The banded morphology is usually associated with the Mn seg-

regation inherited from solidification [KRE 11].

The presence of non-dissolved cementite particles was pointed out inside newly formed martensite islands. Some examples of remaining cementite are marked by a yellow arrow in figure 3.7.b and d. The presence of non-dissolved carbides, even after 5°C/s heating rate to 780°C, suggests slow dissolution of cementite that may be explained by the Mn enrichment stabilizing cementite. Such particularity was also observed by other authors [EST 83] [LAI 16]. However, the cementite features appear different: carbides are enveloped by austenite which was identified as a sign of local chemical heterogeneity [LAI 16]. Lastly, one should note that global approaches, like the JMAK description, do not enable to take into account these local heterogeneities.

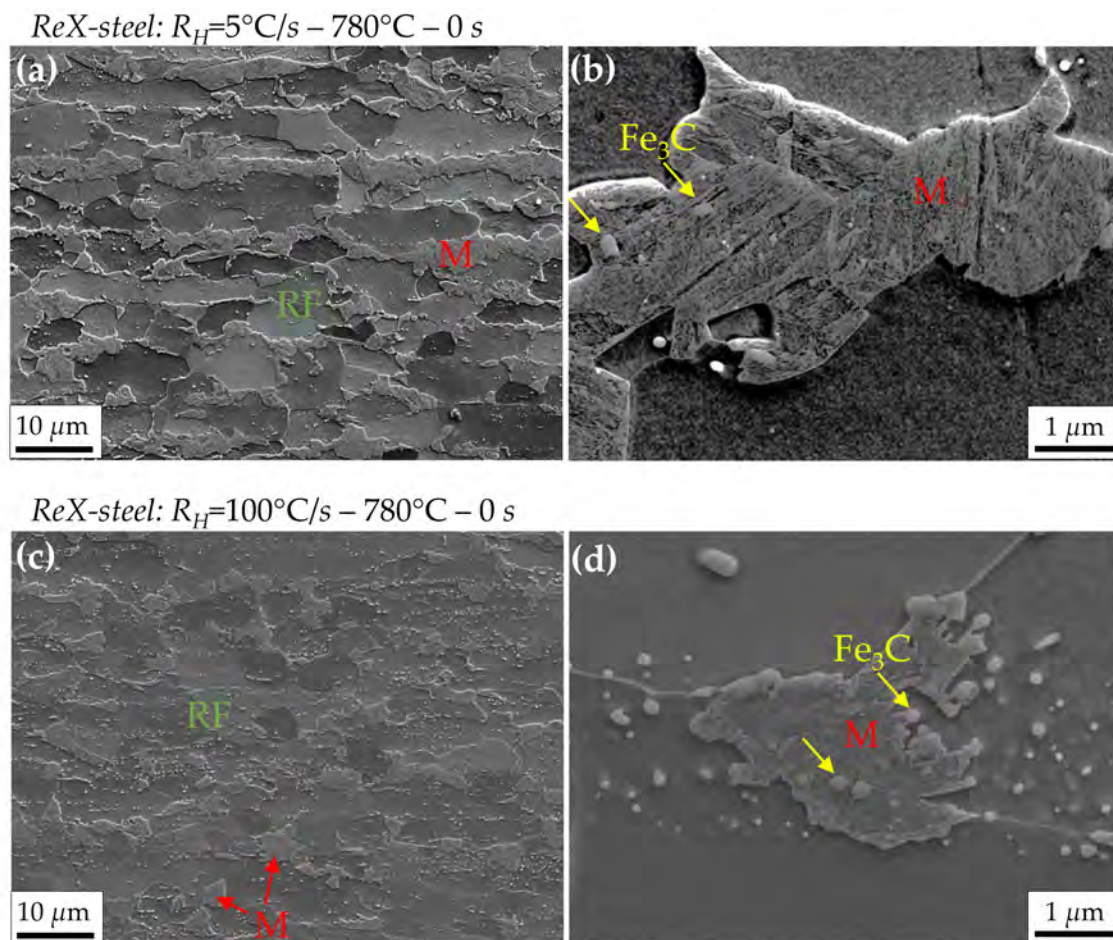


Figure 3.7: SEM micrographs of the ReX-steel heated to 780°C with two heating rates: (a-b) $R_H = 5$ and (c-d) $R_H = 100^\circ\text{C/s}$. Yellow rows point out non-dissolved cementite particles inside newly formed austenite grains.

3.2.2 Recrystallization without austenite formation

The recrystallization of the cold-rolled microstructure was studied on the CR-steel treated below the austenite start temperature ($T < A_{c1}$).

3.2.2.1 Isothermal conditions

In order to model the recrystallization kinetics of the CR-steel using a JMAK approach, the experimental recrystallization kinetics were determined from the curves giving the hardness evolution during isothermal treatments at 650, 675, 700°C (figure 3.8.a). Fast heating rate (100°C/s) was applied in order to focus on the recrystallization occurring in the isothermal holding. From hardness curves, the evolution of the recrystallized fraction (f_{ReX}) could be plotted as a function of the treatment time at each temperature (figure 3.8.b), taking into account the fact that:

$$f_{ReX} = \frac{H_0 - H(t)}{H_0 - H_F} \quad (3.3)$$

where H_0 , $H(t)$ and H_F correspond to the initial hardness (after cold-rolling), the hardness after a given time t , at temperature T , and the hardness of the fully recrystallized steel respectively. The full recrystallization after 1200 s at 700°C was confirmed by SEM observation as illustrated in figure 2.1.(c).

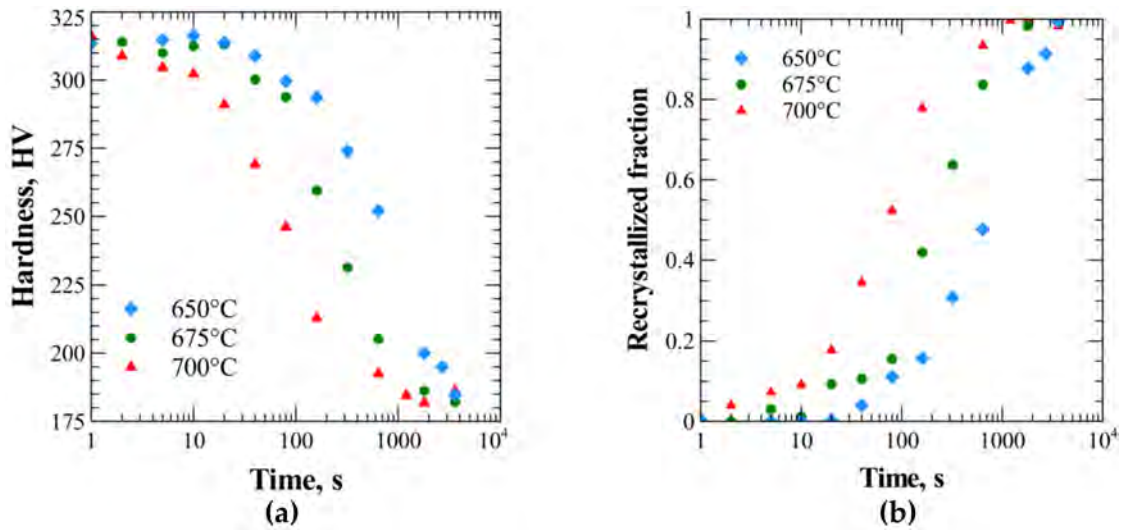


Figure 3.8: (a) Hardness and (b) deduced recrystallized fraction evolutions during isothermal holding at 650, 675 and 700°C.

As expected, recrystallization kinetics depends on holding temperature: recrystallization is shifted towards shorter ageing times at higher temperature, supporting the occurrence of a thermally activated phenomenon. Therefore, a time-temperature equivalence based on an Arrhenius law with an activation energy Q was used to find the “equivalent time at 650°C” for all ageing treatments performed at T and to build a unique master curve. Hence, the equivalent time t_X^{eq} at T_X temperature for the thermal treatments

performed at temperature $T_{650^{\circ}C}$ is expressed by the following relation:

$$t_X^{eq} = \exp\left(\frac{Q}{R}\left(\frac{1}{T_X} - \frac{1}{T_{650^{\circ}C}}\right)\right) t_{650^{\circ}C} \quad (3.4)$$

Figure 3.9.a shows that the superposition of the curves associated with the three annealing temperatures is very good when an activation energy of 326 kJ/mol is used in equation (3.4). The use of a unique activation energy in the whole time-temperature domain suggests that a unique mechanism manages the recrystallization phenomenon. Besides, one can note that the obtained value for Q is higher than that associated with the activation energy of 250 kJ/mol determined for self-diffusion in bcc-iron. This can be explained by the presence of alloying elements such as Mn which may retard the formation of newly recrystallized grains owing to solute drag on migrating grain boundaries [HUA 04]. In addition, the higher value of the recrystallization activation energy may also be due to the steel recovery occurring in parallel (*i.e.* related to plastic deformation, dislocation motion).

Due to the sigmoidal shape of the curves shown in figure 3.8, the isothermal recrystallization kinetics were fitted using an isothermal JMAK model:

$$f_{ReX} = 1 - \exp(-(bt)^n) \quad (3.5)$$

The activation energy Q was assigned to the previously determined value after time-temperature equivalence. The Avrami coefficient n was obtained by a linearisation of the isothermal JMAK law (Eq (1.5)) given in figure 3.9.b. The n parameter represents the slope of the curves and was found to be equal to 1.

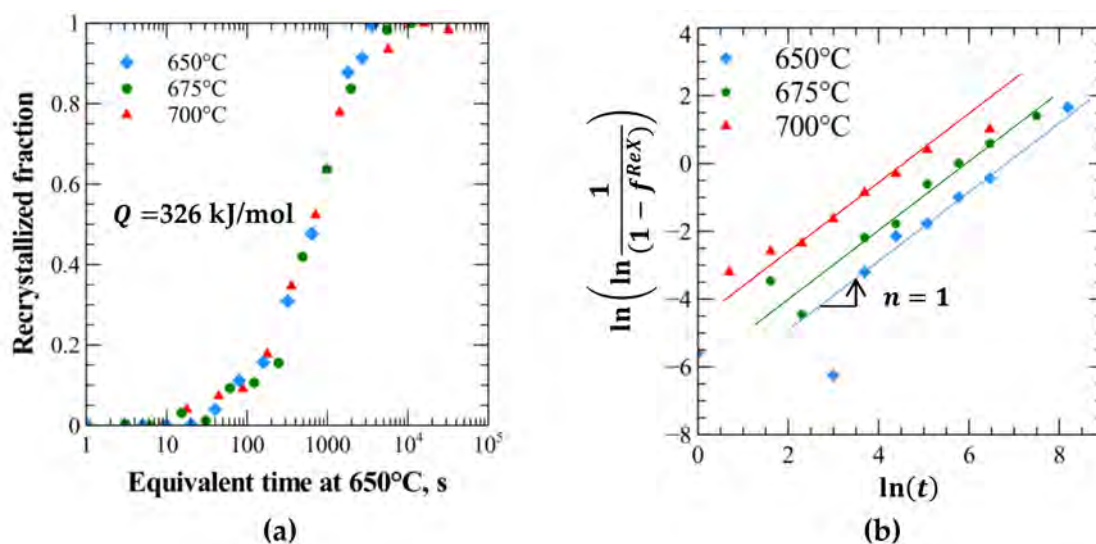


Figure 3.9: (a) Time-temperature equivalence used to determine the activation energy ($Q = 326 \text{ kJ/mol}$) for recrystallization. (b) Linearization of the JMAK law to determine the Avrami exponent ($n = 1$).

Lastly, the third parameter (b_0) was adjusted to obtain the best experimental fit of the experimental recrystallization kinetics with the JMAK law. As can be seen in figure 3.10,

the parameters ($Q = 326$ kJ/mol; $n = 1$; $b_0 = 3.0 \times 10^{15}$ /s) give very good predictions of the recrystallization kinetics. One can note that the parameters reported in the literature have the same orders of magnitude. Yang *et al.* [YAN 85a] determined an activation energy equal to 226 kJ/mol while Huang *et al.* [HUA 04] and Li *et al.* [LI 13] found values close to 350-380 kJ/mol. These higher values are explained by solute alloying elements generating a solute drag effect on the growth of newly recrystallized grains.

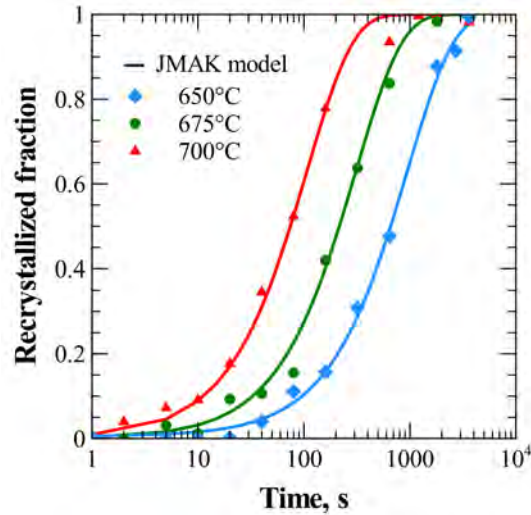


Figure 3.10: JMAK fit of the experimental recrystallization kinetics during isothermal holding at 650, 675, 700°C. JMAK parameters are fixed to: $Q = 326$ kJ/mol, $n = 1$ and $b_0 = 3.0 \times 10^{15}$ /s.

3.2.2.2 Typical industrial annealing conditions: heating plus isothermal holding cycles

The preceding parametrization, determined from isothermal kinetics, was also used to predict non-isothermal kinetics with the JMAK law in its differential form (eq. (3.1)). The model was tested on a complex thermal cycle including a slow heating (with a heating rate of 1°C/s) followed by an isothermal holding at 700°C ($< A_{c1}$). Figure 7 compares the predicted hardness evolution with the experimental ones. The model offers a successful prediction of recrystallization progress.

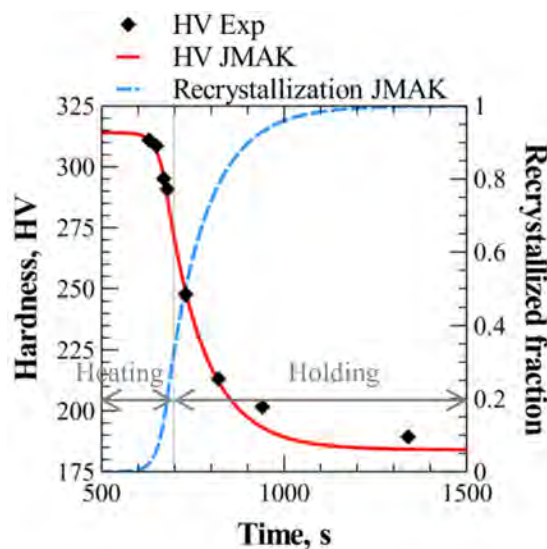


Figure 3.11: Experimental and predicted hardness evolution during a complex cycle (heating at 1°C/s, then holding at 700°C) validating the JMAK model for recrystallization.

3.2.2.3 Microstructural observations

To complete the preceding work, recrystallization progress was followed by SEM micrographs, as shown in figure 3.12. Steel microstructure was studied after interrupted thermal treatments at 700°C after different holding times of (a) 10, (b) 80 and 1200 s. It can be noted that the heating rate R_H was chosen equal to 100°C/s in order to focus on the recrystallization during the holding stage.

After the first holding time (10 s, figure 3.12.(a-b)), the steel remains strongly deformed. Cold-rolled ferrite is characterized by rough surface. Some recrystallized nuclei can be detected: they are surrounded by green ellipses on the micrographs.

After 80 s of holding time (figure 3.12.(c-d)), the microstructure is composed of a mixture of recrystallized and deformed ferrite grains. Recrystallized ferrite is characterized by smooth surface at the foreground. Recrystallization appears to occur preferentially outside cementite bands. Moreover, one can note that cementite has already spheroidized after 80 s at 700°C as identified in figure 3.12.d. The quick cementite spheroidization is in accordance with literature review which pointed out accelerated kinetics after the cold-rolling.

The last micrographs (figure 3.12.(e-f)) show the steel microstructure after a holding at 700°C during 1200 s. The steel is fully recrystallized. However, some deformed ferrite areas persist as shown in figure 3.12.f. Such non-recrystallized regions seem to be mainly localized close to cementite particles. After holding at 700°C for 1200 s, cementite is completely spheroidized. The large diameter of some cementite particles suggests carbide coarsening.

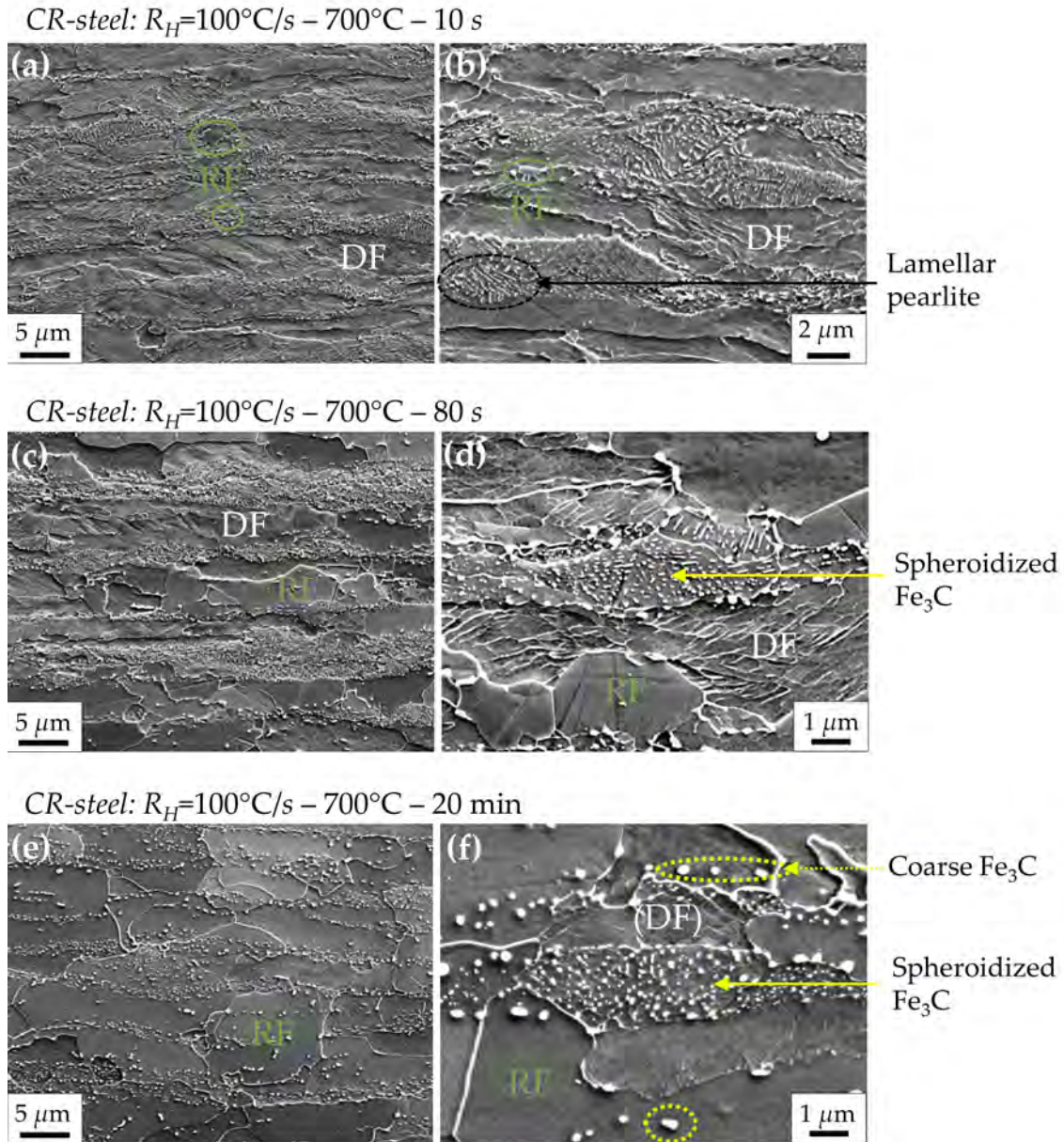


Figure 3.12: SEM micrographs of CR-steel treated at 700°C and water quench after different holding times: (a) 10, (b) 80 and (c) 1200 s. RF= Recrystallized ferrite; DF= Deformed ferrite.

3.3 Case of the cold-rolled steel: interaction between recrystallization and austenite formation

After having studied individually the recrystallization and austenite formation (without recrystallization), microstructural evolutions were investigated during the intercritical an-

nealing of the CR-steel for which both phenomena may occur simultaneously. Figure 3.13.a points out evidence of overlapping of recrystallization and phase transformation phenomena by the combined presence of deformed ferrite grains (DF), recrystallized ferrite grains (RF) and martensite (M, *i.e.* austenite before quench) of a CR-steel heated in the intercritical domain. This microstructural fact strengthens the need to consider the interaction of the recrystallization and phase transformation in cold-rolled steels.

It appears that cementite has completely disappeared because neither pearlite lamellae nor spheroidized cementite are observable. However, as for the ReX-steel, non-dissolved carbides were identified in the newly formed martensite islands as pointed out in figure 3.13.b. These features are less numerous and pronounced than in the ReX-steel suggesting a faster carbide dissolution in the CR-steel case.

The martensite fraction appears larger in the CR-steel (figure 3.13.(a-b)) compared to the ReX-steel treated in the same conditions (figure 3.7) which is in accordance with the accelerated kinetics of this state.

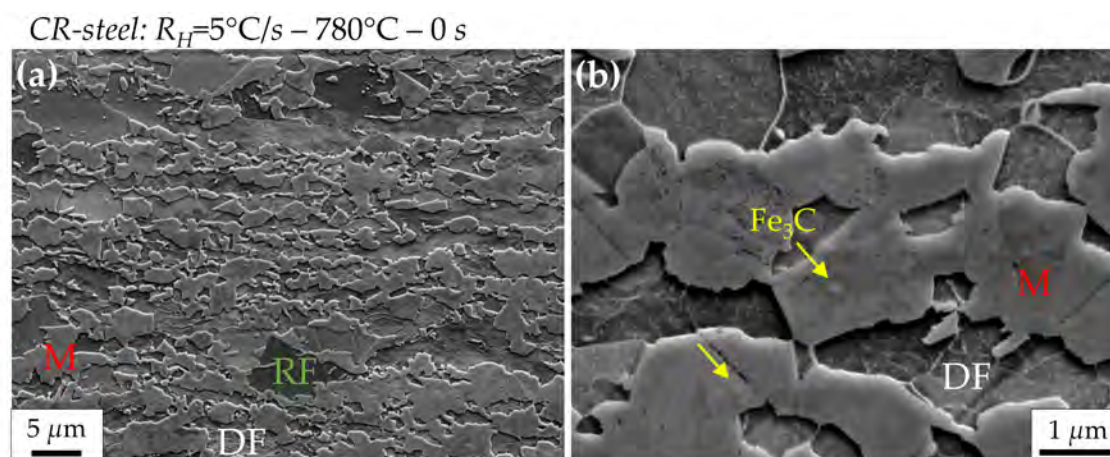


Figure 3.13: SEM observations of the microstructural states of the CR-steel after heating at 5°C/s to 780°C. The microstructure is composed of a mixture of martensite (M, austenite prior cooling), recrystallized ferrite (RF) and deformed ferrite (DF).

3.3.1 Interaction map

The recrystallization domain and the austenite formation domain of the CR-steel were reported in figure 3.14.b on a processing interaction map corresponding to different heating rates (R_H).

The recrystallization model developed in section 3.2.2 has been used to predict the recrystallization kinetics during continuous heating from room temperature to 1000°C with a heating rate between 1°C/s and 100°C/s assuming that the recrystallization kinetics is not modified by the austenite formation in the case of the CR-steel. This latter point will be discussed later. For each considered heating rate (R_H), the recrystallization start temperature (R_{start}) and the recrystallization finish temperature (R_{end}) were determined

for a recrystallized fraction of 5% and 95% respectively as illustrated in figure 3.14.a. R_{start} and R_{end} temperatures were reported as a function of the heating rate in figure 3.14.b. The recrystallization domain is colored in blue.

The austenite formation domain associated with the CR-steel has been added, leading to a map of phenomena occurring during non-isothermal intercritical annealing. The austenite formation domain of the CR-steel (in red colour) was built from the austenite start temperature (A_{c1}) and the austenite finish temperature (A_{c3}) deduced from the dilatometric curves of figure 3.2. For comparison, the austenite formation domain of the ReX-steel was also reported (in green colour).

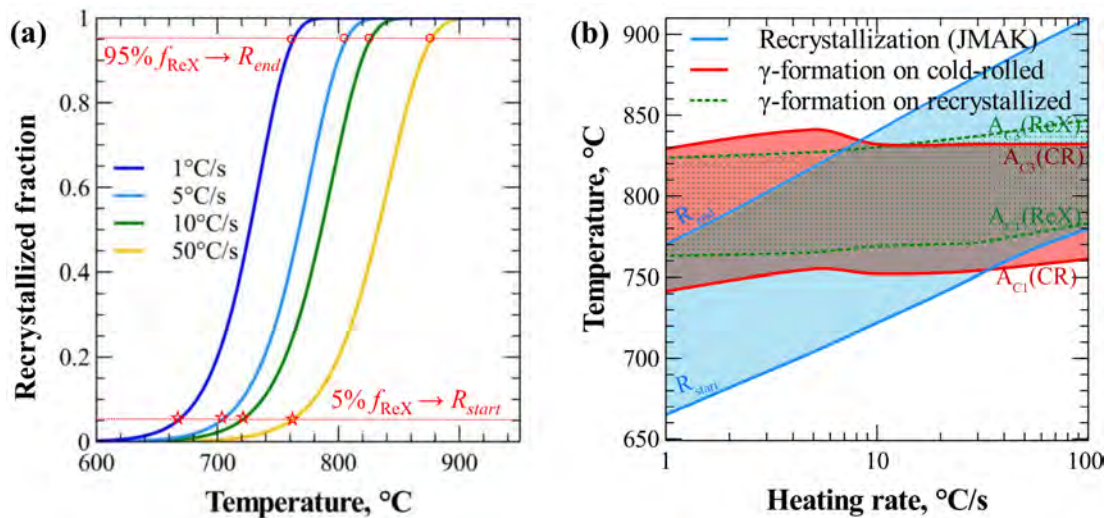


Figure 3.14: (a) Method to evaluate R_{start} and R_{end} temperatures (resp. start and end temperatures of recrystallization) from continuous heating conditions; (b) Interaction map between recrystallization (blue area) and austenite formation (red) in non-isothermal condition.

Several conclusions can be drawn from the map of figure 3.14.b. First, recrystallization is not finished when the austenite start temperature is reached for all heating rates between 1 and 100°C/s. This indicates the occurrence of a wide temperature domain for which recrystallization and austenite formation overlap and can potentially interact.

Secondly, the map of figure 3.14.b clearly shows that austenite starts to form without any recrystallization of the system when the heating rate is higher than 30°C/s. In these conditions, the energy stored during the cold-rolling step is expected to be a supplementary driving force for austenite formation.

Lastly, it has to be noted that for heating rates higher than 15°C/s, recrystallization predicted by the model is not finished while austenite has finished to form. Indeed, the recrystallization model does not consider the phase transformation and assumes that the recrystallization kinetics is not affected by austenite formation. This seems to be effectively the case for austenite fractions lower than 10% because of limited ferrite-austenite interfaces, as suggested by Ogawa *et al.* [OGA 15]. However, when austenite fraction is larger than 30%, recrystallization could be considerably delayed [OGA 10] or even suppressed

[BAR 14], limiting the recrystallization model above A_{C1} .

To complete this work, the recrystallized fraction at the austenite start temperature was plotted as a function of the heating rate in figure 3.15 coupling the recrystallization model with experimental A_{C1} temperature. The increase in the recrystallized fraction at A_{C1} appears to be very abrupt for heating rates lower than 1°C/s . For heating rates greater than 1°C/s , recrystallized fractions are lower than 30%. In other words, recrystallization is just at its beginning when austenite starts to form.

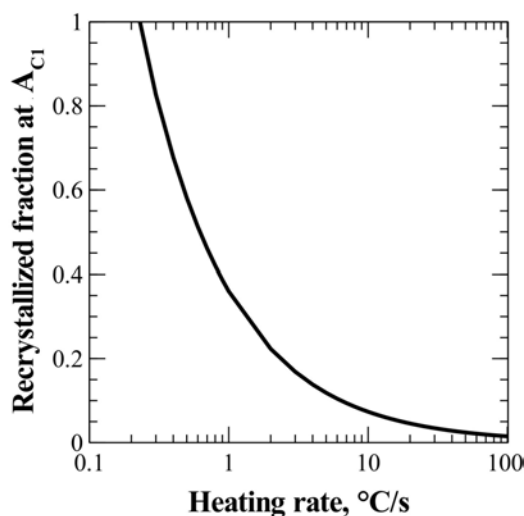


Figure 3.15: Evolution of the recrystallized fraction at A_{C1} temperature as a function of the heating rate.

3.3.2 Austenite formation with recrystallization

In the case of the CR-steel, austenite formation is likely to occur either in a fully recrystallized matrix at very slow heating rates ($R_H < 0.5^\circ\text{C/s}$) or in a matrix combining a mixture of recrystallized ferrite grains and of deformed grains at intermediate and high heating rates. This leads to a rather complex dependence of the austenite formation kinetics with the heating rate, as highlighted on the non-isothermal austenite formation kinetics of figure 3.2.b.

This observation can be explained by the fact that the austenite formation kinetics is very different in the deformed and recrystallized ferrite grains, as suggested by the results of figure 3.3 which support the hypothesis that austenite formation is accelerated when deformed ferrite grains are present in the microstructure. Namely, the energy stored in the deformed ferrite grains during cold-rolling could increase the driving force for the transformation [CHB 14].

3.3.2.1 Non-isothermal conditions

In order to model the non-isothermal austenite formation kinetics of the CR-steel shown in figure 3.2.b, a mixture law taking into account the evolution of the fraction of recrystallized grains during the treatment was employed. The austenite formation kinetics of the CR-steel, f_γ , during a given treatment was thus expressed by the following relation :

$$f_\gamma = f_\alpha^{ReX} f_\gamma^{ReX} + (1 - f_\alpha^{ReX}) f_\gamma^{CR} \quad (3.6)$$

where f_α^{ReX} represents the recrystallization kinetics of the steel (determined in section 3.2.2), f_γ^{ReX} is the austenite formation kinetics in the recrystallized ferrite grains (determined in section 3.2.1) and f_γ^{CR} is the austenite formation kinetics in the deformed ferrite grains. All fractions are time and temperature dependent (*i.e.* $f(t,T)$) as they result from JMAK laws.

In the present work, two different JMAK laws were associated with the austenite formation kinetics in the recrystallized and non-recrystallized ferrite grains. They were characterized by the same values of Q and n but by a different value of b_0 . A higher value of this parameter was assigned to the JMAK law associated with the austenite formation in deformed ferrite grains to take into account the acceleration of the kinetics. This value was adjusted to obtain the best fit of the experimental data at the very beginning of the austenite formation kinetics. Appendix explores another parametrization based on the determination of the JMAK parameters of the CR-steel using the Kissinger method on the kinetics of figure 3.3. However, the difficulty of parametrization was pointed out due to the complex evolution of austenite formation kinetics during continuous heating treatments on the CR-steel. This comforts the present approach with assumes the same values of Q and n for the CR-steel as those for the ReX-steel.

Table 3.1 summarizes the parameters of the three JMAK laws used in the mixture law presented above. One can notice that the activation energy (Q) for austenite formation in recrystallized and deformed ferrite is supposed identical although diffusion could be promoted in deformed steel state (thanks to pipe diffusion). As a consequence, it is supposed that the thermal activation is not dependent on the deformation state.

Phenomenon	Q , kJ/mol	n	b_0 , /s
Recrystallization	326	1	3×10^{15}
Austenite formation in recrystallized ferrite	900	0.62	6×10^{43}
Austenite formation in deformed ferrite	900	0.62	3×10^{45}

Table 3.1: JMAK parameters for recrystallization and for austenite formation kinetics in recrystallized ferrite or in deformed ferrite.

Figure 3.16.a shows the austenite formation kinetics predicted by the mixture law during continuous heating of the CR-steel with a heating rate of 30°C/s and the different components of the law (*i.e.* recrystallization kinetics, austenite formation kinetics in recrystallized ferrite grains or in deformed ferrite grains). The agreement between experiment and theory is good for austenite fractions lower than 0.6. Below this fraction, the

kinetics is mainly controlled by the deformed ferrite grains, the proportion of which is much higher than that of the recrystallized ferrite grains. At higher austenite fractions, the model predicts a slower kinetics than the experimental one. This could be due to the fact that the model considers that the fraction of recrystallized grains gradually increases during heating and that the recrystallization kinetics is not influenced by austenite formation. This is contrary to the observations of [OGA 15] [BAR 15a] which showed that the recrystallization kinetics could be considerably retarded above a critical austenite fraction. In order to check this hypothesis, the mixture law was used considering that recrystallization is blocked when the austenite fraction exceeds 10% (figure 3.16.b). This gives a better prediction of the austenite formation kinetics and supports the fact that recrystallization could be effectively inhibited above a critical austenite fraction. Results from the mixture law applied with these three JMAK laws taking into account recrystallization inhibition are given in appendix D.2 for other heating rates.

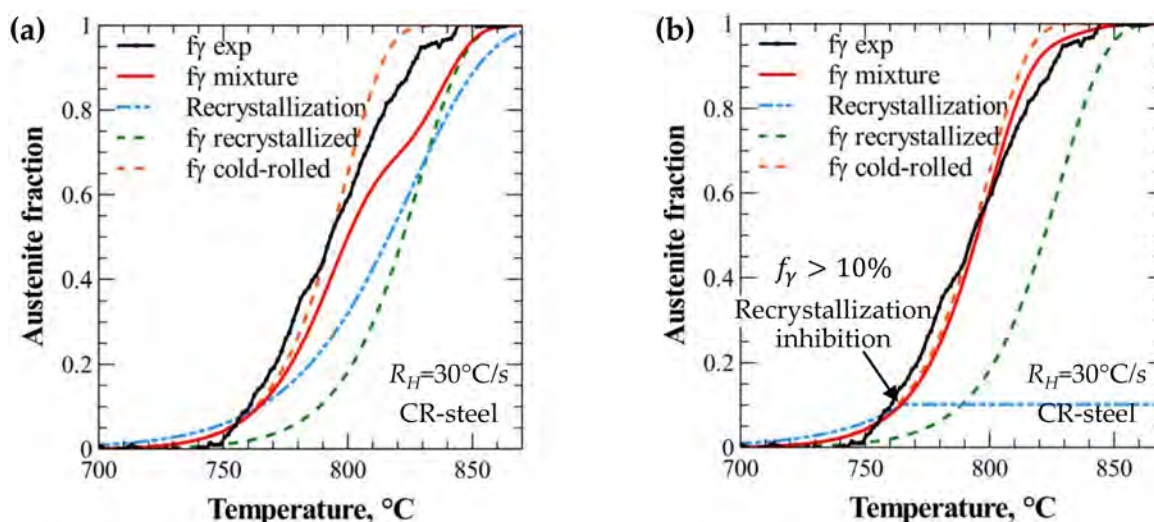


Figure 3.16: Comparison between the experimental austenite formation kinetics of the CR-steel and the theoretical kinetics based on a mixture law during continuous heating at 30°C/s : (a) without recrystallization inhibition; (b) with recrystallization inhibition for austenite fractions higher than 10%. The different components of the mixture law were reported in dash points.

3.3.2.2 Typical industrial annealing conditions: heating plus isothermal holding cycles

The mixture law was also applied to predict the austenite formation kinetics of the CR-steel during thermal cycles including a heating stage ($R_H = 5^\circ\text{C/s}$) and an isothermal holding at a given annealing temperature (between 720 and 780°C). Figure 3.17.a shows the experimental and predicted austenite fractions obtained in two cases: (i) without taking into account the inhibition of recrystallization and (ii) with recrystallization inhibition

above a critical austenite fraction of 10%. As for the ReX-steel, the austenite fractions given by the mixture law were calculated considering the Thermo-Calc local equilibrium conditions. Furthermore, the end of the recrystallization predicted by the JMAK model (presented in section 3.2.2) was marked by a star item on the curves of figure 3.17.a.

As can be seen in figure 3.17.a, at all temperatures, austenite fractions increase before reaching a plateau, suggesting the achievement of an apparent equilibrium. At low temperatures (720, 735°C), austenite fractions are rather well predicted for all annealing times. For these two temperatures, recrystallization inhibition has no influence on the kinetics, since recrystallization is completed before reaching the critical austenite fraction for which recrystallization is blocked. For the intermediate temperature (760°C) and the highest temperature (780°C), a better agreement between experiment and theory is obtained if recrystallization inhibition is taken into account. Namely, at these two temperatures, recrystallization and austenite formation occur simultaneously and this greatly influences the austenite formation kinetics. However, a significant difference can be noted on the values of the equilibrium austenite fractions especially at 780°C. At 760°C, the experimental fraction (around, 40%) is in good agreement with the local equilibrium fraction given by Thermo-Calc. This is not the case at 780°C where the experimental fraction on the plateau (about 88%) is much higher than the local equilibrium fraction (66%). This unexpected result will be discussed further in section 3.4.2.2.

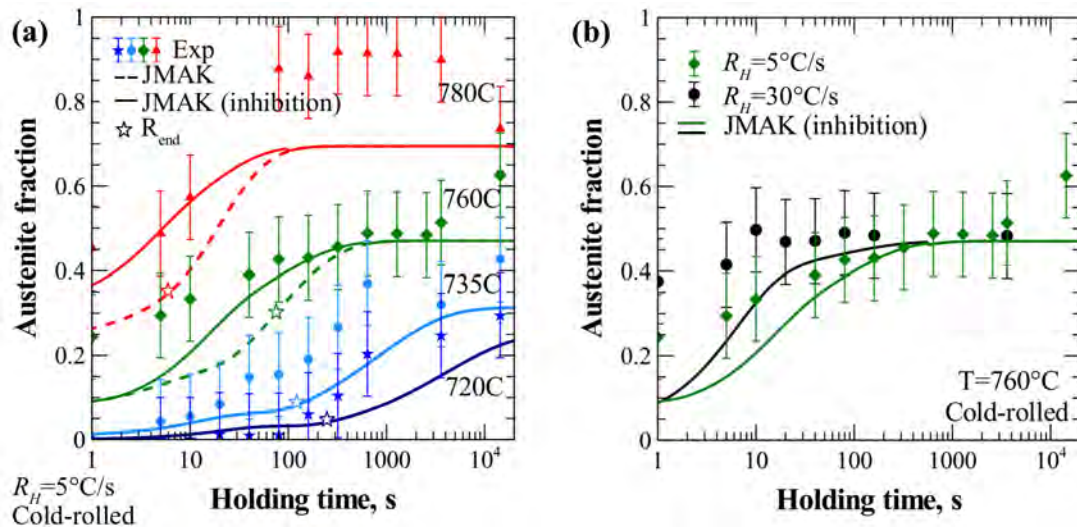


Figure 3.17: (a) Comparison between the experimental austenite formation kinetics of the CR-steel and the theoretical kinetics based on a mixture law during isothermal holding at 720, 735, 760, 780°C after a heating stage with $R_H = 5^\circ\text{C/s}$. The stars correspond to the end of recrystallization and solid lines consider recrystallization inhibition for austenite fraction higher than 10%. (b) Effect of the heating rate on the experimental and modeled austenite formation kinetics during isothermal holding at 760°C

Lastly, figure 3.17.b. presents the effect of the heating rate on the austenite formation kinetics of the CR-steel at 760°C. Increasing the heating rate from 5 to 30°C/s leads to a marked acceleration of the kinetics. This can be explained by the delay of recrystallization

when the heating rate is increased (see figure 3.18). The recrystallization inhibition has consequently higher effect as the recrystallization is interrupted earlier at 30°C/s so that austenite forms on a larger fraction of cold-rolled ferrite. As can be observed in figure 3.17.b, the model captures this acceleration of the kinetics but it is slightly retarded compared to experimental kinetics during the first ten seconds of holding.

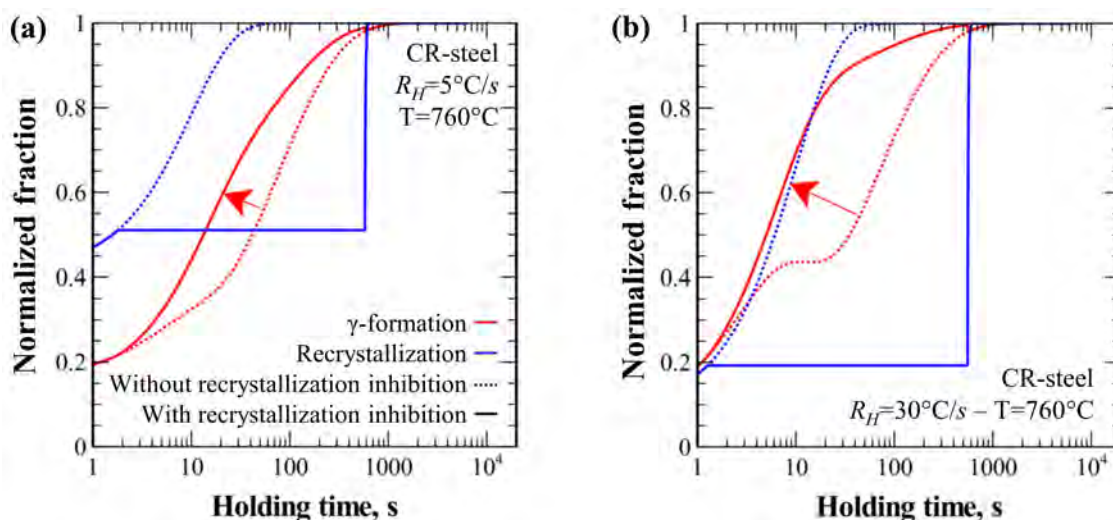


Figure 3.18: Impact of the recrystallization inhibition consideration on the normalized recrystallization and austenite formation kinetics during a holding at 760°C and after a heating rate equal to (a) $R_H = 5$ and (b) 30°C/s

3.3.2.3 A tool to predict microstructural evolutions during the intercritical treatments of CR-steels

The mixture law presented above and defined by relation (3.6) was implemented on an excel worksheet as shown in figure 3.19. Such tool ensures the prediction of microstructural evolutions as a function of different cycle parameters: heating rate (R_H), holding temperature (T_s) and holding time (t_s).

Predictions are based on the mixture law (presented in section 3.3.2.1) which enables to predict the recrystallization and the austenite formation on the recrystallized and cold-rolled ferrite. The recrystallization inhibition above a critical austenite fraction was also implemented, with the critical austenite fraction fixed at 10% according to previous works of the literature. Recrystallization was considered to continue after complete austenite transformation.

The result of the predictions for the complete cycle (including heating and holding) is plotted as a function of time. It should be noted that JMAK laws define normalized fractions (varying between 0 and 1).

In another representation, austenite fractions are calculated using the Thermo-Calc LENP austenite fractions ensuring the evaluation of the real austenite fraction and also

the fractions of deformed and recrystallized ferrite grains during the intercritical thermal treatment.

The corresponding carbon content in austenite (C_C^γ) was evaluated by a mass balance between ferrite and austenite phase:

$$C_C^\gamma = \frac{C_{steel} - (1 - f^\gamma) \times C_C^\alpha}{f^\gamma} \quad (3.7)$$

with C_{steel} and C_C^α respectively the global carbon content and the carbon content in ferrite.

This worksheet was used to evaluate microstructural evolutions changing either the heating rate R_H and/or the holding temperature T_S . This phenomenological model enables to predict the austenite fraction, the recrystallization progress and the evolution of the carbon content in austenite. Easy computational trials may be performed on this worksheet and will be realized in section 3.4 to discuss the influence of the parameters of the thermal cycles.

3.4 Discussion

The aim of this section is to discuss and analyse the influence of several parameters (initial state of the steel, annealing temperature, heating rate) considered in this work.

3.4.1 Influence of the initial state on the austenite formation kinetics

The results presented in the preliminary work of this chapter (section 3.2, figure 3.3) clearly showed that the austenite formation kinetics of the CR-steel is: (i) identical to that of the ReX-steel at low heating rate ($R_H = 0.5^\circ\text{C/s}$) and (ii) tends to be accelerated compared to that of the ReX-steel at higher heating rates, all the more as the heating rate is high.

These observations can be explained by two main effects: (1) the presence of non-recrystallized ferrite grains in the CR-steel could promote the austenite nucleation by increasing the driving force for the austenite formation and accelerate the kinetics of the CR-steel [KUL 13a] [CHB 14]; (2) the cementite spheroidization highlighted by the SEM observations of the initial microstructure of the ReX-steel could be responsible for a delay in austenite nucleation and retard the kinetics of the ReX-steel [LI 13].

In order to analyse these two effects and to identify their respective role on the austenite formation kinetics, the evolution of cementite morphology during the heating stage of the CR-steel was analysed by SEM observations before austenite nucleation (figure 3.20). To this end, the CR-steel was heated up to 720°C with two heating rates (5 and 30°C/s) and subsequently, water-quenched. As can be seen in figure 3.20, cementite spheroidization occurs very rapidly during the heating stage. For the lower heating rate, cementite spheroidization is total and relatively similar to that of the ReX-steel, while it is only partial at the higher heating rate. These results tend to indicate that the effect of cementite spheroidization may play a role on the austenite kinetics but it should not be predominant. Namely, cementite spheroidization takes place very rapidly during the heating stage

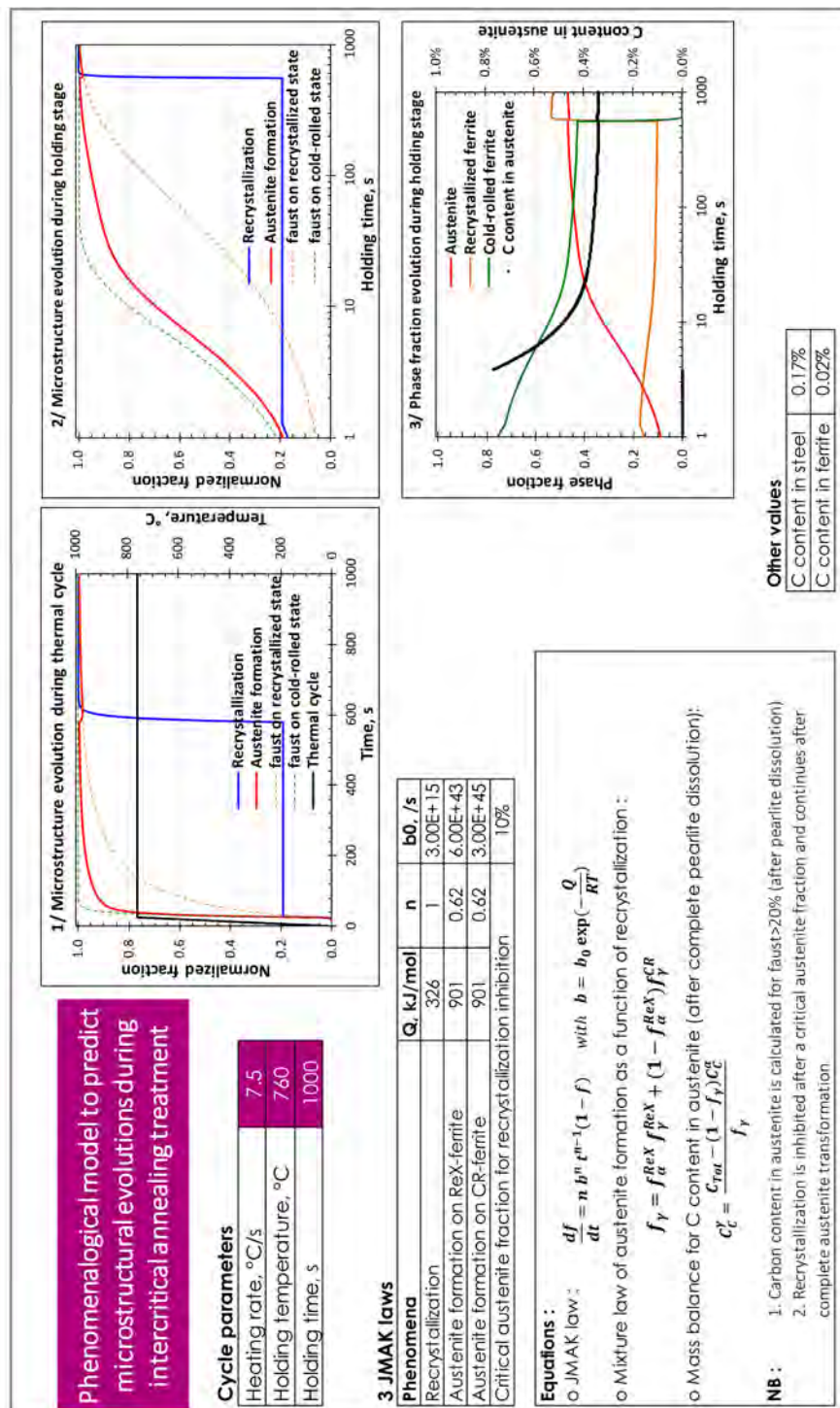


Figure 3.19: Screen print of the developed worksheet to describe microstructural evolutions during intercritical annealing as a function of different thermal parameters: heating rate (R_H), holding temperature (T_s) and holding time (t_s).

of the CR-steel and austenite nucleation is expected to occur mainly from spheroidized cementite both in the CR-steel and in the ReX-steel (especially for heating rates lower than 5°C/s).

In these conditions, the degree of recrystallization of the ferrite matrix before austenite formation seems to be the major parameter to consider, in view of understanding the austenite formation kinetics. For a heating rate of 0.5°C/s , the kinetics of austenite formation are identical for the ReX-steel and for the CR-steel, as recrystallization has largely occurred in the CR-steel before austenite formation (as can be deduced from the results of figure 3.14.b). Such behaviour was also observed by Azizi-Alizamini *et al.* [AZI 11] for a heating rate of 1°C/s . Authors also explained that this is due to the fact that recrystallization of ferrite in the cold-rolled steel takes place before austenite formation. In the case of higher heating rates, recrystallization is just at its very beginning when austenite starts to form and this tends to accelerate strongly the austenite formation kinetics.

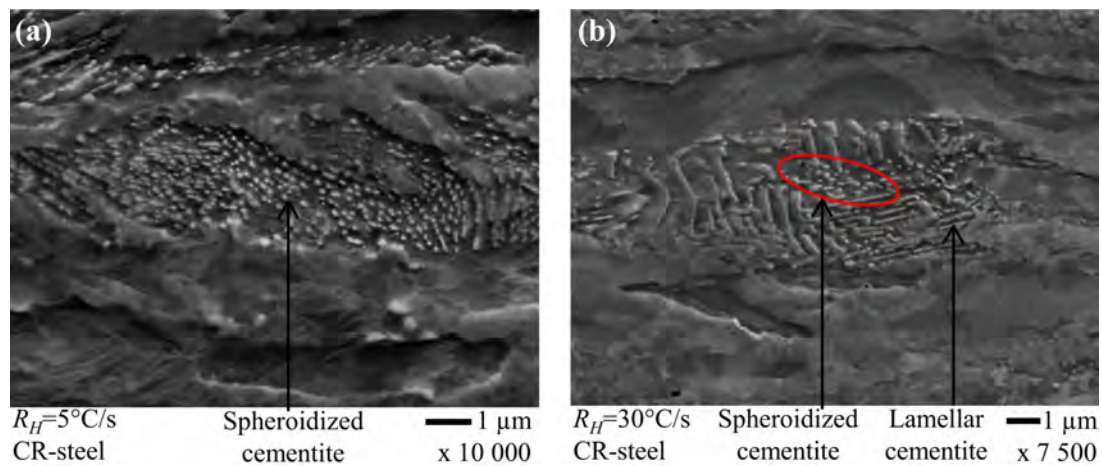


Figure 3.20: SEM observations of microstructural states of a cold-rolled steel after heating at (a) 5 and (b) 30°C/s to 720°C . A full spheroidization of cementite is observed after 5°C/s while spheroidization is partial with 30°C/s heating rate.

3.4.2 Influence of the temperature and of the heating rate on the austenite formation kinetics

3.4.2.1 Case of the ReX-steel

For the ReX-steel, the austenite formation kinetics is accelerated when the annealing temperature is increased and the equilibrium austenite fractions increase. Moreover, the equilibrium fractions obtained at each temperature are in agreement with those given by Thermo-Calc under local equilibrium conditions. These observations are in perfect accordance with those of Chbihi *et al.* [CHB 14] for the description of the metastable equilibrium obtained for short treatment times. They support the fact that the orthoequilibrium is not reached in typical industrial conditions. This was also pointed out by the works of Lai *et al.* [LAI 16] who estimated the time to reach the orthoequilibrium to be of the order of 10^6 s (at 740°C) with DICTRA software. Lastly, it has to be emphasized

that the assumption of paraequilibrium does not describe the equilibrium condition. The difference in the composition of the substitutional elements, such as Mn, in the two initial phases (*i.e.* ferrite and cementite) could explain the fact that the paraequilibrium condition is not verified in the case of the investigated steel. Indeed, the gradient of composition could promote local diffusion through the interface despite the slow diffusivities of Mn and generate a LE condition.

Furthermore, heating rate does not influence the equilibrium austenite fraction at a given annealing temperature. In addition, it has no strong influence on the austenite formation kinetics (figure 3.6). This is particularly true when no austenite formed during the heating stage or when the austenite fraction formed during heating is low (that is to say at low annealing temperature). This is illustrated in figure 3.21.a for an annealing at 760°C. No effect of the heating rate is noted when this parameter passes from 5 to 100°C/s, since no austenite formed during the heating stage. However, a little effect is observed when the heating varies between 0.5 and 100°C/s due to the formation of a low austenite fraction during heating with $R_H = 0.5^\circ\text{C/s}$. At higher annealing temperature 780°C, the effect of the heating rate is more marked, as shown in figure 3.21.b.

It has to be noted that the low influence of the heating rate found in this work for the ReX-steel is not in agreement with the results of Huang *et al.* [HUA 04]. These authors observed that the austenite formation kinetics obtained at 750°C on a hot-rolled Fe-C-Mn-Mo steel was different after a slow heating (1°C/s) or after a rapid heating (100°C/s). In particular, they noted that the measured austenite fractions were much lower when the heating rate was slow without providing any physically based argument. Chbihi *et al.* [CHB 14] obtained also the same conclusions. However, it has to be mentioned that their results concern short treatment times at 740°C (less than 600 s) for which no equilibrium is reached.

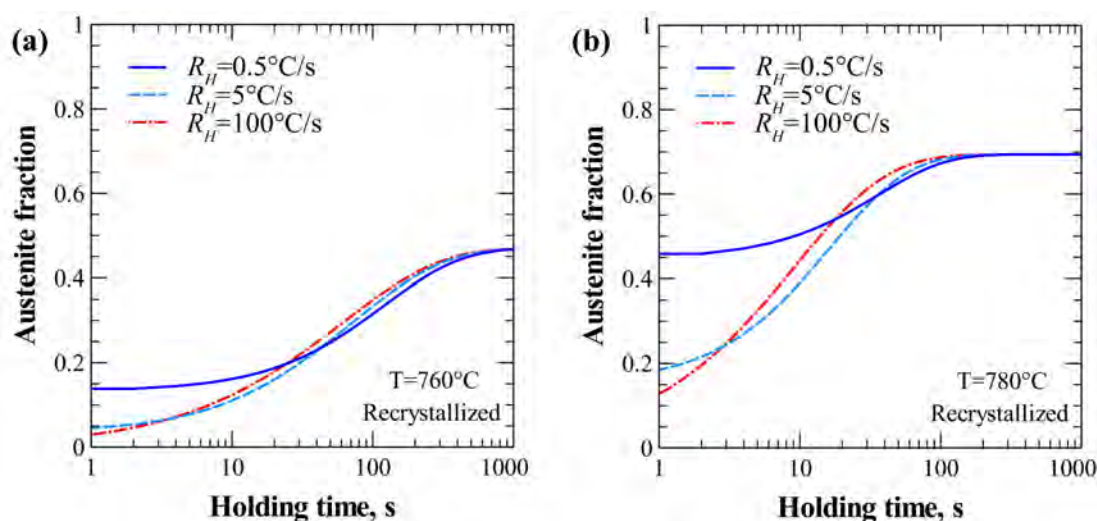


Figure 3.21: Effect of the heating rate (R_H) on the austenite formation kinetics during isothermal holding at (a) 760 and (b) 780°C of the ReX-steel. The kinetics were predicted using the JMAK model defined in section 3.2.1.

3.4.2.2 Case of the CR-Steel

In the case of the CR-steel, the effect of the heating rate and of the temperature is more difficult to analyse due to the interaction between recrystallization and austenite formation. Depending on the parameters of the cycles, this interaction can be weak (at low temperature and low heating rate) or strong (at high temperature and high heating rate) [CHB 14] [BAR 15a].

- *For a weak interaction*, recrystallization occurs mainly before austenite formation, so that the austenite formation kinetics is similar to that determined for the ReX-steel. For the investigated steel, a weak interaction was observed at low temperature (720, 735°C) with $R_H = 5^\circ\text{C/s}$ as shown in figure 3.22. At these two temperatures, recrystallization is finished before 10% of austenite has formed.
- *For a strong interaction*, obtained at higher temperatures, recrystallization and austenite formation are concomitant. This experimental fact has two main consequences.

The first consequence is that the effect of the heating rate is much more pronounced than in the ReX-steel. This is illustrated in figure 3.22, where the austenite formation kinetics during isothermal holding at 760°C was predicted, for three different heating rates, using the mixture law (with recrystallization inhibition) as defined in equation 3.6. Figure 3.22 highlights that increasing the heating rate strongly accelerates the austenite formation kinetics, contrary to the case of the ReX-steel presented in figure 3.21.a at the same temperature. This acceleration can be attributed to the fact that the proportion of non-recrystallized ferrite grains at the austenite start temperature (figure 3.15) is higher at high heating rate. It is estimated to be equal to 1, 53 and 82% at the beginning of the isothermal holding for 0.5, 5 and 30°C/s heating rates. This is due to the shift of the recrystallization kinetics towards higher temperatures and to recrystallization inhibition. These two phenomena lead to an increase in the fraction of deformed ferrite grains on which austenite nucleates and subsequently, to an acceleration of the austenite formation kinetics.

The second consequence of the interaction is that the equilibrium austenite fraction obtained after annealing at high temperature cannot be predicted using the local equilibrium fractions given by Thermo-Calc. This was observed in figure 3.16 in the case of the kinetics at 780°C, where the combination of a high annealing temperature and of a high fraction of deformed ferrite grains probably promoted the diffusion of the alloying elements of the steel. Namely, the dislocations of the ferrite matrix could provide favourable diffusion paths for Mn [KUL 13a] [CHB 14] and this could lead to an achievement of an intermediate state between LE and ORTHO equilibria for times shorter to 100 s. Note that this intermediate state contains more austenite than both LE and ORTHO as shown by Wei *et al.* [WEI 13] and Lai *et al.* [LAI 16]. The transition between LE to ORTHO seems to be also highlighted at the other holding temperatures for long treatment times (4 h) as reported in table 3.2. Table 3.2 compares experimental austenite fractions measured after 1 and 4 h of holding with the ORTHO and LE fractions. Data are also represented in a graph function of the temperature in figure 3.23. Austenite fractions at 720, 735 and 760°C after 1 hour of holding are close to the LENP fractions calculated with Thermo-Calc. Then, for all temperatures between 720 and 760°C, the austenite fractions evolve

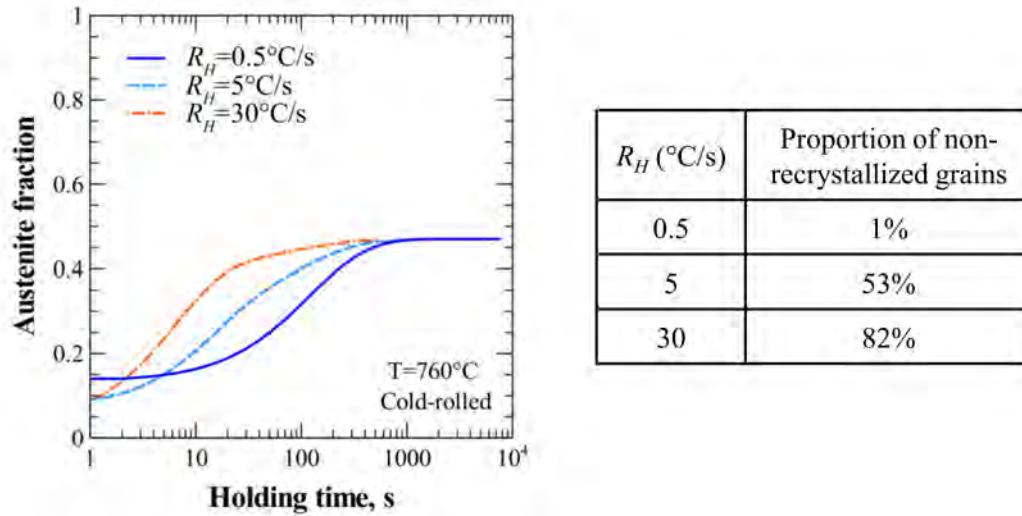


Figure 3.22: Effect of the heating rate R_H on the austenite formation kinetics during isothermal holding at (a) 760 and (b) 780°C of a cold-rolled steel. The kinetics were predicted using the JMAK model defined in section 3.2.1.

and increase between 1 and 4 h of holding to reach the “Mn-diffusion in ferrite” regime and finally, the ORTHO equilibrium [WEI 13] [LAI 16] which could apparently be reached at 780°C for a holding time of 4 h of the CR-steel.

Austenite fraction	720°C	735°C	760°C	780°C
Experimental after 1h of holding	0.24	0.32	0.50	0.88
Experimental after 4h of holding	0.29	0.42	0.62	0.73
ORTHO Fe-C-Mn-Cr-Si-Al	0.34	0.40	0.54	0.70
LENP Fe-C-Mn	0.24	0.31	0.46	0.66

Table 3.2: Comparison of Thermo-Calc and experimental austenite fraction on CR-steel after 1 h and 4 h of isothermal holding.

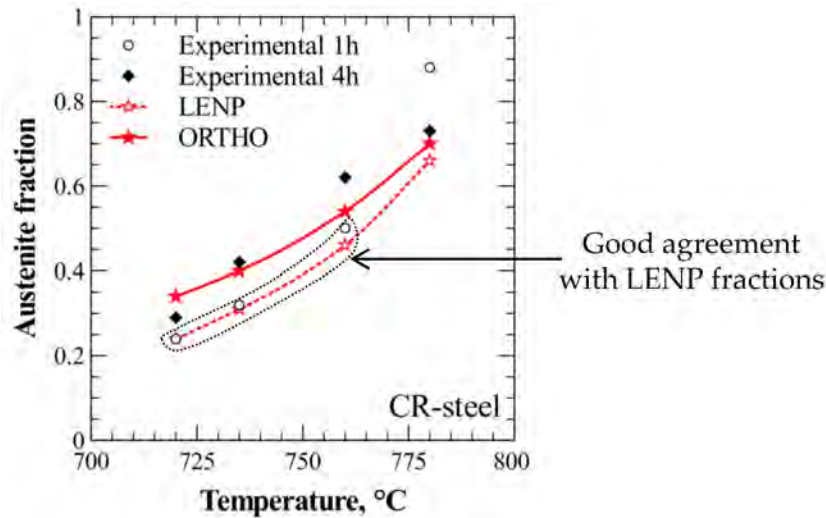


Figure 3.23: Comparison of Thermo-Calc and experimental austenite fraction on CR-steel after 1 h and 4 h of isothermal holding as a function of the temperature.

3.5 Conclusion

The present chapter deals with the experimental characterization and the simple modeling of the austenite formation kinetics of a DP1000 steel with an initial ferrite-pearlite microstructure (either fully recrystallized or cold-rolled). For the experimental study, dilatometric and optical microscopy measurements were used to follow the kinetics of austenite formation during different types of thermal cycles. For the modeling, simple JMAK laws were used to describe the recrystallization kinetics without austenite formation and the austenite formation kinetics without recrystallization. To study the complex case of the cold-rolled steel for which austenite formation and recrystallization are expected to occur simultaneously, a mixture law was employed. The influence of several parameters (initial state of the steel, annealing temperature, heating rate) on the austenite formation kinetics was discussed.

1. In the case of the ReX-steel, the austenite formation kinetics could be successfully described by a simple JMAK law with the following parameters : $Q = 900$ kJ/mol, $n = 0.62$ and $b_0 = 6 \times 10^{43}$ s⁻¹. Using the local equilibrium fractions given by Thermo-Calc, the isothermal austenite formation kinetics of the ReX-steel could be successfully modeled for treatment times from 1 s to 1 hour. Moreover, no strong influence of the heating rate was found on the austenite formation kinetics and on the final austenite fractions, contrary to previous results of the literature.
2. The recrystallization kinetics of the steel without austenite formation was modelled by a JMAK law with the following parameters : $Q = 325$ kJ/mol, $n = 1$ and $b_0 = 3 \times 10^{15}$ s⁻¹. Using this model during continuous heating with different heating rates, an interaction map between recrystallization and austenite formation could be built for the CR-steel. It highlighted that the degree of recrystallization before austenite formation depends strongly on the heating rate and is less than 30% for

heating rates higher than 1°C/s.

3. A simple mixture law was used to describe the austenite formation kinetics of the CR-steel under various conditions. It was based on the assumption that two different JMAK laws are necessary to describe austenite nucleation in the recrystallized ferrite grains and in the deformed ferrite grains. The results presented in this chapter showed that the experimental curves are well fitted in the case of a weak interaction between recrystallization and austenite formation. For a strong interaction (high temperature, high heating rate), the curves are better fitted by the model when recrystallization is inhibited above a critical austenite fraction, supporting the results of several studies [OGA 15] [BAR 15a].
4. In the case of the CR-steel, a strong influence of the heating rate was noted on the austenite formation kinetics when a strong interaction is expected, due to the marked dependence of the recrystallized fraction at the austenite start temperature with this parameter. In addition, it was suggested that the combination of a high temperature and a high deformed structure tends to accelerate the diffusion of the alloying elements in the steel. In these conditions, the final austenite fractions obtained at high temperature cannot be described using the local equilibrium fractions given by Thermo-Calc.
5. Lastly, the present work showed that the acceleration of the austenite formation kinetics in the CR-steel compared to the kinetics of the ReX-steel can be mainly explained by the degree of recrystallization before austenite formation and, partly, by cementite spheroidization which may occur during heating. For usual industrial heating rates, the recrystallized fraction of the CR-steel is low at the A_{c1} temperature, which tends to promote austenite nucleation in the deformed ferrite grains and to accelerate the transformation kinetics.

The 3-JMAK modeling tool was developed in an Excel worksheet, pragmatic tool allowing the austenite formation kinetics to be predicted for different thermal cycle parameters taking into account recrystallization inhibition. Identical approach may be extended to other chemistry in order to implement practical tool to predict microstructure evolutions ongoing intercritical treatments. The two next chapters aim at introducing a more physically based approach in the modeling of the austenite formation.

Chapter 4

Mixed-mode model for austenite formation

A mixed-mode model was proposed to predict the austenite formation kinetics during the intercritical annealing of the investigated prior recrystallized steel (ReX-steel) and to go towards more physically based approach to model the austenite formation. The implementation of the mixed-mode model is detailed in this chapter. For this, the theory of the mixed-mode model is reminded before specifying the numerical algorithm implemented to solve both diffusion and interface mobility equations. The initial state and model parameters are specified to deal with the austenite formation during intercritical annealing treatments. Results of the model are then compared to experimental transformation kinetics. Lastly, model predictions and limitations are discussed.

Contents

4.1	Adaptation of the Mixed-mode model	89
4.1.1	Theory	89
4.1.2	Numerical algorithm	91
4.1.3	Initial state and model parameters	92
4.2	Mixed-mode model <i>versus</i> experimental kinetics	94
4.2.1	Dependence of the kinetics with the mobility parameter M	95
4.2.2	Comparison with experiments	96
4.3	Discussion	100
4.4	Conclusion	102

4.1 Adaptation of the Mixed-mode model

4.1.1 Theory

When the temperature exceeds Ac_1 , austenite starts to form with a composition that may be different from the one of the parent phase. The mixed-mode model [SIE 04] [BOS 07] [BOS 09] [MEC 15] accounts for both C diffusion and the limited mobility of the sharp

ferrite/austenite interface due to drag of the Mn spike [QIU 15] [LAN 17]. In this mixed-mode model, the transformation is hence controlled by both C diffusion and interface mobility.

A schematic representation of the mixed-mode model is given in figure 4.1. Initially, at A_{c1} temperature and at time $t_0=0$, an equilibrium cementite/ferrite system is assumed. When the temperature exceeds A_{c1} , austenite becomes thermodynamically stable. At t_0 , it is assumed that cementite immediately transforms into austenite with the same composition (6.7 wt% of C). The initial austenite is therefore carbon super-saturated.

A 1D simulation cell of size z_M is considered. In this cell, the carbon content in austenite and ferrite phases is modeled according to Fick's equation:

$$\frac{\partial C_X^i}{\partial t} = D_X^i \frac{\partial^2 C_X^i}{\partial z^2} \quad (4.1)$$

with D the diffusion coefficient of carbon.

The limited interface velocity may generate carbon accumulation building up at the interface. The deviation from equilibrium induces a driving force ΔG to move the interface into the ferrite phase:

$$\Delta G = \chi(T) \left(C_C^{\gamma,int} - C_C^{\gamma,eq} \right) \quad (4.2)$$

where $C_C^{\gamma,int}$ and $C_C^{\gamma,eq}$ are the austenite carbon content at the interface and the LEMP C content at the interface, respectively. $\chi(T)$ is a temperature dependent parameter (unit: $\text{J}\cdot\text{mol}^{-1}\cdot\text{wt}\%^{-1}$) linking the transformation driving force ΔG and the carbon concentration $\Delta C = C_C^{\gamma,int} - C_C^{\gamma,eq}$.

The interface velocity (v) is proportional to this driving force (ΔG) via the mobility (M) of the interface:

$$v = M\Delta G \quad (4.3)$$

At an intermediate time t , the concentration profile is characterized by a gradient of carbon on the austenite side. The gap between the carbon concentration at the interface and at equilibrium highlights the coupling between diffusion-controlled and interface-controlled models.

The system evolves until the final state of the mixed-mode model (t_∞) characterized by the equilibrium in γ/α phases in terms of phase fraction and carbon composition.

As in the case of the $\gamma \rightarrow \alpha$ phase transformation, the degree of mixed-mode may be quantified by the mode parameter S [SIE 04]. For the reverse $\alpha \rightarrow \gamma$ transformation, the S parameter is expressed by the following equation:

$$S = \frac{C_C^{\gamma,int} - C_C^{\gamma,eq}}{C_C^{\gamma,\infty} - C_C^{\gamma,eq}} \quad (4.4)$$

with $C_C^{\gamma,int}$, $C_C^{\gamma,eq}$ and $C_C^{\gamma,\infty}$ austenite carbon contents respectively at the interface, at the thermodynamic equilibrium and far away from the interface (*i.e.* $z_M = 0$). When the S value is equal to 0, the transformation is considered to be diffusion-controlled while it is assumed to be interface-controlled for $S = 1$. The mode parameter is in the range $0 < S < 1$ in the case of mixed-mode transformation.

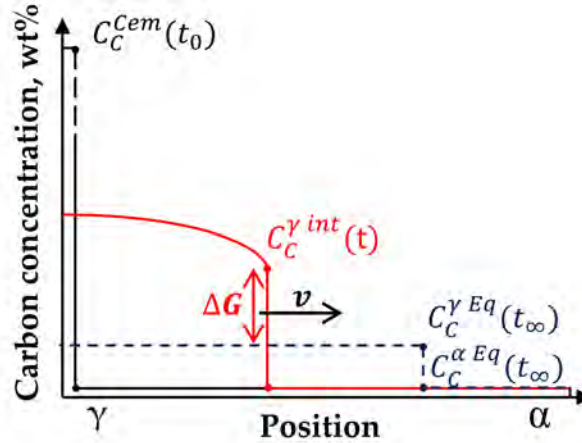


Figure 4.1: Schematic representation of the mixed-mode model system. Carbon concentration profiles are plotted at different times: the initial time t_0 , an intermediate time t and the infinite time when the γ/α equilibrium is reached t_{∞} . The interface velocity is evaluated as the deviation to the equilibrium by the relation $v = M\Delta G$ with $\Delta G = \chi(T) (C_C^{\gamma, int} - C_C^{\gamma, eq})$.

4.1.2 Numerical algorithm

The mixed-mode model is implemented for the cementite-ferrite to austenite transformation based on Mecozzi *et al.*'s method [MEC 15]. The problem is solved with an explicit finite-difference approach and sharp austenite/ferrite interface as schematized in figure 4.2. The green and blue meshing represent respectively the spacial integration at time t and $t + dt$. Between these two time steps, the interface has advanced of $dz^* = v \times dt$. The following nomenclature was established: classes are noted i , the interfacial class is noted i^* , phases (γ or α) are noted j , special grid length is noted δz_t^j . A step-by-step procedure is developed to combine diffusion-controlled model with interface mobility.

1. First, flux are calculated at each class i excepted the interface one (*i.e.* $J_{i^*,t}^j = 0$) according to first Fick's equation:

$$J_{i,t}^j = -D^j \times \frac{C_{i+1,t}^j - C_{i,t}^j}{\delta z_t^j} \quad \forall i \neq i^* \quad (4.5)$$

with D^j the carbon diffusion coefficient in the j phase.

2. Concentrations are updated for the next time step $t + dt$:

$$C_{i,t+dt}^j = C_{i,t}^j + (J_{i-1,t}^j - J_{i,t}^j) \frac{dt}{S \times \delta z_t^j} \quad \forall i \quad (4.6)$$

3. Calculation of the driving force ΔG for the interface mobility is performed:

$$\Delta G = \chi(T) (C_t^{\gamma int} - C_{Eq}^{\gamma}) \quad (4.7)$$

4. The interface velocity v is calculated and the interface is translated of dz^* :

$$v = M \times \Delta G \quad \implies \quad dz^* = v \times dt \quad (4.8)$$

5. Remeshing of the whole system:

$$C_{i,t+dt}^j = \sum_i \frac{C_{i,t+dt}^j}{\delta z_{t+dt}^j} (\delta z_t^j \cap \delta z_{t+dt}^j) \quad \forall i \quad (4.9)$$

6. The austenite interface composition $C_{t+dt}^{\gamma,int}$ is finally adjusted to respect the thermodynamic equilibrium at ferrite interface side (C_{Eq}^α):

$$\begin{cases} C_{t+dt}^{\alpha,int} = C_t^{\alpha,int} + (C_{i+1,t+dt}^\alpha - C_{Eq}^\alpha) \times \frac{\delta z_{t+dt}^\alpha}{\delta z_{t+dt}^\gamma} \\ C_{i+1,t+dt}^\alpha = C_{Eq}^\alpha \end{cases} \quad (4.10)$$

Time is incremented and the loop is repeated until equilibrium is reached. The model parameters are detailed in the next section.

4.1.3 Initial state and model parameters

The length of the system is set to $z_M=2 \mu\text{m}$, which corresponds approximatively to half the ferrite grain size. Initially, the system is defined by the thermodynamic equilibrium state at Ac_1 (675°C). Hence the two-phases, cementite and ferrite, are assumed at the initial time t_0 as schematized in figure 4.1. The length of cementite was set to 48 nm according to Thermo-Calc fraction (2.44 vol.%) and mass balance. The carbon is supposed at equilibrium: carbon concentration in cementite is equal to 6.7 wt% while that of ferrite is assumed equal to 0.005 wt%.

Above Ac_1 , cementite is supposed to transform immediately into austenite phase supposing fast dissolution of cementite as predicted by Gouné *et al.* [GOU 12]. The deviation from thermodynamic equilibrium is considered at the interface and controls system evolution through carbon diffusion and interface velocity. Contrary to Mecozzi *et al.* [MEC 15], the thermodynamic equilibrium is considered to occur through Local Equilibrium with Negligible Partitioning (LENP) condition for the $\text{Fe}_3\text{C} + \alpha \rightarrow \gamma$ transformation. While paraequilibrium assumes a constraint equilibrium where only C is at equilibrium, LENP supposes localized Mn redistribution at the interface (Mn spike). The LENP hypothesis seems to be more realistic because of the initially ferrite-cementite system before Ac_1 temperature. The Mn enrichment in cementite, pointed out by EDS, could promote short-range diffusion through the interface despite the slow diffusivity of Mn leading to a LENP condition. Besides, austenite volume fractions under LENP condition correctly describe the equilibrium states for 1 h holding treatment of prior recrystallized steels, as previously published [WEI 13] [CHE 14] [CHB 14] [LAI 16].

The LENP condition was previously illustrated on the 760°C-isothermal section of the ternary Fe-C-Mn system in figure 1.20 (chapter 1). The investigated composition is identified by a red star and the orthoequilibrium (ORTHO) tieline passing through this

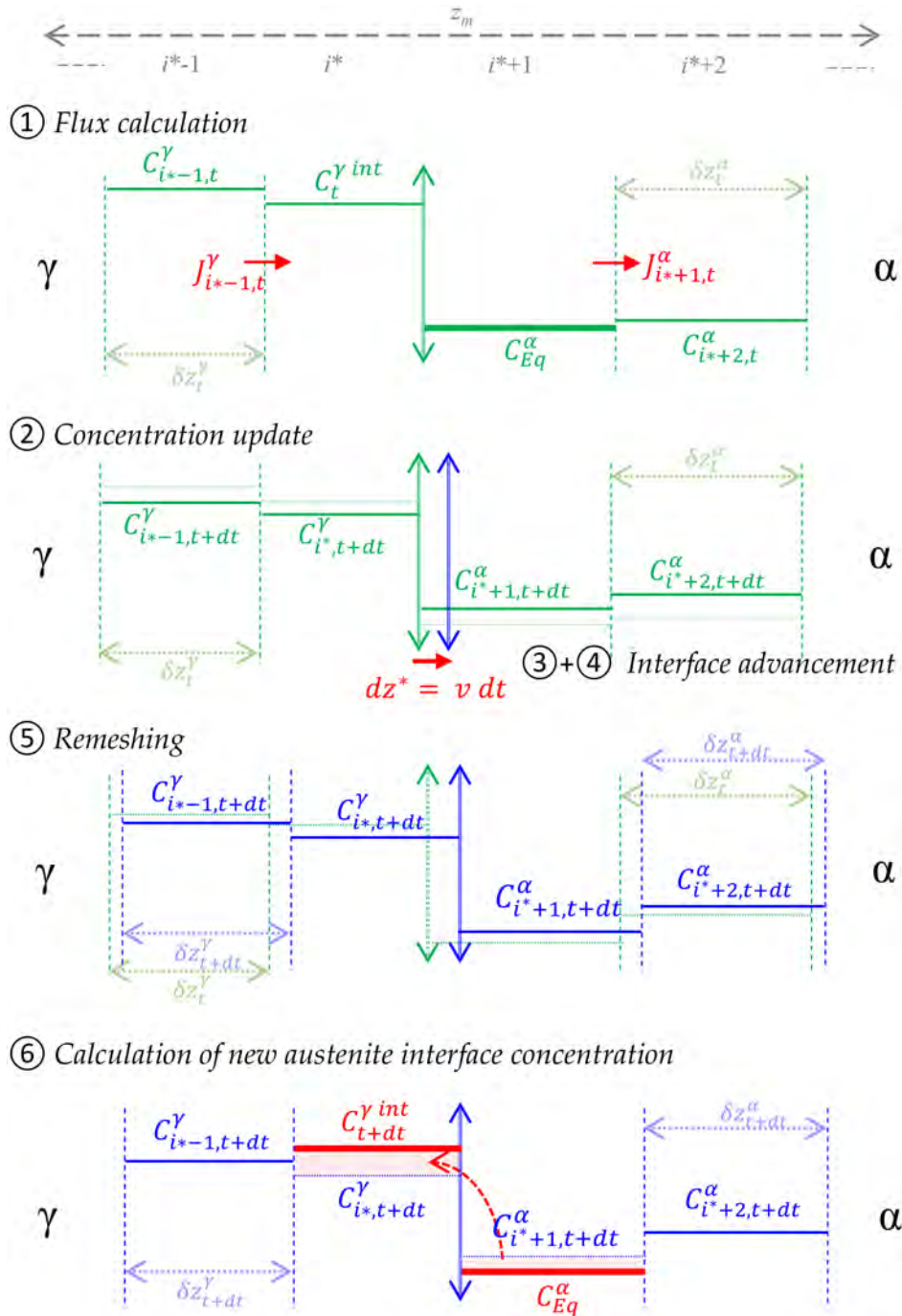


Figure 4.2: Schematic representation of the integration scheme for the austenite formation using the mixed-mode model (around the interface class noted i^*). The green and blue meshing respectively represent the special integration at time t and $t + dt$.

bulk composition is also reported. The local equilibrium (LENP) tieline corresponds to the one for which Mn composition in the newly formed austenite is equal to the Mn content of the parent phase. The final state of LERP condition is characterized by a flat carbon

profile in ferrite and in austenite and a Mn spike at ferrite/austenite. Associated carbon compositions in ferrite and austenite phases, according to LENP condition, are given in figure 4.3.

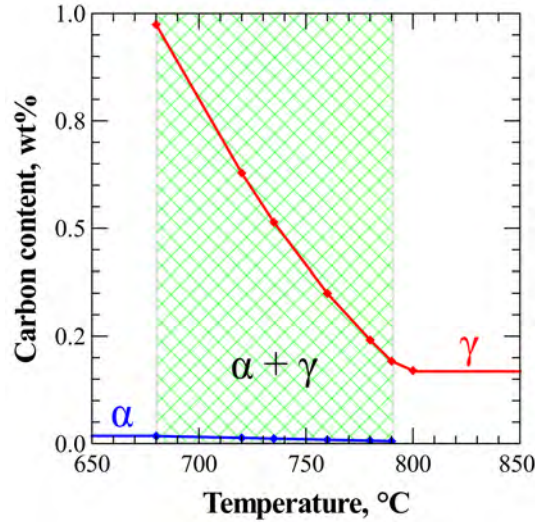


Figure 4.3: Carbon contents in α and γ phases for the nominal composition Fe-0.17C-1.763Mn wt% as a function of temperature assuming LENP condition (Thermo-Calc).

For the diffusion module, the carbon diffusivity was taken from Bhadeshia [BHA 06] with diffusion coefficients for: (i) ferrite equal to $Q_C^\alpha=80$ kJ/mol, $D_{oC}^\alpha = 6.2 \times 10^{-7}$ m²/s and (ii) austenite equal to $Q_C^\gamma=135$ kJ/mol, $D_{oC}^\gamma = 1.0 \times 10^{-5}$ m²/s.

For the interface velocity module, the $\chi(T)$ parameter involved in the driving force (ΔG) was expressed thanks to Thermo-Calc calculations as proposed by Mecozzi *et al.* [MEC 15]. Considering equation (4.2), $\chi(T)$ parameter was determined by the Gibbs energy G^γ of austenite as a function of carbon content C_C^γ and temperature. The $\chi(T)$ parameter is then derived by plotting $\frac{\partial G_C^\gamma}{\partial C_C^\gamma}$ as a function of the temperature as shown in figure 4.b. $\chi(T)$ was fitted by a polynomial function: $\chi(T) = 0.0238T^2 - 44.2420T + 131811$.

The mobility parameter M is considered as a fit parameter in this chapter. Because it represents the interfacial friction due to slow diffusivity of alloying elements, it is consequently difficult to evaluate.

4.2 Mixed-mode model *versus* experimental kinetics

The mixed-mode model was implemented for complex thermal cycles including heating and holding stages. The heating rate (R_H), annealing time and temperature are input parameters of the mixed-mode model.

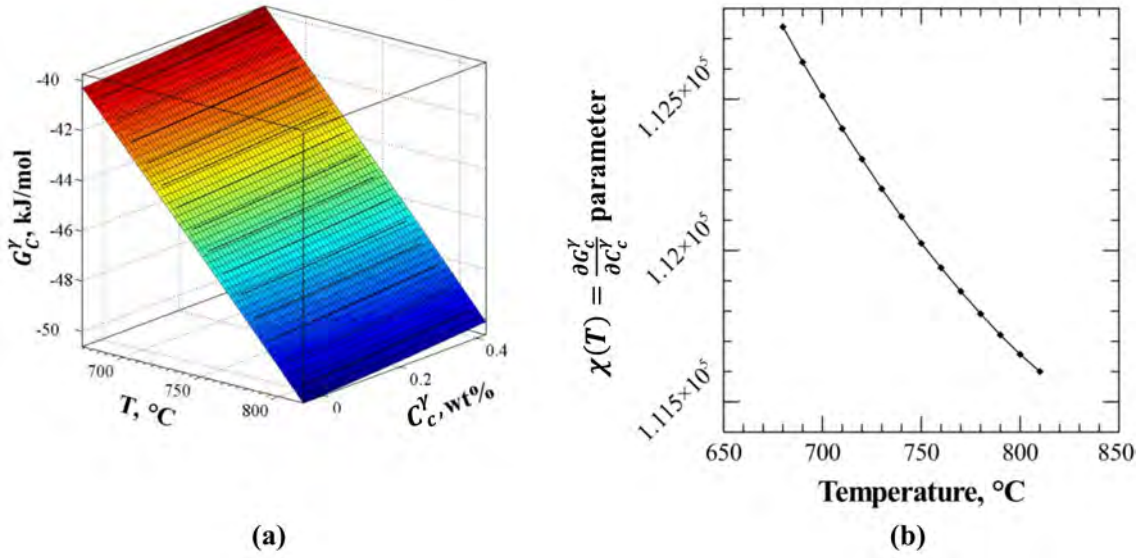


Figure 4.4: (a) Gibbs energy of the austenite phase as a function of temperature and carbon content (Thermo-Calc). (b) Representation of $\partial G_C^\gamma / \partial C_C^\gamma$ as a function of temperature to express $\chi(T)$ parameter of the equation: $\Delta G = \chi(T) (C_C^{\gamma,int} - C_C^{\gamma,eq})$.

4.2.1 Dependence of the kinetics with the mobility parameter M

Figure 4.5 illustrates the influence of the mobility parameter M in the mixed-mode model. The austenite formation kinetics was calculated at 760°C for three different values of the mobility: (i) $M = 7.4 \times 10^{-7} \text{ mol.m.J}^{-1}.\text{s}^{-1}$; (ii) $M = 10^{-8} \text{ mol.m.J}^{-1}.\text{s}^{-1}$ and (iii) $M = 10^{-12} \text{ mol.m.J}^{-1}.\text{s}^{-1}$ as shown in figure 4.5.a. The evolution of S parameter with transformation time is represented in figure 4.5.b. for the three mobility values. In addition, carbon evolution profiles in austenite and ferrite phases are plotted in figure 4.6.a, 4.6.b and 4.6.c respectively.

The highest mobility value ($M = 7.4 \times 10^{-7} \text{ mol.m.J}^{-1}.\text{s}^{-1}$, represented in blue colour) generates a quick austenite formation (less than 1 s). The associated S parameter is equal to 0 highlighting a diffusion-controlled mode. Interface motion is not restricted so that the kinetics is only controlled by carbon diffusion. That is reflected by the equality of carbon content at the austenite interface ($C_C^{\gamma,int}$) with the austenite equilibrium value ($C_C^{\gamma,eq}$) as shown in figure 4.6.a.

On the contrary for a limited mobility value ($M = 10^{-12} \text{ mol.m.J}^{-1}.\text{s}^{-1}$, represented in green colour), the phase transformation kinetics may be considerably delayed to longer holding times. In this case, the mode parameter S is equal to 1 meaning an interface-controlled transformation. The corresponding carbon profiles (figure 4.6.c) point out flat carbon profile in phases. Carbon diffusion is thus no longer controlling the kinetics; only the interface velocity drives the phase transformation. The deviation between equilibrium and interfacial austenite carbon content induces a driving force ΔG for interface motion.

An intermediate mobility value ($M = 10^{-8} \text{ mol.m.J}^{-1}.\text{s}^{-1}$, represented in red colour)

leads to a transformation kinetics between diffusion-controlled and interface-controlled kinetics as expected in the mixed-mode model. The S value is close to 0.5 indicating the coexistence of the diffusion and interface motion contributions in the kinetics of phase transformation. The carbon content at austenite interface evolves and decreases during the simulation (figure 4.6.b) highlighting an interface-controlled condition. Moreover, the curved carbon profile in austenite phase emphasizes the diffusion-controlled condition.

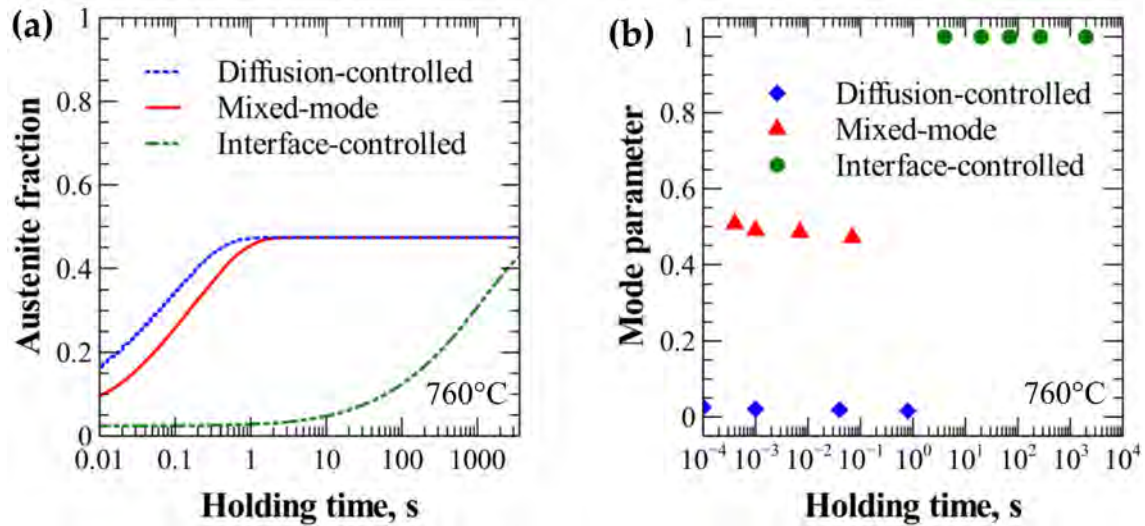


Figure 4.5: (a) Kinetics and (b) respective mode parameter S of austenite formation during isothermal holding at 760°C, for different conditions: diffusion-controlled ($M = 7.4 \times 10^{-7}$ mol.m.J $^{-1}$.s $^{-1}$), mixed-mode ($M = 10^{-8}$ mol.m.J $^{-1}$.s $^{-1}$) and interface-controlled ($M = 10^{-12}$ mol.m.J $^{-1}$.s $^{-1}$).

Based on the limited evolution of the mode parameter S at 760°C with transformation time (figure 4.5.b), the average mode parameter $\langle S \rangle$ was plotted as a function of the interface mobility in figure 4.7. Below a mobility of 10^{-10} mol.m.J $^{-1}$.s $^{-1}$, the mode parameter S is equal to 1 meaning that the transformation is governed by the interface motion. On the contrary, the transformed fraction is managed by the diffusion for mobility values above 7.5×10^{-7} mol.m.J $^{-1}$.s $^{-1}$. The mixed-mode model is thus possible in the case where the values of interface mobility (M) are between 10^{-10} and 7.5×10^{-7} mol.m.J $^{-1}$.s $^{-1}$ at 760°C.

4.2.2 Comparison with experiments

4.2.2.1 Typical industrial cycles: heating plus isothermal holding

The model was applied to describe the massive transformation on typical industrial cycles including heating stage followed by holding at the considered annealing temperature. The Q_m and M_0 parameters of the mobility were adjusted taking into account the experimental kinetics obtained with a heating rate of $R_H=5^\circ\text{C}/\text{s}$ and a holding at 735, 760 and 780°C.

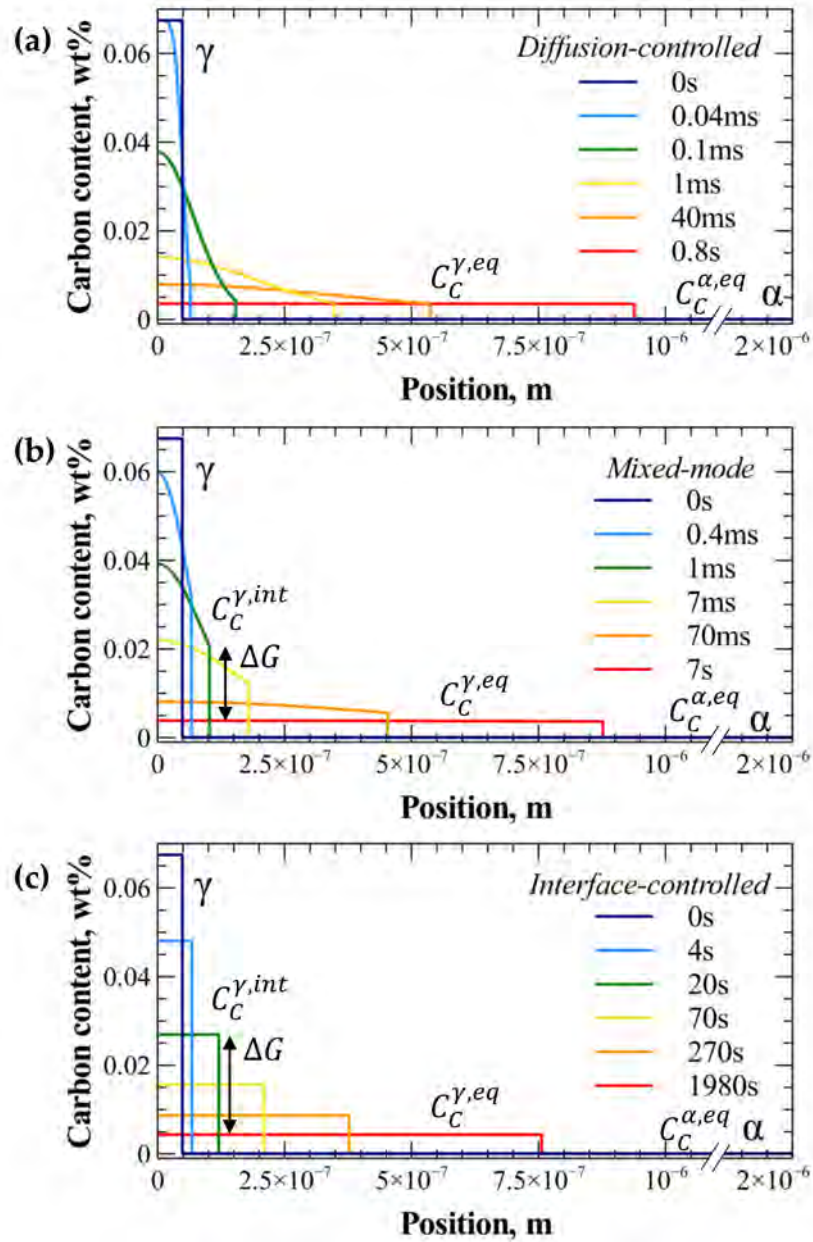


Figure 4.6: Carbon concentration profiles in γ/α phases during austenite formation at 760°C for different times. Three conditions are plotted: (a) diffusion-controlled ($M = 7.4 \times 10^{-7}$ mol.m.J $^{-1}$.s $^{-1}$), (b) mixed-mode ($M = 10^{-8}$ mol.m.J $^{-1}$.s $^{-1}$) and (c) interface-controlled ($M = 10^{-12}$ mol.m.J $^{-1}$.s $^{-1}$).

Figure 4.8.a presents the comparison between the mixed-mode model and the experimental austenite fraction during these complex cycles. The thermal cycles were also added in order to follow the temperature evolution during the heating step. As a reminder, the time scale starts when the temperature reaches $Ac_1=670^\circ\text{C}$.

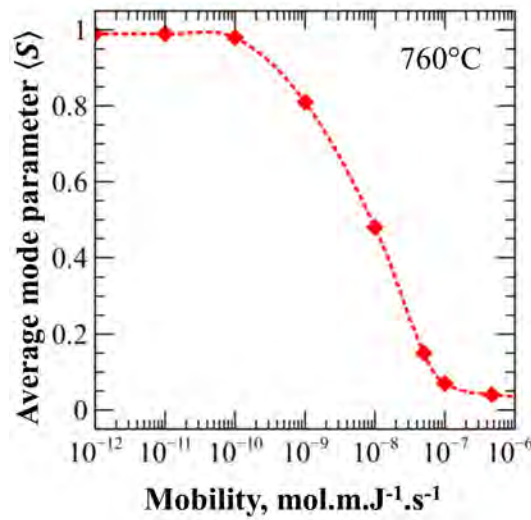


Figure 4.7: Evolution of the average mode parameter $\langle S \rangle$ as a function of the mobility value at 760°C.

The best description of the three experimental kinetics at 735, 760 and 780°C is obtained for $Q_m=900$ kJ/mol and $M_0 = 5 \times 10^{35}$ mol.m.J⁻¹.s⁻¹. The associated mobility value of M of the three studied temperatures are reported in table 4.1. As observed, the interface mobility is increased of a factor 10 raising up the temperature of 20°C. These parameters allow the austenite formation kinetics to be correctly described. Firstly, the model captures the thermal activation of the phase transformation. Increasing temperature leads to an acceleration of the transformation kinetics. Secondly, the equilibrium austenite fractions after 1 hour of holding are in agreement with experimental fractions thanks to the chosen LENP condition for the equilibrium carbon content in phases. Lastly, the model also describes the austenite formation occurring during the heating stage.

Temperature	735°C	760°C	780°C
Mobility parameter M , mol.m.J ⁻¹ .s ⁻¹	1.2×10^{-11}	1.6×10^{-10}	1.1×10^{-9}

Table 4.1: Interface mobility parameter M values at 735, 760 and 780°C considering $Q_m=900$ kJ/mol and $M_0 = 5 \times 10^{35}$ mol.m.J⁻¹.s⁻¹.

The parameter set was applied for 100°C/s heating rate ramp plus holding stage as shown in figure 4.8.b. The experimental kinetics are again well predicted using the same mobility parameters as for 5°C/s heating rate. The thermal activation and the final austenite fractions are in good agreement with experimental kinetics. Moreover, it can be noted that at high heating rate, less austenite is formed during the heating stage because there is less time for transformation to occur. This is particularly visible for the highest holding temperature (780°C) where 23% of austenite was formed during the heating stage at 5°C/s against less than 15% at 100°C/s. The transformation is then accelerated during the holding stage because more favourable sites remain.

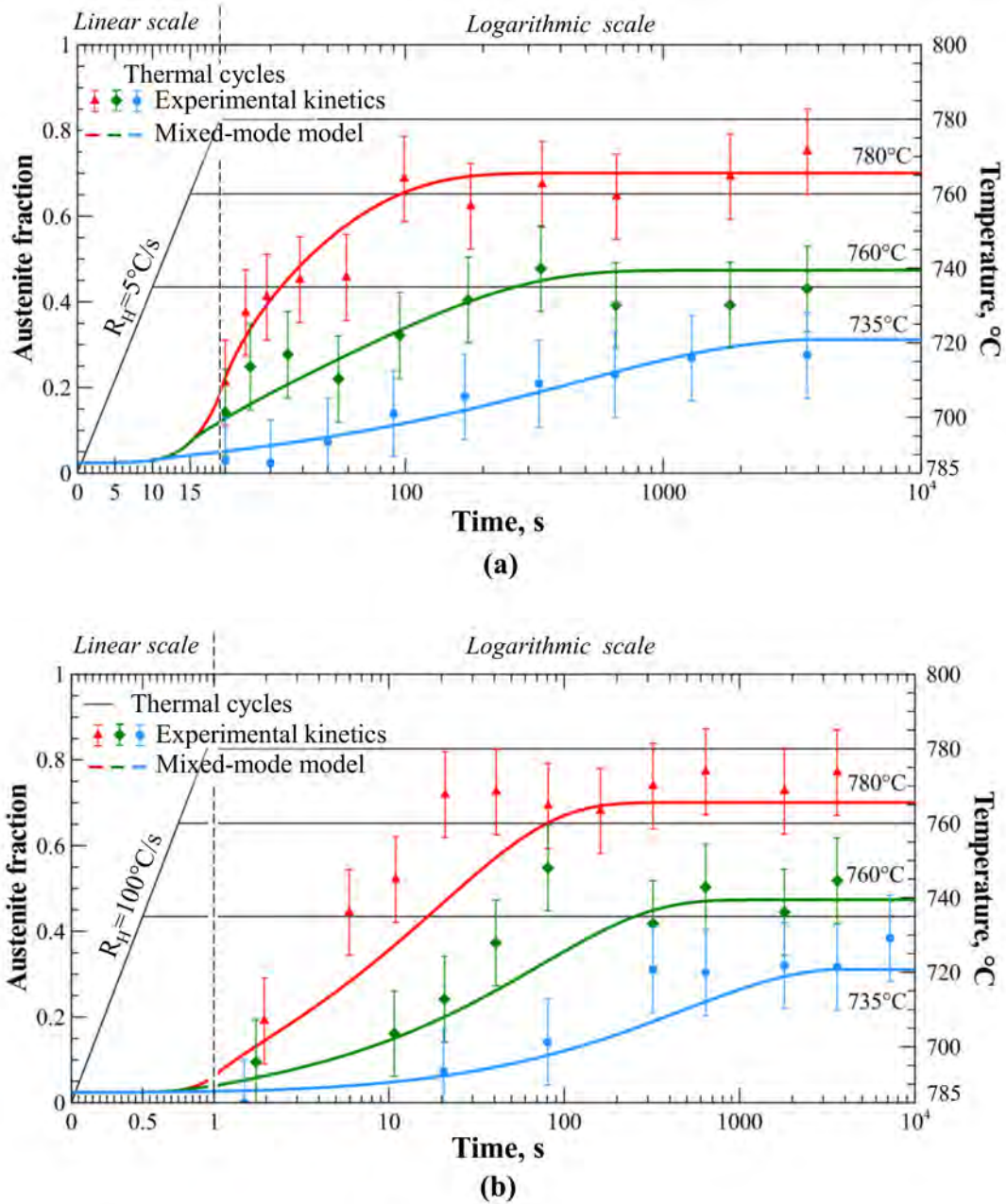


Figure 4.8: Experimental and mixed-mode model kinetics for austenite formation during isothermal holding after a heating stage of (a) 5 and (b) 100°C/s. Mobility parameters were fixed to $Q_m=900$ kJ/mol and $M_0 = 5 \times 10^{35}$ mol.m.J⁻¹.s⁻¹.

4.2.2.2 Non-isothermal cycles

Lastly, experimental and modelled non-isothermal kinetics were compared for different heating rates (5, 7.5, 10 and 30°C/s) in figure 4.9. Mobility parameters are the same

as for heating and isothermal holding conditions. Model correctly describes both (i) the shape of the first 80% of transformation and (ii) the kinetics shift due to the increase in the heating rate. Above 80% of transformation, the model does not capture the saturation effect, characteristic of phase transformation, where the last part to transform is usually the part with the lowest driving force (*i.e.* due to chemical inhomogeneity).

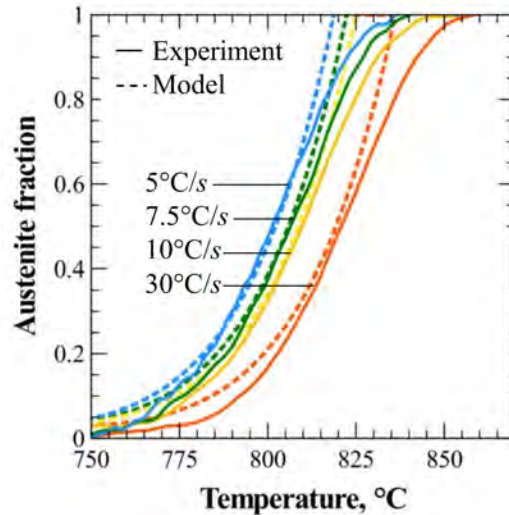


Figure 4.9: Experimental and mixed-mode model kinetics for austenite formation during continuous heating with a heating rate of 5, 7.5, 10 and 30°C/s. Mobility parameters were fixed to $Q_m=900$ kJ/mol and $M_0 = 5 \times 10^{35}$ mol.m.J⁻¹.s⁻¹.

4.3 Discussion

The mixed-mode model proposes a fairly good description of experimental phase transformation kinetics in complex industrial cycles including heating and holding stages. Same mobility parameters were used to predict the ferrite-to-austenite transformation for two different heating rates (5 and 100°C/s) and three annealing temperatures (735, 760 and 780°C). The mobility parameters were fixed to $Q_m=900$ kJ/mol and $M_0 = 5 \times 10^{35}$ mol.m.J⁻¹.s⁻¹.

It has to be noted that the so-called activation energy for mobility, Q_m , is very high and can not be associated with any physical event. With M_0 , they provide a convenient description of the friction force applied to the interface. This slowing down of the interface may be attributed to the Mn diffusion and segregation across the interface as experimentally highlighted in the quaternary system Fe-C-Mn-Si by Qiu *et al.* [QIU 15]. In the literature, Q_m is commonly fixed to 140 kJ/mol [BOS 07] [MEC 15] [CHE 16a] as the typical activation energy for grain-boundary process. The present value for Q_m is considerably higher than the one commonly used but three points should be pointed out: (i) to our knowledge, published mixed-mode model kinetics compared to experimental kinetics are relatively scarce even for the $\gamma \rightarrow \alpha$ transformation [SIE 04] [BOS 07] [BOS 09] while for the $\alpha \rightarrow \gamma$ transformation no comparison was realized [MEC 15]. It

can be supposed that the activation energy for interface mobility is not only linked to grain-boundary but also to the slow diffusion of alloying elements which may contribute to interface mobility due to a solute drag effect [QIU 15]; (ii) Despite large differences between literature and used mobility parameters (Q_m and M_0), the final M value may be compared to published data. High mobility values were reported: Mecozzi *et al.* [MEC 15] used mobility between $[1.5 \times 10^{-8} - 7.6 \times 10^{-9}]$ mol.m.J⁻¹.s⁻¹ in the temperature range of 700 and 800°C; in the same way, Sietsma *et al.* [SIE 04] used a mobility of 5.4×10^{-8} mol.m.J⁻¹.s⁻¹. On the contrary, Bos *et al.* [BOS 07] used more limited mobility values, in the range of $[7.8 \times 10^{-14} - 4.2 \times 10^{-15}]$ mol.m.J⁻¹.s⁻¹ for the reverse transformation in the temperature range of 650-830°C. The present mobility varies in a broader range of $[7.6 \times 10^{-9} - 2.4 \times 10^{-13}]$ mol.m.J⁻¹.s⁻¹ for temperature in between 700-800°C. The broader mobility range is linked to the higher activation energy Q_m which allows the thermal activation for the experimental kinetics to be captured; (iii) Finally, it is well known that the experimental evaluation of Q_m is a long-standing problem [WIT 00].

The present mobility range (above $7.6 \times 10^{-9} - 2.4 \times 10^{-13}$ mol.m.J⁻¹.s⁻¹) points out limited mixed-mode character due to the S value above 0.8 as shown in figure 4.7. Using such mobility parameter, the transformation is mainly interface-controlled. It suggests a transformation strongly dependent on Mn diffusion so that the interface motion is delayed to account for its slow diffusion. However, the mixed-mode character may be observed in the case of quick heating rate where carbon has less time to diffuse as shown in figure 4.10. Curves showing the austenite carbon profiles observed at 800 and 825°C account for diffusion condition in superposition on top of interface motion.

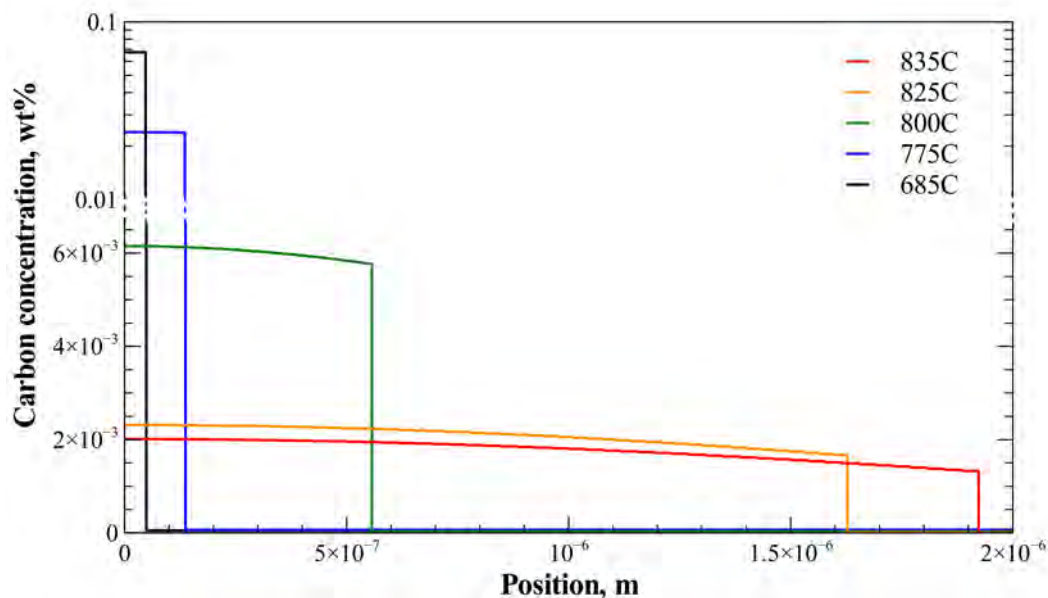


Figure 4.10: Evolution of the carbon evolution profile during a heating at 30°C/s interrupted at different temperatures between 685 and 835°C. Mobility parameters were fixed to $Q_m=900$ kJ/mol and $M_0 = 5 \times 10^{35}$ mol.m.J⁻¹.s⁻¹.

The mixed-mode model is relevant to obtain more fundamental formulations and de-

scription of complex system. It enables to take into account the role of multiple substitutional alloying elements. The diffusion and segregation of elements at the interface are indeed difficult to model. Hence, the interface mobility is an easy way to describe complex system. An artificial mobility value enables to account for the slow Mn diffusion. Such simple tool allows to overpass many difficulties of the modeling of multi-component systems: (i) the determination of operative tie-lines is far from being straightforward, especially when the diffusivity contrast between fast and slow diffusing element is so high; (ii) the initial distribution repartition of some element such as Mn has a great influence on the transformation kinetics and such a modeling would require the precise knowledge of the initial microstructure; (iii) the solute drag and the mobility of the interface do certainly slow down the motion of the interface (even if one cannot determine to which extent). The mixed mode model proposes a framework accounting for such complex phenomena.

The model captures with good accuracy the kinetics of the massive transformation on complex cycle including heating and holding stages.

Note that the mixed-mode model is not self-sufficiency as the mobility parameter needs to be adapted as a function of steel chemistry. Q_m and M_0 are indeed adjustable parameters. Due to these simplified assumptions, the mixed-mode model cannot capture some physical features such as cementite enrichment in Mn that may drastically change the transformation kinetics [WEI 13] [LAI 16].

However, the mixed-mode model, as presented in this chapter can be seen as an intermediate stage between purely descriptive JMAK approaches and heavy thermodynamical multicomponent diffusion calculations (*e.g.* DICTRA). With two fitting parameters, it allows to describe all experimental observations: (i) equilibrium is not orthoequilibrium, but close to LENP, where the forming phase has the same composition as the parent phase; (ii) transformation kinetics are described with a relatively good accuracy; (iii) the effect of the heating rate is also correctly accounted for.

Finally, this model can be seen as a reasonable tool for describing the phase transformations occurring during heating of DP steels in conditions that are typical of industrial production lines. The quickness of calculations could also permit to use such a tool to control and optimize the different parameters of the production line.

4.4 Conclusion

A mixed-mode model was proposed to describe the austenite formation kinetics in a microstructure combining a mixture of ferrite and spheroidized cementite before annealing (ReX-steel). The model is based on carbon diffusivity and interface mobility. The main originalities of the present model are : (i) the LENP conditions (analogue to $\gamma \rightarrow \alpha$ transformation) seem to apply, and; (ii) a unique mobility set (Q_m and M_0) was fixed and validated for all the experiments either in isothermal or non-isothermal conditions. Such model seems to be relevant to describe the austenite formation even with complex chemistry, as generally used in industrial steel, because it globally considers the effect of multiple alloying elements. However, the model does not take into account the effect of one particular element (*e.g.* Mn enrichment of cementite), which could play a predominant role in the transformation kinetics [GOU 12]. While the adjustment of mobility parame-

ters is required, such model is a positive step in modeling phase transformations of alloys with a complex chemistry based on some physical basis.

Ternary Fe-C-Mn diffusive model for austenite formation

Previously developed models (based on JMAK laws and the mixed-mode model) were implemented adjusting some parameters on experimental results (ex. b_0 , M). They are consequently not directly transposable to other steels with different carbon or manganese contents. This chapter aims at modeling the austenite formation kinetics using a model with more physical basis to answer to standalone expectations. The austenite formation was therefore described based on the diffusive character of the phase transformation with the commercial software DICTRA, which is the diffusive module of Thermo-Calc.

In a first step, the representative system is detailed with the objective to choose realistic simulation conditions in agreement with the microstructure. Secondly, an investigation on DICTRA options was performed to get a better understanding of DICTRA capacities and evaluate the effect of each option. DICTRA was finally applied to describe the experimental kinetics of austenite formation at 735, 760 and 780°C of the ReX-steel and the CR-steel (already presented in chapters 3 and 4).

Contents

5.1	DICTRA simulation conditions	106
5.1.1	Definition of a representative system	106
5.1.2	Preliminary study: investigation of DICTRA options	108
5.2	Influence of microstructural parameters	113
5.2.1	System size	113
5.2.2	Cementite's Mn content	114
5.3	Application to austenite formation kinetics on the ReX-steel and on the CR-steel	122
5.3.1	Influence of Mn content in cementite	122
5.3.2	Influence of the representative size	125
5.4	Discussion	125
5.4.1	DICTRA applications to model the austenite formation	125
5.4.2	Others concomitant phenomena	128

5.1 DICTRA simulation conditions

In order to model the kinetics of austenite formation with the best accuracy, a particular care was dedicated to the choice of a representative simulation state. Number of hypotheses were done in order to simplify the industrial and complex microstructure studied in this PhD-work. Choices will be presented, justified and discussed all along this chapter.

5.1.1 Definition of a representative system

Elements and phases

Austenite formation was modeled using the thermodynamic TCFE8 [THE] and mobility MOBFE3 [DIC] databases of Thermo-Calc software. The complex chemistry of the investigated steel was simplified to that of the ternary Fe-0.17C-1.763Mn (wt%) system with cementite, ferrite and austenite phases assessed in these databases.

It has to be noted that higher order systems (*i.e.* number of diffusive elements superior to three) may be defined using DICTRA but predictions are based on extrapolation of binary, ternary and some pre-defined higher order systems (C-Cr-Fe-N-Ni and C-Cr-Fe-Ni) into multicomponent space of data according to the CALPHAD method [DIC]. Multicomponent systems may therefore be less accurate due to deviations coming from data extrapolations or also due to different missing parameters in the database. It was thus chosen to limit elements to a ternary system in order to be confident in the used thermodynamic and mobility databases. Moreover, C and Mn elements are known to be major elements in the austenite formation of Fe-C-Mn systems containing other alloying elements in lower proportion (such as Cr, Si ...) [SPE 81] [SAV 07] [SAV 09] [KIR 73]. The diffusion of the other elements is not considered to drive the phase transformation because their weight fractions are lower and their diffusivities are quicker than that of Mn element. Besides, such system enables to take into account the presence of cementite which may have a preponderant role in austenite formation [ATK 94] [GOU 12]. The initial microstructure, composed of ferrite and cementite before any heat treatments, is thus kept.

Geometry and characteristic lengths

Based on the austenite formation knowledge from the literature and the experimental characterization of chapter 3, several systems may be explored to study austenite formation (figure 5.1):

- (i) *Austenite growth within ferrite bands* may be adopted with a characteristic system size equal to the half-length of ferrite grains. Such system enables to model cementite dissolution and austenite growth inside ferrite bands in a linear geometry.
- (ii) *Dissolution of cementite lamellae* may be modeled supposing austenite formation at the cementite/ferrite interface of pearlite lamella. This problem may be treated considering linear system of size equal to the half-length of interlamellar pearlite

- spacing. Due to the small size of the system, austenite quickly forms so that the global austenite formation kinetics may not be managed by pearlite dissolution.
- (iii) *Isolated cementite dissolution* may also be modeled with DICTRA using spherical geometry and fixing carbide size. Such configuration is scarce in the investigated system as carbides are rarely homogeneously dispersed even in the ReX-steel where bands of cementite particles persist.
 - (iv) *Austenite growth inside ferrite grains* may be treated with a spherical geometry supposing austenite nucleation at cementite area and growth inside ferrite grains. However, this latter configuration is debatable as cementite is not uniformly spread along ferrite grain boundaries.

Each proposed system is likely to be involved in austenite formation. However, it was supposed that the global austenite formation kinetics is driven by the austenite growth within ferrite bands. Indeed the dissolution of pearlite lamellae is faster as the characteristic length of the system is shorter (100-300 nm against 5-10 μm). The dissolution of isolated Fe_3C islands was also excluded because carbide islands are not homogeneously distributed. The microstructure is composed of cementite bands (due to solidification and rolling) rather than dispersed cementite islands as modeled by Lai *et al.* [LAI 14] [LAI 16]. Lastly, the spherical austenite growth inside ferrite grains was not treated because carbide particles are not homogeneously distributed at ferrite grain boundaries in the investigated microstructure.

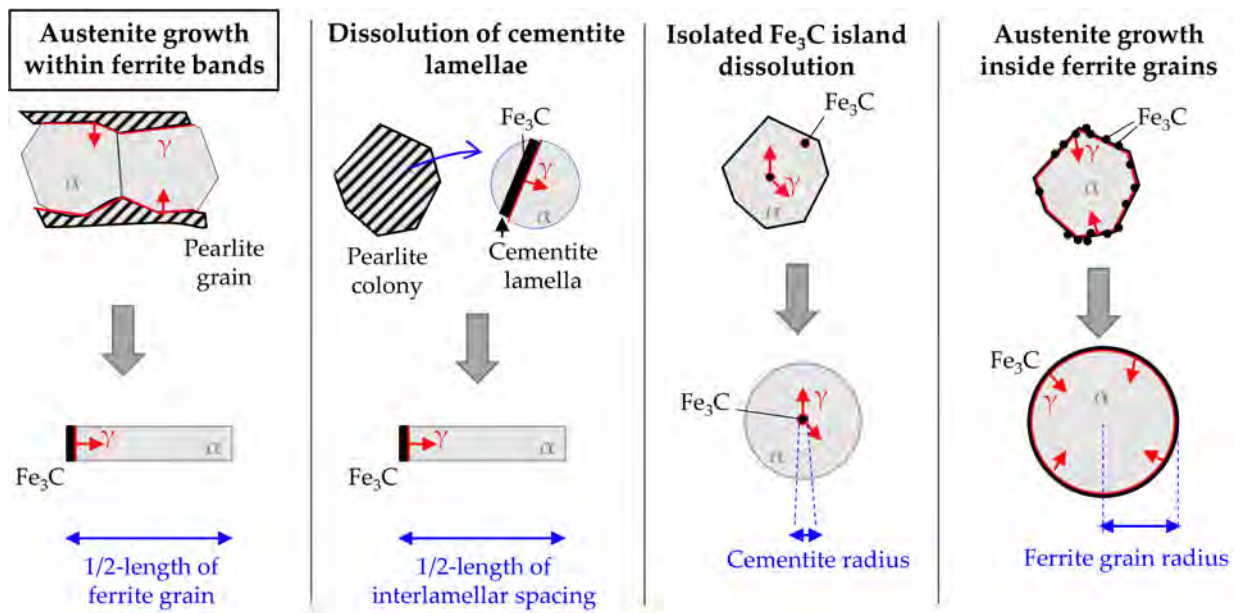


Figure 5.1: Schematic representation of four different modeling configurations: (i) austenite growth within ferrite bands; (ii) cementite lamella dissolution, (iii) isolated carbide dissolution and (iv) austenite growth inside ferrite grains.

A linear geometry, illustrated in figure 5.2, was adopted for austenite formation. The austenite phase was supposed to form at the cementite/ferrite interface. The total system

size (z_m) was chosen to represent half of the ferrite grain size which may vary between 5 and 10 μm according to microstructure observations (chapter 2). Cementite size was hence adjusted to respect its thermodynamic equilibrium fraction at 670°C (temperature just below Ae_1) equal to 2.44% (vol.). Two choices are possible for the austenite phase in the initial configuration:

- “Active” austenite: Austenite exists in the initial state as a thin layer (with a width of 1 nm) compared to cementite and ferrite dimensions.
- “Inactive” austenite: Austenite phase is not present at the initial state and its nucleation will be initiated when the driving force for precipitation exceeds a pre-defined positive value ($10^{-5} \times RT$, J/mol, where R is the gas constant and T the temperature).

Both configurations for austenite phase are compared in part 5.1.2.

Phase chemistry

C and Mn concentrations had to be defined in the initial state. As carbon is a fast diffusive element, it was supposed that carbon is at thermodynamic equilibrium in cementite and ferrite. Carbon contents were thus fixed at $C_C^{Fe_3C} = 6.7 \text{ wt}\%$ in cementite and $C_C^\alpha = 6.683 \times 10^{-3} \text{ wt}\%$ in ferrite. This corresponds to equilibrium carbon value at 670°C. It was thus supposed that carbon element is at equilibrium after the hot-rolling and the consecutive coiling at 630°C.

Manganese content in cementite was imposed from EDS analyses for carbides (*i.e.* $C_{Mn}^{Fe_3C} = 13 \text{ wt}\%$ for the ReX-steel and $C_{Mn}^{Fe_3C} = 10 \text{ wt}\%$ for the CR-steel). The corresponding Mn content in ferrite (C_{Mn}^α) was then adjusted from a mass balance.

In the case of “active” austenite phase, C and Mn contents of the austenite nuclei were set as bulk composition (*i.e.* $C_C^\gamma = 0.17 \text{ wt}\%$ and $C_{Mn}^\gamma = 1.763\%$). Composition of austenite phase will spontaneously tend towards equilibrium values at first simulation times.

Table 5.1 summarizes C and Mn concentrations of ferrite, cementite and austenite used in DICTRA simulations of austenite formation. Characteristic lengths of each phase are also reported.

Phase (i)	C_C^i	C_{Mn}^i	Characteristic length
Ferrite	$6.683 \times 10^{-3} \text{ wt}\%$	[10-13 wt%]	z_m [5-10 μm]
Cementite	6.7 wt%	mass balance	mass balance
Active austenite	0.17 wt%	1.763 wt%	1 nm

Table 5.1: C and Mn concentrations and characteristic length of ferrite, cementite and austenite used in DICTRA simulations of austenite formation.

5.1.2 Preliminary study: investigation of DICTRA options

Before going further in DICTRA simulations, a preliminary study was realized in order to get a better understanding of the influence of DICTRA options for diffusive simulations. To get a better appreciation of this investigation, a complete example of a typical DICTRA

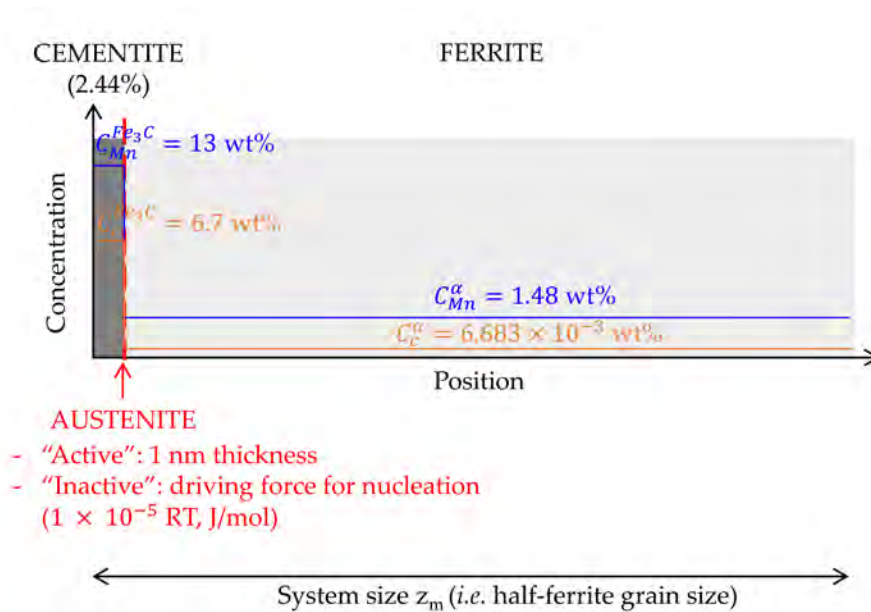


Figure 5.2: Initial state of the DICTRA simulation system used for modeling austenite formation in a cementite–ferrite microstructure.

script for austenite formation is commented in appendix E. In this section, major possible options proposed in DICTRA software are tested to describe the austenite formation on a system containing 14 wt%Mn in cementite. The representative system length was fixed at 6 μm .

The influence of four items on austenite formation kinetics were investigated:

1. the austenite nucleation (*i.e.* “active”/ “inactive” phase);
2. the grid spacing: number of divisions of each region;
3. the option of calculation under either “activities” or “potentials” hypothesis (these two options are integration options rather than physical options);
4. the implicit degree: the value 0 corresponds to so-called Euler forwards (explicit), 0.5 is associated to trapezoidal rule and 1 is the Euler backwards (implicit) useful when large fluctuations occur in the profiles;

Figure 5.3 compares the impact of various DICTRA options on the austenite formation kinetics. A reference state is defined supposing the austenite nucleation in a linear geometry as defined in the scheme of figure 5.2. Calculations were realized varying activities and with an implicit degree fixed at 1 (*i.e.* implicit condition).

All previous item were tested. Different parameters were changed step-by-step: 1/ suppressing only austenite nucleation, austenite is hence initially defined as a thin phase of 1 nm thickness between cementite and ferrite; 2/ using a spatial grid twice finer; 3/ varying potentials rather than pre-defined activities; and finally 4/ imposing the implicit degree equal to 0.5 (trapezoidal scheme).

Numerical parameters

Strong dependence with the DICTRA simulation parameters is pointed out by the two distinct austenite formation kinetics obtained with this parametric study. Kinetics identical to that of the reference state are obtained passing from activities to potentials (3/) or also changing the implicit degree from 1 to 0.5 (4/). Such parameters are indeed numerical parameters influencing the stability of the calculations. On the contrary, a kinetics quicker than that of the reference state is obtained with a finer spatial grid (2/) and it superimposes with the kinetics obtained when austenite nucleation is not taken into account (1/).

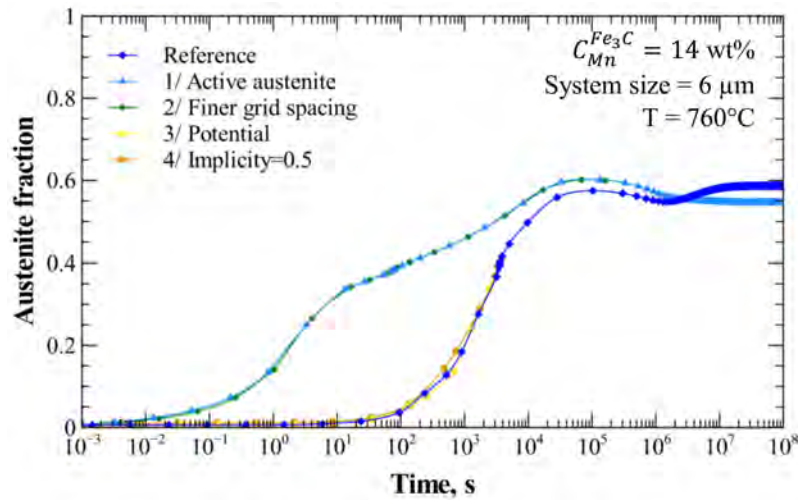


Figure 5.3: Study of the influence of the different DICTRA capabilities on the austenite formation kinetics during an isothermal holding at 760°C of a steel containing 14 wt%Mn in cementite (system size fixed at 6 μm).

In addition, it may be noted that the final ORTHO austenite fractions appear to be different according to the chosen simulation parameters. The global deviation is of the order of 4% and was attributed to DICTRA calculations leading to a loss of mass.

Austenite nucleation

Austenite formation kinetics with nucleation is investigated. It is recalled that the nucleation in DICTRA is dealt by the overrun of the precipitation driving force by a predefined value (usually $10^{-5} \times RT$). Figure 5.4 presents the influence of (a) the system size and (b) the Mn enrichment in cementite considering austenite nucleation at the cementite/ferrite interface. In these two sub-figures, the system size and the Mn enrichment in cementite are gradually increased.

Two austenite formation regimes are observed by simply modifying the system size: austenite starts to grow around 10^{-2} s on system sizes inferior to 5.5 μm while 1 s of holding is required for larger systems. An unexpected brutal transition was revealed passing from 5.5 to 5.75 μm system size.

Identically, abrupt transition appears by changing the Mn enrichment in cementite:

austenite forms much earlier for Mn content between 2 and 13 wt% compared to kinetics obtained with 14 or 15 wt%Mn in cementite.

Such discrepancies with system size and Mn enrichment suggest incoherencies considering austenite nucleation. As the transformation is driven by diffusion, a progressive transition is expected.

Moreover, when austenite nucleation is considered, it seems necessary to refine strongly the grid spacing (see figure 5.3). Namely, finer grid spacing and initially present austenite (“active”) lead to the same result. In the following, due to the above mentioned difficulties, austenite nucleation was not considered and a thin austenite layer between cementite and ferrite was defined in the initial state (hypothesis of “active” austenite).

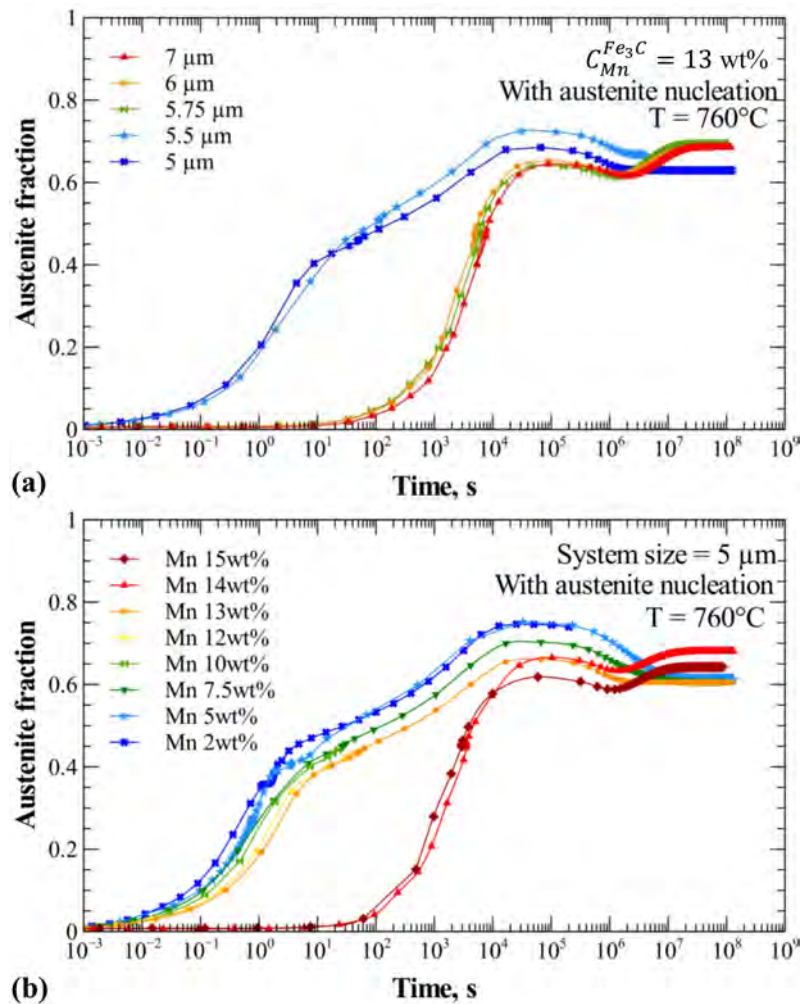


Figure 5.4: Study of the influence of the austenite nucleation on the austenite formation kinetics during an isothermal holding at 760°C varying (a) the system size and (b) the manganese enrichment in cementite.

System geometry

Lastly, the austenite formation kinetics was modeled using a spherical geometry as illustrated in figure 5.5.b. The initial system radius R_{Tot} was fixed equal to $6 \mu\text{m}$ and the associated cementite radius R_{Fe_3C} was found to be equal to $1.74 \mu\text{m}$ based on the relation:

$$f^{Fe_3C} = \frac{R_{Fe_3C}^3}{R_{Tot}^3} \quad (5.1)$$

It should be noticed that the calculated cementite radius is no longer in accordance with the microstructural observations (figure 2.1 and 2.2, chapter 2) where cementite particles were found to have a radius lower than 300 nm (both for the CR-steel and the ReX-steel). Inversely fixing cementite radius at 300 nm , the total system radius is found to be equal to $1.034 \mu\text{m}$ which appears relatively small compared to characteristic lengths of ferrite grains. Such spherical geometry is rather well adapted for systems with dispersed islands of cementite in a ferrite matrix.

The austenite formation kinetics is compared in figure 5.5.a. gathering the linear and spherical geometry. In both cases, austenite nucleation was not taken into account. The austenite fraction in the spherical configuration is calculated thanks to the equation:

$$f^\gamma = \frac{R_{Upper-\gamma}^3 - R_{Lower-\gamma}^3}{R_{Tot}^3} \quad (5.2)$$

The austenite formation kinetics with a spherical geometry is composed of three stages, as in the case of the linear geometry, but the austenite fractions and time scales are significantly different compared to the kinetics obtained with linear geometry. Such discrepancies were mainly attributed to the spherical resolution of Fick's equations. In spherical geometry, exchange surface is increased (*i.e.* sphere envelop) so that the diffusion is increased accelerating thus the austenite formation for long holding times.

Finally, it should be noted that the ORTHO austenite fractions differ of 8% with these two configurations.

Recommendations

To conclude these preliminary works relative to the DICTRA options, a feedback is proposed to use the Thermo-Calc diffusion module.

At first, the system geometry may strongly influence the phase transformation kinetics as the exchange surface is larger in spherical geometry compared to the linear one. It is therefore recommended to carefully choose the system geometry in accordance with the microstructure. The spacial grid appears also to be a critical parameter in DICTRA simulations. It is thus recommended to confirm the spacial grid independence (reducing the grid, for example).

Secondly, based on these preliminary investigations, it is suggested to limit the use of the phase nucleation and to prefer a thin layer of the newly formed phase present at the initial state. The criterion for phase nucleation seems to be dependent on phase composition and system size and it induces a loss of the phase transformation diffusive character pointed out by a brutal transition between two regimes.

Lastly, activities/potentials and implicit degree options appear to have no consequences on the results as they mainly drive the calculation stability. Activities/potentials

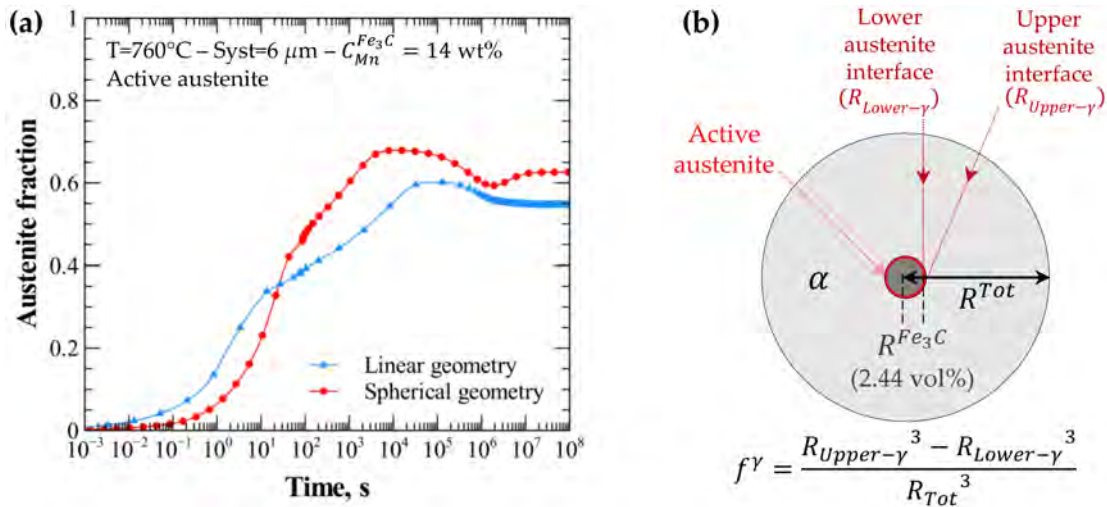


Figure 5.5: (a) Comparison of the austenite formation kinetics for the linear geometry and for the spherical geometry. (b) Schematic representation of the spherical geometry.

option may be varied to ensure the complete calculation. Moreover, an implicit degree equal to 1 should also be preferred because it handles more often strong fluctuations.

5.2 Influence of microstructural parameters

After having studied the influence of DICTRA options, the software was used to describe the kinetics of austenite formation during an isothermal holding at 760°C . The influence of microstructural parameters was investigated: (i) the influence of the representative system size was first analysed and (ii) the impact of the manganese enrichment in cementite was then considered.

Following calculations presented in this chapter are realized under linear geometry, without austenite nucleation, using an implicit resolution method and with activity variations.

5.2.1 System size

The austenite formation kinetics was calculated during an isothermal holding at 760°C of an initial ferrite-cementite microstructure with a manganese content equal to 14 wt% in cementite. Different kinetics were obtained by varying the system length from 5, 10, 100 and $1000\ \mu\text{m}$ as shown in figure 5.6.

The size of the representative system modifies the time scale of the transformation: the austenite formation is quicker with a smaller system. Compared to the case where the austenite nucleation was considered, the transformation is progressively shifted when the system size is changed. It confirms the expected diffusive character of the transformation. System size may therefore be an adjustable parameter within the range of experimental characteristic size in order to shift the kinetics of the modeled microstructure.

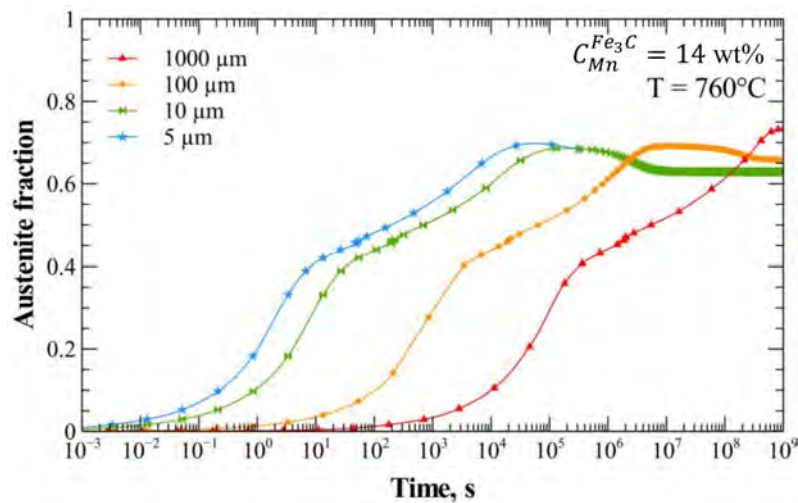


Figure 5.6: Influence of the system size on the austenite formation kinetics at 760°C considering 14 wt%Mn in cementite. Four system lengths are compared: 5, 10, 100 and 1000 μm .

5.2.2 Cementite's Mn content

In a second step, the influence of the Mn content in cementite on austenite formation kinetics was investigated varying the Mn content from 10 to 30 wt% (figure 5.7). Modeling was performed at 760°C on a linear system with a size of 6 μm .

The austenite formation kinetics is progressively shifted to higher time scales with an increase in the Mn content in cementite. Moreover, two types of austenite kinetics may be distinguished as a function of the Mn content in austenite and it will be described in the next sections.

5.2.2.1 Low-Mn enrichment in cementite ($C_{Mn}^{Fe_3C} < 15 \text{ wt}\%$)

The cementite enriched at 10 wt%Mn was chosen as the low-Mn enrichment system. C and Mn concentration and activity profiles as a function of the global distance are reported in figure 5.8 for different holding times at 760°C: 0, 0.1, 1, 10^2 , 10^3 , 10^4 , 10^5 , 10^6 , 10^7 and 3×10^7 s. A better understanding of austenite formation mechanisms is possible thanks to a correlation between concentration and activity profiles and the shape of austenite formation kinetics.

Stage 1: Austenite formation controlled by C-diffusion ($10^{-2} \text{ s} < t < 10 \text{ s}$)

First, a significant C activity gradient is observable in the newly growing austenite grain for times inferior to 10 s (figure 5.8.c) highlighting an austenite formation stage controlled by C-diffusion. The C diffusion in austenite was validated by the C concentration gradient in austenite for holding times of 0.1, 1 and 10 s (figure 5.8.a).

In addition, the absence of Mn activity gradient either in the newly formed austenite or ferrite (figure 5.8.d) confirmed that the Mn diffusion is really limited. However, a Mn

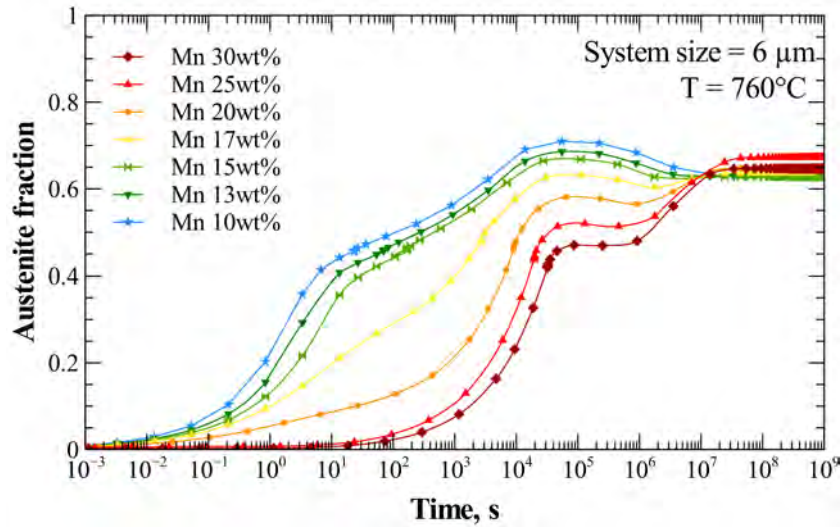


Figure 5.7: Influence of the cementite manganese content on austenite formation kinetics at 760°C (system size fixed at 6 μm). Seven manganese enrichments in cementite are compared: 10, 13, 15, 17, 20, 25 and 30 wt%.

activity gradient exists at the γ/α interface which is in line with the local Mn concentration gradient close to the interface (figure 5.8.b). This gradient surrounding the interface points out a local equilibrium condition with negligible Mn partitioning (LENP): in other words, C and Mn concentrations at the two sides of the interface respect a local equilibrium condition despite limited diffusion of Mn.

Stage 2: Austenite formation controlled by Mn-diffusion in ferrite ($10 \text{ s} < t < 10^5 \text{ s}$)
Above 10 s, the C activity profiles in the newly formed austenite and ferrite are flat so that the transformation is no longer managed by C diffusion. Identically, C concentration is flat all along the system excepted short gradients at the initial cementite location.

The transformation is controlled by Mn-diffusion in ferrite for holding times in the range of 10- 10^4 s. The strong Mn activity gradient at ferrite side for times 10^2 , 10^3 and 10^4 s manages the austenite formation. The Mn concentration spike at ferrite side is therefore filled thanks to Mn-diffusion in ferrite. In parallel to Mn-diffusion in ferrite, the manganese also diffuses in austenite from the prior-cementite area to the γ/α interface. It is confirmed by the Mn activity gradient in austenite core but it remains smaller than the one in ferrite at this stage.

Stage 3: Austenite formation controlled by Mn-diffusion in austenite ($10^5 \text{ s} < t < 3 \times 10^7 \text{ s}$)

Above 10^5 s, the Mn activity profile at ferrite side is flat so that the transformation is no longer controlled by Mn-diffusion in ferrite. The Mn concentration profile is also flat at ferrite side of the interface. Mn concentration and activity gradients at austenite side highlight an austenite formation stage controlled by Mn-diffusion in austenite. The larger time scale of this third stage is due to the slow diffusion of Mn in austenite

($D_{Mn}^{\gamma} = 3.9 \times 10^{-19} \text{ m}^2/\text{s}$) compared to ferrite ($D_{Mn}^{\alpha} = 9.0 \times 10^{-17} \text{ m}^2/\text{s}$). Mn partitions in austenite from the previous cementite side (corresponding to austenite core) to the interface. Mn homogenization all along the austenite side induces a moving back of the interface position between 10^5 and 3×10^7 s of holding times, named as austenite shrinkage.

Stage 4: Orthoequilibrium ($t > 3 \times 10^7$ s)

Finally, orthoequilibrium is achieved after 3×10^7 s of holding time (flat C and Mn profiles).

5.2.2.2 High-Mn enrichment in cementite ($C_{Mn}^{Fe_3C} > 15 \text{ wt}\%$)

Identically to the case of the low-Mn enrichment in cementite, C and Mn concentration and activity profiles are reported in figure 5.9 for a system containing 30 wt%Mn in cementite. Profiles are plotted for different holding times at 760°C: 0, 0.1, 1, 10, 10^2 , 10^3 , 10^4 , 10^5 , 10^6 , 10^7 and 10^8 s. At higher Mn content, the mechanisms driving the phase transformation are different, which explains the change of the shape of the austenite formation kinetics.

Stage 1: Austenite formation controlled by Mn-diffusion in ferrite ($10 \text{ s} < t < 10^5 \text{ s}$)

With an increase in the Mn content in cementite, austenite formation is no longer controlled by C-diffusion as evidenced by the flat C concentration and activity profiles (figure 5.9.a and c).

Stronger Mn activity profile at ferrite side than austenite side (figure 5.9.d) points out Mn-diffusion controlled in ferrite from times equal to 10, 10^2 , 10^3 , 10^4 and 10^5 s. Mn concentration profile at ferrite side flattens (figure 5.9.a). In parallel, Mn slowly diffuses in the austenite region.

Stage 2: Austenite formation controlled by Mn-diffusion in austenite ($10^5 \text{ s} < t < 10^8 \text{ s}$)

Above 10^5 s, the transformation is managed by Mn-diffusion in austenite as Mn concentration and activity profiles are flat at ferrite side. Austenite kinetics is strongly slowed down and managed by Mn diffusion from the prior cementite area to the interface.

Stage 3: Orthoequilibrium ($t > 10^8 \text{ s}$)

Finally, the achievement of the orthoequilibrium condition is validated by flat C and Mn concentration and activity profiles in the whole system after 10^8 s of holding time.

5.2.2.3 Qualitative comparison

A deeper comparison of these two austenite formation regimes is realized focusing on the tie-line evolutions during the thermal holding and the initial C isoactivity lines.

Analysis of tie-line evolutions

Evolutions of α/γ “operative” tielines during isothermal holding at 760°C are reported on the isothermal section of the Fe-C-Mn system. Operative tielines are determined thanks to Mn concentration at γ/α interface as presented in figure 5.8.b. and 5.9.b. Figure 5.10.a

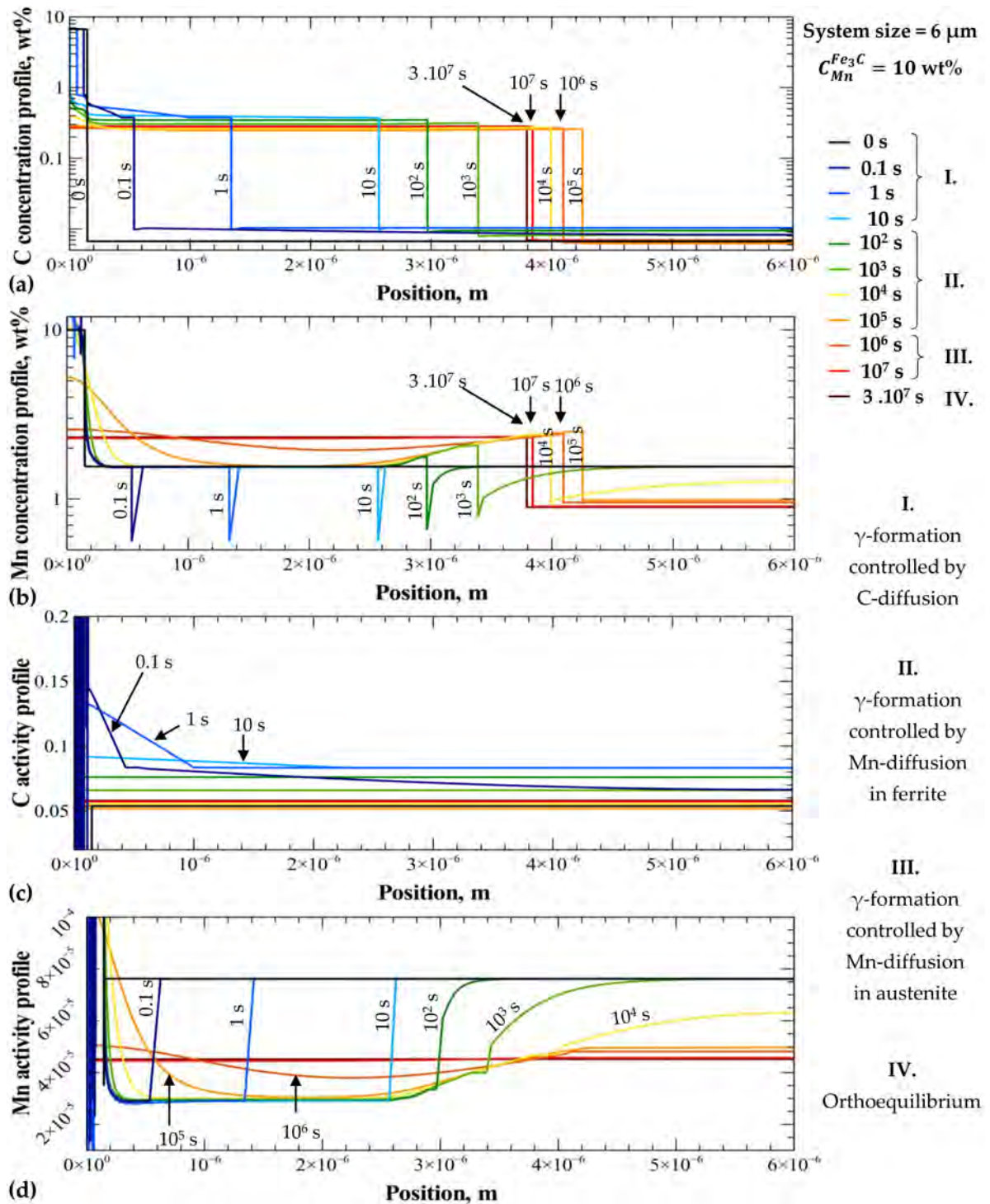


Figure 5.8: C and Mn (a-b) concentration profile and (c-d) activity profile during austenite formation of a steel containing 10 wt%Mn in cementite for different holding times at 760°C: 0, 0.1, 1, 10, 10², 10³, 10⁴, 10⁵, 10⁶, 10⁷ and 3 × 10⁷ s.

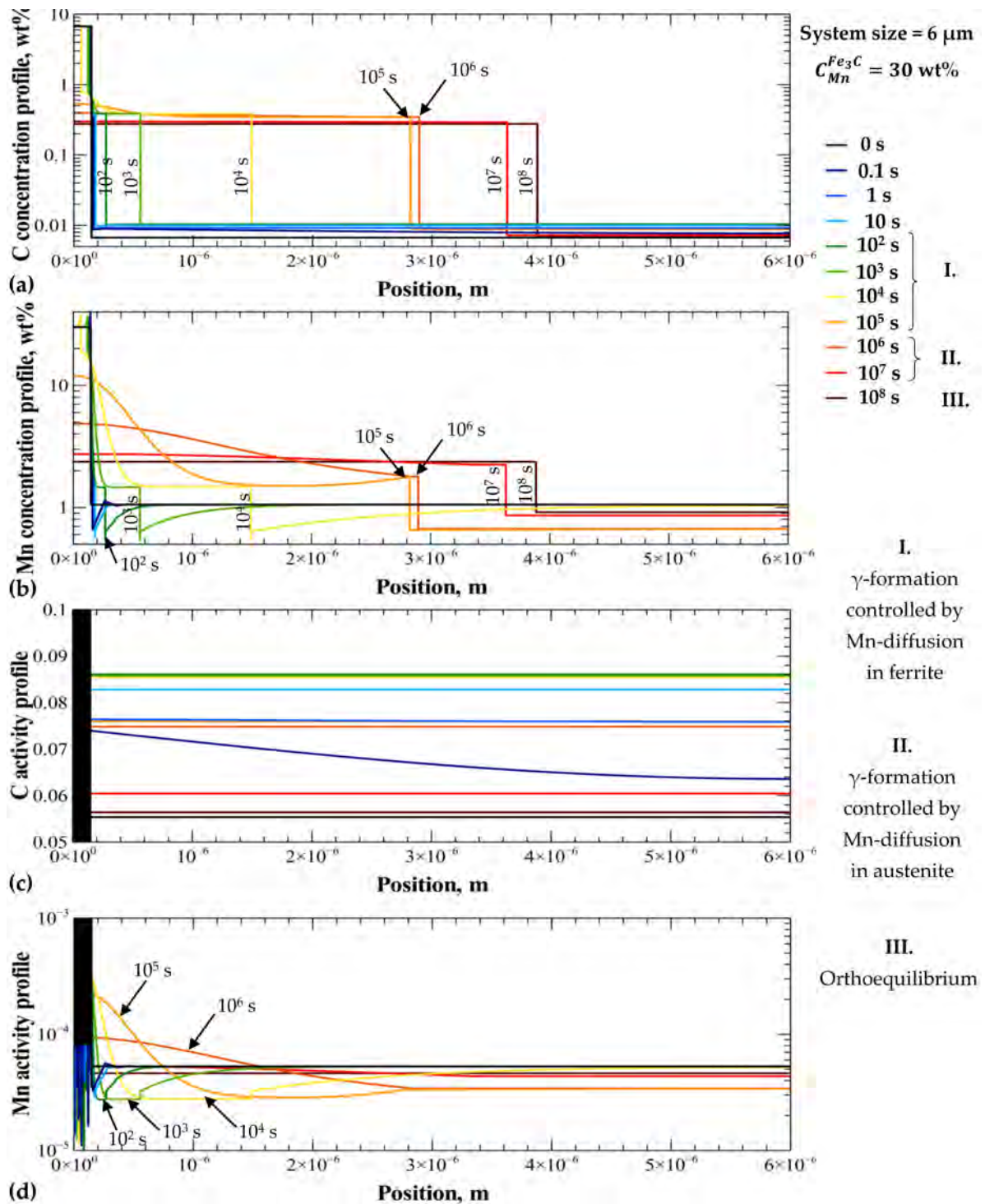


Figure 5.9: C and Mn (a-b) concentration profile and (c-d) activity profile during austenite formation of a steel containing 30 wt%Mn in cementite for different holding times at 760°C: 0, 0.1, 1, 10, 10², 10³, 10⁴, 10⁵, 10⁶, 10⁷ and 10⁸ s.

and b respectively point out tielines of austenite formation considering 10 and 30 wt%Mn enrichment in cementite for various holding times.

It can be noted that the tieline associated with the initial austenite growth is much lower than passing through the bulk composition. This tieline enables the equality of C and Mn interface velocities respecting their difference of diffusivities.

The system containing 30 wt%Mn in cementite shows a progressive evolution of the tieline which tends to approach the ORTHO equilibrium tieline passing through the bulk composition. During the first stage (10^4 s), there is limited evolution of Mn content at the interface. The transformation is indeed driven by Mn-diffusion in ferrite to feed up the austenite phase. During the second stage controlled by Mn-diffusion in austenite, the tieline describing the local equilibrium condition at the interface evolves. Mn atoms coming from the prior cementite tend to increase the Mn content at the interface which becomes the close to the ORTHO equilibrium Mn content.

The evolution of “operative” tielines of the steel containing 10 wt%Mn in cementite is much more complex. Tielines do not evolve below 10 s which corresponds to the C-diffusion controlled stage. Mn has indeed no time to redistribute so that the “Mn-spike” at the interface is kept. During the second stage managed by Mn-diffusion in ferrite ($10^2 - 10^5$ s), the tieline progressively goes up and passes by the nominal composition point. The α/γ “operative” tielines due to γ -shrinkage where Mn partitions all along the austenite phase. Mn homogenizes from the austenite core to the α/γ interface.

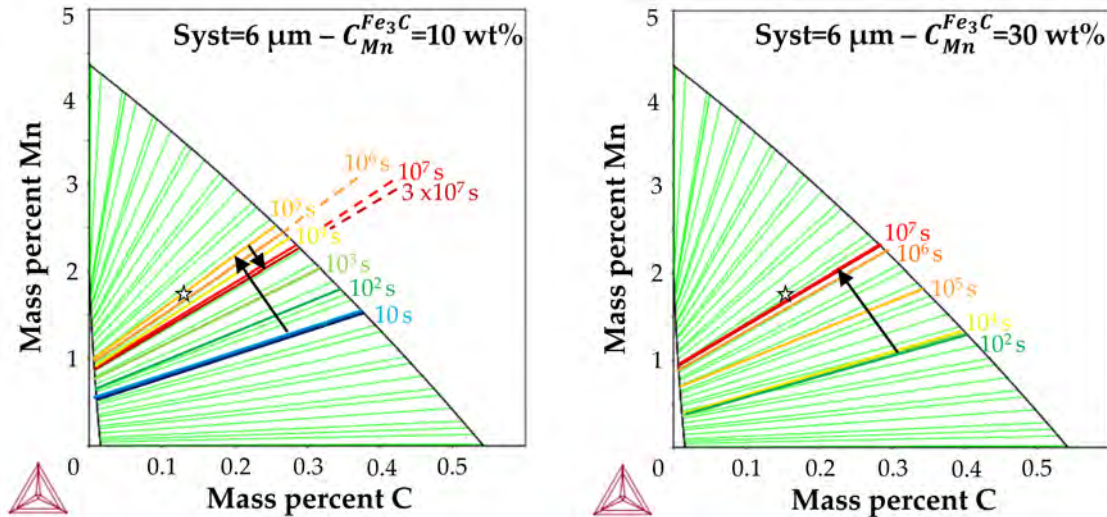


Figure 5.10: Evolutions of the “operative” tie-lines as a function of holding times supposing (a) 10 and (b) 30 wt% of Mn enrichment in cementite.

Analysis of C isoactivity lines

To complete the study, it was proposed to estimate graphically the driving force for cementite dissolution based on a similar approach to Lai *et al.* paper [LAI 16]. This was possible with a plot of the C isoactivity line in austenite passing through the Mn com-

position at the $\gamma/\text{Fe}_3\text{C}$ interface ($C_{Mn}^{\gamma/\text{Fe}_3\text{C}}$) as shown in figure 5.11. This C isoactivity line enables to evaluate the effective carbon composition at the austenite/ferrite interface (C_C^{γ/α^*}) supposing cementite and austenite equilibrium. The deviation between the carbon concentration at the austenite/ferrite interface ($C_C^{\gamma/\alpha}$) and this effective value (C_C^{γ/α^*}) defines the driving force for cementite dissolution. The higher the driving force for cementite dissolution is, the larger this difference is and this will promote the cementite dissolution thanks to carbon diffusion. Inversely, if the two austenite/ferrite carbon concentrations are equal, there is no driving force for cementite dissolution and no phase transformation occurs.

The two isoactivity lines for 10 and 30 wt%Mn in cementite are reported in figure 5.11 using u-fraction representation¹. C isoactivity lines are calculated with Thermo-Calc software considering a single austenite phase. The C activity, determined at the $C^{\gamma/\text{Fe}_3\text{C}}$ concentration, was imposed and the isoactivity line was obtained varying the Mn content. Calculated γ/α and $\gamma/\text{Fe}_3\text{C}$ interface compositions are reported in figure as $C^{\gamma/\alpha}$ and $C^{\gamma/\text{Fe}_3\text{C}}$ points.

Driving forces for austenite growth were evaluated from the C gradient between (i) the C isoactivity line in austenite and (ii) the C content at the γ/α interface ($C^{\gamma/\alpha}$). At 10 wt% of Mn in cementite, the gradient is high and the austenite will be formed under C activity gradient in austenite controlling the C-diffusion mode. Inversely at 30 wt%Mn in cementite, the gradient between the C isoactivity line in austenite and the C content at the γ/α interface is limited so that C-diffusion no longer controls austenite formation.

In a global approach, the C isoactivity lines passing through the Mn composition of $\gamma/\text{Fe}_3\text{C}$ interface were applied for interface concentrations equal to 10, 13, 15, 17, 20, 25 and 30 wt%Mn. Coloured double-arrows of figure 5.12 highlights the C gradient between the C isoactivity line in austenite and the C content at the γ/α interface ($C^{\gamma/\alpha}$) of each condition. It should be noted that the C gradient appears limited above 17 wt%Mn in cementite where the first stage of austenite formation is no longer controlled by C-diffusion. Inversely, larger gradients are pointed out below 15 wt%Mn in cementite, which is accordance with the initial C-diffusion controlled stage of these kinetics.

The analysis of the C isoactivity lines in the austenite phase passing through the Mn composition of $\gamma/\text{Fe}_3\text{C}$ interface validates the absence of C-diffusion controlled stage in the case of high-Mn enrichment in cementite. C isoactivity representation enables to graphically estimate the cementite dissolution driving force as a function of Mn content in cementite based on thermodynamic supports.

¹The “u-fraction” axis leads to a clearer representation of the five phase domains on a same graph: $(\alpha + \gamma)$, γ and $(\gamma + \text{Fe}_3\text{C})$ area. The u-fraction of a component k in a phase i is defined as:

$$u_k = \frac{x_k}{\sum_{j \in S} x_j} \quad (5.3)$$

with x_k being the atom fraction of k element and S all substitutional elements (here Fe and Mn). $u(\text{Mn})$ is hence equal to $\frac{x_{Mn}}{x_{Mn} + x_{Fe}}$ and, in the same way, $u(\text{C})$ is equal to $\frac{x_C}{x_{Mn} + x_{Fe}}$ ratio. The representation of u-fraction supposed that interstitial element (C) do not contribute to the volume of a phase and that all substitutional elements contribute equally to volume.

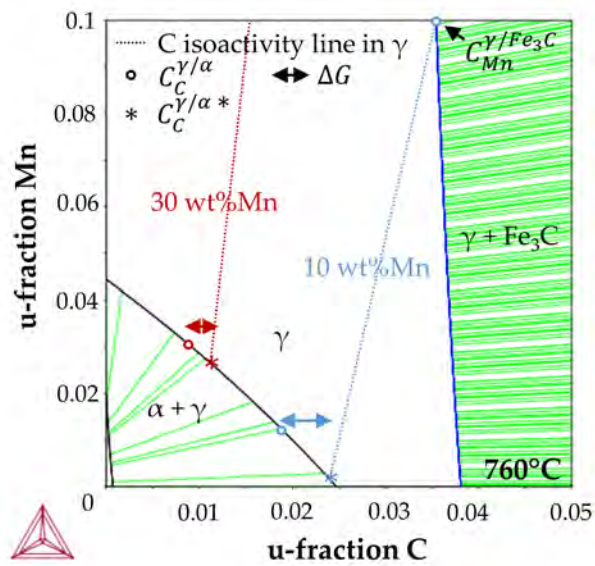


Figure 5.11: Isothermal section of the Fe-C-Mn ternary system at 760°C. Dotted lines correspond to C isoactivity lines passing through Mn composition at the $\gamma/\text{Fe}_3\text{C}$ interface equal to 10 and 30 wt%Mn. Circles point out interfacial composition of austenite and cementite phases.

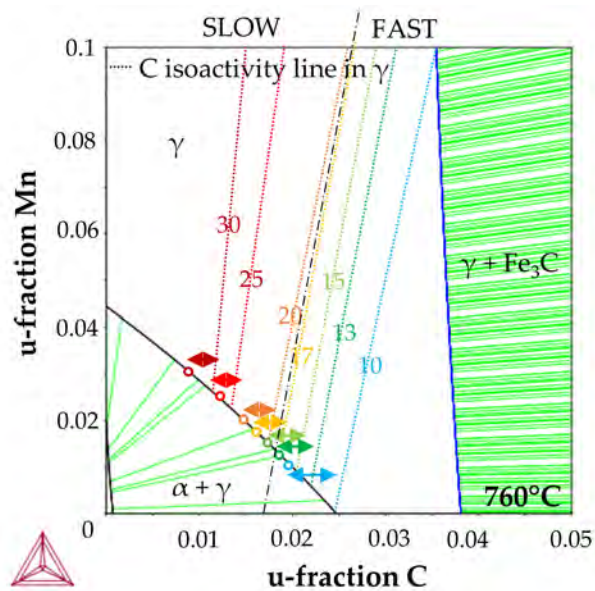


Figure 5.12: Isothermal section of the Fe-C-Mn ternary system at 760°C. Dotted lines correspond to C isoactivity lines passing through different Mn composition at the $\gamma/\text{Fe}_3\text{C}$ interface: 10, 13, 15, 17, 20, 25 and 30 wt%Mn.

5.3 Application to austenite formation kinetics on the ReX-steel and on the CR-steel

DICTRA simulations were finally applied to describe the austenite formation kinetics in the case of the ReX-steel and of the CR-steel during isothermal holding at 735, 760 and 780°C (the heating stage is supposed very quick). First, in section 5.3.1, we will consider the influence of the difference of the Mn content in cementite for these two states on the kinetics. Then, in section 5.3.2, we will try to take into account the effect of the deformation of the CR-steel on the kinetics to account for the experimental results presented in chapter 3.

5.3.1 Influence of Mn content in cementite

The two states were modeled fixing a system state to 10 μm and with two Mn contents in the cementite based on EDS analysis: (i) $C_{Mn}^{Fe_3C} = 10 \text{ wt\%Mn}$ in the case of the CR-steel and (ii) $C_{Mn}^{Fe_3C} = 13 \text{ wt\%Mn}$ for the ReX-steel. Figure 5.13 shows the austenite formation kinetics during holding treatments at (a) 780, (b) 760 and (c) 735°C. For each holding temperature, four kinetics are plotted: two experimental kinetics obtained during isothermal holding of the ReX-steel and the CR-steel (the heating stage was realized at 5°C/s rate) and two DICTRA kinetics to model these two states considering their different Mn contents in cementite.

Considering DICTRA predictions, it may be noted that two types of kinetics can be differentiated depending on the holding temperature. At 735°C, austenite seems to be formed in two stages while three stages are detected at 760 and 780°C. Based on previous study, it is supposed that the transformation is no longer controlled by C-diffusion at 735°C considering 10 and 13 wt%Mn in cementite.

The C isoactivity lines were plotted at 735 and 780°C for the two Mn contents in cementite (10 and 13 wt%) in order to investigate the driving force for C-diffusion in austenite. The driving force for C diffusion in austenite is represented by double-arrow which shows the gradient between the C isoactivity line in austenite and the C content at the γ/α interface for the two considered Mn enrichments. Double-arrows are smaller at 735°C compared to 780°C ones. The driving force seems therefore to be lower at 735°C (figure 5.14.a) than at 780°C (figure 5.14.b) and this may explain the possible absence of the C-diffusion stage in the kinetics of austenite formation at 735°C.

In addition, according to DICTRA, the Mn variation from 10 to 13 wt%Mn in cementite has a lower effect at high temperatures (760 and 780°C). Namely, the austenite formation kinetics is slightly delayed when the Mn enrichment in cementite is increased. The delay is accompanied by a weak decrease in austenite fraction during the first and second stage of austenite formation. Comparatively, the austenite kinetics is much more influenced at 735°C by the Mn enrichment: the first stage is significantly delayed to longer times. Indeed, the Mn diffusivity is significantly smaller, when the temperature is decreased as shown in table 5.2.

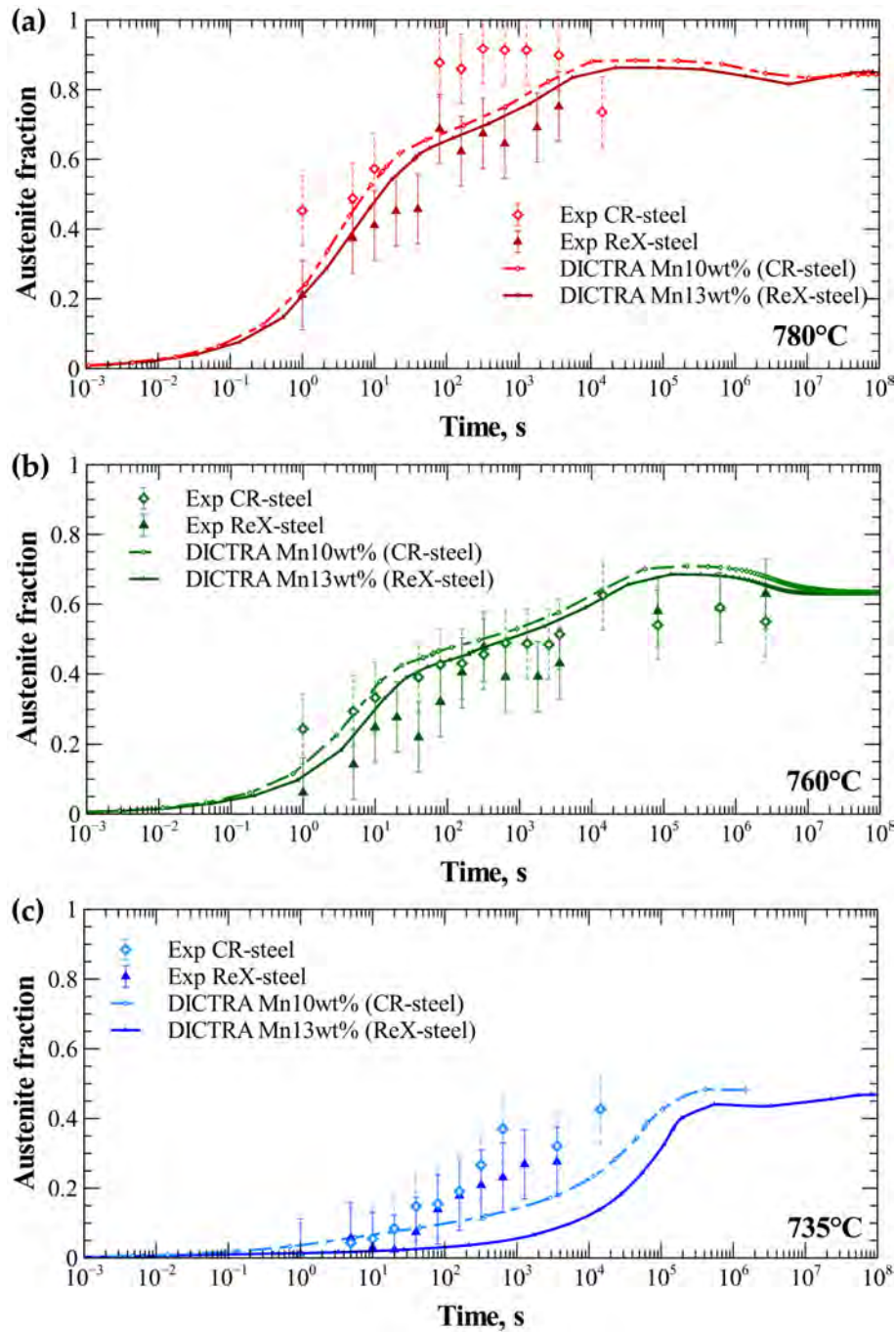


Figure 5.13: Comparison of DICTRA predictions with experimental kinetics of austenite formation on the ReX-steel and on the CR-steel during isothermal holding at (a) 780, (b) 760 and (c) 735°C. Two different conditions were used to differentiate the CR-steel and the ReX-steel considering the difference of Mn enrichment in cementite: (i) $C_{Mn}^{Fe_3C} = 10$ wt%Mn in the case of the CR-steel and (ii) $C_{Mn}^{Fe_3C} = 13$ wt%Mn for the ReX-steel.

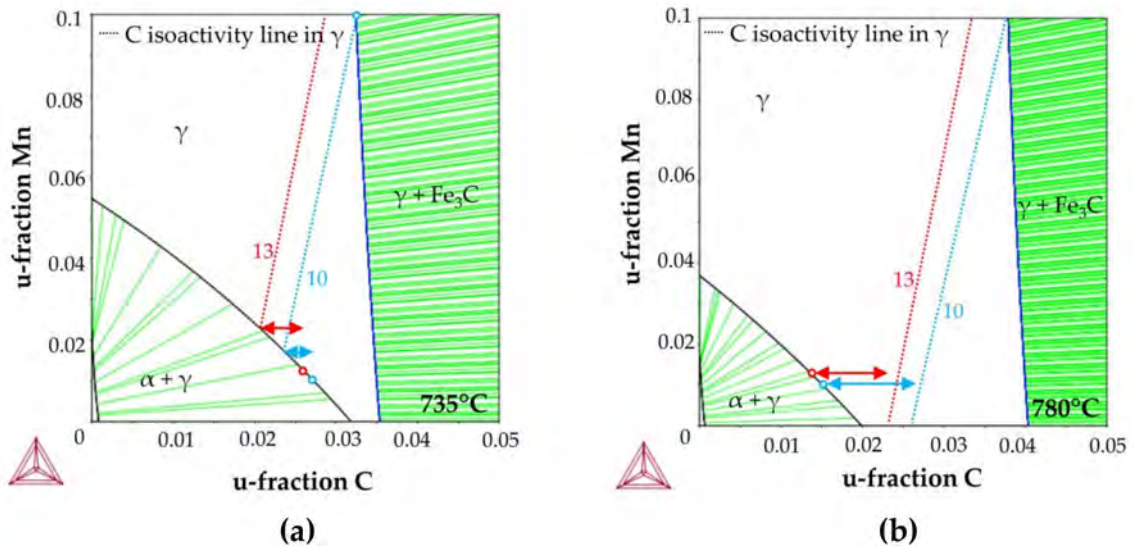


Figure 5.14: Isothermal section of the Fe-C-Mn ternary system at (a) 735 and (b) 780°C. Dotted lines correspond to C isoactivity lines passing through different Mn composition at the $\gamma/\text{Fe}_3\text{C}$ interface: 10 and 13 wt%Mn.

Temperature	D_C^α , m ² /s	D_C^γ , m ² /s	D_{Mn}^α , m ² /s	D_{Mn}^γ , m ² /s
735°C	9.4×10^{-11}	8.5×10^{-13}	9.1×10^{-17}	3.9×10^{-19}
760°C	1.3×10^{-10}	1.1×10^{-12}	2.4×10^{-16}	8.8×10^{-19}
780°C	1.7×10^{-10}	1.4×10^{-12}	4.7×10^{-16}	1.6×10^{-18}

Table 5.2: Diffusion coefficients of C and Mn in ferrite and austenite phases for 735, 760 and 780°C (Thermo-Calc with MOBFE2 database).

Considering the comparison with experimental austenite formation kinetics, it is observed that DICTRA predictions at 735°C are significantly slower than experimental kinetics. Moreover, DICTRA predicts an effect of the Mn content, which was not detected on the experimental kinetics at 735°C. The agreement is better at higher temperatures as DICTRA kinetics are in the range of the experimental error bars. However, it is shown that the difference in the Mn cementite enrichment of the two steels (ReX-steel and CR-steel) tends to accelerate slightly the austenite formation kinetics. The Mn variation from 10 to 13 wt%Mn seems to be non sufficient to explain the difference between the austenite formation kinetics on the ReX-steel and the CR-steel. In order to improve DICTRA predictions, it was thus proposed to adjust the system size as deformed ferrite grains may be expected smaller than recrystallized ones.

5.3.2 Influence of the representative size

Based on first DICTRA predictions, it was chosen to attribute different system sizes to model the austenite formation on the ReX-steel and on the CR-steel. Hence, the size size of the CR-steel was fixed at 5 μm which is twice smaller than that of the ReX-steel. Smaller representative length was chosen as ferrite grains are strongly deformed and contains sub-structures.

Figure 5.15 gathers experimental austenite formation kinetics obtained for the ReX-steel and the CR-steel and DICTRA predictions during isothermal holding at (a) 780, (b) 760 and (c) 735°C.

Changing the system size of the CR-steel model accelerates the austenite formation kinetics of this state. It improves the onset of the austenite formation at higher temperatures.

The next section aims at proposing a critical discussion of various hypothesis (initial phases, system size *etc.*) and DICTRA/experimental comparison of austenite formation kinetics.

5.4 Discussion

The application of DICTRA simulation tools to describe the austenite formation kinetics meets with more physical base modeling expectations as the phase transformation is described by Fick's diffusion equations and thermodynamic bases (respect of interface local equilibrium, element distribution in phases (*i.e.* tielines) *etc.*). Phase evolutions can be justified by physical and/or thermodynamic argument(s) strengthening different mechanisms. For example, different stages of austenite formation were related to different diffusion stages due to carbon or manganese or the absence of the C-diffusion controlled mode was explained considering C isoactivity line.

However, a set of assumptions are needed to model and simplify the real and complex phase transformations of industrial steels. This sections aims at discussing DICTRA simulations in comparison with experimental kinetics and mainly number of assumptions realized to apply the software.

5.4.1 DICTRA applications to model the austenite formation

As shown in figures 5.13 and 5.15, predictions of austenite formation during isothermal holding using DICTRA software are debatable as it was difficult to determine a unique simulation set for each initial state (recrystallized or cold-rolled) to model the austenite formation kinetics at the three considered temperatures (735, 760 and 780°C).

Thermal dependence

The thermal dependence of DICTRA simulations is taken into account as the austenite formation kinetics are quicker when the holding temperature is increased. Accelerated kinetics are obtained increasing the temperature due to the higher diffusivity of C and Mn

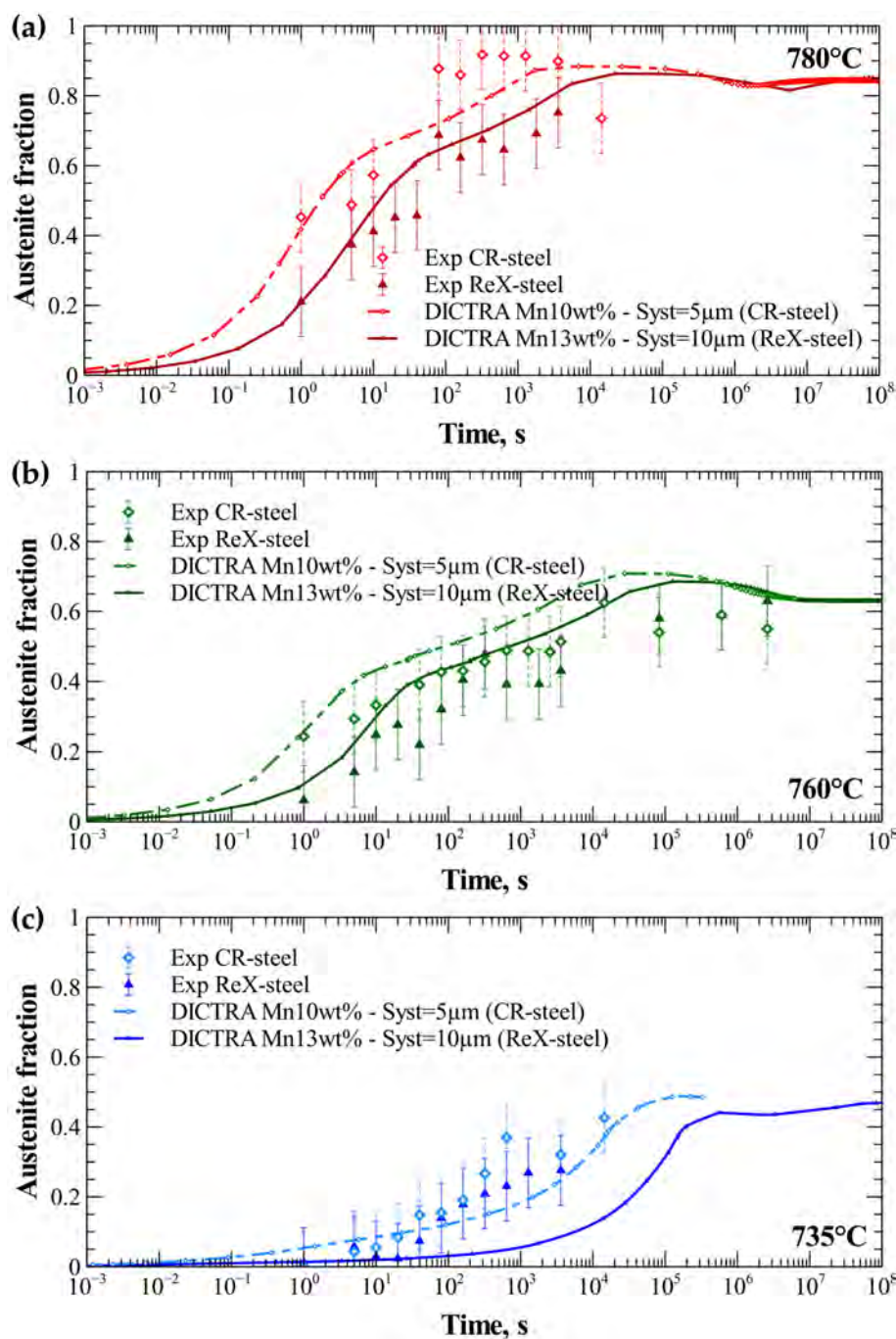


Figure 5.15: Comparison of DICTRA predictions with experimental kinetics of austenite formation on the ReX-steel and on the CR-steel during isothermal holding at (a) 780, (b) 760 and (c) 735°C. Two different conditions were compared: (1) a system of size 5 μm with 10 wt%Mn in the cementite to represent the deformed microstructure of the CR-steel and (2) a system of size 10 μm with 13 wt%Mn in cementite corresponding to larger microstructure of the ReX-steel.

elements with temperature (see table 5.2). However, it should be noticed that the thermal dependence appears staggered compared to experimental kinetics. Notably, the predicted kinetics at 735°C appears shifted to longer time scales compared to the experimental kinetics at this temperature.

This difference could be attributed to the slow/fast transition regime for cementite dissolution published by Gouné *et al.* [GOU 12] (see figure 1.7 of the literature review). Indeed, the critical Mn content in cementite to switch dissolution regime is lower at low temperature so that 10 or 13 wt%Mn in cementite may be enough to induce slow dissolution of carbides.

However, the experimental austenite formation kinetics at 735°C seems to be in accordance with a fast dissolution regime (with a C-diffusion controlled stage) as rapid austenite growth occurs between 1 and 100 s.

It may be supposed that this disagreement is due to the mobility and/or thermodynamic database which may be not validated at low temperature. Errors in the phase diagram could, for example, modify the driving force for C-diffusion and suppress this stage. Nevertheless, this hypothesis seems debatable as Fe-C-Mn is a well known system and no errors have been emphasised.

Cementite's Mn content

The austenite formation kinetics for the ReX-steel and the CR-steel were differentiated by taking into account the measured Mn contents in cementite (determined by EDS analysis). As shown in figure 5.13, the variation of the Mn content from 10 wt%Mn, for the CR-steel, to 13 wt%Mn, for the ReX-steel, is insufficient to explain the delay of the austenite formation kinetics on the ReX-steel. The graph justifies the fact that the Mn enrichment during the recrystallization treatment cannot entirely explain the difference between the austenite formation kinetics on these two states and other modifications or phenomena are needed (recrystallization, grain size modification *etc.*).

In addition, one should note that the Mn content in cementite is fixed to a single value. However, gradient of Mn composition may exist inside a cementite particle (*ex.* core more enriched). Also, the Mn content in cementite particles is not homogeneous as shown in histogram 2.3 (chapter 2) where the Mn range extends over 5 wt%. In these conditions, the hypotheses of an average cementite's Mn content is debatable to represent the non-homogeneous system.

System size

A better compromise between model and experimental austenite formation kinetics for the ReX-steel and the CR-steel was found adjusting not only (i) the Mn enrichment in cementite, based from EDS analysis of the carbides but also (ii) differentiating the system size for the ReX-steel and the CR-steel. Hence, a system with a size twice smaller was attributed to the CR-steel state. It was justified by the fact that the deformed grains of the CR-steel are globally smaller than the ones of the ReX-steel. Moreover, cold-rolled microstructures usually present substructures which may also act as nucleation sites reducing therefore the diffusion length. This tends to accelerate the modeled austenite formation kinetics in the case of the cold-rolled steels and leads to better predictions of

the kinetics.

As shown in chapter 3, recrystallization occurs in parallel to austenite formation in the case of the CR-steel. Therefore, ferrite grains tend to recrystallize during the phase transformation. Especially, it was shown that the recrystallization was completed in the first 100 s of holding at 735°C. Ferrite grains are recrystallized during the major part of austenite formation; so, the finer system size (5 μm) is questionable in the case of the CR-steel modeling at 735°C. A system size equal to 10 μm is in better accordance with the completion of the recrystallization kinetics at 735°C at the onset of the phase transformation despite bad prediction of the DICTRA simulation. Once again, the experimental austenite kinetics at 735°C can be hardly predicted.

At higher temperatures (760 and 780°C), the phase transformation and recrystallization were supposed to occur simultaneously. Ferrite grain sizes evolve in parallel to the austenite formation so that the initial DICTRA system size should ideally be modified proportionally to the recrystallization progress. However, the rate of system size evolution may be supposed low during the thermal treatment of CR-steels as (i) deformed ferrite grains will decrease while recrystallized ferrite grains grow, so that the average diffusing distance may suppose unaffected and (ii) the recrystallization inhibition hypothesis will tend to “stabilize” the ferrite grain size. At these two temperatures, the hypothesis of smaller system size seems to be relevant considering the overlapping with recrystallization.

Chemical composition

The complex chemistry of the investigated steel was simplified to that of a Fe-C-Mn ternary system for three main reasons: (i) larger systems require extrapolation of database and (ii) cementite is not defined for higher order systems and (iii) higher order systems reduce calculation stability to manage the motion of the two $\text{Fe}_3\text{C}/\gamma$ and γ/α interfaces. However the presence of other alloying elements (like Cr [LI 17] or Si [WEI 13]) may modify phase diagrams and therefore explain discrepancies in the austenite formation kinetics.

The initial composition of the two elements (C and Mn) in phases is reasonably confident as it was fixed from (i) EDS analysis for Mn and (ii) thermodynamic equilibrium at 670°C for carbon which is certainly achieved after the hot-rolling and coiling stages.

However, local heterogeneity of element like Mn segregation bands due to solidification are not taken into account in the DICTRA simulation. Substitutional element bands may modify the global austenite formation kinetics generating rich and depleted area of atoms.

Mass balance violation

Lastly, the mass balance violation (ex. figure 5.7) is a recurrent problem identified in the different kinetics of this chapter. This leads to a final deviation of orthoequilibrium phase fractions. The simulation conditions enabling to solve this problem were however not found.

5.4.2 Others concomitant phenomena

This chapter only considers the austenite formation while other phenomena may occur and interfere with the phase transformation:

- *Dislocation density* was not considered neither in the ReX-steel nor in the CR-steel. However, dislocation enrichment of the CR-steel may increase the driving force for austenite formation compared to the ReX-steel and promote the diffusion thanks to pipe-diffusion.
- *Recrystallization* of the deformed microstructure in parallel to the phase transformation was not taken into account while a full chapter was dedicated to it. Recrystallization modifies the dislocation density, deformation field, grain size, diffusional paths and also possible nucleation sites of austenite so that the austenite formation on CR-steel is not only dependent on C and Mn diffusion.
- *Carbide evolution* was not considered. However, carbides may be enriched in substitutional elements, spheroidize or even coarsen during the intercritical treatment.
- *Austenite nucleation* was not considered in these simulations as incoherencies were highlighted considering austenite nucleation (section 5.1.2). Moreover, austenite nucleation is not supposed to be a limiting factor so that this choice appears to be relevant. DICTRA software only treats homogeneous nucleation so that well accepted triple grain boundary nucleation will not be differentiated in the DICTRA nucleation implementation
- *Austenite grain impingements* are not considered.

All this phenomena or considerations may have a possible effect on the kinetics of austenite formation. They are not considered in the DICTRA simulations and may be the cause of model/experimental discrepancies.

5.5 Conclusion

DICTRA software was used to describe the austenite formation of the ReX-steel and the CR-steel. The most relevant representative system was defined paying attention to the elements, geometry, size and composition of the initial states. DICTRA parameters were tested in order to validate the calculation: it mainly enabled to withdraw austenite nucleation as incoherencies were emphasised. The influence of the two main simulation parameters (size system and Mn content in cementite) was investigated to get a better understanding of austenite formation kinetics. Modeling of Fe-C-Mn ternary system enables to explain among other things: (i) different mechanisms controlling various stages of austenite formation kinetics, (ii) the absence of C-diffusion mode for the high Mn contents and also (iii) the austenite shrinkage at the final time step for some modeling conditions.

Results of the DICTRA modeling are debatable because many others concomitant phenomena are not taken into account as discussed in section 5.4.2. However, it was concluded that the Mn enrichment passing from 10 to 13 wt%Mn in cementite during the recrystallization treatment is insufficient to justify the observed delay of the phase transformation kinetics on the ReX-steel. The enrichment has to be combined with an increase in the system size to retard the kinetics.

Finally, it should be emphasised that the real system is much more complex than the simulated one. Number of assumptions were realized and this may explain the discrepancies between the predicted and experimental kinetics of austenite formation.

Chapter 6

Characterization of the microstructural evolutions during the cooling and the tempering stages

Commonly obtained after a partial austenitization, one should ask if the microstructure of DP steels obtained after the cooling and tempering stages is influenced by this incomplete austenitization. This last chapter proposes thus an investigation on the two major steps of the DP thermal cycle occurring after the intercritical annealing: (i) the cooling from the intercritical range to room temperature or even to an intermediate temperature and (ii) the cooling of the steel inducing a tempering of the ferrite-martensite microstructure.

In the first section, the austenite decomposition was studied as a function of the cooling rate (R_C) and of the initial state before cooling (*i.e.* fully or partially austenitic). The study was focused on the monitoring of the austenite decomposition kinetics and also on microstructural observations. Finally, Continuous Cooling Transformation (CCT) diagrams for the two initial states were built and compared. Models, available in the literature, were applied to describe the austenite-to-martensite transformation and the martensite start temperature (M_S) in the two cases.

In a second step, martensite evolutions during tempering treatments were investigated. The influence of the tempering temperature and of time were analysed between 200 and 500°C. Using a time-temperature equivalence, three tempering mechanisms could be identified. A model was then proposed to predict the fraction of precipitated carbon as a function of tempering conditions.

Contents

6.1	Austenite decomposition during cooling stage	132
6.1.1	Characterization of the two initial states considered in this study . . .	132
6.1.2	Cooling of a fully austenitic state (100% γ -state)	133
6.1.3	Cooling of a ferrite-austenite mixture (60% γ -state)	136

6.1.4	Comparison between the CCT diagrams of the 100% γ -state and the 60% γ -state	139
6.1.5	Analysis of the martensite formation kinetics of the steel in the 100% γ -state and in the 60% γ -state	141
6.2	Martensite tempering of the fully martensitic steel	145
6.2.1	Identification of the martensite tempering mechanisms between 200 and 500°C	145
6.2.2	Quantification of the amount of precipitated carbon during tempering	148
6.2.3	Hardness evolution during tempering	154
6.3	Prospective works on the tempering of a ferrite-martensite microstructure	157
6.4	Discussion and conclusion	158

6.1 Austenite decomposition during cooling stage

This section focuses on austenite decomposition during cooling from a fully or partially austenitic state to room temperature. The two states considered in this study were first characterized before monitoring the austenite decomposition kinetics and analysing the microstructure. Then, the obtained CCT diagrams were compared to investigate the effect of the cooling rate and of the initial state before cooling. Lastly, modeling efforts were brought to predict the austenite-to-martensite transformation and the martensite start temperature (M_S) from literature review models.

6.1.1 Characterization of the two initial states considered in this study

The study was performed on two different states to investigate the influence of the microstructural state before cooling. A fully austenitic state was obtained after 120 s of holding at 850°C while an intercritical state, mixture of ferrite and austenite, was produced by a holding at 760°C during 300 s, for which the target austenite fraction was 60%.

The phases present before cooling were identified by performing a direct water quench after annealing in order to obtain the austenite-to-martensite phase transformation. Figure 6.1 presents the optical micrographs, revealed by a Bandoh etching, of (a) the fully austenitized steel and (b) the partially austenitized steel. The complete austenitization was validated by the observation of a fully martensitic microstructure after the water quench (figure 6.1.a). The intercritical state was also confirmed as a ferrite-martensite mixture was observed in figure 6.1.b. The martensite fraction was quantified to be equal to 60%: therefore, the intercritical state leads to 60% of austenite and 40% of ferrite before the cooling stage. This is consistent with the results of the preceding chapters. In the following, the fully austenitic state will be called “100% γ -state” and the partially austenitic state will be referred as “60% γ -state”.

It should be emphasised that the determination of the austenite decomposition kinetics by dilatometry requires a sufficient amount of austenite before cooling [COL 11]. Hence,

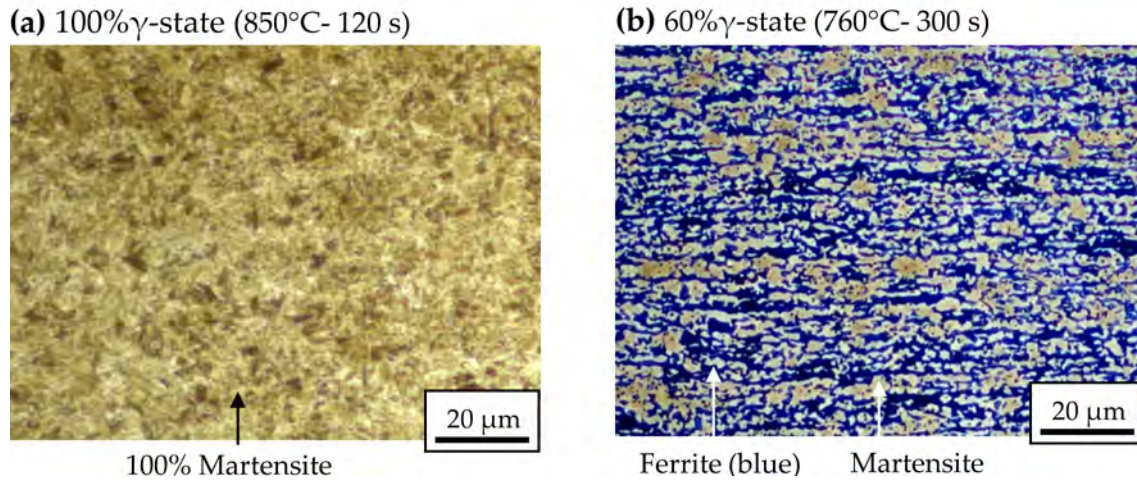


Figure 6.1: Optical micrographs of the two considered states after water quench from (a) the 100% γ -state (850°C - 120 s) and (b) the 60% γ -state (760°C - 300 s). Bandoh etching.

the study was realized on a 60% γ -state, since the dilatometry curves during cooling of a 30% γ -state were not exploitable as slope changes were found negligible during the continuous cooling.

Before going further, it should be kept in mind that the two investigated states are not at thermodynamic equilibrium at high temperature. If we refer to the works presented in chapter 5, chemical gradients are expected inside the microstructure even for the fully austenitic state. However, typical industrial times were used in this work instead of thermodynamic equilibrium times, as they that are not achievable in industrial conditions.

6.1.2 Cooling of a fully austenitic state (100% γ -state)

Austenite decomposition was first studied from the fully austenitic microstructure (so-called 100% γ -state) obtained after 120 s of holding time at 850°C.

6.1.2.1 Kinetics of austenite decomposition of the 100% γ -state

Led dilatometry was used to monitor austenite decomposition kinetics during continuous cooling cycles from 850°C to room temperature with different rates: $R_C=1, 5, 10, 20, 30$ and 40°C/s. Each cooling cycle was repeated twice in order to validate dilatation measurements during austenite decomposition.

Before going further, the monitoring of the cooling rates was validated by plotting the cooling rate $\left(\frac{dT}{dt}\right)$ as a function of the temperature (T) as shown in figure 6.2.a. Prescribed cooling rates were obtained below 20°C/s. However, deviations from the baseline are observed at higher cooling rates (30-40°C/s). It should be noted that the temperature range (220-380°C) where deviations are revealed corresponds to that of the austenite-to-martensite transformation. Namely, phase transformations generate heat transfer requir-

ing *Gleeble* machine compensation which is more difficult to achieve in the case of high cooling rates. Lastly, it has to be pointed out that the final deviation of the cooling rate ($<150^{\circ}\text{C}$) is due to an early stop of the air pushing at the end of the cooling but it has no consequence in this study because all phase transformations occurred before.

Figure 6.2.b. shows the obtained dilatation curves characterized by slope changes typical of phase transformations. Dilatation curves were analysed using the tangent method described in section 2.3.3.1 (of chapter 2) to determine the austenite decomposition kinetics for the different cooling rates as shown in figure 6.2.c. Start and finish temperatures for ferrite and pearlite ($(F + P)_S$, $(F + P)_F$), bainite (B_S , B_F) and martensite (M_S , M_F) formation are gathered in table 6.1. They were used to plot the Continuous Cooling Transformation (CCT) diagram of the 100% γ -state (figure 6.2.d). Such values are in accordance with CCT diagrams available in the literature [COM 12]. Evaluated fraction of austenite decomposition products are also reported in table 6.1.

Three austenite decomposition kinetics were identified for the 100% γ -state as a function of the cooling rates:

- *At low cooling rates (1-10°C/s)*

Phase transformations take place at high temperatures, between 735 and 530°C. This corresponds to the domain of ferrite and pearlite formation. Austenite decomposition kinetics are therefore associated with the austenite-to-ferrite transformation ($\gamma \rightarrow \alpha$) followed by the austenite-to-pearlite transformation ($\gamma \rightarrow P = \alpha + \text{Fe}_3\text{C}$). Moreover, austenite decomposition kinetics are shifted to lower temperatures with increasing cooling rate R_C , which attests for a diffusive transformation.

- *At intermediate cooling rate (20°C/s)*

In this case, austenite decomposition kinetics is characterized by two stages during continuous cooling at 20°C/s. A first transformation is observed between 570 and 470°C: it was attributed to austenite-to-bainite transformation (*i.e.* $\gamma \rightarrow \alpha_B$). The second stage appears between 310 and 270°C and it was related to the austenite-to-martensite (*i.e.* $\gamma \rightarrow \alpha'$) transformation.

- *At high cooling rates (30-40°C/s)*

Austenite decomposition occurs between 370 and 235°C. In this case, austenite transforms into martensite (*i.e.* $\gamma \rightarrow \alpha'$). The fact that the martensitic kinetics superimpose, for the two cooling rates (30 and 40°C/s), points out the diffusionless character of the martensitic transformation. This is in accordance with the demonstrated athermal character of the transformation shown by Van Bohemen and Sietsma [VAN 14]. Moreover, it should be noted that the $\gamma \rightarrow \alpha'$ transformation identified as a second stage of the transformation occurring during the cooling at 20°C/s superimposes on the master $\gamma \rightarrow \alpha'$ kinetics measured at 30-40°C/s in the case of the full $\gamma \rightarrow \alpha'$ transformation.

6.1.2.2 Microstructural observations after cooling of the 100% γ -state

The microstructures obtained after cooling were observed by optical microscopy after Nital etching to complete the dilatometry results. They are shown in figure 6.3.

At low heating rates (1, 5 and 10°C/s), two phases can be clearly distinguished. The

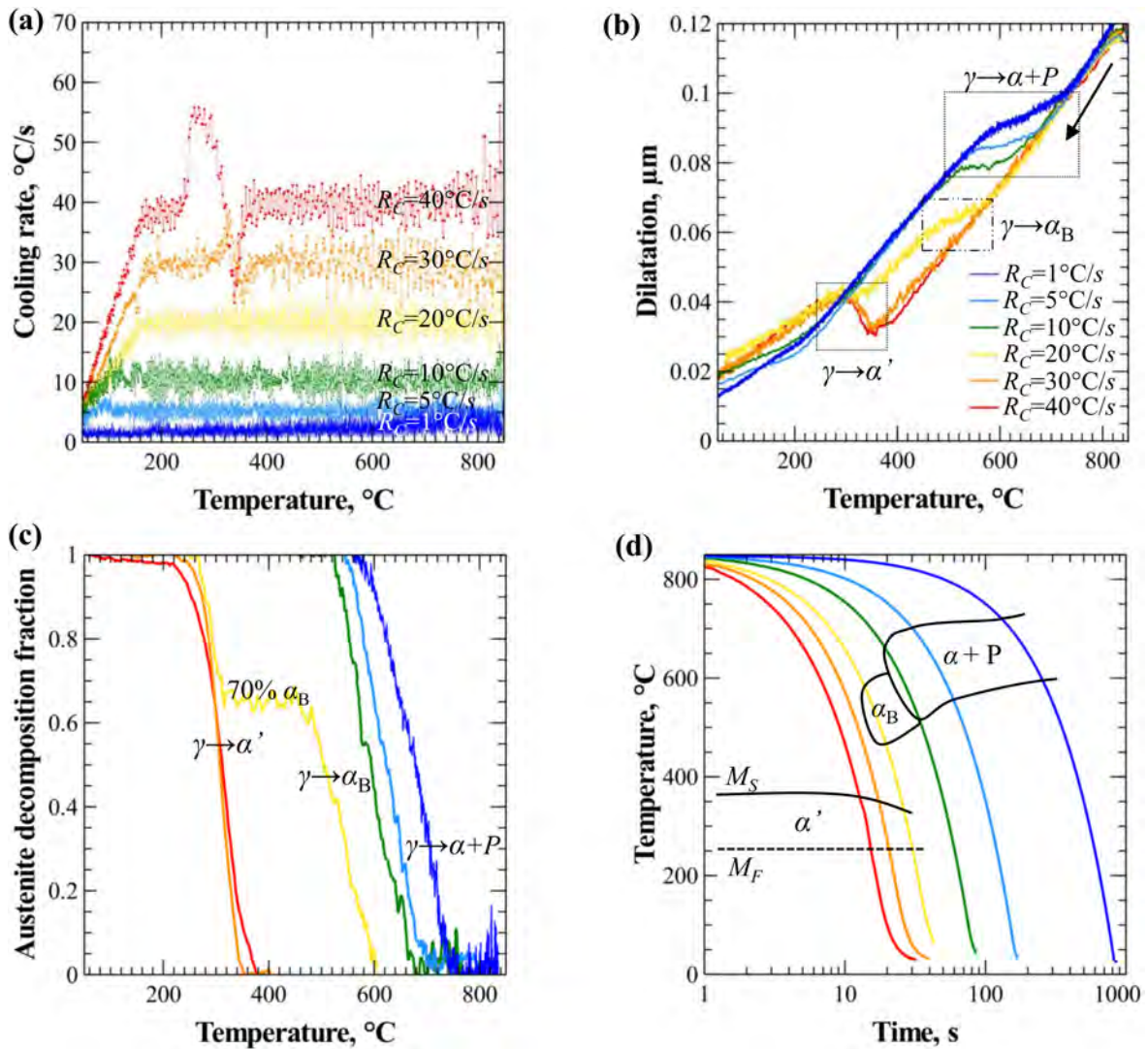


Figure 6.2: (a) Cooling rate evolutions, (b) Dilatation curves, (c) Austenite decomposition fractions and (d) CCT diagram of the 100% γ -state during continuous cooling from 850°C to room temperature at 1, 5, 10, 20, 30 and 40°C/s.

white phase corresponds to ferrite while the brown phase can be attributed to pearlite. It has to be noted that the proportion of phases evolves with the cooling rate: the fraction of pearlite expands with an increase of the cooling rate. It is supposed that at lower cooling rate, there is more time for diffusion so that a higher ferrite fraction can form before reaching the critical temperature where the pearlitic reaction takes place. Inversely, the austenite stability is increased increasing the cooling rate and this promotes pearlite formation. This may explain the decrease in the pearlite fraction with decreasing the cooling rate. Moreover, at 1°C/s cooling rate, black islands are observable in ferrite which are no longer observed at higher cooling rates. These features are supposed to be carbide

particles formed thanks to slow cooling rate.

The microstructure obtained after an intermediate cooling rate (20°C/s) exhibits a more complex microstructure but it is difficult to clearly differentiate bainite from martensite. Other etchant (Lepéra) and/or observation techniques (SEM, EBSD with misorientation analysis) would be necessary to analyse this complex state.

Finally, for the highest cooling rates (30 and 40°C/s), the microstructure appears to be fully martensitic.

Cooling rate	1°C/s	5°C/s	10°C/s	20°C/s	30°C/s	40°C/s
$(F + P)_S$	735°C	700°C	670°C	-	-	-
$(F + P)_F$	590°C	560°C	530°C	-	-	-
B_S	-	-	-	590°C	-	-
B_F	-	-	-	470°C	-	-
M_S	-	-	-	310°C	370°C	340°C
M_F	-	-	-	270°C	270°C	235°C
$f_{\alpha+P}$	1	1	1	-	-	-
f_{α_B}	-	-	-	0.70	-	-
$f_{\alpha'}$	-	-	-	0.30	1	1

Table 6.1: Start and finish temperatures for ferrite and pearlite ($(F + P)_S$, $(F + P)_F$), bainite (B_S , B_F) and martensite (M_S , M_F) formation during continuous cooling of the 100% γ -state with various cooling rates. Evaluated fraction of austenite decomposition products are also reported.

6.1.3 Cooling of a ferrite-austenite mixture (60% γ -state)

The cooling of a ferrite-austenite intercritical mixture (60% γ -state) was investigated using the same approach as for the 100% γ -state. Partially austenitized microstructures differ from those of the fully austenitic state on different aspects: (i) presence of ferrite/austenite interfaces; (ii) smaller austenite grain size; (iii) carbon enrichment in austenite due to ferrite rejection; (iv) eventual austenite enrichment in substitutional elements (Mn, Cr) and finally (v) presence of chemical gradients at the ferrite/austenite interface in the case of not complete transformation [ZHU 13]. All these characteristics may contribute to modify austenite decomposition during the cooling stage.

6.1.3.1 Kinetics of austenite decomposition of the 60% γ -state

Figure 6.4.a presents the austenite decomposition kinetics during continuous cooling from the 60% γ -state to room temperature for different cooling rates between 1 and 40°C/s. Similarly to the study of a 100% γ -state, start and finish temperatures for ferrite and pearlite ($(F + P)_S$, $(F + P)_F$), bainite (B_S , B_F) and martensite (M_S , M_F) formation are summed up in table 6.2 and have enabled to plot the CCT diagram of the 60% γ -state

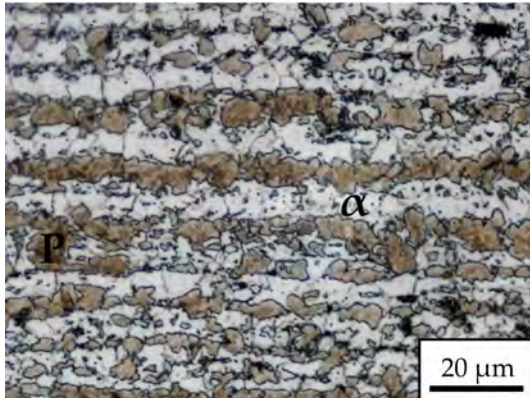
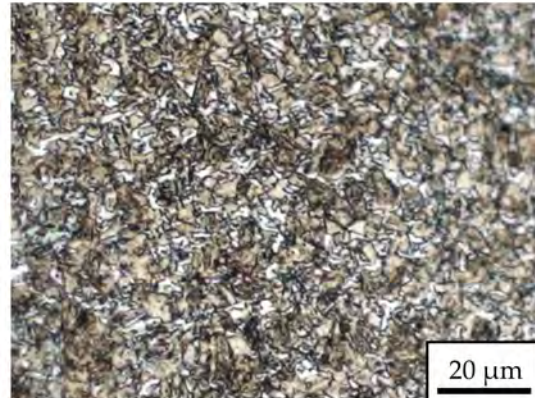
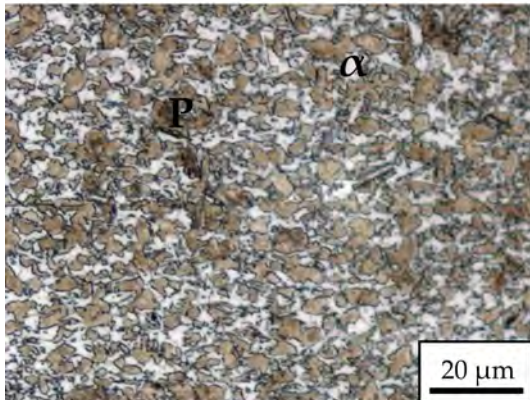
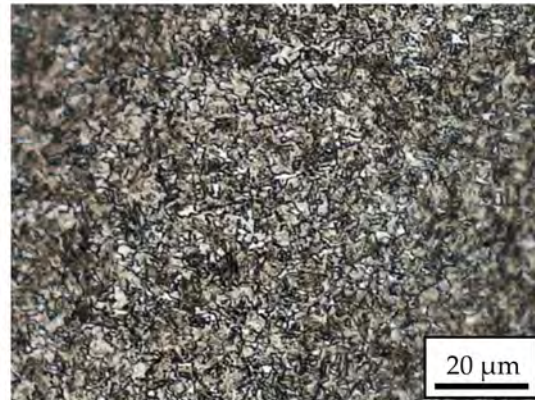
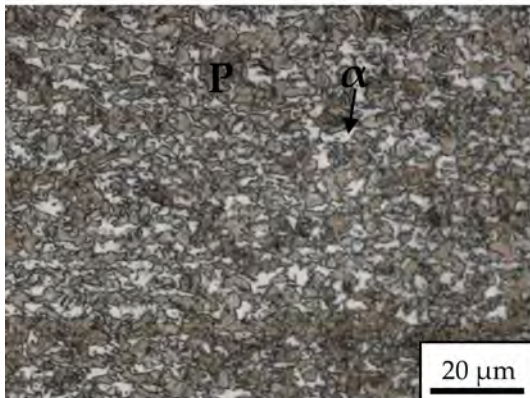
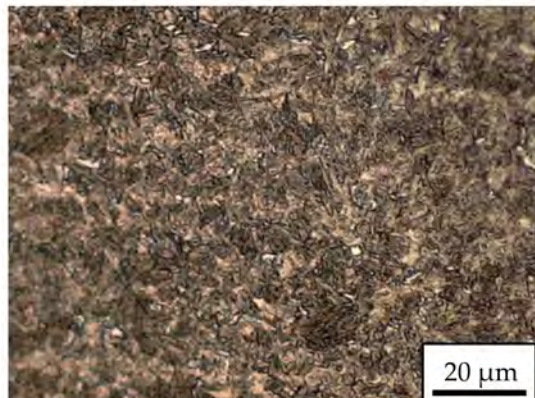
(a) $R_c = 1^\circ\text{C/s}$: 100% ($\alpha + P$)**(d)** $R_c = 20^\circ\text{C/s}$: 70% α_B + 30% α' **(b)** $R_c = 5^\circ\text{C/s}$: 100% ($\alpha + P$)**(e)** $R_c = 30^\circ\text{C/s}$: 100% α' **(c)** $R_c = 10^\circ\text{C/s}$: 100% ($\alpha + P$)**(f)** $R_c = 40^\circ\text{C/s}$: 100% α' 

Figure 6.3: OM micrographs of the 100% γ -state cooled at $R_C = 1, 5, 10, 20, 30$ and 40°C/s (resp. (a-f)). Nital etching. Quantified phase fractions, evaluated by dilatometry analysis, are reported in the caption of each micrograph.

(figure 6.4.b). Evaluated phase fractions induced by austenite decomposition are also reported in table 6.2.

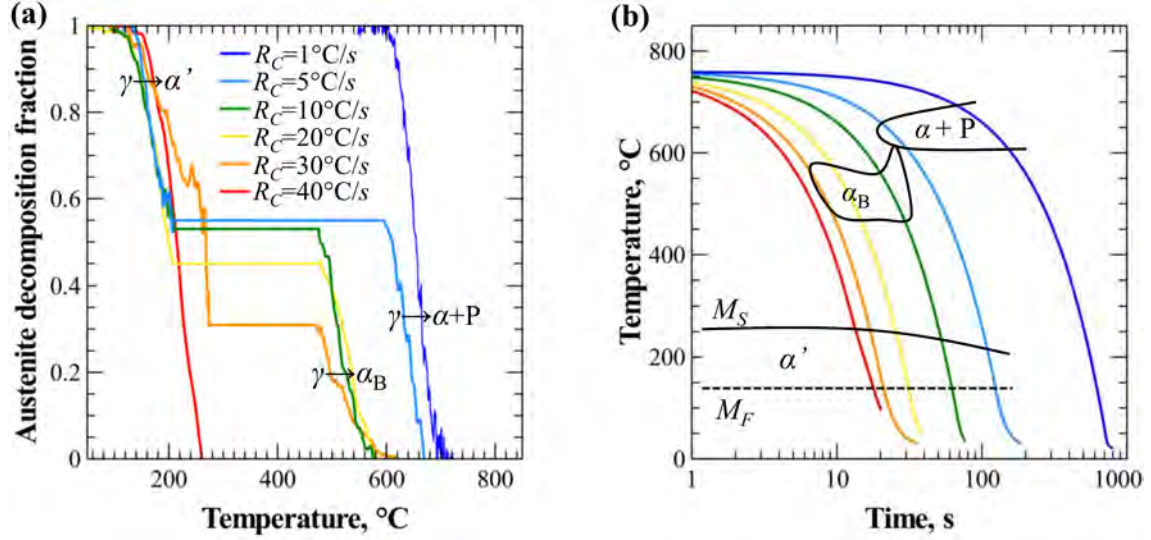


Figure 6.4: (a) Austenite decomposition fractions and (b) evaluated CCT diagram during the continuous cooling from 760°C to room temperature at 1, 5, 10, 20, 30 and 40°C/s.

Cooling rate	1°C/s	5°C/s	10°C/s	20°C/s	30°C/s	40°C/s
$(F + P)_S$	695°C	665°C	-	-	-	-
$(F + P)_F$	615°C	610°C	-	-	-	-
B_S	-	-	555°C	570°C	570°C	-
B_F	-	-	480°C	480°C	485°C	-
M_S	-	205°C	205°C	200°C	275°C	255°C
M_F	-	140°C	130°C	130°C	145°C	150°C
$f_{\alpha+P}$	1	0.55	-	-	-	-
f_{α_B}	-	-	0.53	0.45	0.31	-
$f_{\alpha'}$	-	0.45	0.47	0.55	0.69	1

Table 6.2: Start and finish temperatures for ferrite and pearlite ($(F + P)_S$, $(F + P)_F$), bainite (B_S , B_F) and martensite (M_S , M_F) formation during continuous cooling of the 60% γ -state with various cooling rates. In addition, fraction of austenite decomposition products are also reported.

Three phase transformation domains are once again observable. However, the cooling rate dependence is different from the cooling of a 100% γ -state.

In particular, the cooling path at 5°C/s is different from the one previously monitored because austenite first transforms into ferrite and pearlite (665-610°C) before austenite-

to-martensite transformation between 205 and 140°C. A complete comparison with the CCT diagram of the fully austenitic steel will be realized in section 6.1.4.

6.1.3.2 Microstructural observations after cooling a 60% γ -state

The microstructures obtained after cooling were observed by optical microscopy after a Nital etching and are shown in figure 6.5. It is noted that:

- For a cooling rate of 1°C/s (figure 6.5.a), the microstructure is composed of three different items. Ferrite phase appears in white. In some areas, white ferrite grains can be clearly distinguished from the white ferrite matrix. These ferrite grains formed during the cooling of the steel from the intercritical domain. Pearlite grains appear in brown and, identically to the fully austenitized steel, black islands, previously identified as cementite islands, are observed at this low cooling rate.
- For cooling rates between 5 and 30°C/s, Nital etching does not allow to differentiate martensite from bainite or pearlite because these three phases are coloured in brown with this type of etching.
- Lastly, the martensitic transformation was validated at 40°C/s since the corresponding microstructure is composed of ferrite (coming from the intercritical annealing) and martensite (in brown).

6.1.4 Comparison between the CCT diagrams of the 100% γ -state and the 60% γ -state

The CCT diagrams obtained for the two initial states of the steel are superimposed in figure 6.6. The CCT diagram of the 100% γ -state is plotted in dashed lines with the temperature domains of the different phases represented in light grey, while the one of the 60% γ -state is plotted in full lines (darker grey domains). Different phase domains may be compared:

- *Ferrite plus pearlite domain*
The domain associated with ferrite plus pearlite is globally similar for the cooling from the 100% γ -state or from the 60% γ -state.
- *Bainitic domain*
The bainitic domain is expanded for the partially austenitized steel: bainite is obtained on a larger range of cooling rate (10-30°C/s against only 20°C/s). Bainite temperature range is however not modified.
- *Martensitic domain*
The martensitic domain is notably shifted to lower temperature when austenitization treatment is partial. Moreover, martensite existence range is enlarged: a small amount of martensite seems to be formed even at 5°C/s. This extended martensite domain was related to an enriched carbon content in austenite before cooling, thus stabilizing the austenite phase and promoting the austenite-to-martensite transformation.

The critical cooling rate, ensuring the complete martensitic transformation, is different for the 100% γ -state and the 60% γ -state. It is in the range 20-30°C/s for the 100% γ -state

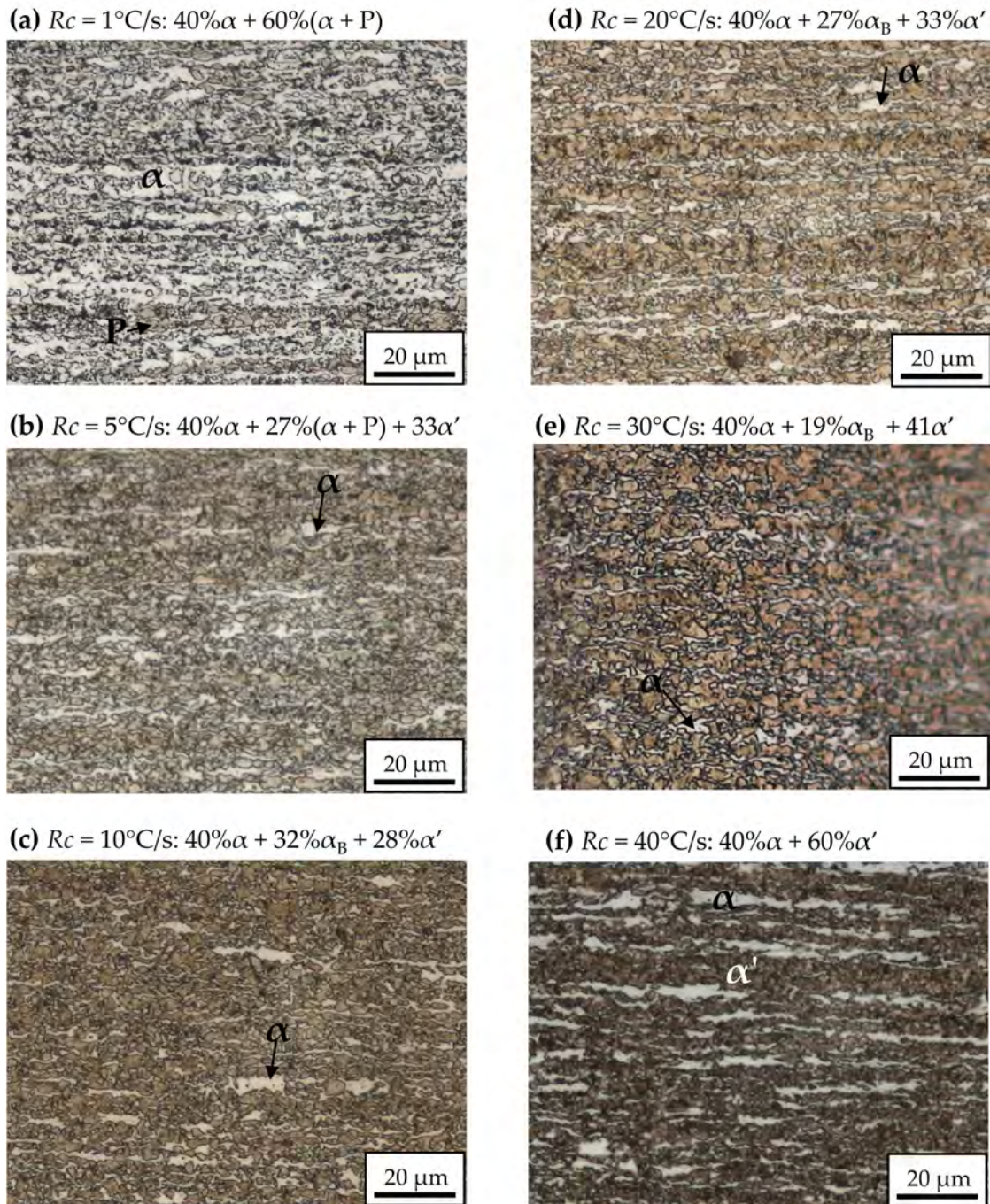


Figure 6.5: OM micrographs of the 60% γ -state cooled at $R_C = 1, 5, 10, 20, 30$ and 40°C/s (resp. (a-f)). Nital etching.

while a cooling rate of 30-40°C/s is required for a 60% γ -state. Higher cooling rate is thus required to ensure the austenite-to-martensite transformation in the case of partial austenitization.

The decrease of all ferrite, bainite and martensite start temperatures with increasing the austenite carbon content is in accordance with Wang *et al.* work [WAN 99] based on an artificial neural network (ANN) using 150 CCT diagrams. This comparison validates obtained evolutions in the case of partial austenitization where austenite contains higher carbon content.

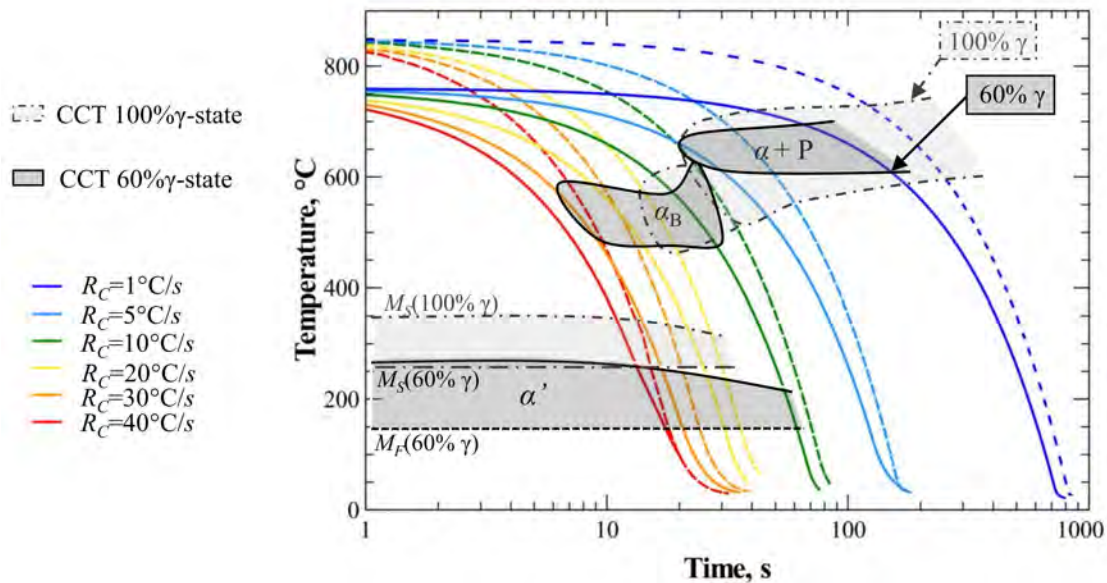


Figure 6.6: Comparison of the CCT diagrams obtained during continuous cooling of the 100% γ -state (dashed lines) and of the 60% γ -state (full lines).

6.1.5 Analysis of the martensite formation kinetics of the steel in the 100% γ -state and in the 60% γ -state

Commonly used models in the literature to describe (i) the martensite start temperature (M_S) and (ii) the austenite-to-martensite transformation kinetics ($f_{\alpha'}$) were applied to the developed experimental database in the case of the 100% γ -state and the 60% γ -state.

6.1.5.1 Martensite start temperature (M_S)

The martensite start temperatures predicted by the empirical models presented in tables 1.2 and 1.3 of chapter 1, are reported in figure 6.7. Martensitic start temperatures of the 100% γ -state were calculated using the bulk steel composition given in chapter 2.

For the 60% γ -state, the austenite carbon content was calculated from the mass balance $\left(C_C^\gamma = \frac{C_C^0 - (1 - f_\gamma) \times C_C^\alpha}{f_\gamma} \right)$ and it was found equal to 0.28 wt%C. The composition of all other substitutional elements was kept at the bulk composition as proposed by Bohemen and Sietsma [BOH 09b].

The experimental range for M_S temperature was also added in figure 6.7 considering $\pm 20\%$ of standard deviation on the dilatometry curves as large deviations were measured

in the determination of M_S temperatures (see tables 6.1 and 6.2). As observed, empirical formulae from the literature predict a large temperature range for the martensite start temperatures: from 335 to 450°C for the 100% γ -state and from 300 to 410°C for the 60% γ -state. First of all, these large prediction ranges may be due to several explanations such as different steel compositions, different austenitization treatments (governing austenite grain size) or different experimental techniques to capture the onset of the transformation.

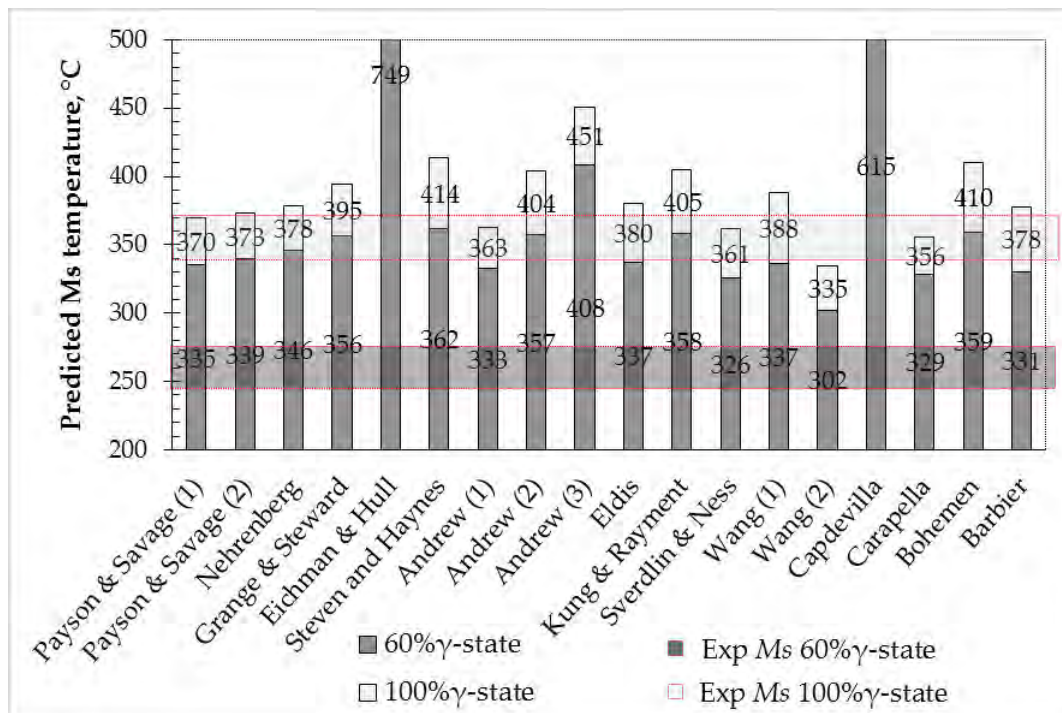


Figure 6.7: Comparison of the values of the martensite start temperature (M_S) calculated with the empirical formulae from the literature review with the experimental value for the 100% γ -state and the 60% γ -state.

For the 100% γ -state, it is possible to find several empirical formulae from the literature which can describe correctly the martensite start temperature. This is the case of the relations of Payson and Savage (1, 2) [PAY 44], Andrews (1), Sverdlin and Ness and Carapella [BAR 14]. It should be noted that Payson and Savage (2) and Andrews equations predict almost the same chemical element dependence for C, Mn and Si contrary to Sverdlin and Ness. Finally, Carapella's equation presents a mathematical product dependence of different elements.

Considering the 60% γ -state, it clearly appears that empirical formulae fail in the prediction of M_S temperature: M_S predictions are overestimated of approximately 50-100°C. Results of this study disagree with the works of Bohemen and Sietsma [BOH 09b] who showed that the carbon content is the only parameter to modify in the chemical composition to predict the M_S temperature of partially austenitized steels. These authors successfully validated the use of the Koistinen-Marburger relation with Andrews's equation for the prediction of the austenite-to-martensite transformation kinetics of three different

steels either fully or partially austenitized. In the case of partially austenitized steels, the carbon content was assessed with a mass balance. The main difference between the works of these authors and the present work concerns the chemical composition of the studied steels: steels have a higher carbon content (0.46-0.8 wt%) and are low alloyed (Mn~0.7, Si~0.3, Ni~0.1, Cr~0.2, Cu~0.2, P~0.01, S~0.03 wt%). Moreover, annealing treatments are longer with holding times between 420 and 1800 s which may lead to less heterogeneous chemical composition of austenite before the cooling stage.

Can Mn composition adjustment lead to a better prediction of M_S temperature?

The difficulty to predict the M_S temperature of the two phase steels shown in the present work could be due to the fact that the distribution of the substitutional elements may have to be taken into account. It should be noted that the assumption of a substitutional enrichment in austenite tends to decrease the predicted martensite start temperature as all substitutional elements have a negative influence on the evaluation of M_S . This strengthens the interest of the development of diffusive models for the description of the substitutional enrichment of austenite before cooling. From investigations of chapter 5, one can deduce that the Mn enrichment of austenite after 10^2 - 10^3 s at 760°C is not homogeneous (see figure 5.8). In this time scale, the Mn content in austenite is mainly equal to the one in prior ferrite with a local diffusion spike at the interface (induced by the LENP condition) and a strong Mn enrichment in the austenite core, footprint of the prior cementite dissolution. The average Mn content in austenite was evaluated as being equal to 1.87 wt%Mn (against a bulk equal to 1.763 wt%Mn) but it is not enough to explain the lower M_S value in the case of partial austenitization. Only a decrease of 10°C is induced considering this average Mn concentration in austenite. To lower the M_S predictions in the range 240 - 270°C , the Mn content in austenite should be equal to 4-5 wt%Mn. Such range of Mn content in austenite can eventually be predicted by the simulation of chapter 5. However, such a content is unreachable in the bulk for the considered thermal treatment. The redistribution of other alloying elements having a strong influence in M_S formulae (as Cr, Si, Ni) should also be considered.

In addition, it should be noted that the presence of ferrite/austenite interfaces and the smaller austenite grain size of the two-phase steel are not taken into account in the empirical formulae, although these two parameters may have a major role on martensite formation.

6.1.5.2 Austenite-to-martensite transformation kinetics ($f_{\alpha'}$)

After having considered the prediction of the M_S temperature, the austenite-to-martensite transformation kinetics was modeled using two approaches:

1. The Koistinen-Marburger law:

$$f_{\alpha'} = 1 - \exp(-\alpha_m (M_S - T)) \quad (6.1)$$

with (1.i) Andrews and (1.ii) Bohemen 's equations for α_m and M_S parameters (table 1.5)

2. Skrotzki equation [SKR 91] which is defined as a function of three adjusting parameters (M_S , M_F and n):

$$f_{\alpha'} = 1 - \left(\frac{T - M_S}{M_S - M_F} \right)^n \quad (6.2)$$

Figure 6.8 presents the results relative to the modeling of the austenite-to-martensite kinetics for the 100% γ -state and the 60% γ -state. Concerning the 60% γ -state, it was chosen to use the average experimental M_S value (260°C) as previous presented empirical formulae were not enable to predict it correctly.

KM law with Andrews' equations enables to describe the phase transformation kinetics of the 100% γ -state while KM with Bohemen's parameters and Strotzki predictions are not accurate. Similarly, the KM equation is applicable to the 60% γ -state when the experimental M_S temperature is taken into account. The main difficulty is thus to be able to predict the M_S temperature of the two-phase steel.

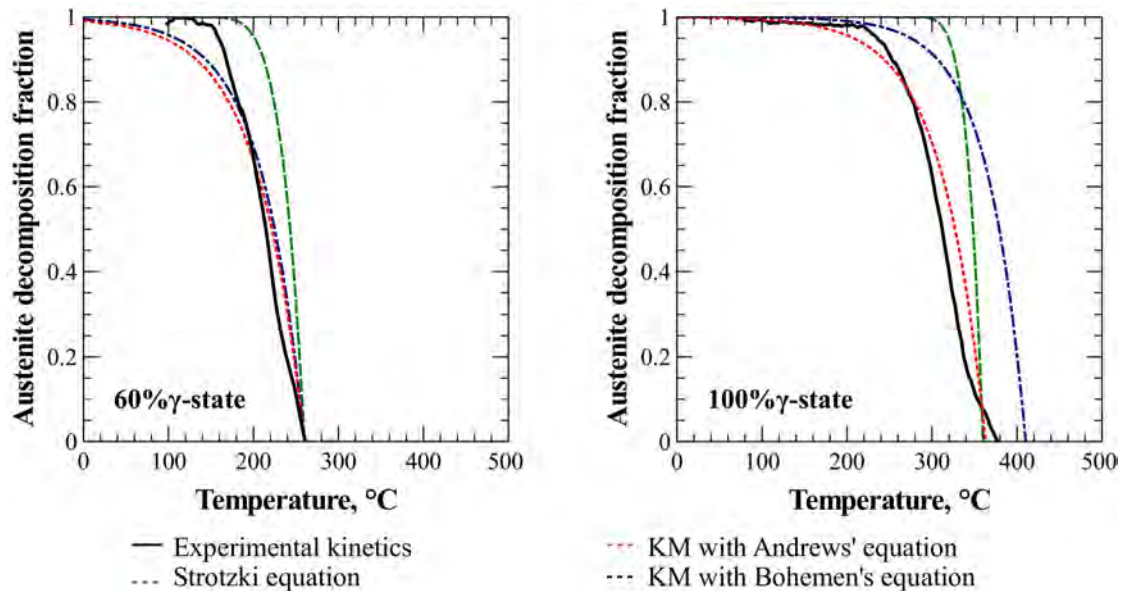


Figure 6.8: Comparison of the austenite-to-martensite transformation kinetics based on empirical formulae from the literature with the experimental kinetics for the 100% γ -state and the 60% γ -state.

6.1.5.3 Conclusion

The martensite start temperature (M_S) and the martensitic transformation kinetics could be modeled in the case of the 100% γ -state. Several empirical formulae for M_S temperature were validated for the investigated steel (Payson and Savage (1, 2) [PAY 44], Andrews (1), Sverdlin and Ness and Carapella [BAR 14]) and the kinetics was correctly modeled by the well-known Koistinen-Marburger equation with Andrews' relationship.

However, commonly used empirical formulae for the martensite start temperature (M_S) and the austenite-to-martensite transformation kinetics ($f_{\alpha'}$) were not directly validated

in the case of partial austenitization when only the austenite carbon content is taken into account in the chemical composition of the steel. It was proposed to take into account the redistribution of substitutional elements in austenite during partially austenitized treatments. However, this was not found sufficient to explain the discrepancies. Other factors have to be considered such as the prior austenite grain size or the number of potential martensite nucleation sites (austenite/ferrite interfaces, smaller austenite grains) which is supposed to be increased in the case of partial austenitization. Moreover, in all reported models, there is no dependence with the prior austenite grain size or with the number of potential martensite nucleation sites (austenite/ferrite interfaces, smaller austenite grains) which is supposed to be increased in the case of partial austenitization. Dependence of the intercritical state on the austenite-to-martensite transformation appears complex and complementary studies are needed before predicting with accuracy the kinetics. In particular, it would be interesting to consider the substitutional element redistribution in austenite by modifying the annealing conditions and by studying other steel chemistries.

6.2 Martensite tempering of the fully martensitic steel

To continue the works on the microstructural evolutions during the thermal treatment of DP steels, the martensite tempering, that may occur during the coating and/or overageing treatment of these steels, was investigated between 200 and 500°C.

It was chosen to focus on the martensite tempering of the fully martensitic steel obtained by a treatment of 120 s at 850°C followed by a water-quench. The first objective of the work was to identify the mechanisms involved in the martensite tempering of the studied steel between 200 and 500°C. To this end, the microstructural evolutions and mechanical changes of the steel were followed by thermoelectric power (TEP) and hardness measurements during isothermal treatments. Then, in a second step, a quantification of the precipitated carbon fraction based on TEP measurements was proposed and confronted with the results given by FIB/SEM tomography. Lastly, the final objective of this work was to show if a correlation can be found between the amount of precipitated carbon (or of the carbon remaining in solid solution in martensite) and the loss of mechanical strength during tempering, with the aim of proposing a modeling of the martensite softening during tempering.

6.2.1 Identification of the martensite tempering mechanisms between 200 and 500°C

6.2.1.1 TEP kinetics

In order to highlight the mechanisms involved in the martensite tempering of the fully martensitic steel, the TEP variations of the steel, were measured during isothermal treatments at temperatures between 200 and 550°C (figure 6.9.a) by the relationship $\Delta S(t,T) = S(t,T) - S_0$, where S_0 is the initial TEP before any tempering and $S(t,T)$ is the TEP value after a tempering at temperature T for a time t . Except at the highest temperatures (450 and 550°C), TEP tends to gradually increase during tempering and the measured TEP variations become higher when the tempering temperature is increased.

At first sight, the measured TEP variations can be related to the evolution of the carbon content in solid solution, as this element is known to have a strong negative influence on TEP when it is in solution in iron. Hence, a departure of this element from the solid solution due to segregation or precipitation phenomena is expected to lead to a TEP increase. According to the TEP kinetics shown in figure 6.9.a, the amount of carbon atoms leaving the solid solution seems to increase with increasing the time and the temperature of the tempering treatment.

Another important point is that the TEP kinetics are shifted towards shorter treatment times when the temperature is increased, suggesting that phenomena, responsible for the TEP variations, are thermally activated. Therefore, a time-temperature equivalence based on an Arrhenius law was used to find the equivalent time at 200°C for all tempering treatments performed at T and to build a unique master curve.

As can be seen in 6.9.b, a unique master curve could be built, using two different apparent activation energies: (i) one for the low tempering temperatures (200, 250 and 300°C) and (ii) another one for the high temperatures (350, 450 and 550°C). This suggests that at least two different tempering mechanisms might be involved in the investigated temperature range. In fact, a third mechanism is visible, on the TEP master curve, for long tempering times at high temperatures. Namely, after having reached a maximum, TEP starts to decrease.

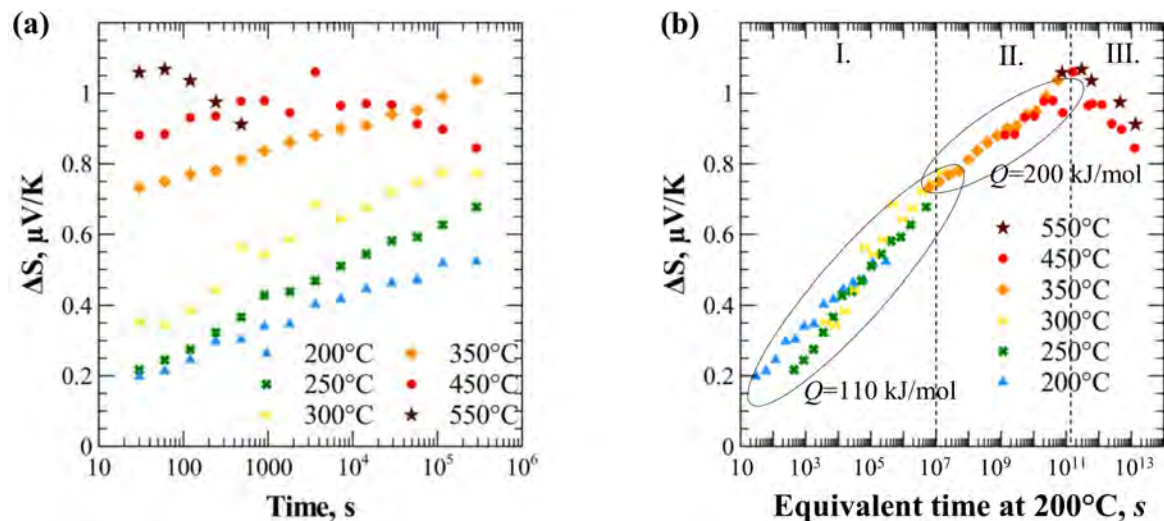


Figure 6.9: (a) TEP kinetics during isothermal tempering treatments at 200, 250, 300, 350, 450 and 550°C. (b) Master curve at 200°C obtained by a time-temperature equivalence.

At low temperature, the apparent activation energy of 110 kJ/mol is close to that reported by Mittemejer *et al.* [MIT 88], Morra *et al.* [MOR 01] and Waterschoot *et al.* [WAT 06] for intermediate carbide precipitation. At high temperature, the apparent activation energy of 200 kJ/mol can be attributed to cementite precipitation. This is consistent with the values of activation energy (176-212 kJ/mol) determined by Mittemejer and Morra for cementite precipitation.

With regard to the third mechanism, it could be due to the fact that the diffusion of the substitutional elements can be important at high temperature (for long tempering times) and can lead to a progressive substitutional enrichment of the cementite particles already reported in the literature (chapter 1). In the studied steel, the two main elements which are likely to diffuse and enrich the cementite particles are chromium and manganese. Taking into account the fact that chromium in solution in iron is known to have a positive influence on TEP, its departure from the solid solution is expected to lead to a TEP decrease [HOU 02]. This is not the case for manganese which has a negative influence on TEP [MAS 03]. In these conditions, it seems that the third mechanism could be attributed to a gradual chromium enrichment of the cementite particles.

It has also to be pointed out that above 400°C, other phenomena (such as the recovery of the lath structure) are expected to occur. Recovery may lead to a progressive decrease in the dislocation density which could be responsible for a slight TEP increase (due to the negative influence of dislocations on TEP).

As a conclusion, the analysis of the TEP kinetics highlighted that three mechanisms are involved in the martensite tempering of the fully martensitic steel between 200 and 500°C. A first identification of these phenomena, requiring further analyses, was proposed :

- I. the first mechanism was attributed to the precipitation of intermediate carbide (ε , η or Hägg) below 300°C,
- II. the second mechanism was assigned to cementite precipitation above 300°C,
- III. the third mechanism was considered to be due to the possible chromium enrichment of the cementite particles for times superior to 1 hour at 450°C and for short treatment times at 550°C.

The aim of the next sections is to validate these three mechanisms using TEM observations on carbon replicas.

6.2.1.2 EDS analysis on TEM replicas

The cementite enrichment in substitutional elements (Mn, Cr) was quantified by EDS analysis on TEM replicas. It was initially planned to evaluate the cementite chemistry after three tempering times at 450°C: (i) 30 s, (ii) 3600 s and after (iii) 10 days, where the carbide enrichment is supposed to be marked. However, no carbides were found on the carbon replicas for the first two tempering conditions due to the difficulties in the preparation of the samples for TEM observations. Only, the last condition will therefore be presented.

As shown in figure 6.10, after 10 days at 450°C, carbide particles are enriched in Cr and Mn elements with average contents equal to 8.5 wt%Cr and 21.6 wt%Mn and large dispersion ranges. These values are close to the thermodynamic equilibrium concentrations calculated at 13.3 wt%Cr and 33.5 wt%Mn for the system Fe-0.17C-1.763Mn-0.427Cr-0.345Si-0.037Al (wt%) at 450°C. The Cr enrichment may explain the decrease in the TEP value for long tempering times at 450°C as the Cr element leaves the martensitic solid solution.

In addition, it should be noted that cementite particles are strongly enriched in manganese despite the low temperature treatment (450°C). This suggests that the diffusion of substitutional elements is promoted by the high dislocation density of martensite responsible for pipe-diffusion.

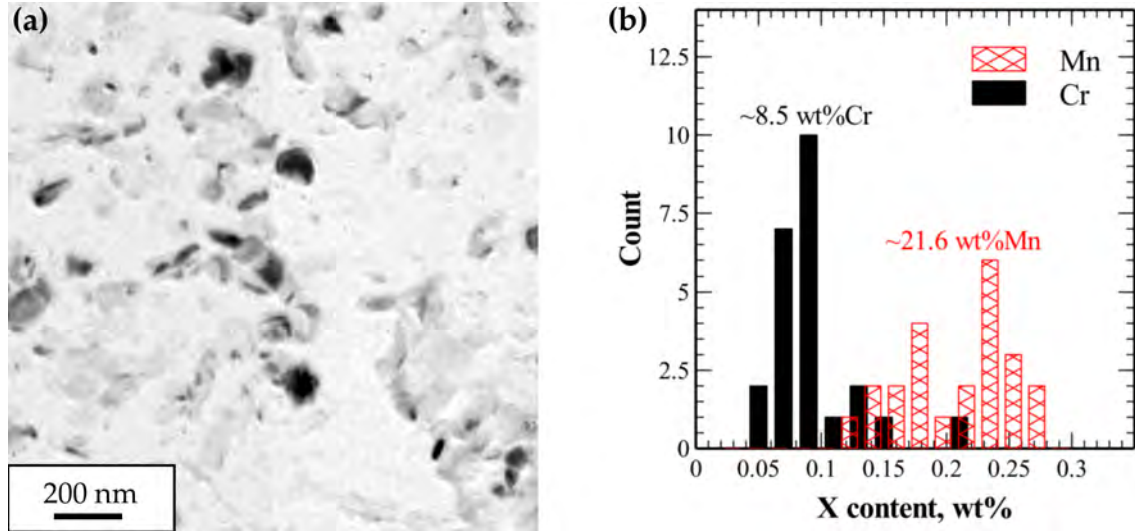


Figure 6.10: (a) TEM micrograph and (b) EDS analysis of carbide particles after 10 days at 450°C.

6.2.2 Quantification of the amount of precipitated carbon during tempering

Previous presented TEP results were analysed to estimate the amount of precipitated carbon during martensite tempering treatments.

6.2.2.1 Quantification by TEP

The TEP kinetics of figure 6.9.a were used to assess the amount of precipitated carbon during the different tempering treatments performed between 200 and 550°C. To this end, the TEP variations measured after each tempering condition were converted into precipitated carbon using the Gorter-Nordheim relation:

$$C_C^{pre} = \frac{\Delta S}{P_C} \quad \text{with} \quad P_C (\mu V \cdot ^\circ C / \%wt) = \frac{\alpha_c s_c}{\rho} = \frac{517.5 (\mu V / ^\circ C \cdot \mu \Omega \cdot cm / wt\%)}{\rho} \quad (6.3)$$

where P_C is the influence coefficient of carbon in iron which depends on the resistivity of the steel. In this analysis, we assumed that the precipitates formed during tempering have a negligible effect on TEP.

Using a device developed at MATEIS laboratory, based on the four-point method, the resistivity of the studied steel was measured at 20°C on a long sample which was fully

austenitized and then water-quenched before the resistivity measurement. The value of the resistivity was found to be equal to $29.5 \mu\Omega\cdot\text{cm}$, leading to an influence coefficient of carbon in iron equal to $17.6 \mu\text{V}\cdot^\circ\text{C}/\% \text{wt}$. This value was considered to be constant during all the tempering treatments, although it may be slightly modified during tempering due to the carbon precipitation.

Taking into account this value for P_C , it was possible to plot the kinetics given the precipitated carbon content (C_C^{pre}) during tempering as a function of time for different temperatures (figure 6.11.a). The points corresponding to the third tempering stage were not taken into account in this analysis, as they are not only related to the departure of carbon from the solid solution. In addition, the fraction of precipitated carbon ($f_C^{pre} = \frac{C_C^{pre}}{C_C^{tot}}$) after each considered tempering condition was plotted in figure 6.11.b: it clearly highlights that this fraction is rather low and never exceeds 40%, suggesting that a non negligible amount of carbon atoms remains in solid solution after tempering or that carbon atoms have already precipitated/segregated before tempering (austempering effect).

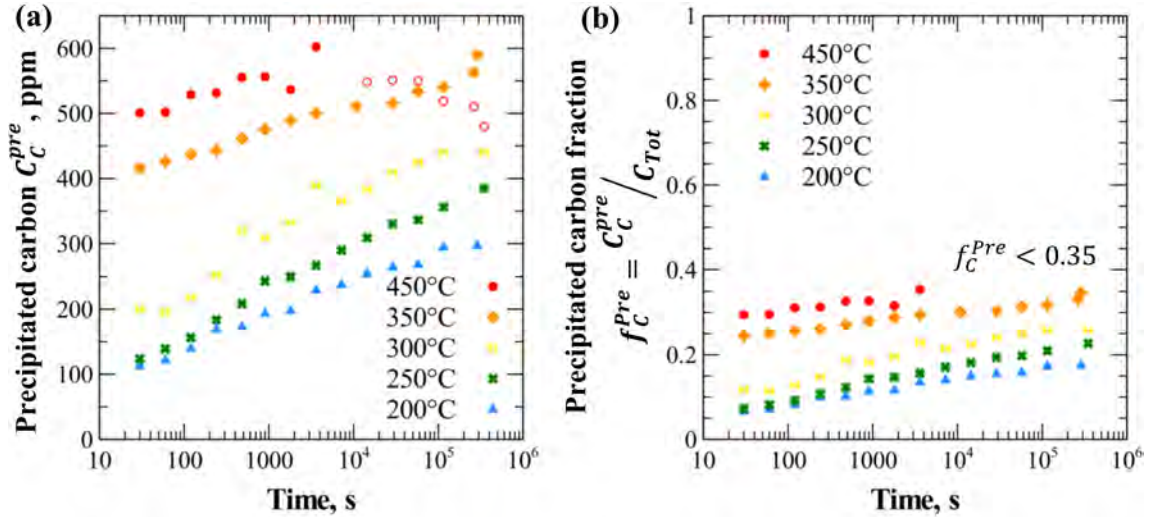


Figure 6.11: Determination of (a) the precipitated carbon content (C_C^{pre}) and (b) the fraction of precipitated carbon (f_C^{pre}) in martensite determined from TEP experiments.

In fact, it has to be noted that the TEP variations measured during tempering only take into account the amount of carbon atoms that precipitated during tempering and do not consider the carbon atoms which could potentially segregate to the dislocations or lath boundaries during the water-quench from the annealing temperature due to the relatively high M_s value of the steel (of the order of 380°C). This means that TEP could underestimate the amount of segregated or precipitated carbon atoms.

In order to check the validity of the analysis conducted by TEP, the amount of precipitated carbon was assessed by 3D reconstructions by FIB/SEM tomography of a volume of matter treated for 30 s at 450°C . According to TEP, after such a tempering, the amount of precipitated carbon is expected to be of the order of 0.05% (500 ppm).

6.2.2.2 Quantification by FIB/SEM tomography

The results of the quantification by FIB obtained on the steel treated for 30 s at 450°C are represented in figure 6.12. For such a short treatment, no enrichment of cementite in substitutional elements is expected. In order to dissociate the precipitates from their surrounding matrix, the recorded BSE images for each ablated section (figure 6.12.a) were first filtered and treated with *Image J* (figure 6.12.b). Then, sub-volumes were reconstructed: they were chosen in areas where the crystallographic contrast was sufficient to distinguish easily the precipitates from the surrounding matrix. Figure 6.12.c shows such a sub-volume which was used to estimate the precipitated volume fraction.

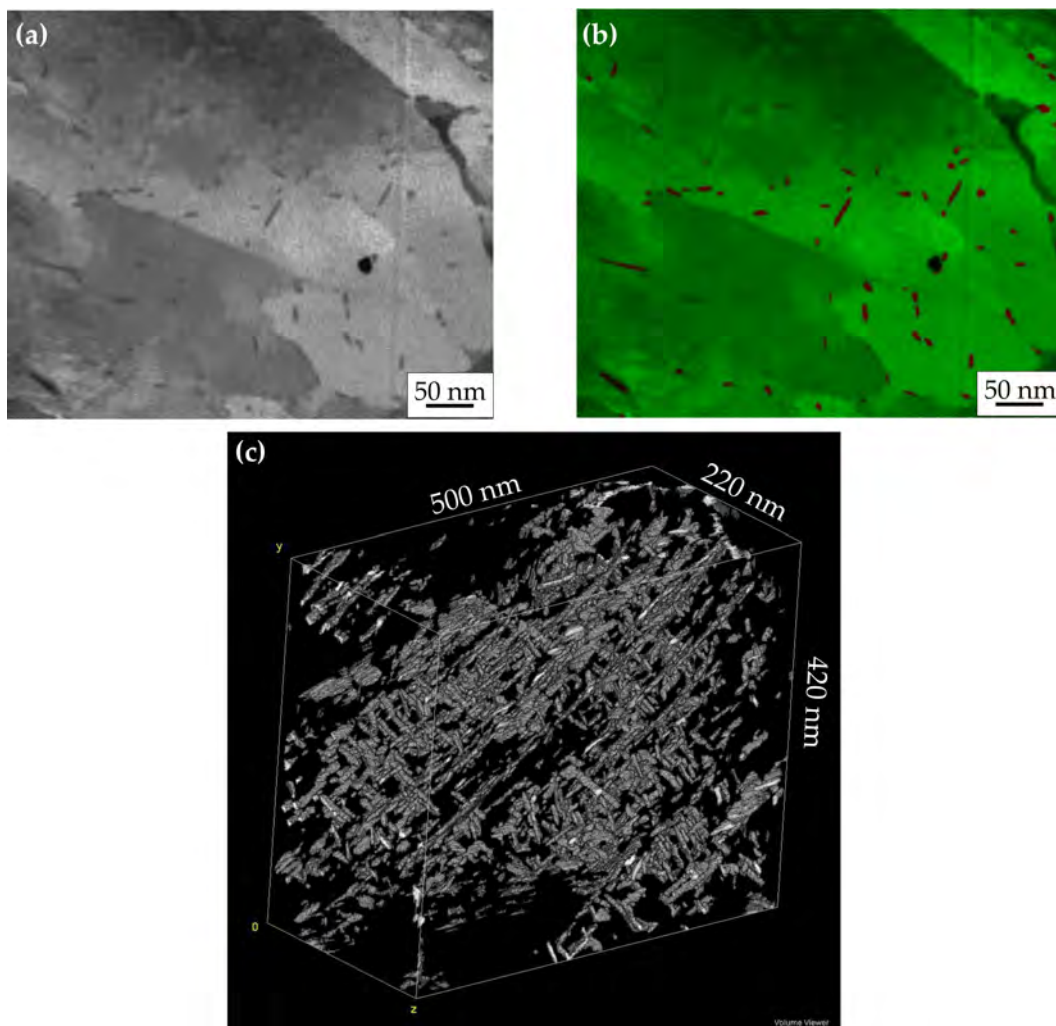


Figure 6.12: (a) BSE image and (b) corresponding analyzed image revealing carbides. (c) 3D-reconstruction by FIB/SEM tomography of a volume showing precipitates present in the steel treated for 30 s at 450°C.

From the analysis of several sub-volumes, the cementite volume fraction was evaluated to $1.35 \pm 0.3 \%$. If we consider that cementite is formed according to the following relation:

$3\text{Fe} + \text{C} \longrightarrow \text{Fe}_3\text{C}$, this volume fraction corresponds to an amount of precipitated carbon of 0.09 wt%. This amount is much less than the total carbon content of the steel (0.17 wt%) which should lead to a volume fraction of precipitates of 2.55%.

Consequently, the preceding results confirm the fact that the amount of precipitated carbon after 30 s at 450°C is notably inferior to the total carbon content of the steel. While TEP estimates that this amount is of the order of 0.05 wt%, it is assumed to be of the order of 0.09 wt% according to FIB tomography.

As already explained in the preceding section, TEP could underestimate the amount of precipitated carbon, as this technique does not consider the phenomena that could occur during the water-quench of the steel. Moreover, the proposed quantification of carbide precipitation by TEP depends on the value of the influence coefficient of carbon (P_C): a precise calibration would be necessary. However, this technique presents the advantage to be global and to give a quantification of the average precipitated carbon content in the whole sample.

At the same time, it has to be noted that errors can come from the quantification by FIB. Firstly, threshold errors can be induced by image analysis. Secondly, the choice of the analysed sub-volumes can introduce errors, as the chosen sub-volumes are not necessarily representative of the precipitation state in the whole material. Lastly, it has to be pointed out that precipitates other than cementite can be taken into account in the quantification. Namely, carbo-nitrides rich in Ti and Nb were clearly detected by EDS during the observation of carbon extraction replicas (figure 6.13). Such precipitates have different sizes and morphology. Hence, it is difficult to use a selection criterion to withdraw them from the quantification.

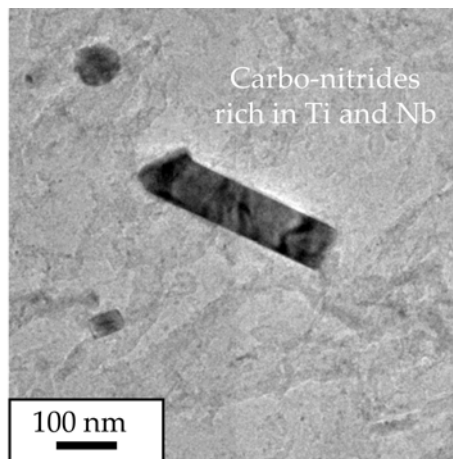


Figure 6.13: TEM micrograph of carbo-nitrides rich in Ti and Nb observed after a martensite tempering of 30 s at 450°C (carbon replica).

In spite of all these difficulties, the important point to note is that the two techniques used for the quantification give the same tendency: the amount of precipitated carbon in the temperature range between 200 and 450°C is relatively low compared to the total carbon of the steel. In other words, this means that a substantial amount of carbon atoms

remains in solid solution (or is segregated on dislocations or at laths boundaries) after tempering in this temperature range as clearly observed by APT by Xiao *et al.* [XIA 16].

Based on evaluated carbon contents from TEP measurements and FIB analysis, a scenario of carbon distribution after a tempering treatment at 450°C during 30 s is proposed in figure 6.14. After such a treatment, the carbon fraction involved in cementite particles appears relatively low compared to the total carbon content (C_C^{Tot}). Indeed, only 35% of the total carbon content is assumed to contribute to cementite precipitation. This latter fraction was quantified from the TEP variation measured during the martensite tempering for 30 s at 450°C: it is only related to the departure of carbon atoms from the solid solution during the tempering. The remaining carbon atoms seem to be partly precipitated in other types of precipitates (ex. carbonitrides as shown in figure 6.13) or segregated to dislocations or lath boundaries [XIA 16]. An estimation of the carbon content precipitated in other types of precipitates can be performed using the FIB measurement: around 0.03 wt% of carbon atoms seem to be included in these precipitates (that is say, about 20% of the total carbon content). In these conditions, one can estimate that the fraction of segregated carbon atoms is of the order of 45% of the total carbon content. Higher energy (*i.e.* higher temperature) is required to allow segregated carbon atoms to displace and become available for cementite precipitation thanks to recovery mechanism. The segregation of carbon atoms probably occurred during the quenching stage (*i.e.* austempering). These carbon atoms seem to be no longer available for carbon precipitation in usual industrial time scale (450°C - time < 1 h).

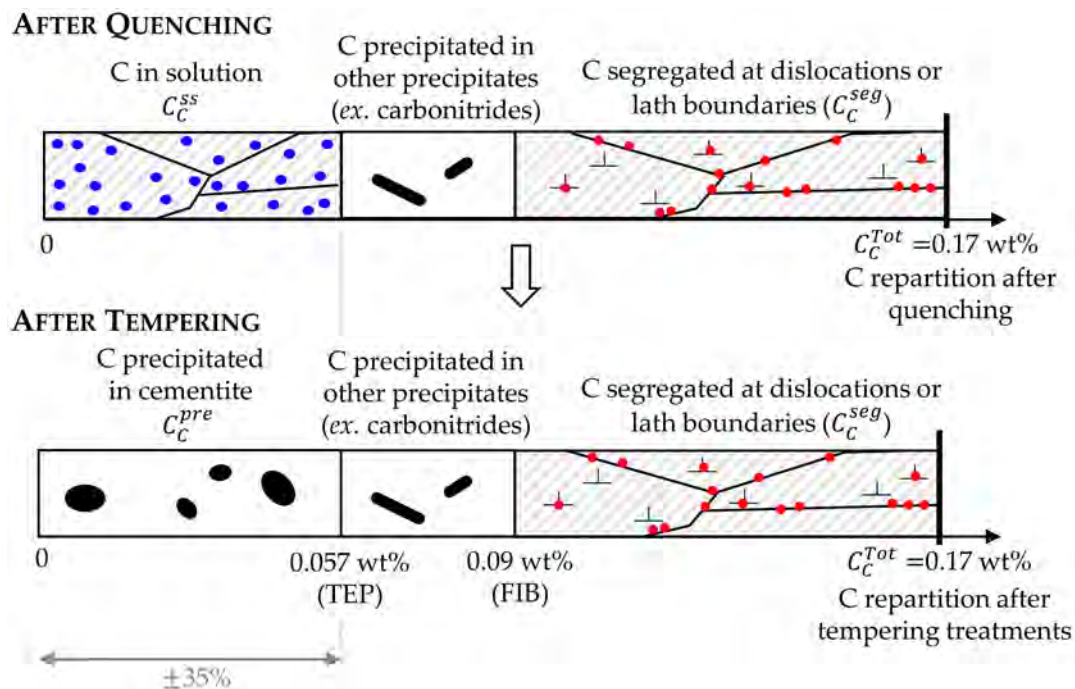


Figure 6.14: Scenario of C distribution during a tempering treatment at 450°C for 30 s: only 35% of the total carbon content contributes to cementite precipitation.

In order to go further in these investigations, it would be necessary to ensure accurate calibration of the TEP technique by comparing the results given by this technique and by other techniques. A first possibility would be to use ICP (Inductively Coupled Plasma) spectrometry to evaluate the volume fraction of precipitates after different tempering treatments [LEG 10]. Another possibility would be to evaluate the carbon content in solution in martensite by Atom Probe Tomography. X-ray diffraction on tempering martensite could also be used to quantify the carbon content in martensite. This requires very important investigations which could not be conducted in the present PhD-work.

6.2.2.3 Prediction of the fraction of precipitated carbon

The evolution of the fraction of precipitated carbon was modeled using the isothermal JMAK formalism expressed as follows:

$$f_C^{pre} = \frac{C_C^{pre}}{C_C^{tot}} = 1 - \exp(-(bt)^n) \quad (6.4)$$

Two JMAK laws were considered, taking into account the results of the study based on the TEP kinetics (presented in section 6.2.1). The two activation energies, previously determined in section 6.2.1, were kept in the JMAK modeling: 110 kJ/mol for $200^\circ\text{C} \leq T \leq 300^\circ\text{C}$ and 200 kJ/mol for $350^\circ\text{C} \leq T \leq 450^\circ\text{C}$.

The avrami parameters (n) were determined by linearization of the JMAK law (according to equation (1.5), chapter 1). The JMAK linearization is shown in figure 6.15.a. Two n values were determined for the two temperature ranges: n_1 was found to be equal to 0.15 for 200-300°C while n_2 was fixed at 0.13 for 350-450°C.

Lastly, the b_0 parameter of the JMAK laws was adjusted to obtain the best fit of the experimental kinetics. JMAK prediction of the precipitated carbon content at various holding temperatures is shown in figure 6.15.b using the two sets of parameters given in table 6.3. The predicted kinetics are in good agreement with the experimental tempering kinetics. Once again, this simple approach based on a JMAK law allows diffusional phenomenon to be predicted with good accuracy.

Phenomenon	Q , kJ/mol	n	b_0 , /s
Precipitation of intermediate carbides (JMAK_1) (200-300°C)	110	0.15	2×10^6
Precipitation of cementite (JMAK_2) (350-450°C)	200	0.13	9×10^{15}

Table 6.3: JMAK parameters for the two tempering mechanisms: (i) precipitation of intermediate carbides (JMAK_1) and (ii) precipitation of cementite (JMAK_2).

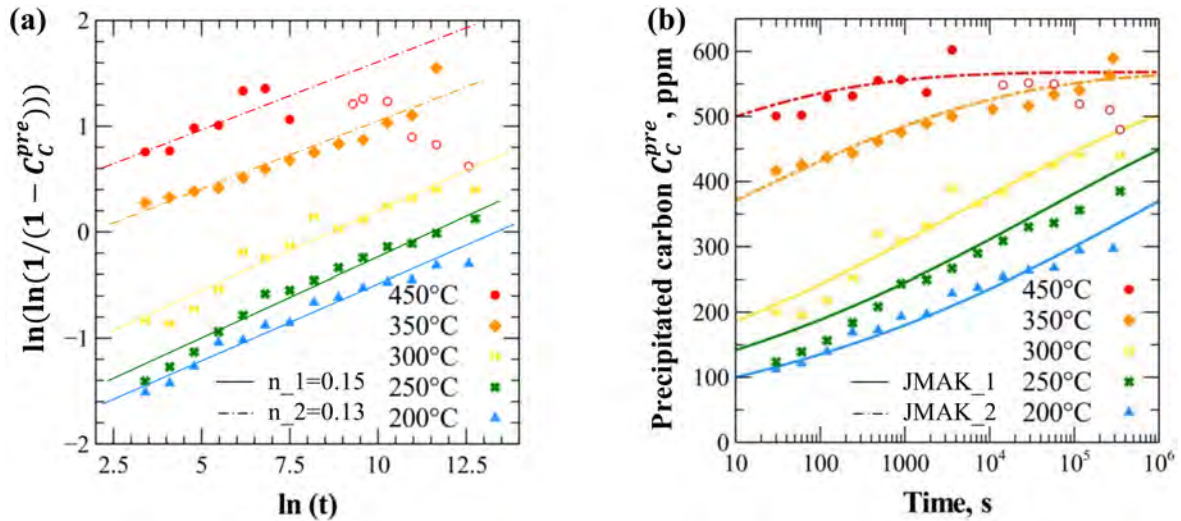


Figure 6.15: (a) Linearization of the isothermal JMAK law for the determination of the Avrami coefficient. (b) JMAK modeling of the precipitated carbon during tempering for intermediate carbide and cementite precipitation as given in table 6.3.

6.2.3 Hardness evolution during tempering

6.2.3.1 Hardness kinetics

In parallel to the TEP measurements, the kinetics associated with the loss of hardness during martensite tempering were determined at different temperatures. They are shown in figure 6.16.a. Hardness gradually decreases during isothermal holding and the loss of hardness appears to be more marked and faster at high temperature.

As in the case of the TEP kinetics, a time-temperature equivalence was applied at 200°C with the hardness kinetics using the same activation energies as those determined from TEP measurements: 110 kJ/mol at low temperature ($T < 300^\circ\text{C}$) and 200 kJ/mol at high temperature ($T > 300^\circ\text{C}$). Figure 6.16.b shows that these two activation energies give rise to a good superimposition of the kinetics on the same master curve. This suggests that phenomena responsible for TEP decrease and hardness decrease are the same.

Figure 6.17 represents the hardness evolution of the tempered martensite as a function of the tempering temperature for different tempering times equal to 30, 120 and 3600 s. A holding time inferior or equal to 3600 s at 200°C has a low impact on martensite hardness. This is also the case for an holding time less than 120 s at 250°C. By contrast, martensite is considerably softened during the first seconds of tempering at 450°C. Coating and overageing treatments may therefore strongly lower the mechanical strength of martensite. There is consequently a need of predictive tools to evaluate the martensite softening occurring during these stages. This is why, in the following sections, a link will be established between the model for carbide precipitation and the loss of mechanical properties during tempering.

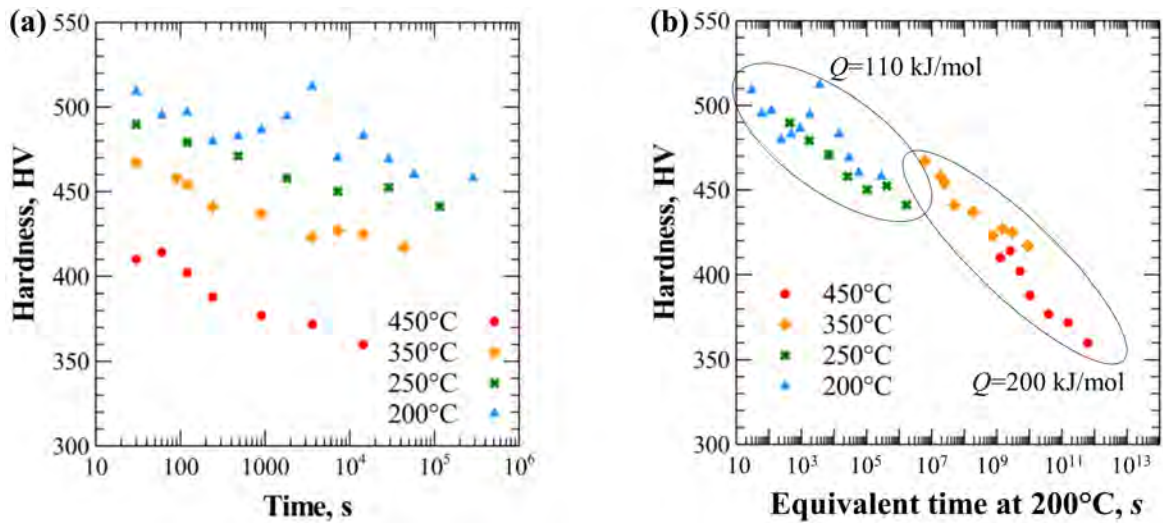


Figure 6.16: (a) Evolution of the hardness during isothermal tempering treatments at 200, 250, 300, 350 and 450°C. (b) Time-temperature equivalence at 200°C of hardness values using the same activation energies as those determined from TEP measurements.

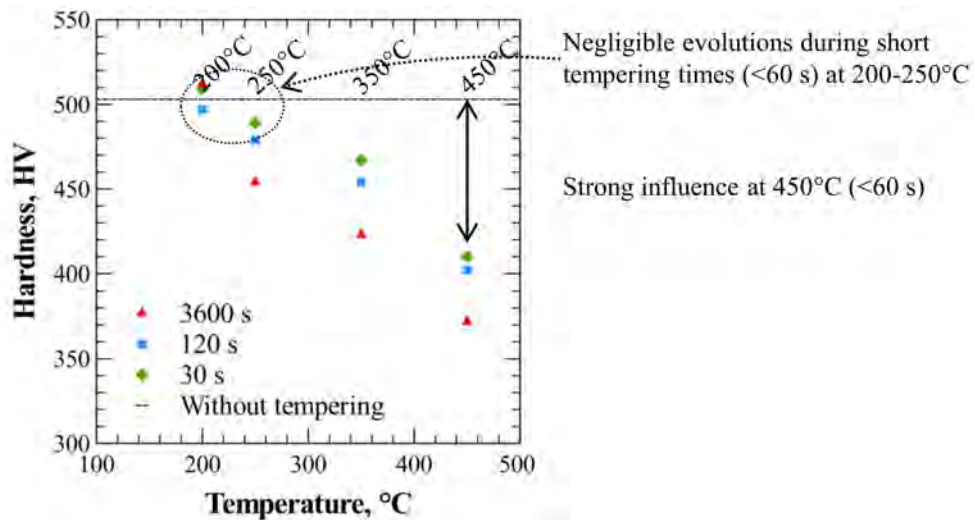


Figure 6.17: Hardness evolution of the tempered martensite as a function of the tempering temperature for different tempering times: 30, 120 and 3600 s.

6.2.3.2 Comparison of estimated carbon content in solid solution and segregated

In order to compare estimated carbon contents remaining in solid solution (C_C^{ss}) and segregated at dislocations or lath boundaries (C_C^{seg}) in martensite after different tempering conditions with literature, the hardness of the tempered martensite was plotted, in fig-

ure 6.18, as a function of its non-precipitated carbon content assessed by TEP or FIB for different tempering conditions ($C_C^{non-pre} = C_C^{tot} - C_C^{pre}$). The experimental points corresponding to a tempering at 450°C for times superior to 240 s were removed, as the amount of precipitated carbon (and thus, of the non-precipitated carbon) cannot be calculated with accuracy from TEP measurements due to the non-negligible influence of the diffusion of the substitutional elements at high temperature.

In the same figure, the points coming from the works of Speich *et al.* [SPE 72] (shown in figure 1.14 of chapter 1) were added. They give the evolution of the martensite hardness as a function of its total carbon content (before any tempering treatment, “fresh” martensite) and show that martensite hardness evolves linearly with the carbon content of the steel for carbon contents lower than 0.4%. Here, it has to be noted that Speich *et al.* worked on binary Fe-C alloys. However, as was shown by Grange *et al.* [GRA 77], hardness of fresh martensite is not affected by the amount of alloying elements (such as Mn, P, Si, Ni, Cr, Mo and V) as long as their content does not exceed 1.95 %Mn, 0.28 %P, 0.85 %Si, 1.55 %Ni, 0.63 %Cr, 0.41%Mo and 0.18%V respectively. These conditions are satisfied in the case of the steel studied in this PhD-work.

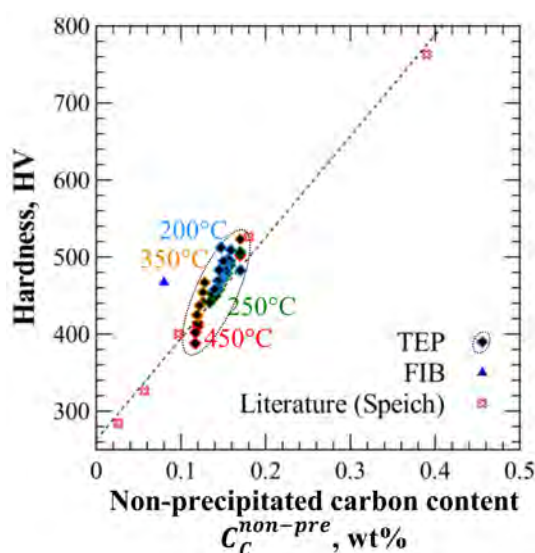


Figure 6.18: Hardness evolution of the tempered martensite as a function of its non-precipitated carbon content assessed by TEP or FIB. Comparison with data of the literature for “fresh” martensite with different carbon contents.

As can be seen in figure 6.18, the experimental points obtained in the present work for different tempering conditions are (surprisingly) rather well aligned with the straight line deduced from the works of Speich *et al.* This suggests that the hardness of tempered martensite could be mainly controlled by its non-precipitated carbon content (either in solid solution or segregated) and that the effect of the precipitates formed during tempering is not predominant. Carbon atoms in solid solution and segregated have a similar effect on the mechanical behaviour, with a strong strain hardening effect. However, it is impossible to dissociate these two populations.

Moreover, the dependence between hardness and non-precipitated carbon content appears quite similar between experimental and literature values. This representation therefore tends to comfort the estimated precipitated carbon contents and strengthens the hypotheses of limited carbon fraction involved in cementite precipitation.

6.3 Prospective works on the tempering of a ferrite-martensite microstructure

The study was then extended to the tempering of a ferrite-martensite microstructure typical of that of DP steels. The two-phase microstructure was obtained by a treatment at 760°C during 180 s followed by a water-quench leading to a microstructure with 60% of martensite and 40% of ferrite.

Similarly to the case of the fully martensitic steel, hardness evolutions of the dual-phase microstructure were measured on interrupted isothermal treatments realized at 250, 350 and 450°C. Figure 6.19.a shows hardness evolutions. As expected, hardness decreases during tempering all the more as the tempering temperature is high, suggesting that the phenomena responsible for the loss of hardness are thermally activated.

A time-temperature equivalence was thus performed at 250°C using the same activation energies as those determined for the tempering of the fully martensitic microstructure (figure 6.19.b). As can be seen, hardness points superimpose on a same master curve validating the activation energies for intermediate carbide (110 kJ/mol) and cementite (200 kJ/mol) precipitation (200 kJ/mol).

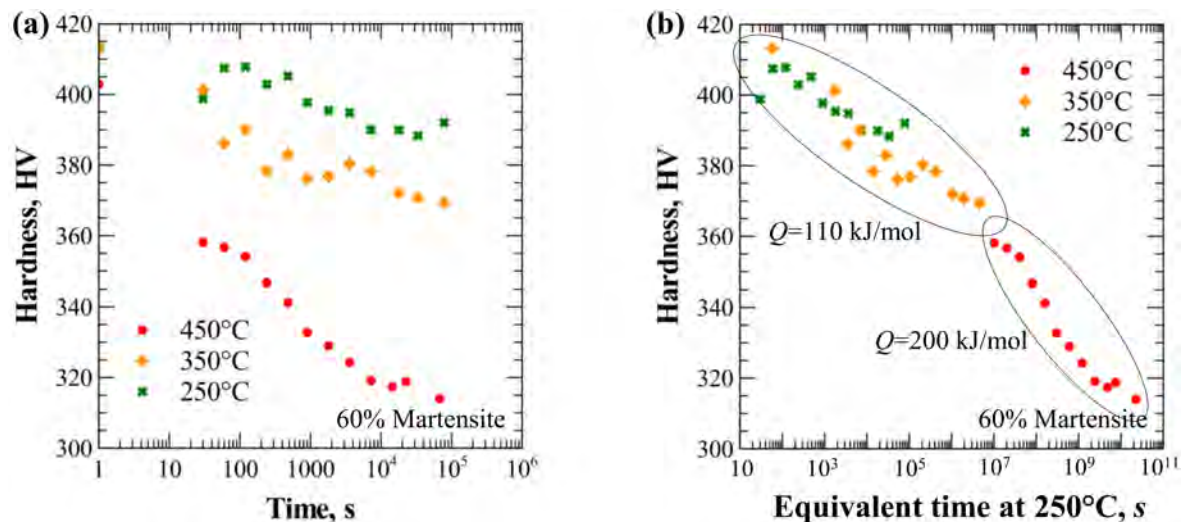


Figure 6.19: (a) Evolution of the hardness during isothermal tempering treatments of the ferrite-martensite mixture. (b) Time-temperature equivalence at 250°C using two activation energies for intermediate carbide (110 kJ/mol) and cementite (200 kJ/mol) precipitation.

To model the hardness evolution during the tempering treatments of a ferrite-martensite mixture, hardness of the two phases should be evaluated individually and linked together in a mixture law function of type:

$$HV = f_{\alpha'}HV_{\alpha'} + (1 - f_{\alpha'})HV_{\alpha} \quad (6.5)$$

This requires to be able to estimate: (i) the martensite hardness ($HV_{\alpha'}$) of the two phase steel as a function of the precipitated carbon fraction (f_C^{pre}) and (ii) the ferrite hardness (HV_{α}) which is likely to be influenced by the presence of martensite islands.

6.4 Discussion and conclusion

This last chapter focused on microstructural evolutions occurring during the cooling and the tempering stages of the DP thermal treatment. A special care was dedicated to investigate typical industrial conditions. Namely, the austenite decomposition was studied not only from a single phase fully austenitized state but also from an intercritical state where austenite and ferrite phases are present before cooling. With regard to the steel tempering, the studies were performed mainly from a fully martensitic state. Before investigating, in detail, the more complex case of the two phase steel, several works would be necessary to validate the assumptions obtained on the single phase steel. They could not be done in the present PhD-thesis due to a lack of time.

Cooling stage

The austenite decomposition kinetics were analysed varying the cooling rate from 1 to 40°C/s. Three phase transformation were identified:

- I. Austenite-to-(ferrite+pearlite) above 600°C. This transformation is progressively shifted to lower temperature range with an increase in the cooling rate, proof of diffusive mode. Concerning the microstructure, the pearlite fraction was found to increase when the cooling rate was increased which was related to improved austenite stability;
- II. Austenite-to-bainite around 500-600°C;
- III. Austenite-to-martensite below 400°C. The athermal character of this transformation was verified by cooling rate independence above the critical cooling rate for martensite transformation;

CCT diagrams were evaluated from the fully and partially austenitic states highlighting the key importance of the intercritical state before cooling. Phase transformation domains evolve: ferrite, bainite and martensite start temperatures are decreased; the bainitic domain is enlarged and the martensitic domain is lowered in the case of the partially austenitized state.

Concerning the martensitic transformation, CCT diagram comparison pointed out the evolution of the critical cooling rate for which the austenite-to-martensite transformation occurs. The critical cooling rate increases from 20-30°C/s for the fully austenitized state to 30-40°C/s for the partial austenitization composed of 60% of austenite. This evolution was attributed to the carbon enriched austenite as previously reported by Bohemen and

Siestma [BOH 09b]. A chemical stabilization of the austenite, by carbon enrichment, leads to lower the start temperature and the rate of transformation. Industrially, the modification of the critical cooling rate has to be taken into account because it may be necessary to adapt the cooling technology to reach higher cooling rates and to ensure the austenite-to-martensite transformation.

Common models of the literature were applied to describe the martensite start temperature M_S and the austenite-to-martensite transformation kinetics. Models allow to describe the martensite formation in fully austenitized steels. It was however pointed out that well approved models for the fully austenitized steels appear no more validated neither for the M_S nor for the kinetics (mainly due to the fact that the M_S value is not well described) in the case of the partially austenitized states. Only C adjustment is insufficient to ensure a good description of the transformation shift in low-alloyed steels while Bohemen and Sietsma [BOH 09b] successfully showed a correlation with austenite carbon content in the case of the intercritical annealing of a 0.46-0.8C, 0.7Mn, 0.3Si, 0.1Ni, 0.2 Cr, 0.2Cu wt% steel at 725 and 735°C. Discrepancies were explained by the need to take into account the chemical concentration of various substitutional alloying elements (for example, Mn) for times between 620 and 1800 s. These results strengthen the need to predict the intercritical state before cooling, in particular to describe the “on-time” chemical composition of the austenite phase at the end of the annealing stage.

In addition, it should be noted that applied models were developed only on the chemical composition. Other microstructural information may be supposed to be mandatory to describe the austenite-to-martensite transformation in the case of partial austenitization. As an example, while Bohemen and Sietsma stated that the effect of austenite grain size is negligible above 20% of martensite fraction [VAN 14], the austenite grain size may be an important parameter in the case of partial austenitization.

Tempering stage

The tempering study was studied on a fully martensitic steel to simplify the problem to a single-phase state. Three mechanisms involved in the martensite tempering were identified as a function of the temperature range:

- I. Precipitation of intermediate carbide between 100 and 300°C;
- II. Precipitation of cementite occurring in the temperature range between 350 and 450°C;
- III. Chromium enrichment of cementite particles above 450°C;

These three mechanisms were pointed out combining TEP, hardness and EDS analyses of cementite particles by TEM microscopy of carbon replicas. Two different activation energies were identified for these two first phenomena: 110 kJ/mol for the intermediate carbide precipitation and then 200 kJ/mol for the cementite precipitation.

TEP evolutions during tempering treatment were analysed to evaluate the precipitated carbon content ($C_{pre}^{\alpha'}$), the carbon content in solid solution ($C_{ss}^{\alpha'}$) and the precipitated carbon fraction (f_C^{pre}) in martensite during tempering treatments.

Carbon evolutions were modeled using two consecutive JMAK laws for:

1. the intermediate carbide precipitation with the parameter set: $Q=110$ kJ/mol;

$$n=0.15, b_0=2 \times 10^6 \text{ /s}$$

2. the cementite precipitation with the parameter set: $Q=200 \text{ kJ/mol}$; $n=0.13$, $b_0=9 \times 10^{15} \text{ /s}$

JMAK models enable to describe the carbon evolution below 450°C. Above this temperature, TEP values on which the model was developed are influenced by the chromium enrichment in cementite. Hence, the amount of precipitated carbon cannot be assessed from the TEP measurements above 450°C. JMAK descriptions are thus validated below 450°C.

A scenario was proposed to describe the carbon atom repartition after tempering treatments in typical industrial conditions. The proportion of carbon atoms involved in the cementite precipitation appears restricted (35% of C_C^{Tot}). The remaining carbon atoms are assumed to be precipitated in the form of other types of precipitates (*ex.* carbonitrides) and to be segregated at dislocations or lath boundaries.

Lastly, some tempering treatments were realized on a ferrite-martensite mixture. It was suggested, from hardness measurements, that the same mechanisms as those determined on the fully martensitic steel (intermediate carbide precipitation, carbide precipitation, cementite equilibration) occur in the two phase steel. This was explained by the fact that the evolution of the ferrite phase during tempering is low and the martensite carbon enrichment of the two-phase steel has no pronounced effect on the tempering mechanisms.

Conclusion and Perspectives

Conclusion

The present PhD-work was aimed at characterizing and modeling microstructural evolutions occurring during the thermal treatment of cold-rolled dual-phase steels. Three main stages of thermal cycles were investigated: (1) the intercritical annealing leading to recrystallization and austenite formation, (2) the cooling where austenite decomposes into different possible products and lastly (3) the tempering of the ferrite-martensite microstructure. The influence of cycle parameters (such as the heating rate, intercritical temperature *etc.*) on microstructure was analysed.

This PhD-work was mainly focused on the intercritical stage which plays a major role on the metallurgical evolutions occurring during the cooling and tempering stages. Chapters 3, 4 and 5 were dedicated to this first thermal stage, while chapter 6 dealt with the microstructural evolutions during the cooling and tempering stages of the DP thermal treatments.

Main steel evolutions during the intercritical step (carbide spheroidization, recrystallization and austenite formation) were first experimentally characterized in **chapter 3**. An adapted protocol has been defined to decorrelate recrystallization and austenite formation which may occur at the same time: (i) austenite formation was investigated without recrystallization (on prior recrystallized steels) and (ii) recrystallization was monitored without phase transformation (below the austenite start temperature). These studies allowed simple JMAK models to be developed both for recrystallization and austenite formation under non-isothermal conditions. The austenite fractions were calculated using LENP conditions which were found to predict successfully the austenite fractions in typical industrial times ($t < 3600$ s). This work enabled to point out large cycle parameter conditions where recrystallization and austenite formation occur simultaneously and may interact in cold-rolled steels.

The study was then focused on the metallurgical evolutions of cold-rolled steel states where both recrystallization and austenite formation are expected. An acceleration of austenite formation kinetics was reported in the cold-rolled steel compared to the prior recrystallized steel. This was mainly attributed to the interaction with recrystallization kinetics. Non-recrystallized ferrite grains could: (i) promote austenite nucleation as the stored energy during the cold-rolling could increase the driving force for austenite formation, (ii) increase the number of nucleation sites (due to the high fraction of deformed grains) and (iii) accelerate the diffusion of elements driving the phase transformation (pipe

diffusion). It was thus supposed that the austenite formation kinetics is different in the deformed ferrite grains and in the recrystallized ferrite grains. This was modeled by a mixture law taking into account the recrystallization progress and the two different austenite formation kinetics for the cold-rolled and recrystallized ferrite grains. In addition, the recrystallization inhibition above a critical austenite fraction was implemented to test this experimental fact which was reported several times in the literature. The proposed model enabled to predict the austenite formation kinetics in cold-rolled steels and to describe complex evolutions during continuous heating cycles with various heating rates.

To our knowledge, the proposed approach to describe microstructural evolutions in cold-rolled steels is original as the interaction is modeled by the well-known analytical JMAK laws and a mixture law dependent on recrystallization progress and distinguishing the two types of austenite formation sites. The previously discussed recrystallization inhibition above a critical austenite fraction was implemented and ensured a satisfactory description of experimentally characterized evolutions. A better description of the strong interaction is thus achieved. The model captures the influence of cycles parameters (heating rate, annealing temperature and time) on the microstructural evolutions of cold-rolled DP steels. This tool is pragmatic to predict evolutions but, as it is based on phenomenological assumptions, the model is defined for the investigated steel chemistry and reduction ratio. More standalone models are required to take into account the steel chemistry and its initial state.

A more physical description of the ferrite-to-austenite formation was proposed in **chapter 4** on the prior recrystallized steel (without interaction with the recrystallization). A mixed-mode model was implemented to describe the austenite formation kinetics because it enables to take into account steel informations ensuring a first step in physical based modeling. In this type of approach, the austenite formation is driven by the coupling of carbon diffusion and limited interface motion due to lower diffusivity of substitutional atoms. The model considers the steel chemistry which governs number of input parameters (initial cementite fraction, driving force, LENP condition *etc.*). A unique mobility parameter set (Q_m and M_0) was fixed and validated for all experimental conditions; either in non-isothermal conditions ($5 < R_H < 30^\circ\text{C/s}$) or during complex thermal cycles ($R_H = 5$ or 100°C/s ; $T = 735, 760$ or 780°C). The mixed-mode model was found to describe correctly the influence of the cycle parameters on the austenite formation kinetics.

The model analysis showed that the fixed activation energy for interface mobility (Q_m) is very high and can not be related to any physical event. The mobility parameter acts as a friction force slowing down carbon diffusion and representing the global effect of different substitutional elements. Moreover, the high value of the mobility (M) pointed out limited mixed-mode character; the austenite formation is “interface-controlled” in most thermal cycle conditions. This was attributed to the fact that the interface motion is very limited due to the very slow Mn diffusion compared to C diffusion (factor 10^3). Based on this fact, the PhD-work was then oriented on fully diffusive models (chapter 5). However, the mixed-mode model is relevant to describe the austenite formation kinetics in multiple substitutional alloying elements, the diffusion of which may be difficult to model (ex. N-dimension planes of equilibrium for N-order system).

Due to the major role played by the diffusion of the substitutional elements in austenite formation, the transformation was modeled by a fully diffusive model in **chapter 5** to answer to standalone expectations. The diffusion module of Thermo-Calc, DICTRA, was used in this study to describe the austenite formation from an initially cementite-ferrite system. It was chosen to limit the system to Fe-C-Mn ternary system supposing that other alloying element do not drive austenite formation. Moreover, the use of a ternary system enables to be confident in the used thermodynamic database and to model the two cementite/austenite and austenite/ferrite interfaces. In a first step, various capabilities of DICTRA were investigated in order to define calculation parameters (*ex.* austenite nucleation was not taken into account). Secondly, the study was focused on the influence of microstructural characteristics, like the system size or cementite Mn content, on the austenite formation kinetics.

The simulation was then applied to describe the experimental austenite formation kinetics, determined in chapter 3, for the ReX-steel and the CR-steel. To this end, the Mn cementite content and the system size were adapted. The austenite formation kinetics was quite well predicted at 780 and 760°C although the phase transformation modeling was not convincing at 735°C where experimental austenite formation kinetics appear quicker than the calculated ones. The consideration of other alloying elements driving the austenite formation kinetics should be tested. Apparently, the difference of Mn content between the ReX-steel and the CR-steel seems insufficient to explain the marked acceleration in the CR-steel case. A better agreement may be obtained considering different system size with larger grains in the case of prior recrystallized steel. However, it should be kept in mind that the ferrite grain size of CR-steel is expected to evolve in parallel to the austenite formation.

Lastly, **chapter 6** investigated the characterization of microstructural evolutions occurring during the cooling and tempering stages of DP thermal treatments. Firstly, the cooling was realized from two annealing states: a fully austenitized state and a partially austenitized state before cooling. This study pointed out the strong influence of the annealing state before cooling, as austenite decomposition kinetics and phase existence domains of the partially austenitized state were found to be different from the fully austenitized state. Namely, three major changes were highlighted with partially austenitized states: (i) the martensitic domain is lowered to lower temperature range; (ii) the critical cooling rate ensuring complete austenite-to-martensite transformation is increased; and (iii) the bainitic domain is enlarged to wider cooling rate ranges. Consequently, it may be more difficult to transform austenite into martensite because the transformation occurs at lower temperatures. This may be critical in the case of direct tempering treatments. Moreover, the higher critical cooling rate may require adapted cooling technologies to achieve higher velocity. Lastly, the extended bainite existence domain has to be taken into account because bainite is detrimental for the mechanical properties of DP steels. All these facts strengthen the need of predictive tools to describe the austenite decomposition in the case of partial austenitization treatments.

Models from the literature were applied to describe the martensite start temperature

(M_S) and the austenite-to-martensite transformation kinetics. While it was possible to find several empirical formulae to describe M_S in the case of fully austenitized steels, models appeared not directly applicable in the case of partial austenitization by changing only the austenite C content in the formulae for M_S evaluation. This result differs from the conclusions of the works of Bohemen and Sietsma [BOH 09b] or also Waterschoot *et al.* [WAT 06], who successively predicted the M_S temperature of partially austenitized steels by modifying only the austenite C content. The redistribution of other alloying elements in the austenite before cooling or more reliable models taking into account the effect of other parameters (austenite grain size, nucleation sites *etc.*) are thus required to describe the austenite decomposition of partially austenitized steels.

Secondly, the tempering stage was investigated. Full martensite steel tempering was first studied highlighting three main mechanisms: I/ the precipitation of intermediate carbides, II/ the cementite precipitation and III/ the Cr enrichment of cementite. The carbon precipitation of the first two stages were evaluated and described with JMAK approaches. The low fraction of precipitated carbon during the tempering stage was pointed by our study (both by TEP and 3D-FIB analysis). This was attributed to austempering effect and carbon precipitation on dislocation and grain boundaries. It was estimated that only 35% of the total carbon content is available for cementite precipitation. The remaining carbon atoms are assumed to be precipitated in the form of other precipitates (*ex.* carbonitrides) or to be segregated at dislocations or lath boundaries. They are therefore not available for cementite precipitation during tempering at temperature below 450°C (recovery is required to displace these segregated atoms). Finally, the hardness measurements during tempering treatments have shown a similar dependency with carbon content in solution as the one extracted from the literature [SPE 72]. This strengthens the evaluated carbon contents in solution and the hypotheses of limited carbon for cementite precipitation during tempering treatments.

This PhD-work allowed to get a better understanding on the microstructural evolutions occurring during the thermal treatment of DP steels. As detailed, various modeling approaches were undertaken to describe metallurgical phenomena passing from pragmatic phenomenological models (JMAK law, mixture law *etc.*) to more or less physical based approaches. The main difficulty of this work was to obtain the best compromise between reliability, versatility and calculation time.

Globally, phenomenological approaches have a low computational cost but such models are often defined for a set of given conditions (chemistry, initial microstructural state *etc.*) and it is risky to use them outside their application domain. Such models require adjustments involving experimental data obtained under various conditions. However, empirical laws are very simple to use and were validated many times in the literature and in the present work for very different conditions. So, such approaches should not be ruled out from modeling intent. They are likely to take into account external parameters (cycle parameters, steel chemistry *etc.*) and to lead to a better understanding of the involved mechanism. They are, thus, very useful as a first stage of modeling to describe the dependence of external parameters on metallurgical phenomena.

To go further in modeling, there is a global work towards more physical based models

where fitting parameters of phenomenological laws are expected to be substituted by physical and material characteristic constants. The “ideal” physical based model should be able to describe metallurgical mechanisms in all possible conditions by changing only the physical and material constants. The main difficulty of such approaches is to identify the major phenomena driving the evolutions, to select the most reliable assumptions and also the representative system. It may be difficult to define the representative system in complex and heterogeneous microstructural states; such models require therefore a good knowledge of metallurgical evolutions. Two main disadvantages of such modeling approaches are that they generally require high computational costs and that it may be difficult to evaluate some physical and material constants.

These two different schools of modeling may question on what kind of modeling approach is needed for steel-makers: are pragmatic phenomenological approaches sufficient? Are more robust physical based models required? What is acceptable for the calculation time? *etc.* This PhD-work does not entirely answer these questions but proposes phenomenological and physical based models highlighting strengths and disadvantages of each type of approaches.

Perspectives

To continue this study, several ways of exploration can be proposed to complete and deepen the characterization and modeling of microstructural evolutions during the thermal treatments of dual-phase steels. Main ideas are developed below:

1. Evaluation of the reliability and versatility of models

At first, the reliability and versatility of the proposed models should be analysed in different conditions with, for example, various DP steel chemistries (different carbon contents and/or substitutional contents) or with several cold-rolling reduction ratios. Furthermore, they could be applied to other types of multiphase steels. Objectives will be to validate developed approaches and, eventually, to propose modifications.

2. Better understanding of industrial conditions

Major difficulties of the present works are due to the fact that the investigated steel present typical industrial characteristics (multi-alloyed chemistry, Mn segregation bands, cold-rolled state *etc.*). The initial microstructure is non-homogeneous and complex with gradients of deformation ratio in the steel thickness and deformed ferrite and pearlite bands. Microstructural evolutions may therefore have different kinetics in the steel thickness and even more locally, at the grain scale. It is thus proposed to prefer global experimental techniques to characterize the average microstructural evolutions of each phenomenon. Namely, the modeling efforts of the isothermal austenite formation kinetics may require a more precise and regular follow-up of the phase transformation before going further in the development of modeling tools. Two experimental techniques are proposed to reach this goal. The explored in-situ XRD technique may ensure a more accurate austenite fraction monitoring provided that the steel texture can be properly described [BAR 15c][BAR 15b]. In-situ laser ultrasonic may also be an appropriate technique

as the ultrasound attenuation properties may be related to the average grain size and the ultrasound velocity depends on the elasticity and density of the bulk material [MIL 13][GAR 17]. Such technique may thus be used to monitor recrystallization, austenite formation and grain growth. However, these two different techniques may require heavy analyses. The problem is complex because of the superposition of different phenomena which require to be isolated.

3. Study of the cooling and the tempering stages

As pointed out in chapter 6, the study of the cooling and tempering stages needs to be continued. The strong dependency with the intercritical annealing has been pointed out. Indeed, it was shown that the austenite-to-martensite transformation kinetics is modified by the intercritical state (section 6.1). However, existing models of the literature are no longer validated for the prediction of the martensite start temperature or the transformation kinetics of transformation in the case of incomplete austenitization. Experimental works may be continued studying the martensitic transformation from other intercritical states.

Moreover, some points need to be clarified considering the martensite tempering. Tempering mechanisms need to be validated and it could be interesting to quantify the solute carbon content using other techniques. Then it would be necessary to link the mechanical properties of the tempered martensite to the carbon content in solid solution, before investigating the more complex case of the ferrite-martensite mixture.

4. Towards mean field with local law models

As a more challenging perspective, the modeling of metallurgical evolutions in industrial conditions may be oriented towards mean field modeling but still using local laws [SAI 16]. This approach is likely to take into account the heterogeneity of microstructures (like various cementite's Mn content or different morphology) which may evolve with different local evolutions. However, the main difficulty of this kind of approach rests on the fact that different sub-models need to be linked each other (ex. mixture law) and it is difficult to evaluate their respective dependences.

5. Link between microstructure and mechanical properties

This PhD-work is included in a more global approach to go towards the prediction of mechanical property evolutions as a function of the thermal treatment. The present PhD work was aimed at developing some modeling tools dedicated to the prediction of microstructural evolutions as a function of the thermal treatment conditions as schematically represented in figure 6.20 (arrow number 1). The next step is to link the microstructural state to the mechanical properties (arrow number 2). This latter is the objective of the next PhD-work launched in October 2017, in the continuation of the present PhD, with the goal to link the mechanical behavior of DP steels to the microstructure. This work will also be attached to develop predictive tools.

This axis may be started from the iso-work approach developed by Bouaziz and Alain *et al.* [BOU 08][ALL 12][ALL 15] to describe the tensile behavior of DP steels

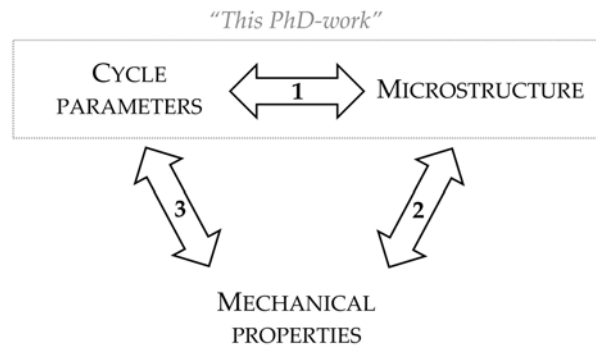


Figure 6.20: Cycle parameters-Microstructure-Mechanical properties relationship to optimize steels.

(yield strength, ultimate tensile strength, uniform elongation, work hardening behavior). This model was validated for sixties different steel chemistries from fully ferritic microstructures to fully martensitic steels. The mechanical behavior of ferrite and martensite are individually defined before linking together these two mechanical behaviors by a iso-work condition (*i.e.* $\sigma^{\alpha'} d\varepsilon^{\alpha'} = \sigma^{\alpha} d\varepsilon^{\alpha}$), a geometrically necessary dislocation term and a mixture law. Improvements may be suggested to enhance the prediction in high deformation ranges or also to consider the mechanical behavior of tempered martensite for example (for now, only “fresh” martensite is considered).

6. Optimization of thermal cycles

Lastly, the development of predictive tools to describe the microstructural and mechanical properties evolutions as a function of thermal conditions may be used inversely to optimize thermal treatments. Models may help to obtain the desired microstructures and/or given mechanical properties optimizing with an optimization of the cycle parameters as schematically represented in figure 6.20.

In the same idea, modeling tools may benefit to save energy in the production line and improve the production yield.

Appendix A

Local Equilibrium conditions for the $\gamma \longrightarrow \alpha$ transformation

This appendix aims at describing the Local Equilibrium with Partitioning (LEP) and the Local Equilibrium with Negligible Partitioning (LENP) conditions commonly used in the literature of ferrite formation. These two local equilibria were defined because the newly formed ferrite may not be as enriched as the parent austenite phase. Austenite composition indeed extends on the 0-3.5 wt%Mn and 0-0.43 wt%C composition ranges while ferrite is limited to 0-1.7 wt%Mn and 0-0.02 wt%C enrichment. The diffusion of the substitutional element X may therefore be required to form the ferrite phase.

A.1 Two-modes of ferrite formation: LEP *versus* LENP

Due to the large difference of diffusivity $\left(\frac{D_C^\gamma}{D_X^\gamma}\right)$ in steel, the operative tie-line may be supposed time-independent in commonly industrial conditions (treatment time <1 hour). The time-independent tie-line may be determined by geometric construction as described below.

In 1972, Coates proposed a concept allowing the time-independent tie-line to be determined in the case of ferrite formation [COA 72] [COA 73]. The concept lies on the following consideration: a given tie-line defines all bulk compositions having the same interface tie-line. From that, Coates inverted the problem and sought those compositions corresponds to a given tie-line.

Figure A.1.b shows the composition locus points for a given tie-line as a function of the diffusivity ratio of C and X elements. If the C and X diffusion coefficients are equal (*i.e.* $\left(\frac{D_C^\gamma}{D_X^\gamma}\right) = 1$), the operative tie-line corresponds to the orthoequilibrium tie-line. Coates geometrically determined other composition locus points corresponding to a given tie-line in the case of different diffusivity ratio [COA 72]. Examples of composition locus points are reported in the figure for several diffusivity ratio values in between 1 to infinite. In the case of “infinite” diffusivity ratio, the composition locus points are reported in red dotted line. It corresponds to the two basal lines of the right angle triangle for which the given

tie-line defined the hypotenuse. The right angle triangle corresponding to a given tie-line is named as “Interface composition contour” or IC contour and defines all compositions corresponding to the hypotenuse tie-line in the case of infinite diffusivity ratio.

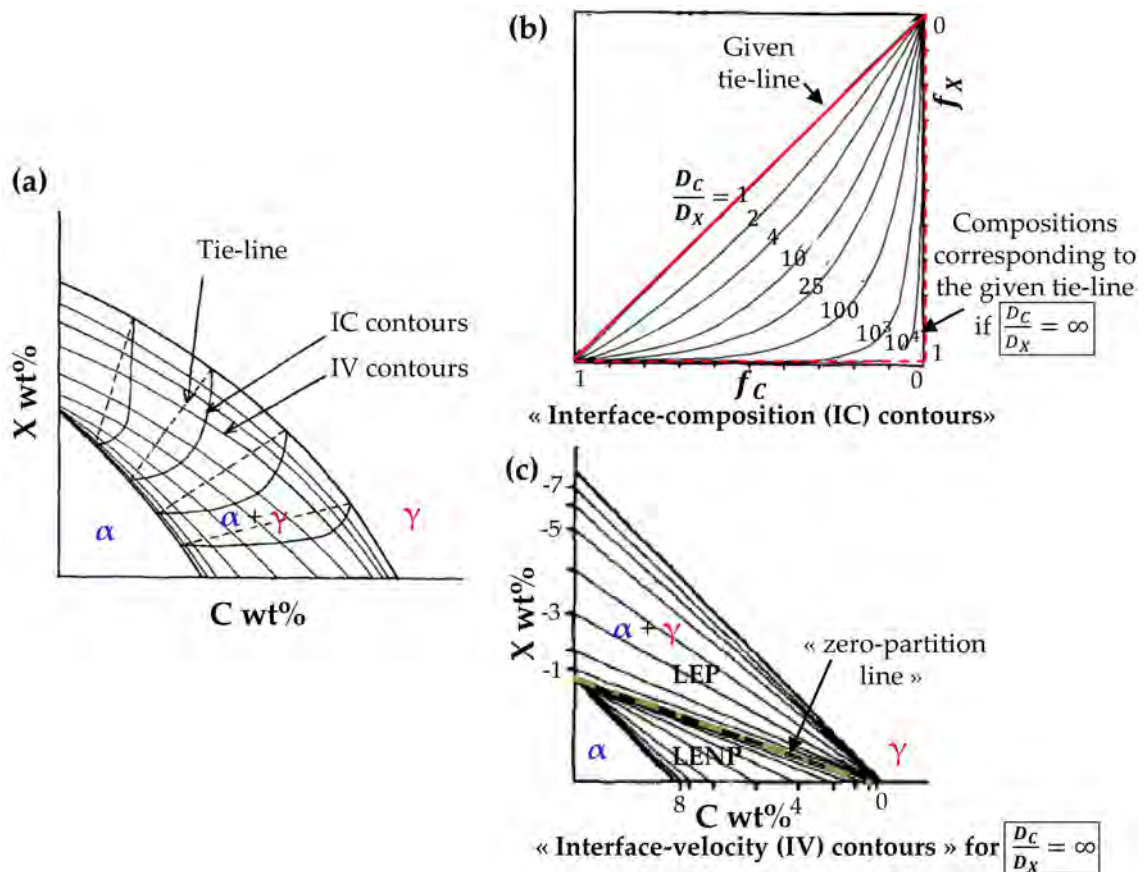


Figure A.1: (a) Schematical representation of an isothermal section of the Fe-C-X system. Examples of interface composition (IC) and velocity (IV) contours are represented for some given tie-lines. (b) Composition locus (named as IC-contours) for a given tie-line as a function of diffusivity ratio. (c) Interface velocity for high diffusivity ratio, it highlights the “zero-partition line” differentiating the LEP and LENP domains [COA 72].

Geometrically, the right-angle of IC contour passes by the so-called “zero-partition line” defined by Purdy *et al.* [PUR 64]. Such “zero-partition line” only exists for high diffusivity ratio. The “zero-partition line” appears on the interface-velocity contour graph as shown in figure A.1.c and defines the transition between two velocity transformation domains:

- The LEP domain, Local Equilibrium with Partitioning, characterized by low velocity where the transformation rate is managed by the slow diffuser and low supersaturation thanks to X redistribution.
- The LENP, Local Equilibrium with Negligible Partitioning, characterized by high velocity where the transformation rate is controlled by the fast diffuser and high

supersaturation due to low partitioning of X specie.

In practice, the localization of the bulk composition defines the formation mode of ferrite formation (*i.e.* LEP or LENP respectively superior or inferior composition domain to the “zero-partition line”). The construction of the right-angle triangle passing through the bulk composition and the “zero-partition line”(right-angle) allows the time-independent tie-line for LE condition to be determined as detailed below.

A.2 Local Equilibrium with Partitioning (LEP)

For alloys with bulk composition above the “zero-partition line”, the massive transformation is managed by the diffusion of C and X elements. The LE model is defined as local equilibrium with partitioning (LEP). The alloy has a low supersaturation because both species diffuse and X element redistribute across the interface.

Figure A.2 presents the isothermal section of a Fe-C-Mn system at 760°C. The respective concentration profile of X and Mn for a steel with a bulk concentration above the “zero-partitioning line”. The construction of the IC contour passing from this bulk composition allows to determine the operative time independent LEP tie-line of the alloy. The transformation is controlled under the LEP condition and Mn redistribution is observed across the interface.

A.3 Local Equilibrium with Negligible Partitioning (LENP)

For alloys with bulk composition below the “zero-partitioning line”, the transformation is controlled under local equilibrium with negligible partitioning (LENP). Similarly to LEP, the construction of the IC contour allows to determine the operative time independent LENP tie-line. The partition of the substitutional element is negligible across large distance and a narrow “spike” forms at the interface as illustrated in figure A.3.

The thickness of the narrow LENP “spike” has nevertheless been evaluated smaller than the inter-atomic distance [COA 73]. For this latter reason, some authors qualified the LENP model as non-realistic [COA 73] [HUL 47] [BHA 16] [DAN 16]. To deal with this, Hulgren introduced the paraequilibrium model presented in the chapter 1 [HUL 47].

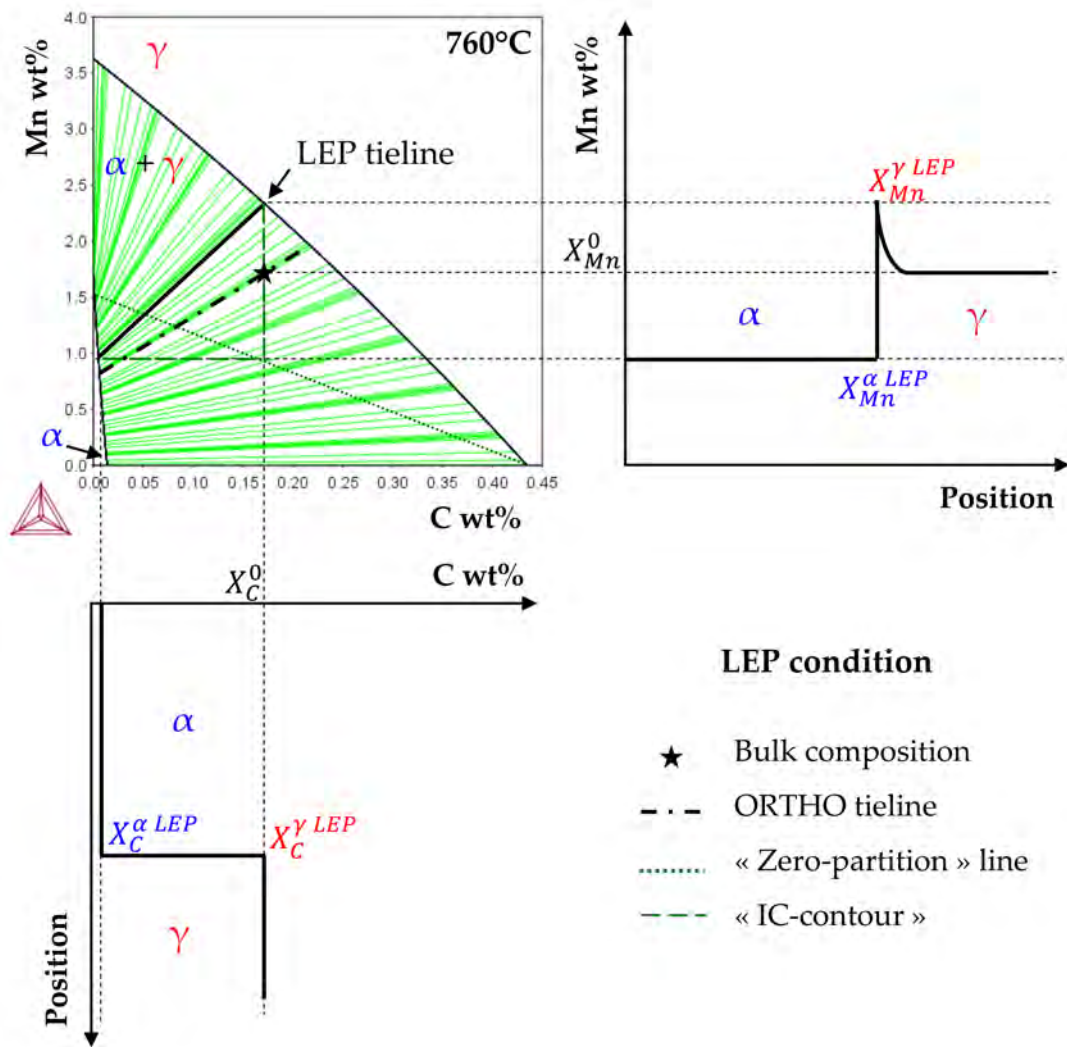


Figure A.2: Schematic representation of LEP condition for the $\gamma \rightarrow \alpha$ transformation. Isothermal C and Mn concentration profiles are reported.

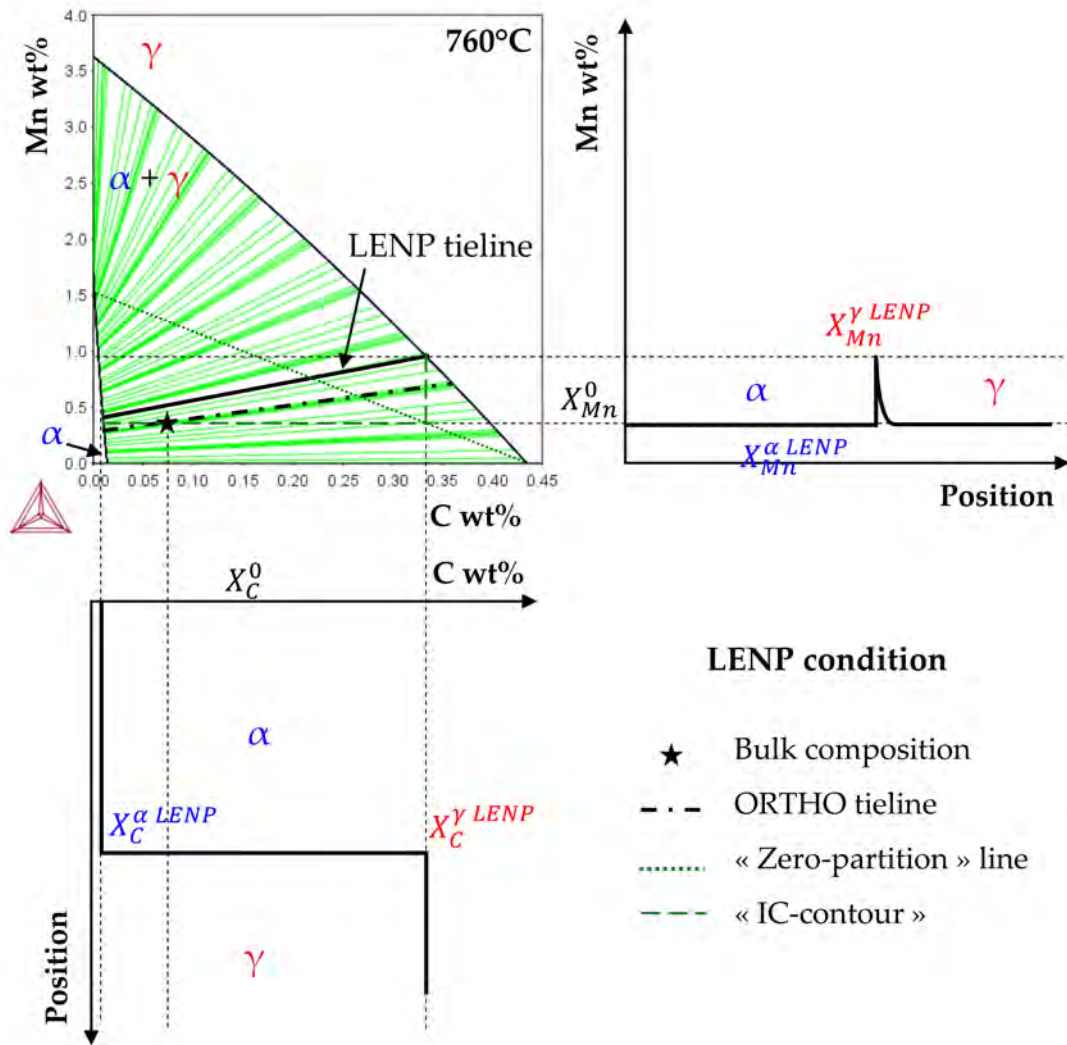


Figure A.3: Schematic representation of LENP condition for the $\gamma \rightarrow \alpha$ transformation. Isothermal C and Mn concentration profiles are reported.

Appendix B

Monitoring of austenite formation by experimental techniques

B.1 Isothermal monitoring of austenite formation

In the following of section 3.1.1, isothermal austenite formation kinetics were monitored by different experimental techniques: (1) phase quantification on optical micrographs, (2) TEP measurements and (3) hardness measurements on interrupted thermal treatments. The monitoring of austenite formation on the ReX-steel by each technique (before normalization) is given in figure B.1.a, b and c during isothermal holding at 735, 760 and 780°C (after a ramp of 100°C/s, limiting the transformation during the heating stage). The normalized austenite kinetics are then reported in figure B.1.d considering the final plateau as the equilibrium.

It can be noted that the different techniques lead to master kinetics with standard deviations which can reach $\pm 10\%$. It is thus interesting to choose carefully the trial plan in order to have enough points in the area of interest and reveal the global kinetics of evolution.

The main difficulty of isothermal conditions is due to the fact that the orthoequilibrium is not achieved in suitable times. The optical quantification enables to determine the determination of the real phase fractions in any treatment conditions whereas TEP and hardness methods are indirect techniques which can only predict the normalized austenite fraction after normalization of the kinetics with the final TEP or hardness value.

It was chosen to quantify martensite fraction by optical phase quantification in order to avoid any normalization issues. An average of at least 20 measurements was realized for the optical quantification of each studied state.

B.2 Overview of strength/error sources of experimental techniques

Table B.2 and B.2 propose an overview of main advantages and error sources of applied experimental techniques used during this PhD-work to monitor the austenite formation.

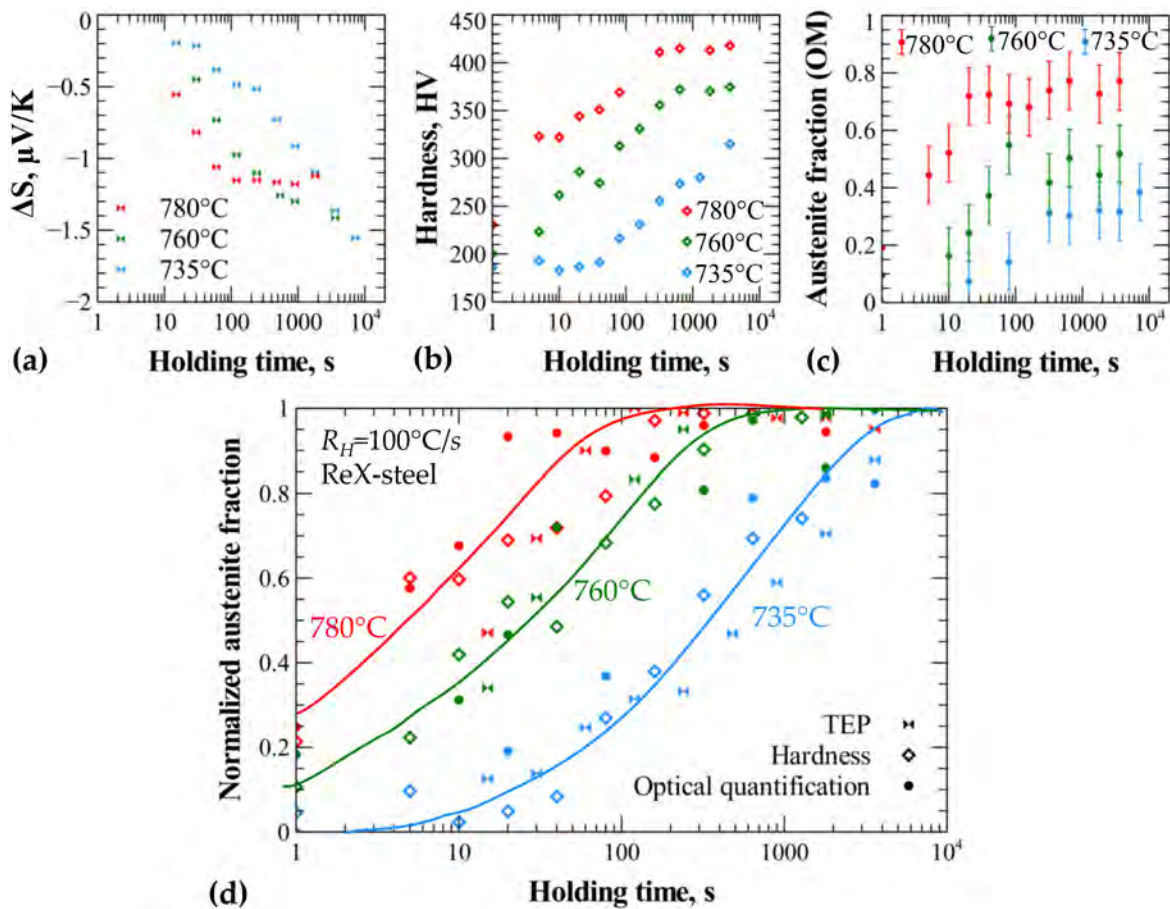


Figure B.1: Austenite formation kinetics monitored by (a) TEP; (b) hardness and (c) optical phase quantification during isothermal holding at 735, 760 and 780°C. Normalized austenite fraction are represented in (d).

As shown, each technique has its own measurement uncertainties, which is important to keep in mind. Errors may come from various sources from machine, characteristics of the measured values to data analysis (ex. dilatometry, optical quantification).

Experimental techniques	Characteristics of the method	Advantages	Error sources
Led dilatometer	Specimen dilatation during thermal treatments is measured by optical dilatometry in the sample width (10 mm, see figure 2.4.a)	<ul style="list-style-type: none"> - Volume measurement - No dilatometer stress (no contact) 	<ul style="list-style-type: none"> - Evaluation of the tangent lines to the curves - May be influenced by oxidation or sample creep - Inhomogeneity of thermal treatment in the sample width (Joule heating) - Possible influence of the current (Joule heating) on metallurgical evolutions [FAB 14] - Dilatation may evolve with recrystallization (inducing possible error in phase quantification)
Bahr dilatometer	Specimen dilatation is measured by contact dilatometer (quartz) in the sample length (10 mm)	<ul style="list-style-type: none"> - Volume measurement 	<ul style="list-style-type: none"> - Idem to led dilatometer: tangent evaluation, recrystallization, oxidation or creep influence - Possible stress due to contact dilatometer - Inhomogeneity of thermal treatment in the sample length (induction heating)
In-situ XRD	XRD analysis ensures the quantification of phase fraction using peak position and intensity	<ul style="list-style-type: none"> - Complementary information: lattice parameter, deformation, microstrain <i>etc.</i> - Volume measurement 	<ul style="list-style-type: none"> - XRD analysis (conversion of 2D-pattern into spectra, spectra fit, texture modeling <i>etc.</i>) - Inhomogeneity of thermal treatment (adaptated Bahr dilatometer system)

Table B.1: Comparison of various in-situ experimental techniques to monitor the kinetics of austenite formation.

Experimental techniques	Method characteristics	Advantages	Error sources
Optical phase quantification	Phase fractions are quantified by image analysis after etching to reveal the microstructure	<ul style="list-style-type: none"> - Not influenced by the recrystallization degree - Possibility to analyse phases after complex thermal treatment 	<ul style="list-style-type: none"> - Image analysis for phase quantification (eventual preliminary treatments, threshold) - Etching (accuracy, repeatability, contrast) - Local measurement
TEP	TEP evolution on different thermal treatments may be used to evaluate phase fractions	<ul style="list-style-type: none"> - Volume measurement independent of sample geometry 	<ul style="list-style-type: none"> - Normalized value (importance of the initial and "equilibrium" values to evaluate the transformation kinetics)
Hardness	Hardness evolution on different thermal treatments may be used to evaluate martensite fractions	<ul style="list-style-type: none"> - Hardness points cover several grains (sub-volume measurement) 	<ul style="list-style-type: none"> - No only related to martensite fraction (also dependent on martensite carbon content and recrystallization state) - Normalized value (importance of the initial and "equilibrium" values to evaluate the transformation kinetics) - Indent evaluation - Local measurement

Table B-2: Comparison of various indirect experimental techniques to monitor the kinetics of austenite formation.

Appendix C

XRD method to follow microstructure evolutions

Three in-situ XRD trials were performed at PETRA III using the modified Bahr dilatometer available on beamline P07. These trials appear very promising and fruitful to monitor microstructure evolutions even if some misunderstanding points persist. This appendix shortly summarizes results after *Maud* analysis of XRD-patterns pointing out new contributions of such experiment and, to our state of advancement, misunderstanding points. According to author's appreciation, in-situ XRD experiments could improve knowledge of austenite formation kinetics for long annealing times.

C.1 Annealing in the austenitic domain

C.1.1 Case of the ReX-steel

Figure C.1 presents results of an in-situ XRD measurement realized on the ReX-steel. The thermal cycle was composed of a heating stage at $5^{\circ}\text{C}/\text{s}$ to 900°C and of a holding stage of 600 s before cooling with a rate of $5^{\circ}\text{C}/\text{s}$.

The ferrite-to-austenite transformation during heating was revealed by XRD analysis in the same temperature range of dilatation slope change. It should be noted that the cementite fraction is too small to be detected from 2D-patterns. Moreover, the global steel dilatation continues to decrease during the holding of the single-phase austenite. Such feature was also observed by Led and classical Bahr dilatometry explaining why no monitoring was realized in isothermal conditions. During cooling at $5^{\circ}\text{C}/\text{s}$, austenite decomposes as pointed out by dilatometry slope change and phase fraction determined by XRD analysis. It can be noted that austenite continues to transform even at low temperature domain ($<300^{\circ}\text{C}$) suggesting austenite-to-bainite and austenite-to-martensite transformations. XRD analysis software may index bainite and martensite as ferrite phase.

In addition, the XRD analysis allows the phase deformations to be plotted. The deformation was expressed thanks to the following equation: $\left(\frac{a}{a_0} - \varepsilon_{thermal}\right)$ with a_0 , a and $\varepsilon_{thermal}$ respectively the initial lattice parameter, the lattice parameter at a given time and

the thermal deformation. Such parameter may bring additional information concerning the lattice evolution: a decrease of the deformation translates compressive stress on the crystal lattice. At the beginning of the heating stage, ferrite deformation decreases characterizing stress relaxation and recovery. When austenite nucleates, ferrite and austenite are under tensile stress because the newly formed phase is more compact than ferrite. This leads to a decrease in the deformation value. The two phases accommodate. During the progress of the phase transformation, austenite phase continues to be under tensile stress while the evolution of ferrite appears more complex. Austenite deformation during holding step appear then negligible. Lastly, the two phases are under compression stress during austenite decomposition where denser phases than austenite appear.

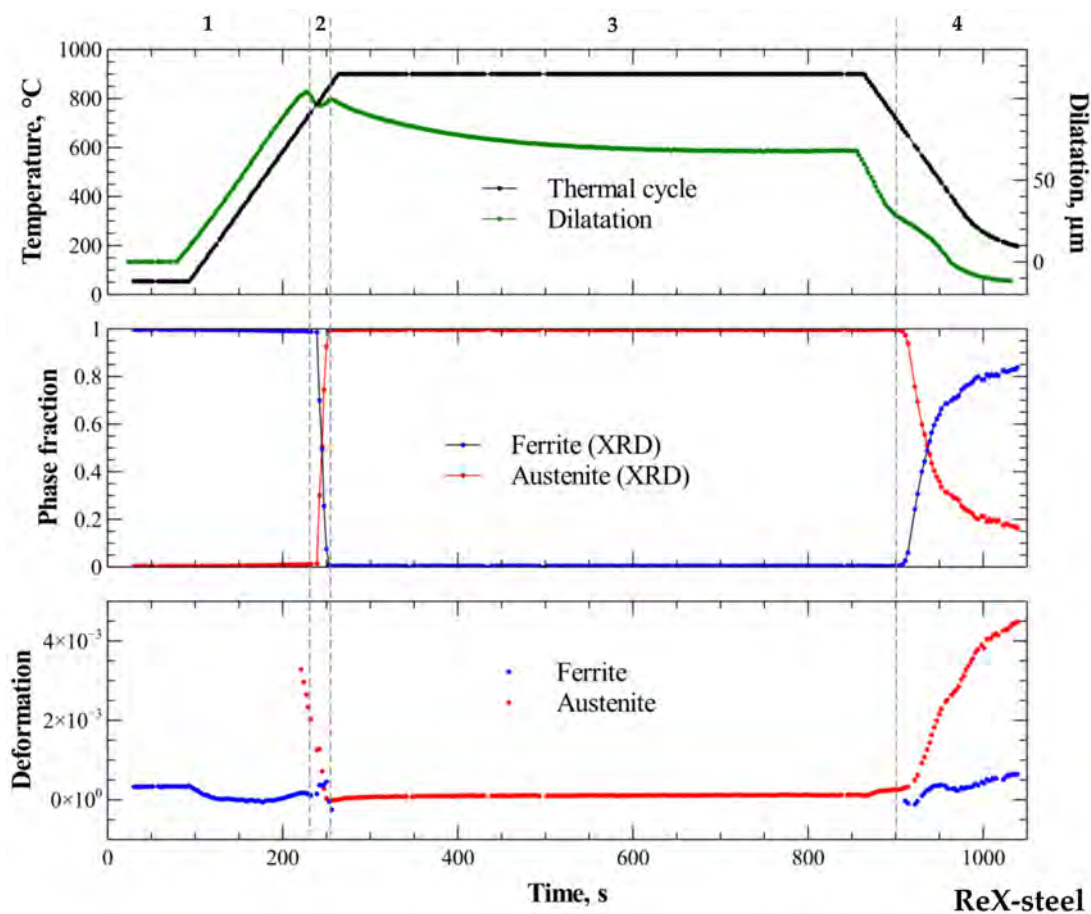


Figure C.1: XRD analysis during a thermal cycle including a heating stage at $5^{\circ}\text{C}/\text{s}$ to 900°C , a holding of 600 s and finally a cooling at $5^{\circ}\text{C}/\text{s}$. Case of the ReX-steel.

C.1.2 CR-steel case

Identically, an in-situ XRD experiment was performed on the CR-steel. Phase transformation range, evaluated from XRD analysis and dilatometry, is shifted to lower temperatures compared to ReX-steel as expected from this PhD-work. Comparable phenomena to ReX-

steel are observed while the first ferrite tensile deformation is more pronounced due to the recovery of the cold-rolled steel.

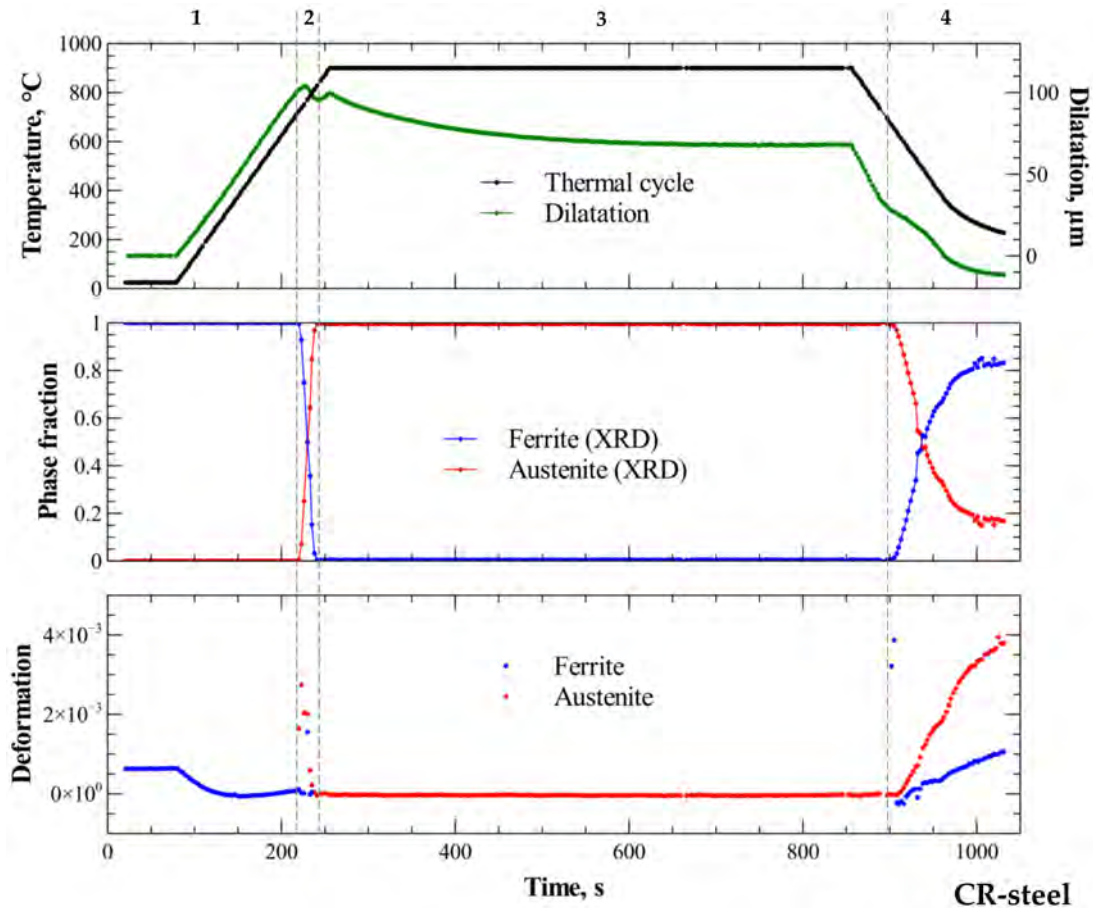


Figure C.2: XRD analysis of a thermal cycle realized on the CR-steel and composed of a heating at 5°C/s to 900°C, an holding of 600 s and finally a cooling at 5°C/s.

C.2 Annealing in the intercritical domain

A thermal cycle was also performed in the intercritical domain with a holding at 760°C during 1800 s as given in figure C.3. Like previous trials, in-situ XRD enables to monitor phase fraction and global steel deformation ongoing treatment. It should be noticed that so-called austenite “shrinkage” during the isothermal holding is pointed out for very short holding times (200 first seconds) with a gap close to 0.1%. Thanks to this accuracy, in-situ XRD could be a promising way to capture the complex evolution of austenite formation with chosen cycles. There is however various misunderstanding points in this first isothermal trial:

- Austenite fraction achieved during holding at 760°C are close to 80-90% while the results obtained by optical phase quantification led to an equilibrium fraction of

60%. The XRD quantified austenite appears relatively high for this treatment.

- Both dilatometry and deformation data exhibited a brutal jump at the end of phase 2 which was supposed to be an error of measurement (probably sample sliding).
- Lastly, deformation evolution during heating stage is different from the one obtained during heating to 900°C presented in figure C.2. In this test, the evolution appears to be more complex and disturbed.

According to the author, the gap of austenite fraction could be related to texture modeling in *Maud* software. Errors in specimen texture modeling may generate errors in the quantified fractions as peak heights may be not well predicted. Moreover, the brutal jump at the end of stage 2 was supposed to be due to an experimental error not associated with a microstructural change. To go further in in-situ XRD analyses, trials should be repeated to eliminate any experimental uncertainty.

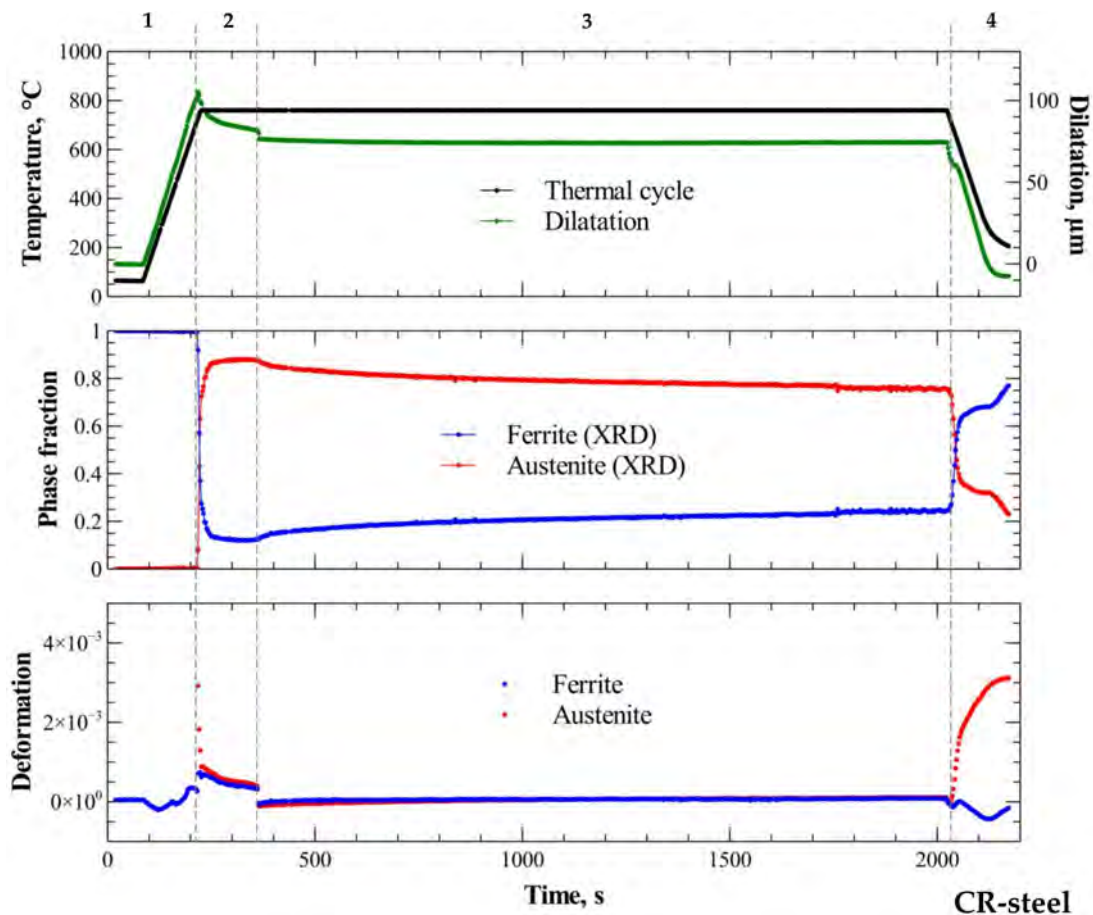


Figure C.3: XRD analysis of a thermal cycle realized on the CR-steel and composed of a heating at 5°C/s to 760°C, an holding of 1800 s and finally a cooling at 5°C/s rate.

Appendix D

Modeling of the austenite formation kinetics on the CR-steel

D.1 JMAK parametrization of non-isothermal conditions

Austenite formation kinetics during continuous heating treatments of the CR-steel were modeled using a mixture law linking two different models for austenite formation on recrystallized and deformed ferrite grains as a function of the recrystallization progress (section 3.3.2.1, chapter 3). However, one should ask why the JMAK parametrization was not directly realized on austenite formation kinetics of the CR-steel. This section aims at pointing out difficulties in the parametrization of the law to describe austenite formation kinetics of the CR-steel.

Similarly to the ReX-steel (section 3.2.1.1), Kissinger analysis method was applied to evaluate the Q and n parameters from the kinetics of figure 3.2.b. Figure D.1.a shows the representation of $\ln\left(\frac{R_H}{T_{max}^2}\right)$ as a function of $\frac{1}{R \times T_{max}}$. As observed, points do not line up on a straight line due to the complexity of austenite formation evolution. The activation energy for austenite formation on CR-steel can not be determined through this method.

Moreover, the Avrami coefficient (n) is commonly obtained thanks to the representation of $\ln\left(\frac{R_H}{T_{max}^2}\right)$ as a function of $\left(\ln\left(\frac{T_{max}^2}{R_H}\right) \times \exp\left(-\frac{Q}{RT}\right)\right)$ for austenite fraction between 25 and 75%. The plot was realized for the heating rate equal to 30°C/s, as the recrystallization advancement appears really restricted (figure 3.15) at this condition (*i.e.* austenite only forms on deformed grains), and using the same activation energy as the one determined for the ReX-steel (901 kJ/mol) as it was not possible to determine it for the CR-steel (precedent paragraph). As shown in figure D.1.b, the n parameter associated with austenite formation on deformed ferrite may therefore be evaluated to be equal to 0.32. This smaller value is in accordance with the fact that smaller Avrami value is associated with more needlelike or platelike morphology, which is expected to be formed in the case of deformed structure [LEE 98]. However, a smaller n value will tend to slow down the kinetics as illustrated in figure D.1.c where the influence of n parameter is plotted.

Consequently, the proposed parametrization of chapter 3 appears to be more convincing due to the difficulties in the JMAK parametrization of the kinetics of the CR-steel.

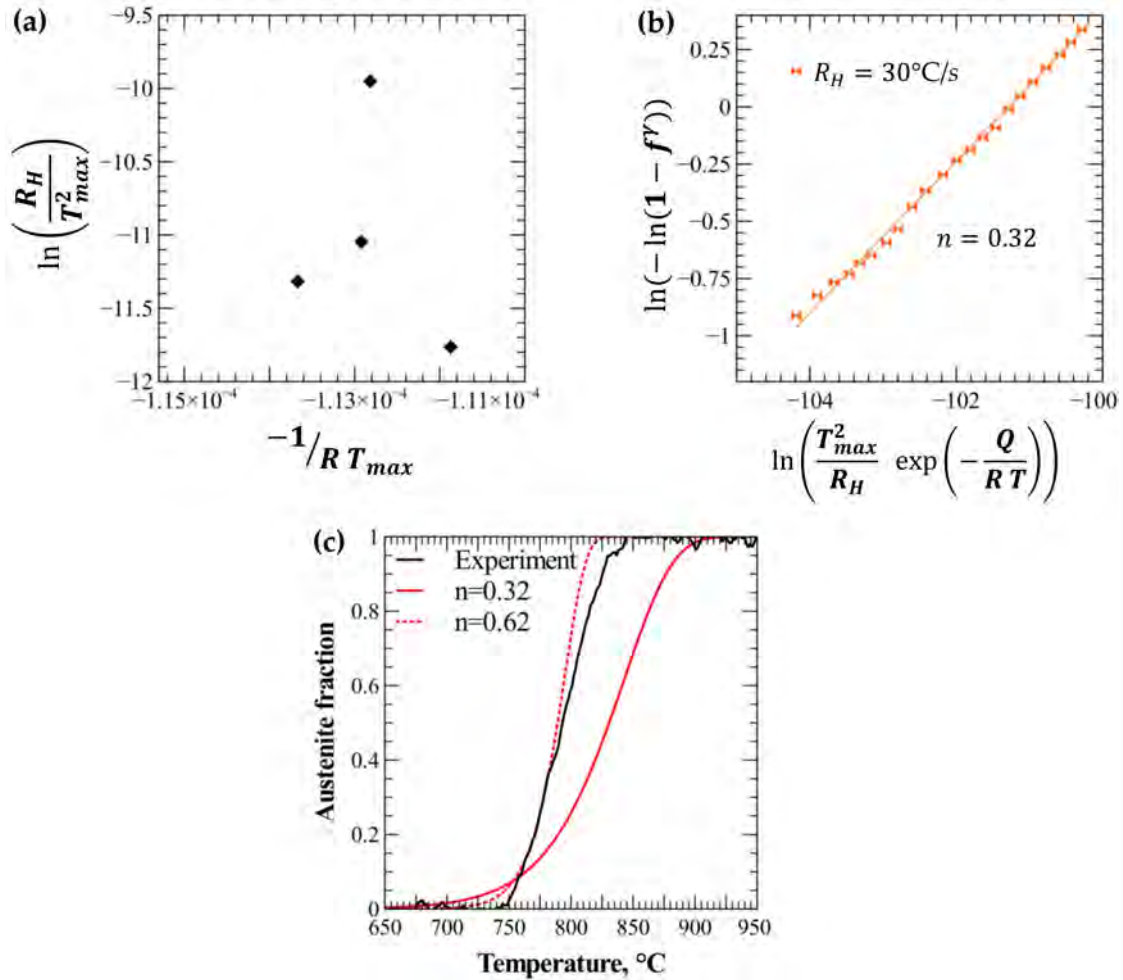


Figure D.1: Methodology to determine JMAK parameters: (a) Q for heating rates equal to $R_H=5, 7.5, 10$ and 30°C/s ; and (b) n using the experimental kinetics at 30°C/s , *i.e.* austenite forms on fully deformed ferrite ($Q=901$ kJ/mol). (c) Influence of the Avrami parameter on the austenite formation kinetics with $n=0.32$ or 0.62 ($Q=901$ kJ/mol; $b_0=3 \times 10^{43}$ /s).

D.2 Recrystallization inhibition in non-isothermal conditions

This appendix presents the austenite formation kinetics predicted from the mixture law with 3 JMAK laws for heating rates R_H equal to 0.5, 5, 7.5, 10 and 100°C/s . Figures D.2 and D.3 compare results from the model. The left column corresponds to the 3-JMAK law results while right column figures consider, in addition, the recrystallization inhibition above 10% of austenite fraction.

It can be noted that the recrystallization inhibition hypothesis ensures a better accordance of the JMAK model for heating rate of 5, 7.5, 10, 30 and 100°C/s. The consideration of the recrystallization inhibition accelerates the austenite formation kinetics predicted by the 3-JMAK model. Moreover, this hypothesis allow the transition between austenite formation on prior recrystallized and cold-rolled ferrite grains to become smoother.

However, it should be pointed out that the model predictions are not accurate for 0.5 and 5°C/s. The case at 0.5°C/s is managed by the austenite formation on recrystallized ferrite grains as the recrystallization is almost finished when austenite starts to form. The kinetics at 0.5°C/s is probably site-saturated explaining the deviation from the JMAK model (*i.e.* inferior velocity kinetics).

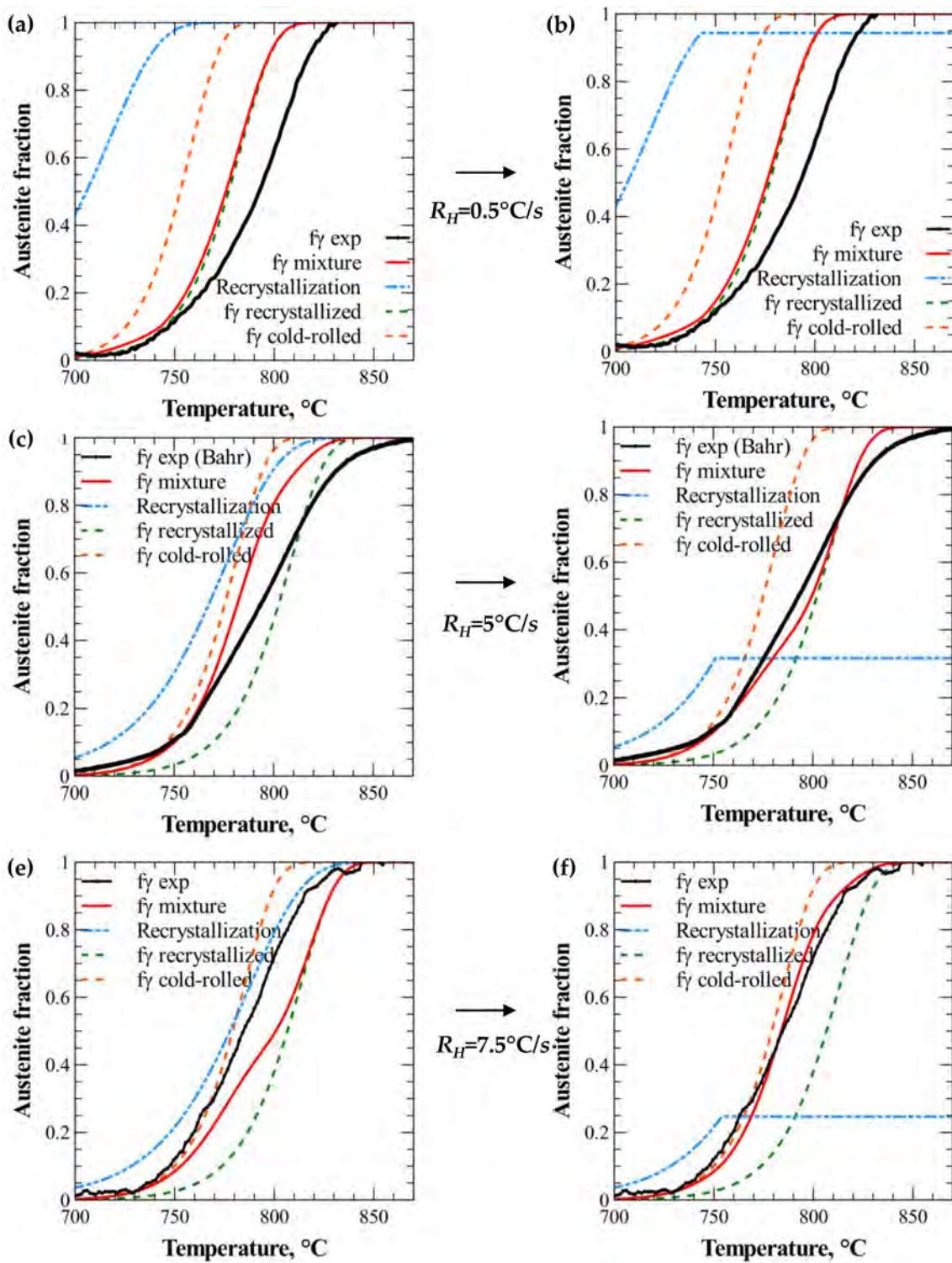


Figure D.2: Comparison of austenite formation kinetics for different heating rates (a-b) 0.5, (c-d) 5 and (e-f) 7.5°C/s predicted with (a) the 3-JMAK mixture model and (b) taking into account recrystallization inhibition above 10% of austenite fraction.

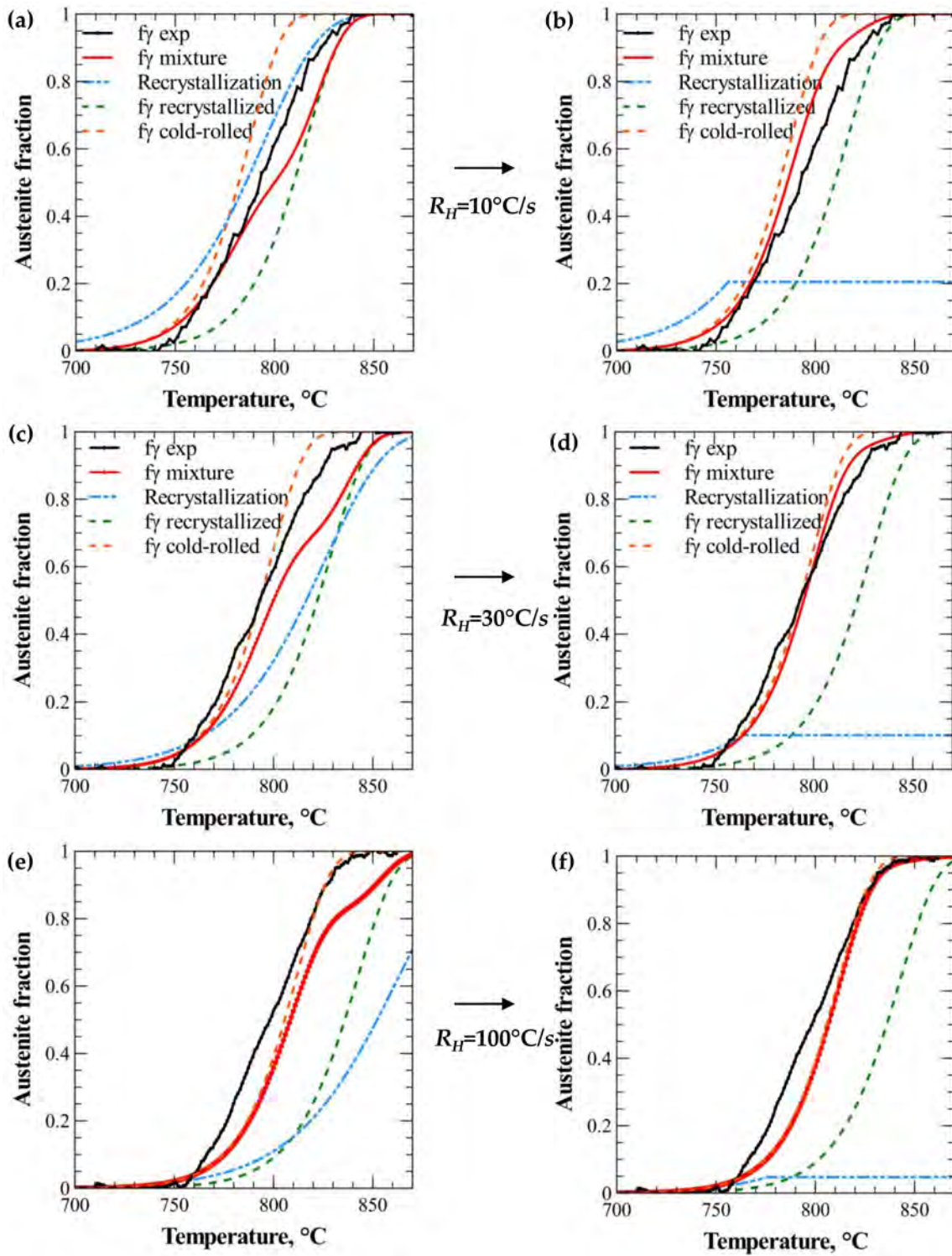


Figure D.3: Comparison of austenite formation kinetics for different heating rates (a-b) 10, (c-d) 30 and (e-f) 100°C/s predicted with (a) the 3-JMAK mixture model and (b) taking into account recrystallization inhibition above 10% of austenite fraction.

Appendix E

DICTRA calculation of the $\text{Fe}_3\text{C} + \alpha \longrightarrow \gamma$ transformation

This appendix aims at detailing a DICTRA code implemented to describe the formation of austenite in an initially cementite and ferrite system. This example is defined for the Fe-C-Mn system used in this PhD-work.

System size is chosen equal to 5 μm . Cementite size is thus fixed at 122 nm to respect the thermodynamic fraction of cementite (*i.e.* 2.44%). Mn concentration in cementite is fixed at 14 wt% imposing 1.46 wt%Mn in ferrite according to the mass balance. In addition, C concentration in ferrite was calculated to 0.007 wt% supposing 6.77 wt%C in cementite. The phase transformation problem is solved at 760°C. Different stages of the DICTRA calculation are commented.

THERMODYNAMIC DATABASE

```
GO-TO DATABASE
SWITCH TCFE8 //Steel thermodynamic database
DEFINE-SYSTEM FE C MN //Elements of the system
REJECT PHASE *
RESTORE PHASE BCC CEM FCC//Phases of the system (BCC: ferrite, CEM: cementite,
FCC: austenite)
GET
```

MOBILITY DATABASE

```
APPEND MOBFE3 //Steel mobility database
DEFINE-SYSTEM FE C MN //Elements of the system
REJECT PHASE *
RESTORE PHASE BCC CEM FCC//Phases of the system (BCC: ferrite, CEM: cementite,
FCC: austenite)
GET
```

TEMPERATURE CONDITION

```
GO-TO DICTRA-MONITOR
```

SET-CONDITION GLOBAL T 0 1033.15; * N //Temperature fixed at 1033.15K (760°C)

DEFINE REGIONS OF THE SYSTEM

ENTER-REGION

CARBIDE //First region is carbide

ENTER-REGION

AUSTENITE //Second region is austenite

CARBIDE

YES //Ferrite is at the right side of carbide

ENTER-REGION

FERRITE //Third region is ferrite

AUSTENITE

YES //Ferrite is at the right side of austenite

DEFINE GRID IN EACH REGION

ENTER-GRID

CARBIDE

122E-9 //Cementite sizes 122 nm

LIN

35 //Linear grid composed of 35 cells

ENTER-GRID

AUSTENITE

1E-9 //Ferrite sizes 1 nm

LIN

10 //Linear grid composed of 10 cells

ENTER-GRID

FERRITE

4.878E-6 //Ferrite sizes 4.878 μm

LIN

60 //Linear grid composed of 60 cells

Note: The meshing may be improved using a geometric meshing finer at the interface. Moreover, the grid number defines the spatial spacing and is thus an adjustable parameter to improve the calculation stability.

DEFINE PHASE IN EACH REGION

ENTER-PHASE

ACTIVE

CARBIDE

MATRIX

CEM //Carbide is a cementite phase (CEM)

ENTER-PHASE

ACTIVE

AUSTENITE

MATRIX

FCC //Austenite is a FCC phase

ENTER-PHASE

ACTIVE

FERRITE

MATRIX

BCC //Ferrite is a BCC phase

Note: If the austenite nucleation is considered in the DICTRA simulation, the definition of the region and grid of the austenite phase has to be withdrawn. The austenite nucleation is imposed by:

ENTER-PHASE

INACTIVE //Austenite is defined as an “inactive” phase in between cementite and ferrite phases, *i.e.* austenite has to nucleate

CARBIDE //The nucleate phase is attached to the right of carbide

YES //Austenite is attached to the right of carbide phase

FCC //Austenite is the FCC phase

FE //Independent element

1E-5 //Required driving force for austenite nucleation (value proposed by DICTRA)

CLOSE

DEFINE COMPOSITION OF EACH (ACTIVE) REGION

ENTER-COMPOSITION

CARBIDE

CEM

WEIGHT-FRACTION //Concentration are in weight fraction

MN LIN 14E-2 14E-2 //Mn concentration in cementite is fixed at 14 wt%

ENTER-COMPOSITION

AUSTENITE

FCC

FE //Independent element

WEIGHT-FRACTION

C LIN 0.17E-2 0.17E-2

MN LIN 1.763E-2 1.763E-2 //Concentrations calculated from mass balance

ENTER-COMPOSITION

FERRITE

BCC
FE //Independent element
WEIGHT-FRACTION
C LIN 7E-5 7E-5
MN LIN 1.46E-2 1.46E-2 //Concentrations calculated from mass balance

Note: the composition of the austenite nuclei was assigned to that of the nominal composition.

SET SIMULATION TIME

SET-SIMULATION-TIME
1E9 //Last time for simulation
YES //Option of automatic timestep control
1E5 //Maximal timestep
1E-8 //Initial timestep
1E-10 //Minimal timestep

Note: Timestep parameters are adjustable parameters to ensure either the initialization or stability of DICTRA calculations.

SET SIMULATION PREFERENCES

SET-SIMULATION-CONDITION
0 (//NS01A Print control)
1 (//Flux correction factor)
2 (//Number of delta timesteps in calling multidif)
NO (//Check interface position)
ACTIVATION //Option of calculation: vary activities or potentials
YES (//Allow automatic switch of varying element)
2 //Save workspace on file each 2 steps
1 //Degree of implicitity (0/0.5: Trapezoidal/1:Implicit)
2 //Maximal timestep change per timestep (*i.e.* double)
NO //Use forced starting value in equilibrium calculation
YES (//Always calculate stiffness matrix in multidif)
NO (//calculate residual for dependent component)

Note: Comments under parentheses are definition given by DICTRA code. Predefined DICTRA values were not changed.

SAVE THE SET-UP IN A NEW STORE FILE

SAVE CemLin-Syst5000-Mn14-760C YES

LAUNCH SIMULATION

SIMULATE

Note: DICTRA asks validations during the calculation process to accept either the nucleation of the austenite (which size was fixed at 1 nm in this work) or the disappearance of cementite phase.

ANALYSE OF SIMULATIONS

POST //Post-treatment module

SET-DIAGRAM-AXIS X TIME //Plot upper austenite interface as a function of time

SET-AXIS-TYPE X LOG

SET-DIAGRAM-AXIS Y POSITION R-FCC UPPER

PLOT

Here it is possible to plot position/velocity of Carbide/R-FCC(Austenite name chosen by DICTRA)/Ferrite phases at the upper/lower interface side.

SET-DIAGRAM-AXIS X DISTANCE GLOBAL //Plot Mn profile at different times: 0, 1000, 1E6 and 1E9 s

SET-DIAGRAM-AXIS Y W-P MN //Mn concentration in weight percent (AC: activity)

S-P-C TIME 0 1E3 1E6 1E9 //Different plotted times

PLOT

MAKE FILE //Save plotted data in a table

References

- [AGR 06] AGREN J., BRECHET Y., HUTCHINSON C., PHILIBERT J., PURDY G.
Thermodynamics and phase transformations, the selected works of Mats Hillert. *EDP Sciences, Metallurgie/Materiaux*, 2006.
- [AKB 93] AKBAY T., REED R., ATKINSON C.
Modelling re-austenitisation from ferrite/cementite mixtures in Fe-C steels. *Acta Metallurgical Material*, vol. 47, n° 4, 1993, p. 1469-1490.
- [ALL 12] ALLAIN S., BOUAZIZ O., TAKAHASHI M.
Toward a new interpretation of the mechanical behaviour of as-quenched low alloyed martensitic steels. *ISIJ International*, vol. 52, n° 4, 2012, p. 717-722.
- [ALL 15] ALLAIN S., BOUAZIZ O., PUSHKAREVA I., SCOTT C.
Towards the microstructure design of DP steels: a generic size-sensitive mean-field mechanical model. *Materials Science Engineering A*, vol. 637, 2015, p. 222-234.
- [AND 65] ANDREWS K.
Empirical formulae for the calculation of some transformation temperatures. *Journal Iron Steel Institute*, vol. 203, n° 7, 1965, p. 721-727.
- [AND 02] ANDERSSON J., HELANDER T., L. H., SHI P., SUNDMAN B.
Computational tools for materials science. *Calphad*, vol. 26, 2002, p. 273-312.
- [ASH 17] ASHRAFI H., SHAMANIAN M., EMADI R., SAEIDI N.
Examination of phase transformation kinetics during step quenching of dual-phase steels. *Materials Chemistry and Physics*, vol. 187, 2017, p. 2013-2017.
- [ATK 94] ATKINSON C., AKBAY T., REED R.
Theory for re-austenitisation from ferrite/cementite mixtures in Fe-C-X steels. *Acta Metallurgical Material*, vol. 43, n° 5, 1994, p. 2013-2031.
- [AUT] AUTOSTEEL.Steel Market Development Institute, url: <http://http://www.autosteel.org/research/growth-of-ahss.aspx>.
- [AVR 39] AVRAMI M.
Kinetics of phase change. I General theory. *The Journal of Chemical Physics*, vol. 7, n° 12, 1939, p. 1103-1112.
- [AZI 11] AZIZI-ALIZAMINI H., MILITZER M., POOLE W.
Austenite formation in plain low-carbon steels. *Metallurgical and Materials Transactions A*, vol. 42A, 2011, p. 1544-1557.
- [BAB 94] BABU S., HONO K., SAKURAI T.
Atom probe field ion microscopy study of the partitioning of substitutional elements

- during tempering of a low-alloy steel martensite. *Metallurgical and Materials Transactions A*, vol. 25, 1994, p. 499-508.
- [BAL 11] BALTAZAR HERNANDEZ V., NAYAK S., ZHOU Y.
Tempering of martensite in dual-phase steels and its effects on softening behavior. *Metallurgical and Materials Transactions A*, vol. 42A, 2011, p. 3115-3129.
- [BAR 14] BARBIER D.
Extension of the martensite transformation temperature relation to larger alloying elements and contents. *Advanced Engineering Materials*, vol. 16, n° 1, 2014, p. 122-127.
- [BAR 15a] BARBIER D., GERMAIN L., HAZOTTE A., GOUNE M., CHBIHI A.
Microstructures resulting from the interaction between ferrite recrystallization and austenite formation in dual-phase steels. *Journal of Materials Science*, vol. 50, 2015, p. 374-381.
- [BAR 15b] BARRIOBERO-VILA P., REQUENA G., SCHWARZ S., WARCHOMICKA F., BUSLAPS T.
Influence of phase transformation kinetics of the formation of alpha in a beta-quenched Ti-10V-2Fe-3Al alloy. *Acta Materialia*, vol. 95, 2015, p. 90-101.
- [BAR 15c] BARRIOBERO-VILA P., REQUENA G., WARCHOMICKA F., STARK A., SCHELL N., BUSLAPS T.
Phase transformation kinetics during continuous heating of a beta-quenched Ti-10V-2Fe-3Al alloy. *Journal of Materials Science*, vol. 50, 2015, p. 1412-1423.
- [BHA 01] BHADSHIA H.
Bainite in steels. *IOM Communication*, 2001.
- [BHA 06] BHADSHIA H., HONEYCOMBE R.
Steels: Microstructure and properties. *Butterworth-Heinemann*, 2006.
- [BHA 16] BHADSHIA H.
Some difficulties in the theory of diffusion-controlled growth in substitutionally alloyed steels. *Current Opinion in Solid State and Materials Science*, vol. 20, n° 6, 2016, p. 396-400.
- [BLE 05] BLECK W., PHU-ON K.
Microalloying of cold-formable multi-phase steel grades. *Materials Science Forum*, vol. 500-501, 2005, p. 97-114.
- [BOH 09a] BOHEMEN S. V., SIETSMA J.
Effect of composition of athermal martensite formation in plain carbon steels. *Materials science and technology*, vol. 25, 2009, p. 1009-1012.
- [BOH 09b] BOHEMEN S. V., SIETSMA J.
Martensite formation in partially and fully austenitic plain carbon steels. *Metallurgical and Materials Transactions A*, vol. 40A, 2009, p. 1059-1068.
- [BOH 12] BOHEMEN S. V.
Bainite and martensite start temperature calculated with exponential carbon dependence. *Materials Science and technology*, vol. 28, 2012, p. 487-495.
- [BOS 07] BOS C., SIETSMA J.
A mixed-mode model for partitioning phase transformations. *Scripta Materialia*, vol. 57, 2007, p. 1085-1088.

- [BOS 09] BOS C., SIETSMA J.
Application of the maximum driving force concept for solid-state partitioning phase transformations in multi-component system. *Acta Materialia*, vol. 57, 2009, p. 136-144.
- [BOS 10] BOS C., MECOZZI M.G. SIETSMA J.
A microstructure model for recrystallization and phase transformation during the dual-phase steel annealing cycle. *Computational Materials Science*, vol. 48, 2010, p. 692-699.
- [BOU 08] BOUAZIZ O., AOUAFI A., ALLAIN S.
Effect of grain refinement on the mechanical behaviour of ferritic steels: evolution of isotropic hardening and kinematic hardening. *Materials Science Forum*, vol. 584-586, 2008, p. 605-609.
- [BOU 13] BOUAZIZ O., ZUROB H., HUANG M.
Driving force and logic of development of advanced high strength steels for automotive applications. *Steel Research International*, vol. 84, n° 10, 2013, p. 937-947.
- [BRA 93] BRAHMIE A.
Etude de la précipitation des carbures de fer en présence de manganèse et du nitrure d'aluminium dans les aciers extra-doux par mesure du pouvoir thermoelectrique. *Thesis*, , 1993.
- [BUS 15] BUSCARLET E., NAUZIN J., CLUZEL X., MEHRIN S.
CAL and CGL metallurgical specifications for AHSS and associated furnaces for automotive deliveries since 1970 and for the future. *Galvatech 2015 proceedings*, , 2015.
- [CHB 14] CHBIHI A., BARBIER D., GERMAIN L., HAZOTTE A., GOUNE M.
Interactions between ferrite recrystallization and austenite formation in high-strength steels. *Journal of Materials Science*, vol. 49, 2014, p. 3608-3621.
- [CHE 88] CHEN L., BRAKMAN C., KOREVAAR B., MITTEMEIJER E.
The tempering of iron-carbon martensite; dilatometric and calorimetric analysis. *Metallurgical Transactions A*, vol. 19A, 1988, p. 2415-2426.
- [CHE 14] CHEN H., XU X., XU W., ZWAAG S. v. D.
Predicting the austenite fraction after intercritical annealing in lean steels as a function of the initial microstructure. *Metallurgical and Materials Transactions A*, vol. 45A, 2014, p. 1675-1679.
- [CHE 16a] CHEN G., ZHANG F., RUIMI A., FIELD D., SUN X.
Quantifying the effects of tempering on individual phase properties of DP980 steel with nanoindentation. *Materials Science and Engineering A*, vol. 667, 2016, p. 240-249.
- [CHE 16b] CHEN H., ZHU B., MILITZER M.
Phase field modeling of cyclic austenite-ferrite transformations in Fe-C-Mn alloys. *Metallurgical and Materials Transactions A*, vol. 47, 2016, p. 3373-3881.
- [CHO 68] CHOJNOWSKI E., TEGART W.
Accelerated spheroidization of pearlite. *Metal Science Journal*, vol. 2, 1968, p. 14-18.
- [CHR 81] CHRISTIAN J.
The theory of transformation in metals and alloys. *Pergamon*, 1981.

- [COA 72] COATES D.
Diffusion-controlled precipitate growth in ternary system I. *Metallurgical Transactions*, vol. 3, 1972, p. 1203-1212.
- [COA 73] COATES D.
Diffusion-controlled precipitate growth in ternary system II. *Metallurgical Transactions*, vol. 4, 1973, p. 1077-1086.
- [COL 11] COLLA V., DESANCTIS M., DIMATTEO A., LOVICU G., VALENTINI R.
Prediction of continuous cooling transformation diagrams for dual-phase steels from the intercritical region. *Metallurgical and Materials Transactions A*, vol. 42, 2011, p. 2781-2793.
- [COM 12] COMMISSION E.
Research fund for coal and steel. Cold-rolled complex phase (CP) steel grades with optimised bendability, stretch-flangeability and anisotropy (CP-steels). , 2012.
- [COU 14] OF THE COUNCIL E. P.
Regulation (EU) No 333/2014 of the European Parliament and of the Council of 11 March 2014 amending Regulation (EC) No 443/2009 to define the modalities for reaching the 2020 target to reduce CO2 emissions from new passenger cars. , 2014, p. L103/15-L103/21.
- [DAN 16] DANOIX F., SAUVAGE X., HUIN D., GERMAIN L., GOUNE M.
A direct evidence of solute interactions with a moving ferrite/austenite interface in a model Fe-C-Mn alloy. *Scripta Materialia*, vol. 121, 2016, p. 61-65.
- [DIC] DICTRA.Diffusion module of Thermo-Calc software, MOBFE3 database Steels/Fe-alloys mobility database version 3 (accessed 23 July 2016).
- [EST 83] ESTAY S., CHENGJI L., PURDY G.
Carbide dissolution and austenite growth in the intercritical annealing of Fe-C-Mn dual-phase steels. *Canadian Institute of Mining and Metallurgy*, vol. 23, n° 1, 1983, p. 121-130.
- [FAB 14] FABREGUE D., MOUAWAD B., HUTCHINSON C.
Enhanced recovery and recrystallization of metals due to an applied current. *Scripta Materialia*, vol. 92, 2014, p. 3-6.
- [FIN 03] FINEL A., MAZIERE D., VERON M.
Thermodynamics, microstructures and plasticity. *Kluwer Academic Publishers*, 2003.
- [FUR 04] FURUHARA T., KOBASYAH K., MAKI T.
Control of cementite precipitation in lath martensite by rapid heating and tempering. *ISIJ International*, vol. 44, n° 11, 2004, p. 1937-1944.
- [GAR 17] GARCIN T., UEDA K., MILITZER M.
Reverse austenite transformation and grain growth in a low-carbon steel. *Metallurgical and Materials Transactions A*, vol. 48, n° 2, 2017, p. 796-808.
- [GLE a] GLEEBLE.Dilatometer, url: <https://www.leeble.com/dilatometer.html>.
- [GLE b] GLEEBLE.Thermomechanical simulator 3500, url: <https://www.leeble.com/products/leeble-3500.html>.

- [GOU 12] GOUNE M., MAUGIS P., DRILLET J.
A criterion for the change from fast to slow regime of cementite dissolution in Fe-C-Mn steels. *Journal of Materials Science*, vol. 28, n° 8, 2012, p. 728-736.
- [GOU 15] GOUNE M., DANOIX F., AGREN J., BRECHET Y., HUTCHINSON C., MILITZER M., PURDY G., ZWAAG S. V. D., ZUROB H.
Overview of the current issues in austenite to ferrite transformation and the role of migrating interfaces therein for low alloyed steels. *Materials Science and Engineering R*, vol. 92, 2015, p. 1-38.
- [GRA 47] GRANGE R. A., HOLT W. S., TKAC E. T.
Transformation of Austenite in an Aluminum-chromium-molybdenum Steel. *Transactions of the American Institute of mining and metallurgical engineers*, vol. 172, 1947, p. 452-466.
- [GRA 77] GRANGE R., HARIBAL C., PORTER L.
Hardness of tempered martensite in carbon and low-alloy steels. *Metallurgical Transactions A*, vol. 8A, 1977, p. 1775-1785.
- [HAN 10] HANTCHERLI M.
Influence d elements d addition sur les transformations de la martensite revenue dans des aciers faiblement allies. *PhD, Ecole Nationale Supérieure des Mines de Saint-Etienne*, 2010.
- [HIL 98] HILLERT M.
Phase equilibria, Phase diagrams and phase transformations, their thermodynamic basis. *Cambridge*, 1998.
- [HOU 02] HOUZE M. Influence des traitements thermiques sur le pouvoir thermoelectrique des aciers de cuve: effet des evolutions microstructurales des zones fortement segregées, 2002.
- [HUA 04] HUANG J., POOLE W., MILITZER M.
Austenite formation during intercritical annealing. *Metallurgical and Materials Transactions A*, vol. 35A, 2004, p. 3363-3375.
- [HUL 47] HULTGREN A.
Isothermal transformation of austenite. *Transactions of the American Society for Metals*, vol. 39, 1947, p. 915-1005.
- [HUM 95] HUMPHREYS F., HATHERLY M.
Recrystallization and related annealing phenomena. *Elsevier*, 1995.
- [III] III. P. Deutsches Elektronen-Synchrotron (DESY, Hambourg), url: http://photon-science.desy.de/facilities/petra_iii/beamlines/p07_high_energy_materials_science/index_eng.html.
- [JOH 39] JOHNSON W., MEHL R.
Reaction kinetics in processes of nucleation and growth. *Trans. Aime*, vol. 135, n° 8, 1939, p. 396-415.
- [KHA 90] KHAN S., BHADESHIA H.
Kinetics of martensitic transformation in partially bainitic 300M steel. *Materials Science and Engineering A*, vol. 129, n° 2, 1990, p. 257-272.

- [KIR 73] KIRCHNER G., NISHIZAWA T., UHRENIUS B.
The distribution of chromium between ferrite and austenite and the thermodynamics of the alpha/gamma equilibrium in the Fe-Cr and Fe-Mn systems. *Metallurgical Transactions*, vol. 4, 1973, p. 167-174.
- [KIS 57] KISSINGER H.
Reaction kinetics in differential thermal analysis. *Analytical chemistry*, vol. 29, n° 11, 1957, p. 1702-1706.
- [KLE 05] KLEBER X., MASSARDIER V., MERLIN J.
La mesure du pouvoir thermoelectrique: une technique originale de controle des alliages metalliques. *Techniques de l'Ingenieur*, vol. 9, 2005, p. 1-9.
- [KOI 59] KOISTINEN D., MARBURGER R.
A general equation prescribing the extent of the austenite-martensite transformation in pure iron-carbon alloys and plain carbon steels. *Acta Materialia*, vol. 7, 1959, p. 59-60.
- [KOL 37] KOLMOGOROV A.
On the statistical theory of the crystallization of metals. *Bull. Acad. Sci. USSR, Math. Ser.*, vol. 1, 1937, p. 355-359.
- [KRA 99] KRAUSS G.
Martensite in steel: strength and structure. *Materials Science and Engineering A*, vol. 273, 1999, p. 40-57.
- [KRE 11] KREBS B., GERMAIN L., HAZOTTE A., GOUNE M.
Banded structure in Dual Phase steels in relation with the austenite-to-ferrite transformation mechanisms. *Journal of Materials Science*, vol. 46, n° 21, 2011, p. 7026-7038.
- [KRI 97] KRIELAART G., SIETSMA J., ZWAAG S. v. D.
Ferrite formation in Fe-C alloys during austenite decomposition under non-equilibrium interface conditions. *Materials Science and Engineering*, vol. 237, 1997, p. 216-233.
- [KUL 13a] KULAKOV M., POOLE W., MILITZER M.
The effect of the initial microstructure on recrystallization and austenite formation in a DP600 steel. *ISIJ International*, vol. 54, 2013, p. 3564-3576.
- [KUL 13b] KULAKOV M. Microstructure evolution during intercritical annealing of Mn-Cr Dual-Phase Steel, 2013.
- [KUL 14] KULAKOV M., POOLE W., MILITZER M.
A microstructure evolution model for intercritical annealing of a low-carbon dual-phase steel. *Metallurgical and Materials Transactions A*, vol. 44A, n° 11, 2014, p. 2627-2636.
- [LAI 14] LAI Q. Optimisation de la microstructure d'aciers ferrito-martensitiques a 3.5pds% Mn: des transformations de phase a la micro-mecaniques, 2014.
- [LAI 16] LAI Q., GOUNE M., PIERLADE A., PARDOEN T., JACQUES P., BOUAZIZ O., BRECHET Y.
Mechanism of austenite formation from spheroidized microstructure in an intermediate Fe-0.1C-3.5Mn steel. *Metallurgical and Materials Transactions A*, vol. 47, n° 7, 2016, p. 3375-3386.
- [LAM 14] LAMONTAGNE A. Etude des mecanismes physiques responsables des evolutions microstructurales des aciers perlitiques au cours du trefilage et du vieillissement post-trefilage, 2014.

- [LAM 16] LAMONTAGNE A., MASSARDIER V., SAUVAGE X., KLEBER X., MARI D.
Evolution of carbon distribution and mechanical properties during the static strain ageing of heavily drawn pearlitic steel wires. *Materials Science and Engineering A*, vol. 667, 2016, p. 115-124.
- [LAN 17] LANDEGHEM H. V., LANGELIER B., GAULT B., PANAH D., KORINEK A., PURDY G., ZUROB H.
Investigation of solute/interphase interaction during ferrite growth. *Metallurgical and Materials Transactions A*, vol. 124, 2017, p. 536-543.
- [LEE 98] LEEUWAN Y. V., VOOLJS S., SIETSMA J., ZWAAG S. V. D.
The effect of geometrical assumptions in modeling solid-state transformation kinetics. *Metallurgical and Materials Transactions A*, vol. 29, 1998, p. 2925-2931.
- [LEG 10] LEGUEN C. Precipitation controlled prior austenite grain size in steels, 2010.
- [LI 13] LI P., LI J., HU W., XU D.
Effect of the heating rate on ferrite recrystallization and austenite formation of cold-rolled dual-phase steel. *Journal of Alloys and Compounds*, vol. 578, 2013, p. 320-327.
- [LI 17] LI H., ZHANG H., LV Z., ZHU Z.
Cementite dissolution kinetics of high carbon chromium steel during intercritical austenitization. *Journal of Phase Equilibrium Diffusion*, , 2017.
- [LU 11] LU Y., MOLODOV D. A., GOTTSTEIN G.
Recrystallization kinetics and microstructure evolution during annealing of a cold-rolled Fe-Mn-C alloy. *Acta Materialia*, vol. 59, 2011, p. 3229-3243.
- [LUP 72] LUPTON D., WARRINGTON D.
The influence of deformation on the spheroidization and coarsening of pearlite. *Metal Science Journal*, vol. 6, 1972, p. 200-204.
- [MAA 16] MAALEKIAN M., AZIZI-ALIZAMINI H., MILITZER M.
Phase field modeling of microstructure banding in steels. *Metallurgical and Materials Transactions A*, vol. 47, n° 1, 2016, p. 608-622.
- [MAR 00] MARDER A.
The metallurgy of zinc-coated steel. *Progress in Materials Science*, vol. 45, n° 3, 2000, p. 191-271.
- [MAS 03] MASSARDIER V., GUETAZ M., MERLIN J., SOLER M.
Kinetics and microstructural study of aluminium nitride precipitation in a low carbon aluminium-killed steel. *Materials Science and Engineering A*, vol. 355, 2003, p. 299-310.
- [MAS 14] MASSARDIER V., GOUNE M., FABREGUE D., SELOUANE A., DOUILLARD T., BOUAZIZ O.
Evolution of microstructure and strength during ultra-fast tempering of Fe-Mn-C martensitic steels. *Journal of Materials Science*, vol. 49, 2014, p. 7782-7796.
- [MAT 12] MATLOCK D., SPEER J., DE MOOR E., GIBBS P.
Recent developments in advanced high strength sheet steels for automotive applications: an overview. *JESTECH*, vol. 15, n° 1, 2012, p. 1-12.

- [MAT 17] MATUSIEWICZ P., AUGUSTYN-NADZIEJA J., CZARSKI A., SKOWRONEK T.
Kinetics of pearlite spheroidization. *Archi. Metall. Mater.*, vol. 62, n° 1, 2017, p. 241-244.
- [MCQ 77] MCQUEEN H.
The production and utility of recovered dislocation substructures. *Metallurgical Transactions A*, vol. 8, 1977, p. 807-824.
- [MEC 15] MECOZZI M., BOS C., SIETSMA J.
A mixed-mode model for the ferrite-to-austenite transformation in a ferrite/pearlite microstructure. *Acta Materialia*, vol. 88, 2015, p. 302-313.
- [MIL 11] MILITZER M.
Phase field modeling of microstructure evolution in steels. *Current Opinion in Solid State and Materials Science*, vol. 15, 2011, p. 106-115.
- [MIL 13] MILITZER M., GARCIN T., POOLE W.
In-situ measurements of grain growth and recrystallization by laser ultrasonics. *Materials Science Forum*, vol. 753, 2013, p. 25-30.
- [MIT 88] MITTEMEJER E., CHENG L., SCHAAF V. D. P., BRAKMAN C., KOREVAAR B.
Analysis of non-isothermal transformation kinetics; tempering of iron-carbon and iron-nitrogen martensites. *Metallurgical Transactions A*, vol. 19, 1988, p. 925-932.
- [MIY 07] MIYAMOTO G., OH J., HONO K., FURUHARA T., MAKI T.
Effect of partitioning of Mn and Si on the growth kinetics of cementite in tempered Fe-0.6mass% C. *Acta Materialia*, vol. 55, 2007, p. 5027-5038.
- [MOH 11] MOHANTY R., GIRINA O., FONSTEIN N.
Effect of the heating rate on the austenite formation in low-carbon high-strength steels annealed in the intercritical region. *Metallurgical and Materials Transactions A*, vol. 42A, 2011, p. 3680-3690.
- [MOR 01] MORRA P., BOTTGER A., MITTEMEJER E.
Decomposition of iron-based martensite. A kinetics analysis by means of differential scanning calorimetry and dilatometry. *Metallurgical Transactions A*, vol. 64, 2001, p. 905-914.
- [MOR 05] MORITO S., SAITO H., OGAWA T., FURUHARA T., MAKI T.
Effect of austenite grain size on the morphology and crystallography of lath martensite in low carbon steels. *Acta Materialia*, vol. 45, 2005, p. 91-94.
- [MOR 15] MORSDOLF L., TASAN C., PONGE D., RAABE D.
3D structural and atomic-scale analysis of lath martensite: effect of the transformation sequence. *Acta Materialia*, vol. 95, 2015, p. 366-377.
- [NAR 14] NARAGHI R., SELLEBY M., AGREN J.
Thermodynamics of stable and metastable structures in Fe-C system. *CALPHAD: Computer Coupling of Phase Diagrams and Thermochemistry*, vol. 46, 2014, p. 148-158.
- [NOR 35] NORDHEIM L., GORTER G.
Bemerkungen über Thermokraft und Widerstand. *Physica*, vol. 2, 1935, p. 383-390.

-
- [OFF 12] OFFERMAN S., SHARMA H.
Following individual grains during solid-state phase transformation with 3DXRD microscopy. *Comptes rendus physiques*, vol. 13, n° 3, 2012, p. 268-279.
- [OGA 10] OGAWA T., MARUYAMA N., SUGIURA N., YOSHINAGA N.
Incomplete recrystallization and subsequent microstructural evolution during intercritical annealing in cold-rolled low-carbon steels. *ISIJ International*, vol. 50, n° 3, 2010, p. 469-475.
- [OGA 15] OGAWA T.
Ferrite recrystallization and austenite formation at the early stage of annealing in cold-rolled low-carbon steels. *International Journal of Mechanical and Materials Engineering*, , 2015.
- [OGA 17] OGAWA T., DANNOSHITA H., MARUOKA K., USHIODA K.
Microstructural evolution during cold rolling and subsequent annealing in low-carbon steel with different initial microstructures. *Journal of Materials Engineering and Performance*, vol. 26, n° 8, 2017, p. 469-4753821-3830.
- [OLI 07] OLIVEIRA F., ANDRADE M., COTA A.
Kinetics of austenite formation during continuous heating in a low carbon steel. *Materials characterization*, vol. 58, 2007, p. 256-261.
- [OLL 17] OLLAT M., MASSARDIER V., FABREGUE D., KEOVILAY F., BUSCARLET E., PEREZ M.
Modeling of the recrystallization and austenite formation overlapping in cold-rolled dual-phase steels during intercritical treatments. *Metallurgical and Materials Transactions A*, , 2017, p. 1-14.
- [OLS 76a] OLSON G., COHEN M.
A general mechanism of martensitic nucleation: Part I. General concepts and the FCC->HCP transformation. *Metallurgical Transactions A*, vol. 7A, 1976, p. 1897-1904.
- [OLS 76b] OLSON G., COHEN M.
A general mechanism of martensitic nucleation: Part II. FCC->HCP and other martensitic transformation. *Metallurgical Transactions A*, vol. 7A, 1976, p. 1905-1914.
- [OLS 76c] OLSON G., COHEN M.
A general mechanism of martensitic nucleation: Part III. Kinetics of martensitic nucleation. *Metallurgical Transactions A*, vol. 7A, 1976, p. 1915-1923.
- [OYA 08] OYARZABAL M., MARTINEZ-DE GUERENU A., GUTIERREZ I.
Effect of stored energy and recovery on the overall recrystallization kinetics of a cold rolled low carbon steel. *Materials Science and Engineering A*, vol. 485, 2008, p. 200-209.
- [PAY 44] PAYSON P., SAVAGE C.
Martensite reactions in alloy steels. *Trans ASM*, vol. 33, 1944, p. 261-280.
- [PER 08] PEREZ M., DUMONT M., ACEVEDO-REYES D.
Implementation of classical nucleation and growth theories for precipitation. *Acta Materialia*, vol. 56, n° 9, 2008, p. 2119-2132.

- [PIE 14] PIERMAN A., BOUAZIZ O., PARDOEN T., JACQUES P., BRASSART L.
The influence of microstructure and composition on the plastic behaviour of dual-phase steels. *Acta Materialia*, vol. 73, 2014, p. 298-311.
- [POR 09] PORTER D., EASTERLING K., SHERIF M.
Phase transformations in Metals and Alloys, Third edition. 2009.
- [PUR 64] PURDY G., WEICHERT D., KIRKALDY J.
Growth of eutectoid ferrite in ternary iron-carbon-manganese austenites. *Transactions of the Metallurgical Society of AIME*, vol. 230, n° 5, 1964, Page 1025.
- [PUR 11] PURDY G., AGREN J., BORGSTAM A., BRECHET Y., ENOMOTO M., FURUHARA T., GAMSJAGER E., GOUNE M., HILLERT M., HUTCHINSON C., MILITZER M., ZUROB H.
ALEMI: a ten-year history of discussion of alloying-element interaction with migrating interfaces. *Metallurgical and Material Transaction A*, vol. 42A, 2011, p. 3703-3718.
- [QIU 15] QIU C., ZUROB H., HUTCHINSON C.
The coupled solute drag effect during ferrite growth in Fe-C-Mn-Si alloys using controlled decarburization. *Acta Materialia*, vol. 100, 2015, p. 333-343.
- [ROC 05] ROCHA R., MELO T., PERELOMA E., SANTOS D.
Microstructural evolution at the initial stages of continuous annealing of cold-rolled dual-phase steel. *Materials Science and Engineering A*, vol. 381, 2005, p. 296-304.
- [RUD 11] RUDNIZKI J., BOTTGER B., PRAHL U., BLECK W.
Phase-field modeling of austenite formation from a ferrite plus pearlite microstructure during annealing of cold-rolled dual-phase steel. *Metallurgical and Materials Transactions A*, vol. 42, 2011, p. 2516-2525.
- [RUD 12] RUDNIZKI J., PRAHL U., BLECK W.
Phase-field modeling of microstructure evolution during processing of cold-rolled dual phase steel. *Integrating Materials and Manufacturing Innovation*, vol. 1:3, 2012, p. 1-13.
- [SAI 16] SAIED M. Experimental and numerical modeling of the dissolution of ferrite in the Fe-Cr-Ni system: application to austenitic stainless steels, 2016.
- [SAV 07] SAVRAN V., VAN LEEUWEN Y., HANLON D., KWAKERNAK C., SLOOF W., SIESTMA J.
Microstructural features of austenite formation in C35 and C45 alloys. *Metallurgical and Materials Transactions A*, vol. 38A, 2007, p. 946-955.
- [SAV 09] SAVRAN V. I. Austenite formation in C-Mn steel, 2009.
- [SAV 10] SAVRAN V., OFFERMAN S., SIESTMA J.
Austenite nucleation and growth observed on the level of individual grains by three-dimension X-ray diffraction microscopy. *Metallurgical and Materials Transactions A*, vol. 41, n° 3, 2010, p. 538-591.
- [SCH 07] SCHNEIDER A., INDEN G.
Carbon diffusion in cementite and Hagg carbide. *Computer Coupling of Phase Diagrams and Thermochemistry*, vol. 31, 2007, p. 141-147.

- [SIE 04] SIETSMA J., ZWAAG S. v. D.
A concise model for mixed-mode phase transformation in the solid state. *Acta Materialia*, vol. 52, 2004, p. 4143-4152.
- [SKR 91] SKROTZKI B.
The course of the volume fraction of martensite vs. temperature function $M_x(T)$. *Journal de Physique IV*, vol. C4, 1991, p. 367-.
- [SON 11] SONG T., KWAK J., COOMAN D. D.
On the processing of martensitic steels in continuous galvanizing lines: part I. *Metallurgical and Materials Transactions A*, vol. 12A, 2011.
- [SPE 72] SPEICH G., LESLIE W.
Tempering of steel. *Metallurgical Transactions A*, vol. 3, 1972, p. 1043-1054.
- [SPE 81] SPEICH G., DEMAREST V., MILLER R.
Formation of austenite during intercritical annealing of dual-phase steels. *Metallurgical Transactions A*, vol. 12A, 1981, p. 1419-1428.
- [THE] THERMO-CALC.TCFE8 database Steels/Fe-alloys database version 8 (accessed 23 July 2016).
- [THO 90] THOMPSON S., COLVIN D., KRAUSS G.
Continuous cooling transformations and microstructures in a low-carbon, high-strength low-alloy plate steel. *Metallurgical Transactions A*, vol. 21A, 1990, p. 1493-1506.
- [THO 97] THOMSON R., MILLER M.
Carbide precipitation in martensite during the early stages of tempering Cr- and Mo-containing low alloy steels. *Acta Materialia*, vol. 46, n° 6, 1997, p. 2203-2213.
- [TIA 87] TIAN Y., KRAFT R.
Mechanisms of pearlite spheroidization. *Metallurgical Transactions A*, vol. 18A, 1987, p. 1403-1414.
- [VAN 10] VAN BOHEMEN S., SIETSMA J.
The kinetics of bainite and martensite formation in steels during cooling. *Materials Science and Engineering A*, vol. 527, 2010, p. 6672-6676.
- [VAN 14] VAN BOHEMEN S., SIETSMA J.
Kinetics of martensite formation in plain carbon steels: critical assessment of possible influence of austenite grain boundaries and autocatalysis. *Materials Science and Technology*, vol. 30, n° 9, 2014, p. 1024-1033.
- [WAN 99] WANG J., VAN DER WOLK P., VAN DER ZWAAG S.
Effect of carbon concentration and cooling rate on continuous cooling transformations predicted by artificial neural network. *ISIJ International*, vol. 39, n° 10, 1999, p. 1038-1046.
- [WAN 00] WANG J., VAN DER WOLK P., VAN DER ZWAAG S.
Determination of martensite start temperature in engineering steels. Part I Empirical relations describing the effect of steel chemistry. *Material Transactions*, vol. 41, n° 7, 2000, p. 761-768.
- [WAT 03] WATERSCHOOT T. Ferrous alloys: static strain aging and tempering in dual phase steels, 2003.

- [WAT 06] WATERSCHOOT T., VERBEKEN K., DE COOMAN B.
Tempering kinetics of the martensite phase in DP steel. *ISIJ International*, vol. 46, n° 1, 2006, p. 138-146.
- [WEI 13] WEI R., ENOMOTO M., HADIAN R., ZUROB H., PURDY G.
Growth of austenite from as-quenched martensite during intercritical annealing in an Fe-0.1C-3Mn-1.5Si alloy. *Acta Materialia*, vol. 61, 2013, p. 697-707.
- [WIT 00] WITS J., KOP T., LEEUWEN V. Y., SIETSMA J., ZWAAG S. V. D.
A study on the austenite-to-ferrite phase transformation in binary substitutional iron alloys. *Materials Science and Engineering A*, vol. 283, 2000, p. 234-241.
- [XIA 16] XIAO Y., LI W., ZHAO H., LU X., JIN X.
Investigation of carbon segregation during low temperature tempering in a medium carbon steel. *Materials Characterization*, vol. 117, 2016, p. 84-90.
- [YAN 85a] YANG D., BROWN E., MATLOCK D., KRAUSS G.
Ferrite recrystallization and austenite formation in cold-rolled intercritically annealed steel. *Metallurgical Transactions A*, vol. 16, n° 8, 1985, p. 1385-1392.
- [YAN 85b] YANG D., BROWN E., MATLOCK D., KRAUSS G.
The formation of austenite at low intercritical annealing temperatures in a normalized 0.08C-1.45Mn-0.21Si steel. *Metallurgical Transactions A*, vol. 16A, 1985, p. 1523-1526.
- [ZHE 13] ZHENG C., RAABE D.
Interaction between recrystallization and phase transformation during intercritical annealing in a cold-rolled dual-phase steel: a cellular automaton model. *Acta Materialia*, vol. 61, 2013, p. 5504-5517.
- [ZHU 12] ZHU B., MILITZER M.
3D phase field modelling of recrystallization in a low-carbon steel. *Modelling and Simulation in Materials Science and Engineering*, vol. 20, 2012, p. 1-17.
- [ZHU 13] ZHU K., CHEN H., MASSE J., BOUAZIZ O., GACHET G.
The effect of prior ferrite formation on bainite and martensite transformation kinetics in advanced high-strength steels. *Acta Materialia*, vol. 61, 2013, p. 6025-6036.
- [ZHU 15] ZHU B., MILITZER M.
Phase-field modelling for intercritical annealing of a dual-phase steel. *Metallurgical and Materials Transactions A*, vol. 46, 2015, p. 1073-1084.
- [ZUR 09] ZUROB H., HUTCHINSON C., BRECHET Y., SEYEDREZAI H., PURDY G.
Kinetics transitions during non-partitioned ferrite growth in Fe-C-X alloys. *Acta Materialia*, vol. 57, 2009, p. 2781-2792.



FOLIO ADMINISTRATIF

THESE DE L'UNIVERSITE DE LYON OPEREE AU SEIN DE L'INSA LYON

NOM : OLLAT

DATE de SOUTENANCE : le 20 octobre 2017

Prénoms : Mélanie

TITRE : Characterization and modeling of microstructural evolutions occurring during thermal treatment of cold-rolled Dual-Phase steels

NATURE : Doctorat

Numéro d'ordre : 2017LYSEI097

École doctorale : ED 34 Matériaux de Lyon

Spécialité : Matériaux

RÉSUMÉ :

Dual-Phase steels (DP) are one of the most used Advanced High Strength Steels (AHSS) in automotive applications because they present a good strength/ductility compromise and they adapt to number of industrial constraints (low price, shaping, welding, coating etc.). Nowadays, the development of DP steels seems to be promising and sustainable for the body-in-white structure. The typical ferrite-martensite microstructure, characteristic of DP steels, is obtained by a thermal treatment composed of different stages during which metallurgical evolutions occur. Major difficulties of their processing are due to the fact that (i) microstructural evolution kinetics are influenced by cycle parameters (heating rate, annealing temperature...), (ii) different stages are interconnected and (iii) some microstructural evolutions may overlap and therefore, interact.

This PhD-work aimed at getting a better understanding of microstructural evolutions during the thermal cycle of DP steels and, namely, the influence of cycle parameters. Different microstructural evolutions occurring during the thermal cycle were first characterized coupling different experimental techniques (dilatometry, hardness, TEP etc.) and with a particular protocol in order to decorrelate overlapping and interconnected phenomena. For example, two major evolutions occurring during the intercritical annealing were first studied individually ((1) Recrystallization was investigated below austenite formation temperature and (2) Austenite formation was investigated on prior recrystallized steels) before investigating cold-rolled steel where recrystallization and austenite formation overlap.

The study also aimed at developing some predictive tools to describe microstructural evolutions based on phenomenological approaches (JMAK law) towards more physical based models (mixed-mode, diffusive models). A particular care was attached to discuss on model reliability, versatility, strengths and limitations.

MOTS-CLÉS : Dual-Phase steels, Thermal treatment, Recrystallization, Phase transformation, Modeling

Laboratoire (s) de recherche : MATEIS – UMR CNRS 5510
INSA de Lyon
25 Avenue Jean Capelle
69621 VILLEURBANNE CEDEX

Directeur de thèse : Véronique MASSARDIER (Maitre de conférences), Michel PEREZ (Professeur) et Damien FABREGUE (Professeur)

Président de jury :

Composition du jury :	Sybrand Van Der ZWAAG	(Professeur)
	Elisabeth GAUTIER	(Directeur de recherches)
	Yves BRECHET	(Professeur)
	Mohamed GOUNE	(Professeur)
	Eric BUSCARLET	(Ingénieur Docteur)
	Philippe ROCABOIS	(Ingénieur Docteur)